



I. R. IRAN

ISSN: 2423-7167

e-ISSN: 1735-9244



International Journal of Engineering

Journal Homepage: www.ije.ir



TRANSACTIONS C: ASPECTS

Volume 35, Number 09, September 2022

Materials and Energy Research Center

INTERNATIONAL JOURNAL OF ENGINEERING

Transactions C: Aspects

DIRECTOR-IN-CHARGE

A. R. Khavandi

EDITOR-IN-CHIEF

G. D. Najafpour

ASSOCIATE EDITOR

A. Haerian

EDITORIAL BOARD

- | | | | |
|------|--|-------|---|
| S.B. | Adeloju, Charles Sturt University, Wagga, Australia | A. | Mahmoudi, Bu-Ali Sina University, Hamedan, Iran |
| K. | Badie, Iran Telecomm. Research Center, Tehran, Iran | O.P. | Malik, University of Calgary, Alberta, Canada |
| M. | Balaban, Massachusetts Ins. of Technology (MIT), USA | G.D. | Najafpour, Babol Noshirvani Univ. of Tech., Babol, Iran |
| M. | Bodaghi, Nottingham Trent University, Nottingham, UK | F. | Nateghi-A, Int. Ins. Earthquake Eng. Seis., Tehran, Iran |
| E. | Clausen, Univ. of Arkansas, North Carolina, USA | S. E. | Oh, Kangwon National University, Korea |
| W.R. | Daud, University Kebangsaan Malaysia, Selangor, Malaysia | M. | Osanloo, Amirkabir Univ. of Tech., Tehran, Iran |
| M. | Ehsan, Sharif University of Technology, Tehran, Iran | M. | Pazouki, Material and Energy Research Center, Meshkindasht, Karaj, Iran |
| J. | Faiz, Univ. of Tehran, Tehran, Iran | J. | Rashed-Mohassel, Univ. of Tehran, Tehran, Iran |
| H. | Farrahi, Sharif University of Technology, Tehran, Iran | S. K. | Sadrnezhaad, Sharif Univ. of Tech, Tehran, Iran |
| K. | Firoozbakhsh, Sharif Univ. of Technology, Tehran, Iran | R. | Sahraeian, Shahed University, Tehran, Iran |
| A. | Haerian, Sajad Univ., Mashhad, Iran | A. | Shokuhfar, K. N. Toosi Univ. of Tech., Tehran, Iran |
| H. | Hassanpour, Shahrood Univ. of Tech., Shahrood, Iran | R. | Tavakkoli-Moghaddam, Univ. of Tehran, Tehran, Iran |
| W. | Hogland, Linnaeus Univ, Kalmar Sweden | T. | Teng, Univ. Sains Malaysia, Gelugor, Malaysia |
| A.F. | Ismail, Univ. Tech. Malaysia, Skudai, Malaysia | L. J. | Thibodeaux, Louisiana State Univ, Baton Rouge, U.S.A |
| M. | Jain, University of Nebraska Medical Center, Omaha, USA | P. | Tiong, Nanyang Technological University, Singapore |
| M. | Keyanpour rad, Materials and Energy Research Center, Meshkindasht, Karaj, Iran | X. | Wang, Deakin University, Geelong VIC 3217, Australia |
| A. | Khavandi, Iran Univ. of Science and Tech., Tehran, Iran | | |

EDITORIAL ADVISORY BOARD

- | | | | |
|-------|--|-------|--|
| S. T. | Akhavan-Niaki, Sharif Univ. of Tech., Tehran, Iran | A. | Kheyroddin, Semnan Univ., Semnan, Iran |
| M. | Amidpour, K. N. Toosi Univ of Tech., Tehran, Iran | N. | Latifi, Mississippi State Univ., Mississippi State, USA |
| M. | Azadi, Semnan university, Semnan, Iran | H. | Oraee, Sharif Univ. of Tech., Tehran, Iran |
| M. | Azadi, Semnan University, Semnan, Iran | S. M. | Seyed-Hosseini, Iran Univ. of Sc. & Tech., Tehran, Iran |
| F. | Behnamfar, Isfahan University of Technology, Isfahan | M. T. | Shervani-Tabar, Tabriz Univ., Tabriz, Iran |
| R. | Dutta, Sharda University, India | E. | Shirani, Isfahan Univ. of Tech., Isfahan, Iran |
| M. | Eslami, Amirkabir Univ. of Technology, Tehran, Iran | A. | Siadat, Arts et Métiers, France |
| H. | Hamidi, K.N.Toosi Univ. of Technology, Tehran, Iran | C. | Triki, Hamad Bin Khalifa Univ., Doha, Qatar |
| S. | Jafarmadar, Urmia Univ., Urmia, Iran | S. | Hajati, Material and Energy Research Center, Meshkindasht, Karaj, Iran |
| S. | Hesaraki, Material and Energy Research Center, Meshkindasht, Karaj, Iran | | |

TECHNICAL STAFF

M. Khavarpour; M. Mohammadi; V. H. Bazzaz, R. Esfandiar; T. Ebadi

DISCLAIMER

The publication of papers in International Journal of Engineering does not imply that the editorial board, reviewers or publisher accept, approve or endorse the data and conclusions of authors.

CONTENTS

Transactions C: Aspects

S. M. Jameii; K. Khanzadi	A Latency Reduction Method for Cloud-fog Gaming based on Reinforcement Learning	1674-1681
A. J. Naji; H. M. Al-Jelawy; A. Hassoon; A. Al-Rumaithi	Axial Behavior of Concrete Filled-steel Tube Columns Reinforced with Steel Fibers	1682-1689
T. Tuswan; E. N. Sari; A. Ismail; A. R. Prabowo	Experimental Evaluation on Palm Oil and Sesame Oil-based Resin Properties as Core Sandwich Material for Lightweight Ship Structure	1690-1698
G. D. Dhadse; G. Ramtekkar; G. Bhatt	Effect of Particle Size, Moisture Content and Density on the Hyperbolic Model Parameters for Non-cohesive Soil	1699-1706
M. Mahmoodi; H. Tagimalek; M. R. Maraki; S. Karimi	Experimental and Numerical Investigation of the Formability of Cross and Accumulative Roll Bonded 1050 Aluminum Alloy Sheets in Single Point Incremental Forming Process	1707-1715
B. Thakur; A. Desai	Aspects of Foundation-soil Interaction of Nuclear Structures under Seismic Conditions through the State-of-art Review	1716-1722
F. Ghorbani Valikchali; M. Rahimnejad; A. Ramiar; M. Ezoji	Diagnostics Devices for Improving the World: μ PADs Integrated with Smartphone for Colorimetric Detection of Dopamine	1723-1727
M. Gholami; S. Zarei	Testable MUXED-D Scan Cell in Quantum-dot Cellular Technology	1728-1734
K. D. Tandel; J. V. Menghani	Effect of Friction Stir Processing on Fusion Welded Joint of Al-5083	1735-1743
O. M. Makki; H. M. K. Al-Mutairee	Mechanical and Dynamical Properties of Structural Rubcrete Mixes	1744-1751
M. Q. Mutair; M. A. Abdulrehman; K. M. Eweed	Relationship Between Compressive Strength and Non-destructive Tests of Colored Geopolymer Concrete Based on Fly Ash	1752-1758
M. Arehpanahi; A. M. Entekhabi	A New Technique for Online Open Switch Fault Detection and Location in Single-phase Pulse Width Modulation Rectifier	1759-1764
M. Sadeghian	The Reliability Assessment of a Ship Structure under Corrosion and Fatigue, using Structural Health Monitoring	1765-1778

M. Pasra; M. W. Tjaronge; M. A. Caronge; A. R. Djamaluddin; F. E. P. Lapian; M. Tumpu	Influence of Tensile Load on Bonding Strength of Asphalt Concrete Containing Modified Buton Asphalt and Polyethylene Terephthalate Waste: A Case Study of Indonesian Roads	1779-1786
S. Naveen; G. Bhat	Effect of Elevated Temperature on Engineered Cementitious Composites using Natural River Sand	1787-1794
J. Sivamani	Sustainable Utilization of Dumped Concrete Wastes as Fine Aggregates in Concrete – An Experimental Study	1795-1802



A Latency Reduction Method for Cloud-fog Gaming based on Reinforcement Learning

S. M. Jameii^a, K. Khanzadi^b

^a Department of Computer Engineering, Shahr-e-Qods Branch, Islamic Azad University, Tehran, Iran

^b Department of Computer Engineering, Science and Research Branch, Islamic Azad University, Tehran, Iran

PAPER INFO

Paper history:

Received 27 January 2022

Received in revised form 27 March 2022

Accepted 01 April 2022

Keywords:

Reinforcement Learning

Computation Latency

Cloud-fog Gaming

Principal Component Analysis

ABSTRACT

Unlike traditional gaming where a game runs locally on a user's device, in cloud gaming, an online video game runs on remote servers and streams directly to a user's device. This caused players to become independent of having high hardware resources in their local computers. Since video games are a kind of latency-sensitive application, cloud servers far from users are not suitable. In fog computing, fog nodes are in the vicinity of users and can reduce the latency. In this paper, a latency reduction method based on reinforcement learning is proposed to determine which computing fog node can run the video games with the lowest latency. In the proposed method, a Principal Component Analysis (PCA) based approach is used to extract the most important features of each video game as the input of the learning process. The proposed method was implemented using Python. Experimental results show that the proposed method compared to some existing methods can reduce the frame latency and increase the frame rate of video games.

doi: 10.5829/ije.2022.35.09c.01

1. INTRODUCTION

Nowadays, users are capable of executing video games on different platforms such as smartphones, personal computers, etc. Execution of these video games is independent of the computation resources of the users' local devices. In 2009, cloud gaming was introduced and its main idea was to run the video game on remote servers and stream them directly to a user's device [1]. Hence, video games would be developed for computers in the cloud rather than for personal computers. Afterward, game producers rent the cloud's computer and bandwidth. User Experience (UX) is an important aspect of playing video games in which latency is one of the most important issues in UX for playing video games in Cloud-Fog Computing (CFC). In 2013, Huang et al. [2] proposed the first open-source cloud gaming system called "Gaming anywhere". Cloud gaming systems such as Gaikai, OnLive, and Stream My Game, had been proposed before Gaming anywhere but these cloud gaming systems suffered from inappropriate response

time. Bonomi et al. [3] proposed the first fog computing paradigm in 2012. Fog computing has characteristics such as low latency which can bring services to the edge of the network. Another advantage of fog computing is geographical distribution. In a fog computing environment, many nodes in each region can serve as sufficiently as possible. We should consider another type of latency called system latency for playing a video game on the fog and cloud nodes¹. This latency is the delay between the mouse or keyboard actions and the resulting pixel changes on the user's display and should be considered for calculating the total latency of video games.

In this paper, a latency reduction method based on reinforcement learning is proposed to determine which computing fog node can run the video games with the lowest latency. At the first of the proposed method, a Principal Component Analysis (PCA) based approach is used to extract the most important features of each video game as the input of the learning process.

Reinforcement learning is dynamically learning by

*Corresponding Author Institutional Email: Jamei@qodsiau.ac.ir (S. M. Jameii)

¹ <https://www.nvidia.com/en-us/geforce/news/reflex-low-latency-platform>

adjusting actions based on continuous feedback to maximize a reward [4]. Since the objective of this paper is dynamically select the best fog node in a distributed manner to play the video game, we can have a learning agent for each fog node to interact with the environment. This kind of learning expresses how states can be mapped to actions to maximize reward signals. This way the agent does not tell what actions it should do, but it discovers which actions have the most reward signal.

Markov Decision Processes (MDP) is a mathematical framework to describe an environment in reinforcement learning. It provides a mathematical framework for modeling decision-making in situations where outcomes are partly random and partly under the control of a decision-maker [5]. Since the problem of this paper will be solved by reinforcement learning, the Markov chain is a very useful framework to model this problem based on by taking a sequence of actions. From a time perspective, MDPs can be sub-divided into two categories named Discrete-Time Markov Chain (DTMC) and Continuous-Time Markov Chain (CTMC) [6]. A random process can be defined as a chain of random variables. There is a feature named Markov property that refers to a memory-less property of random processes. A random process has Markov property if the future probability distribution is dependent only on the current state but not on a sequence of events that preceded it [6]. MDPs, consist of three aspects: sensing, action, and goal. An agent must sense the state of the environment and then consider actions that take effect on the state. Each method that can solve this kind of problem, is known as the reinforcement learning method.

Since each video game has many features (more than 26 features) and analyzing these features incurs high overhead, we have used PCA to reduce the number of features. So essential features which are a lot informative will be selected and less informative features will not be considered. PCA combines essential features with a substituted feature which leads to smaller sets of features. Since the feature reduction is done before starting the game and it is done on the machines of the users (not on fog nodes), it does not incur significant overhead.

The contributions of this paper are as follows:

- 1) A PCA-based approach is used to extract the most important features of each video game to be considered as the input of the learning process.
- 2) A distributed reinforcement learning process is proposed that can compute the score of each fog node and select the best fog node to play each video game based on its characteristics and consuming resources.
- 3) The proposed method can significantly reduce the frame latency and increase the frame rate of video games.

The rest of our paper is organized as follows: In section 2, we overview the related works. In section 3, we present

the proposed algorithm. Section 4 is the simulation and experimental results. Finally, we conclude the paper in section 5.

2. RELATED WORKS

In this section, some of the works that used reinforcement learning for decision-making in cloud-fog environments were reviewed. Talaat et al. [7] used reinforcement learning for resource allocation and process migration. For resource allocation, the reinforcement algorithm selects the best fog server based on the fast response time. For process migration, the reinforcement algorithm selects the process for migration based on the process weight to designate priority for selecting the suitable process for migration. Zhang et al. [8] proposed a framework named EdgeGame to adjust video bit rate adaptively to match the network dynamics. Also, in the paradigm of cloud gaming to compensate for the dynamic nature of networks; they used deep reinforcement learning to adjust the traffic from the edge nodes to the users and to accommodate the varying bandwidth in the dynamic network. In the paradigm of Mobile Edge Computing (MEC), Zhang and Zheng [9] proposed a technique for task migration based on the Deep-Q network. In their work, the agent can learn optimal task migration policy from previous experiences without the need for a user's mobility pattern in the future. Chen et al. [10] proposed an adaptive real-time video game streaming policy in the dynamic network based on deep reinforcement learning to control bit rate adaptively. In 2018, Chen et al. [11] proposed a computation of floating algorithm based on deep q-network named Darling to learn the optimal policy without knowing prior knowledge of network dynamics. This algorithm was proposed for the MEC in which mobile devices are not fully capable of computing intensive tasks locally. Thus there should be a policy to determine whether to compute the tasks locally or offload them to the MEC server, considering the dynamic nature of the network. Dutreilh et al. [12] proposed an automatic decision-making approach for resource allocation without previous knowledge of the application performance model. In their work, the agent learns to add, maintain or reduce the number of VMs allocated to the application. In 2018, Wang et al. [13] tried to make a tradeoff between energy consumption and service delay in vehicular networks. They proposed a novel model to depict the users' willingness of contributing their resources to the public. In 2018, Dinh et al. [14] proposed a model-free reinforcement learning offloading mechanism in which mobile users can learn their long-term offloading strategy to maximize their long-term utilization. This mechanism

was proposed to prevent a scenario in which many mobile users offload their tasks to the same edge node at the same time. In 2019, Huang et al. [15] proposed an online offloading framework that utilizes deep reinforcement learning that learns the offloading decisions from the experience. This offloading policy was done in the MEC network which could decide to compute tasks locally or offload them to the MEC server. Because the channel state conditions are time-varying in wireless networks, the offloading decisions and resource allocations should adapt themselves to these dynamic conditions.

3. THE PROPOSED METHOD

In this section, a latency reduction method based on reinforcement learning is proposed to determine which computing fog node can run the video games with the lowest latency. At first in subsection 3.1, a Principal Component Analysis (PCA) based approach is used to extract the most important features of each video game as the input of subsection 3.2.

3.1. Feature Selection using PCA

PCA is a feature reduction method in which the original data transfers to a smaller space which leads to the reduction of the features. On the other hand, PCA combines essential features with a substituted feature which leads to a smaller set of features. In this section, by utilizing the PCA method, we try to apply PCA to reduce the 26 features of video games to 2 primary components and then extract the most important features from them. The steps of applying PCA to reduce the features are as follows:

1. Assume X_1, X_2, \dots, X_Z are feature set and each X_i represents as $N \times 1$ vectors. (Z is the total number of features and is assumed equal to 26 and N is the number of rows in the dataset. At the first step, each feature is normalized between 0 to 1).
2. The average vector is calculated as follows:

$$\bar{X} = \frac{1}{Z} \sum_{i=1}^Z X_i \quad (1)$$

3. For each vector, subtract the average vector of it and produce the matrix $A = [\Phi_1, \Phi_2, \dots, \Phi_Z]$ ($N \times Z$ matrix) as follows:

$$\Phi_i = X_i - \bar{X} \quad (2)$$

4. Covariance matrix is calculated as follows:

$$Cov = \frac{1}{Z} \sum_{i=1}^Z \Phi_i \Phi_i^T \quad (3)$$

where Φ_i^T is the transformation matrix of Φ_i

5. From the covariance matrix, we can compute eigenvalues and eigenvectors and sort the

eigenvectors ascendingly. The highest value of eigenvalue means the highest significance of the corresponding features. Top 2 eigenvectors with the highest eigenvalue form the principal components of the data set.

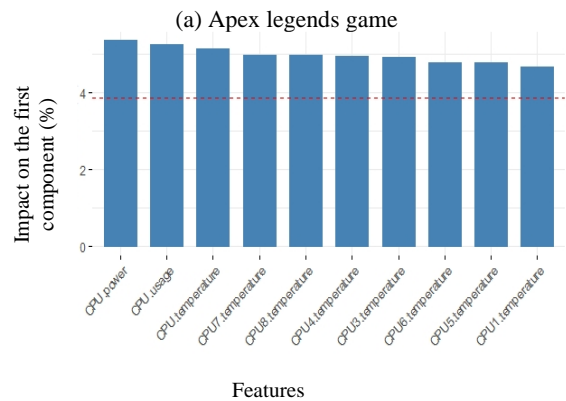
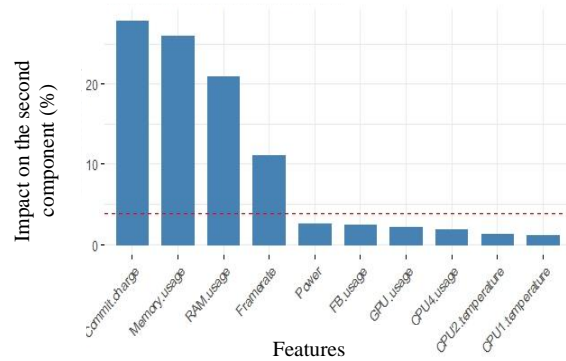
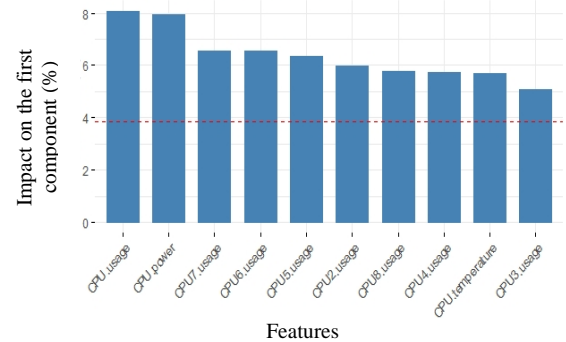
The impact of the important features on the 2 primary components categorized by video games are depicted in Figure 1.

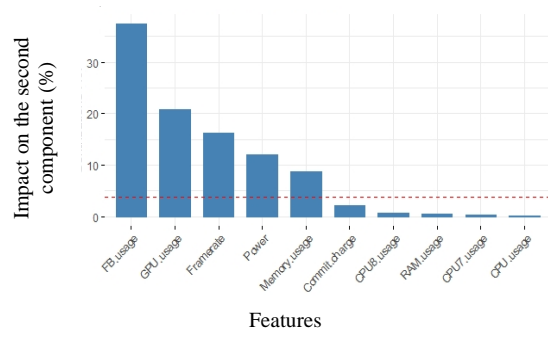
In Table 1, the selected features for each video game that have more impact on the primary components are demonstrated.

3.2. Fog Node Score Calculation

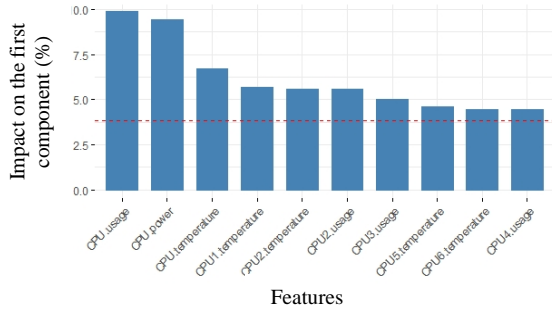
Algorithm1

calculates the score for each fog node. The less difference between video game consumed resource and fog node remainder resource is, the more score the related fog node

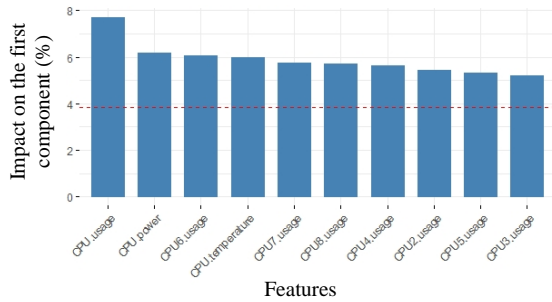




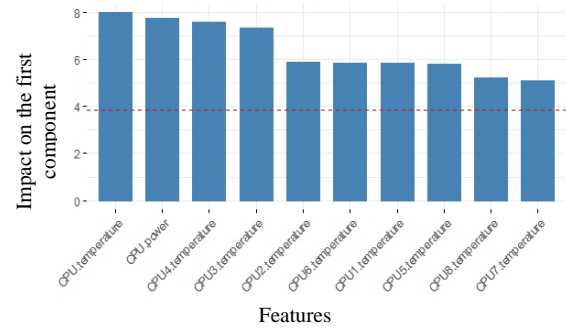
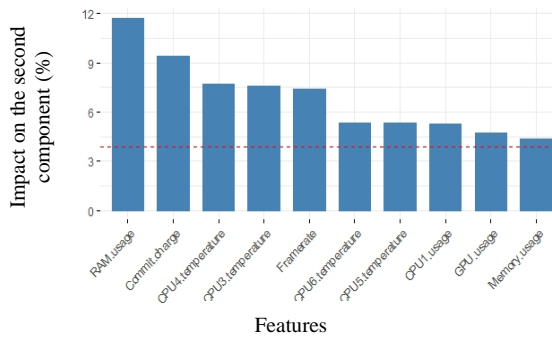
(b) Battlefield 4 game



(c) Warthunder game



(d) Forza horizon 4 game



(e) CS: GO game

Figure 1. The impact of the important features on the 2 primary components categorized by video games**TABLE 1.** Selected features for each video game

Video game	Selected features
Apex Legends	CPU.usage, CPU.power, Commit. charge
Battlefield 4	CPU.power, CPU.usage, FB.usage
Warthunder	CPU.usage, CPU.power, GPU.usage
Forza horizon 4	CPU.usage, CPU.power, RAM.usage
CS: GO	CPU.temprature, CPU.power, CPU.usage

Algorithm 1

- **Input:** Randomly generated numbers for fog nodes resources and the captured resources from video games.
- **Output:** Fog node scores for each video game

For each video game

For each fog node

Calculate the difference between video game consumed resources and the remainder of fog nodes resources

Calculate the plural of differences of all fog node resources

Sort plural of differences in ascending manner

Give more scores to fewer plural differences

Return the calculated fog node score.

will receive. To be more clear, for example, two fog nodes have been compared to see which of them is a better fog node in terms of remainder resources.

In this paper, only 3 fog nodes have been considered, thus scores are designated between 0 to 2. Only features that have been selected by PCA are considered for selecting the fog node. In the next subsection, the produced scores for fog nodes are used as input for the reinforcement algorithm for selecting the best fog node.

3. 3. Calculating the Fog Node Selection Priorities using Reinforcement Learning

In this subsection, an algorithm based on reinforcement learning is proposed for selecting the best fog node. After calculating the scores of the fog nodes by Algorithm 1, the Q matrix will be initialized. Each element of this matrix has two parts which are called the actions 0 and 1. With these actions, we can say whether the agent selects the current fog node or selects another fog node with a higher score. Each action has its related q-value. The action with a higher q-value will be selected. The agent periodically monitors the environment that consists of fog nodes. The agent learns which fog nodes could receive more scores. The problem is modeled as a Markov Decision Process (MDP) in Figure 2. The MDP that models our approach to select the best fog node is defined as Equation (4):

$$M = \langle B, A, T, P, \gamma \rangle \quad (4)$$

in which,

$B = \{(n, p) \mid 1 < n < n_{\max} \wedge 1 < p < p_{\max}\}$ is the state of the MDP where n is the fog node index and p is the score which is calculated for fog node.

- $A = \{a \mid 0 < a \leq 1\}$ is the action set. When the agent compares two fog nodes' scores, if the first fog node has higher a score than the second fog node, the action 0 will be selected which means the selection of the first fog node with the probability of $P_{S_1S_1}$ or $P_{S_2S_2}$. But if the second fog node has a higher score than the first fog node, action 1 will be selected which means the selection of the second fog node with the probability of $P_{S_1S_2}$ or $P_{S_2S_1}$.

P is the probability distribution $p(r/s, a)$ of observing reward r when the agent is in state s and action a is taken.

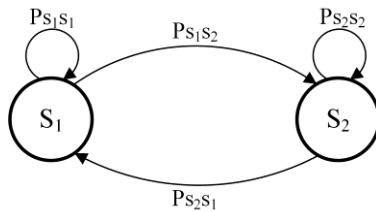


Figure 2. MDP for solving the stated problem

- γ , $0 < \gamma < 1$ is defined as a discount factor that determines how important a future reward is. When it has a value near 0, the agent tends more to the current state and when it has a value near 1, the agent tends more to the future state.
- T is the probability distribution $P(s'|s, a)$ of transition to state s' when the agent is in state s and action a is taken.

According to Dutreilh et al. [12], T and P are difficult to estimate because they require heavy experimentation and measurement. Due to this fact and to overcome these limitations, reinforcement learning has been proposed to learn these two parameters by interaction with the environment. In the proposed method, Q-learning has been used as one of the reinforcement learning approaches. After calculating each score of fog nodes by Algorithm 1, the Q-matrix will be created with mentioned characteristics. In this step, the agent interacts with the environment and then updates the current state and q-value in Q-matrix. Then the action with a higher q-value will be selected. Eventually, the q-values in Q-table will be updated. The agent updates Q-values by Q-learning formula which is as Equation (5):

$$Q(\text{CurrentState}, \text{Action}) = (1 - \text{LearningRate}) * \text{Current}_q + \text{LearningRate} * (\text{reward} + \text{Discount} * \text{MaxFuture}_q) \quad (5)$$

Now the Q-table has been formed and we can use its policies for selecting the fog nodes. Algorithm 2 for calculating the Q-table is as follows:

Algorithm 2

- Input:** Calculated scores by Algorithm 1 for each video game.
- Output:** Q-table policies for selecting the best fog node

For each score calculated score by Algorithm 1

Create fog node objects and assign the related scores

Initialize the Q-table

Agent updates the current state and actions by interaction with the environment

Observing possible actions from Q-table, then the agent selects the action with higher q-value

Updating q-values in q-table

If learning process reward == pre-designated reward:

Move to the next episode

Else:

Continue steps from the beginning

The end of the episodes

4. PERFORMANCE EVALUATION

4.1. Experimental Setup The proposed method was implemented using *Python 3.6*. At first, we ran 5 video games distinctly to capture resource consumption by *MSI Afterburner*. The obtained data frame in CSV format had 26 columns of features. Thus we had to extract the most important features which had the most variance among others. By using the PCA approach mentioned in the previous section, the first 3 features have been extracted. Then by using *Python* and utilizing object-oriented programming, fog nodes have been created as objects. A total of 3 fog nodes have been considered. For each fog node and each episode of the learning process, resources have been initialized using calculated scores by Algorithm 1. By assigning fog node scores, the learning process starts. Totally 5000 episodes have been considered. For each episode, 200 steps have been considered.

4.2. Experimental Results Our data has been captured from playing 15 minutes of 5 video games named Battlefield 4, Warthunder, Counter Strike Global Offensive (CS:GO), Forza horizon 4, Apex legends. Each tuple of the data contains 26 attributes. Each tuple indicates one second. All of the features have been normalized, transferred into the same scale between zero and one.

The results of the reinforcement learning for determining each fog node priority are stated in Table 2 categorized by each video game. For instance, to play apex Legends video game, fog node number 0 has the highest priority.

To evaluate the suggested fog nodes priorities, the frame rate per second and frame latency have been measured for three fog nodes and all of the five video games during 15 minutes. Each game was run for 15 minutes and the average of the results is demonstrated in Table 3. The fog node with a higher frame rate has a lower frame latency. As can be seen in Table 3, for the Apex legends game, fog node 0 has the lowest latency compared to the other fog nodes. For Battlefield 4 game, fog node 2 has the lowest latency and for CS: GO game, fog node 0 has the lowest latency. Fog node 1 has the lowest latency for the Forza Horizon 4 game and the Warthunder game, fog node 0 has the lowest latency.

TABLE 2. Fog node priority for each video game

	Priority #1	Priority #2	Priority #3
Apex Legends	Fog node #0	Fog node #1	Fog node #2
Battlefield 4	Fog node #2	Fog node #0	Fog node #1
CS: GO	Fog node #0	Fog node #1	Fog node #2
Forza horizon 4	Fog node #1	Fog node #2	Fog node #0
Warthunder	Fog node #0	Fog node #2	Fog node #1

TABLE 3. The average of FPS and frame latency of fog nodes for video games

Video Games	Fog nodes	Average FPS	Average frame latency (ms)
Apex legends	Fog node # 0	143	6.26
	Fog node # 1	139	6.31
	Fog node # 2	135	6.37
Battlefield 4	Fog node # 0	195	4.61
	Fog node # 1	166	5.36
	Fog node # 2	268	3.19
CS: GO	Fog node # 0	123	7.3
	Fog node # 1	55	23.8
	Fog node # 2	22	45.5
Forza horizon 4	Fog node # 0	120	7.1
	Fog node # 1	240	3.9
	Fog node # 2	184	5
Warthunder	Fog node # 0	290	2.8
	Fog node # 1	42	29.3
	Fog node # 2	129	6.7

Based on Table 3, the best fog nodes are selected for each video game and the corresponding results (FPS and latency) are compared to the approaches proposed by Zhang et al. [8] and Chen et al. [11]. Table 4 and Figure 3 demonstrate the results of comparing the average frame per second of the proposed method and the approaches proposed by Zhang et al. [8] and Chen et al. [11].

As can be seen, the proposed method has a higher average frame rate in all video games. This is because, in the proposed method, reinforcement learning is utilized to determine the best fog node for playing video games considering the frame rate. The objective of Zhang et al. [8] was to reduce bandwidth consumption and the objective of Chen et al. [11] was to maximize the long-term utility performance. After the proposed method, the EdgeGame has a better frame rate than the Darling approach.

Table 5 and Figure 4 demonstrate the result of comparing the average frame latency of the proposed method and the approaches proposed by Zhang et al. [8] and Chen et al. [11].

TABLE 4. The average of frame per second

	Apex Legends	Battlefield 4	CS: GO	Forza horizon 4	Warthunder
proposed method	143	268	123	240	290
EdgeGame [8]	118	255	115	200	188
Darling [11]	80	145	45	110	90

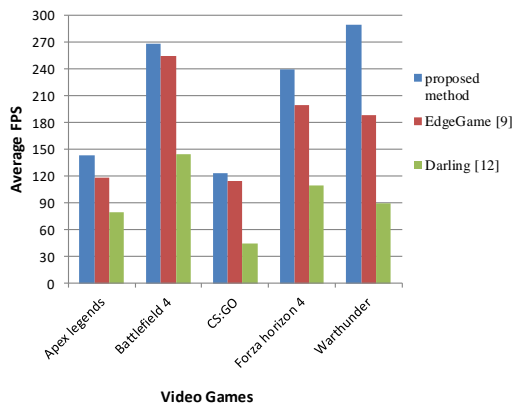


Figure 3. Comparing the average of frame per second

TABLE 5. The average frame latency

	Apex Legends	Battlefield 4	CS: GO	Forza horizon 4	Warthunder
proposed method	6.26	3.19	7.3	3.9	2.8
EdgeGame [8]	8.8	5	9	6.3	5.6
Darling [11]	14	8.1	13.4	12	11

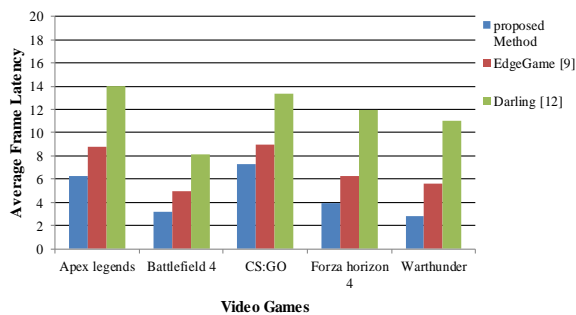


Figure 4. Comparing the average of frame latency

It can be observed that the average frame latency in the proposed method is less than two other approaches. This can be explained by the reason that the proposed method has a better frame rate and more frame rate leads to less frame latency. Among all video games, playing Battlefield 4 resulted in the least frame latency, and CS:GO resulted in the most frame latency.

5. CONCLUSION

Cloud gaming is a new paradigm that makes game players independent of having high-end hardware on

their local computers. Since video games are a kind of latency-sensitive application, a latency reduction method based on reinforcement learning was proposed in this paper to appropriately select the fog node for running the video games on it with the lowest latency. We tried to apply PCA to reduce the 26 features of video games to 2 primary components and then extracted the most important features from them. The proposed method was implemented using Python and 5 video games named Battlefield 4, Warthunder, Counter Strike Global Offensive (CS:GO), Forza horizon 4, Apex legends were run for 15 minutes. Experimental results demonstrated that the proposed method compared to some existing methods reduced the frame latency and increase the frame rate of video games.

6. REFERENCES

- Ross, P. E., "Cloud computing's killer app: Gaming," *IEEE Spectrum*, Vol. 46, No. 3, (2009), 4-14, doi: 10.1109/MSPEC.2009.4795441.
- Huang, C. Y., Hsu, C. H., Chang, Y.C., and Chen, K.T., "GamingAnywhere: an open cloud gaming system," in 4th ACM multimedia systems conference, Oslo, Norway (2013), 36-47, <https://doi.org/10.1145/2537855>.
- Bonomi, F., Milito, R., Zhu, J., and Addepalli, S., "Fog computing and its role in the internet of things," first edition of the MCC workshop on Mobile cloud computing, New York, United States, (2012), 13-16, <https://doi.org/10.1145/2342509.2342513>.
- Yaghmaee, F., Koohi, H., "Dynamic Obstacle Avoidance by Distributed Algorithm based on Reinforcement Learning," *International Journal of Engineering, Transactions B: Applications*, Vol. 28, No. 2, (2015), 198-204, doi: 10.5829/idosi.ije.2015.28.02b.05.
- rezaei, H., Motameni, H., Barzegar, B., "A Hidden Markov Model for Morphology of Compound Roles in Persian Text Part of Tagging," *International Journal of Engineering, Transactions B: Applications*, Vol. 34, No. 11, (2021), 2494-2507, doi: 10.5829/IJE.2021.34.11B.12.
- Mo, J., "Performance modeling of communication networks with Markov chains," *Synthesis Lectures on Data Management*, Vol. 3, No. 1, (2010), 1-90, doi: 10.2200/S00269ED1V01Y201004CNT005.
- Talaat, F.M., Saraya, M.S., Saleh, A.I., Ali, H. A., and Ali, S.H., "A load balancing and optimization strategy (LBOS) using reinforcement learning in fog computing environment", *Journal of Ambient Intelligence and Humanized Computing* (2020), 1-16, <https://doi.org/10.1007/s12652-020-01768-8>.
- Zhang, X., Chen, H., Zhao, Y., Ma, Z., Xu, Y., Huang, H., and Wu, D. O. "Improving cloud gaming experience through mobile edge computing", *IEEE Wireless Communications*, Vol. 26, No. 4, (2019), 178-183, doi: 10.1109/MWC.2019.1800440.
- Zhang, C., and Zheng, Z., "Task migration for mobile edge computing using deep reinforcement learning," *Future Generation Computer Systems*, Vol. 96, (2019), 111-118, <https://doi.org/10.1016/j.future.2019.01.059>.
- Chen, H., Zhang, X., Xu, Y., Ren, J., Fan, J., Ma, Z. and Zhang, W., "T-Gaming: A Cost-Efficient Cloud Gaming System at Scale", *IEEE Transactions on Parallel and Distributed Systems*, Vol. 30, No. 12, (2019), 2849-2865, doi: 10.1109/TPDS.2019.2922205.

11. Chen, X., Zhang, H., Wu, C., Mao, S., Ji, Y. and Bennis, M., "Optimized computation offloading performance in virtual edge computing systems via deep reinforcement learning," *IEEE Internet of Things Journal*, Vol. 6, No. 3, (2018), 4005-4018, doi: 10.1109/JIOT.2018.2876279.
12. Dutreilh, X., Kirgizov, S., Melekhova, O., Malenfant, J., Rivierre, N. and Truck, I., "Using reinforcement learning for autonomic resource allocation in clouds: towards a fully automated workflow," The Seventh International Conference on Autonomic and Autonomous Systems, Venice, Italy, (2011), 67-74, ISBN: 978-1-61208-134-2.
13. Wang, Y., Wang, K., Huang, H., Miyazaki, T. and Guo, S., "Traffic and computation co-offloading with reinforcement learning in fog computing for industrial applications," *IEEE Transactions on Industrial Informatics*, Vol. 15, No. 2, (2018), 976-986, doi: 10.1109/TII.2018.2883991.
14. Dinh, T.Q., La, Q.D., Quek, T.Q. and Shin, H., "Learning for Computation Offloading in Mobile Edge Computing," *IEEE Transactions on Communications*, Vol. 66, No. 12, (2018), 6353-6367, doi: 10.1109/TCOMM.2018.2866572.
15. Huang, L., Bi, S. and Zhang, Y.J.A., "Deep reinforcement learning for online computation offloading in wireless powered mobile-edge computing networks," *IEEE Transactions on Mobile Computing*, Vol. 19, No. 11, (2019), 2581-2593, doi: 10.1109/TMC.2019.2928811.

Persian Abstract

چکیده

بر خلاف بازی های قدیمی که یک بازی روی یک دستگاه کاربر بصورت محلی اجرا می شد، در بازی های ابری یک بازی ویدئویی برخط روی سرورهای راه دور ابری اجرا می شوند و نتایج پردازش ها بصورت مستقیم به دستگاه کاربر ارسال می شوند. این باعث می شود که بازیکنان از داشتن منابع سخت افزاری با قابلیت بالا در کامپیوتر های محلی خود بی نیاز شوند. از آنجا که بازی های ویدئویی نوعی از برنامه های حساس به تاخیر هستند، سرورهای ابری که دور از کاربران قرار گرفته اند مناسب نیستند. در محاسبات مه، گره های مه در مجاورت کاربران قرار گرفته اند و قادرند تاخیر را کاهش دهند. در این مقاله، روشی مبتنی بر یادگیری تقویتی جهت کاهش تاخیر ارائه شده است تا مشخص کند کدام گره محاسباتی مه می تواند بازی های ویدئویی را با کمترین تاخیر اجرا کند. همچنین در روش پیشنهادی، یک روش مبتنی بر تحلیل مولفه اصلی (PCA) استفاده شده تا مهمترین ویژگی های هر بازی ویدئویی را به عنوان ورودی فرآیند یادگیری استخراج کند. روش پیشنهادی توسط نرم افزار پاپتون پیاده سازی شد. نتایج آزمایشات نشان می دهد روش پیشنهادی در مقایسه با برخی روش های موجود می تواند برای بازی های ویدئویی تاخیر فریم را کاهش داده و نرخ فریم را افزایش دهد.



Axial Behavior of Concrete Filled-steel Tube Columns Reinforced with Steel Fibers

A. J. Najja^{a,b}, H. M. Al-Jelawy^{*a}, A. Hassoon^c, A. Al-Rumaithi^d

^a Roads and Transport Engineering Department, University of Al-Qadisiyah, Diwaniyah, Iraq

^b Civil Engineering Department, Peoples' Friendship University of Russia (RUDN University), Moscow, Russia

^c Civil Engineering Department, University of Al-Qadisiyah, Diwaniyah, Iraq

^d Department of Civil Engineering, University of Baghdad, Baghdad, Iraq

PAPER INFO

Paper history:

Received 19 December 2021

Received in revised form 02 April 2022

Accepted 07 April 2022

Keywords:

Concrete

Steel Tube

Composite Elements

Steel Fibers

Ductility

Columns

ABSTRACT

Concrete filled steel tube (CFST) columns are being popular in civil engineering due to their superior structural characteristics. This paper investigates enhancement in axial behavior of CFST columns by adding steel fibers to plain concrete that infill steel tubes. Four specimens were prepared: two square columns (100*100 mm) and two circular columns (100 mm in diameter). All columns were 60 cm in length. Plain concrete mix and concrete reinforced with steel fibers were used to infill steel tube columns. Ultimate axial load capacity, ductility and failure mode are discussed in this study. The results showed that the ultimate axial load capacity of CFST columns reinforced with steel fibers increased by 28% and 20 % for circular and square columns, respectively. Also, the circular CFST columns exhibited better ductility than the square CFST columns due to better concrete confinement. Circular and square CFST columns with steel fibers showed improved ductility by 16.3% and 12%, respectively. The failure mode of the square CFST columns were local buckling which occurred near the end of columns, while, for the circular CFST columns, local buckling occurred near the mid-height. Also, the study involved sectional analysis that captured the behavior of CFST columns very well. The sectional analysis showed that increasing steel fiber content to 2% increased the axial load capacity by 51 and 38% for circular and square CFST columns, respectively. Furthermore, sectional analysis showed that doubling section size increased axial load capacity by approximately 4 and 5 times for circular and square columns, respectively.

doi: 10.5829/ije.2022.35.09c.02

NOMENCLATURE

N_u	Analytical ultimate axial load capacity of CFST specimens (kN)	D	Steel tube diameter (mm)
N_{mu}	Measured ultimate axial load capacity of CFST specimens (kN)	DI	Ductility index
f_y	yield stress of steel (MPa)	$\Delta_{85\%}$	Column axial shortening when the column reaches to 85 % of its ultimate strength during the post-peak region (mm)
f'_c	Compressive strength of concrete (MPa)	Δ_u	Column axial shortening measured at ultimate strength (mm)
A_s	Cross-sectional area of the steel tube (mm ²)	E_c	Modulus of elasticity for concrete
A_c	Cross-sectional area of concrete (mm ²)	E_o	Modulus of elasticity for steel
SI	Strength index	E_p	Strain hardening modulus for steel
B	Steel tube width (mm)	ϵ_y	Yield strain of steel
t	Steel tube thickness (mm)		

1. INTRODUCTION

The idea of composite elements appeared as an attempt for maximum utilization of properties of various construction materials. A composite construction

element is a construction element which is produced from two or more constituent materials where the properties of the composite section become different from, and ultimately better than those of the individual constituent material [1].

*Corresponding Author Institutional Email:
haider.aljelawy@qu.edu.iq (H. M. Al-Jelawy)

Please cite this article as: A. J. Naji, H. M. Al-Jelawy, A. Hassoon, A. Al-Rumaithi, Axial Behavior of Concrete Filled-steel Tube Columns Reinforced with Steel Fibers, *International Journal of Engineering, Transactions C: Aspects*, Vol. 35, No. 09, (2022) 1682-1689

One of the most common applications to utilize composite action to enhance properties of concrete members is using FRP composites [2-6].

Concrete filled steel tube (CFST) columns are widely being used in civil engineering applications, especially in large-span trusses in industrial cities, steel bridges and high-rise building structures. CFST columns have many advantages such as enhancement in column performance to fire resistance, increased concrete compression strength due to steel tube confinement effect, delayed local buckling due to the interaction between steel tube and concrete, and much less shrinkage and creep effects compared with conventional reinforced concrete column [7]. Using steel tube columns in construction field exhibited some issues like low resistance to fire and loss of stability under lateral and axial loads. Several solutions to strengthen steel columns have been presented such as covering the steel columns with concrete. This type of columns is used in steel structures exposed to fire. Usually, "I-section" or "T-section" steel are used for this type. Sometimes additional reinforcing steel is placed in the concrete layer around the section to prevent cracking under axial stress. Another type of steel columns is CFST columns. These columns are used in structures where risk of the fire is limited and they consist of square, circular or rectangular sections filled with concrete. These columns are commonly used in pillars of bridges, multi-story buildings, where they feature easy implementation when they do not need a template or any additional reinforcement. CFST columns can be a competitive choice for the common accelerated bridge construction techniques [8-13].

Several studies have been devoted to the field of CFST where properties of concrete infill was the main parameter discussed in these studies [14, 15].

The use of waste material in concrete has led to achieve economic benefits and improve environmental protection [16, 17], as well as enhancement in CFST behavior in the construction field. Yu et al. [18] conducted a study to investigate the replacement effect of different types of waste materials as alternatives for coarse aggregates on the performance of CFST. Five concrete mixes were used with different types of aggregate (normal coarse aggregate, lightweight coarse aggregate, steel slag coarse and fine aggregate, steel slag coarse aggregate and steel slag and glass coarse

aggregate). The results indicated that using different types of aggregate influenced the failure mode, improved axial and lateral strain, decreased the ultimate strength of lightweight concrete by 8.2% compared with normal concrete. The ultimate strength of steel slag coarse aggregate concrete, steel slag coarse and fine aggregate concrete, steel slag coarse aggregate concrete and steel slag and glass coarse aggregate concrete increased by 15.1-24.9% compared with normal concrete. Ductility of CFST with steel slag coarse and fine aggregate concrete and steel slag coarse aggregate concrete enhanced, while lightweight concrete and steel slag and glass coarse aggregate concrete exhibited decreased ductility.

Recently, reinforced CFST piles are widely used in foundations of piers and bridges for its good mechanical properties. Li et al. [19] investigated enhancement of CFST using concrete with reinforcing bars to infill steel columns. All specimens were tested under axial compression load. The results showed that the CFST column with concrete reinforcing bars has a higher ultimate load capacity and more effective plastic behavior compared with columns without reinforcing bars.

Fire resistance is an important parameter that influences the design of CFST columns that should be seriously treated, specifically in large constructions. Exposure to fire temperatures can decrease the strength and durability of concrete, appearance and structural performance. Furthermore, CFST columns are widely used in large and high-performance constructions. The post-fire strength of CFST was investigated by Alhatmey et al. [20]. Fire exposure of CFST columns for 30 min increased the compression resistance a little, while fire exposure of one hour decreased the compression resistance for the tested specimens. The effect of confined concrete in the CFST played an essential role and led to smaller resistance losses.

Many methods considered enhancing the bond stress between steel tube and concrete in previous studies. Tao et al. [21, 22] studied the efficiency of using shear studs and an internal welded ring to improve the bond strength of CFST members. A series of push-out tests on circular and square CFST specimens showed that internal welded ring onto the inner surface of the steel tube is more effective than shear studs to enhance bond stress.

TABLE 1. Proportions of concrete mixes

Mix	Column ID	Cement (kg)	Coarse Agg. (kg)	Fine Agg. (kg)	W/C	Steel Fibers	Compressive Strength (MPa)	Tensile Strength (MPa)
M1	MC0	340	1110	729	0.45	0%	27.5	3.0
	MS0	340	1110	729	0.45	0%	27.5	3.0
M2	MC1	340	1110	729	0.45	0.5%	30.1	3.9
	MS1	340	1110	729	0.45	0.5%	30.1	3.9

Adding fibers to concrete improves its homogeneity and isotropy and makes it a ductile material [23]. The present study is thus an attempt to study the efficiency of adding steel fibers to concrete mix to improve the behavior of CFST columns in terms of ultimate axial load capacity, ductility and failure mode.

2. EXPERIMENTAL WORK

2.1. Material Properties Ordinary Portland cement was used with water cement ratio of 0.45 to produce plain concrete in the laboratory. In fiber-reinforced concrete mixes, hooked end steel fibers (tensile stress between 200-2600 MPa, modulus of elasticity 200 GPa, ultimate elongation 0.5-5 %, specific gravity 7.8 g/cm³) were added with a ratio of 0.5 %. Fine and coarse aggregate from local sources were used according to Iraqi Specification No.45 (1984). Compression strength of concrete mixes were determined using concrete cubes (150*150*150 mm) and tensile strength for all mixes were determined by indirect tensile test (Brazilian Test) by using cylinder samples (100*200 mm). Proportion of concrete mixes and properties are presented in Table 1. Four CFST column specimens with a constant length of 60 cm were used and their steel tubes had a yield strength of 350 MPa.

2.2. Specimen Preparation and Testing The experimental study included two circular columns with 100 mm in diameter and two square columns with a cross sectional area of 100*100 mm (Figure 1). All columns had the same length (L) of 60 cm. Also, all columns were closed in one direction to avoid concrete leakage (Figure 2). Two types of concrete mixes were used to infill columns: plain concrete and concrete reinforced with steel fibers.

Columns were filled with concrete mixes at three layers and compacted (25 blows per layer) with steel rod having a diameter of 20 mm. All the specimens were tested under axial loading in a vertical setup using a universal testing machine. Figure 3 shows the specimens after casting.

3. RESULTS AND DISCUSSION

3.1. Ultimate Load The measured ultimate strength (N_{mu}) for CFST specimens is listed in Table 2. Equation (1) is used to calculate the analytical axial load capacity (N_u) for CSFT columns [24].

$$N_u = f_y A_s + 1.3 f'_c A_c \quad (1)$$

where N_u is the sum of section capacities of the steel tube and concrete, f_y and f'_c are the yield stress of steel and

compressive strength of concrete, respectively; A_s and A_c are the cross-sectional areas of the steel tube and concrete, respectively. Equation (2) is used to calculate the strength index (SI) [25].

$$SI = \frac{N_{mu}}{N_u} \quad (2)$$



Figure 1. Steel tubes for the CFST columns



Figure 2. Closing specimens from the bottom side



Figure 3. Specimens after casting

TABLE 2. Test results of columns

Column ID	Section			A_s (mm ²)	A_c (mm ²)	f'_c (MPa)	f_y (MPa)	N_u (kN)	N_{mu} (kN)	SI	DI
	B	D	t								
MC0	-	100	1.8	280	7574	27.5	350	368.8	398	1.08	2.83
MS0	100	-	2	392	9216	27.5	350	466.7	507	1.09	2.75
MC1	-	100	1.8	280	7574	30.1	350	394.4	507	1.28	3.29
MS1	100	-	2	392	9216	30.1	350	497.8	609	1.23	3.08

Figures 4 and 5 show the relationship between the axial load capacity and displacement for the columns in this study. The ultimate axial load capacity of circular

CFST column reinforced with steel fibers (MC1) increased by 28% compared with the control column (MC0), while it increased by 20% for square CFST column reinforced with steel fibers (MS1) compared with the control CFST column (MS0). This increase is related to the increase in compressive strength of the concrete that infills the tubes. The analytical ultimate strength estimated using Equation (1) was close to the experimental strength as seen in SI values in Table 2. However, the analytical strength was more conservative for CFST columns reinforced with steel fibers as seen in SI values. More accurate expressions are needed to estimate the axial strength for CFST columns reinforced with steel fibers.

3. 2. Ductility

Ductility usually refers to the ability of the structure or the element to undergo deformation beyond the yield point. For CFST columns, the axial ductility is measured using the ductility index (DI). The ductility index (DI) is the ratio between the measured axial shortening when the column reaches to 85 % of its ultimate strength during the post-peak region and the axial shortening measured at ultimate strength, and it is defined in the following equation [22, 26]:

$$DI = \frac{\Delta_{85\%}}{\Delta_u} \quad (3)$$

Generally, the circular columns exhibited better ductility than the square columns due to more uniform confinement that the circular shape provides for the concrete compared with the square shape. Circular and square CFST columns with steel fibers showed improved ductility by 16.3 and 12%, respectively, compared with the control columns without steel fibers. The improvement was due to the ductile behavior of steel fiber.

3. 3. Failure Mode

Test observations showed that the failure mode of the circular CFST column was local buckling near the mid-height (Figure 6a), while the failure mode for square CFST columns was local buckling that appeared near the column ends (Figure 6b). Future

studies are suggested to investigate seismic damage of CFST columns [27, 28].

4. MODELING VALIDATION

To verify the test outcomes and investigate the effect of other parameters on the axial behavior of CFST columns, numerical modeling can be very helpful.

Recent numerical studies have been conducted on axial behavior of CFST columns filled with conventional concrete and steel fiber-reinforced concrete that showed results which were in very good agreement with the test results [29-31]. Also, those numerical results are in good agreement with the experimental results in the current study. However, for axial behavior of composite



a) Circular column- local buckling at the mid-height b) square column- Local buckling at the column end

Figure 6. Failure modes of the columns

members, complex finite element softwares are not necessary to conduct the numerical analysis. Section analysis using any available software can be sufficient. In this study, section analyses were performed using MATLAB software package.

The specimens tested in the study were modeled using the uniaxial behavior of both concrete and steel materials shown in Figures 7 and 8. Concrete was modeled using stress-strain relationship proposed by Hognestad [32] and steel was modeled using a bilinear stress-strain relationship.

The modeling results are shown in Figures 9 and 10 for circular and square columns, respectively. It can be observed that modeling adequately captured the behavior of CFST columns. The initial stiffness of all columns is well captured using the numerical modeling.

The peak loads are also captured very well. Numerical post-peak behavior is comparable to the experimental behavior except that linear decay is observed due to the use of Hognestad' model for concrete.

4. 1. Effect of Steel Fiber Content

The tested specimens investigated one steel fiber content. However, using section analysis can be useful in investigating the behavior of other steel fiber contents. This is simply done by modifying the concrete stress-strain curve used in the

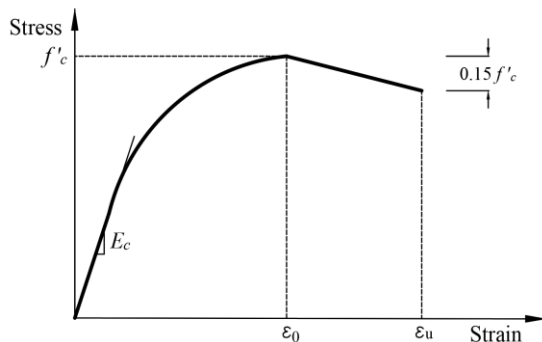


Figure 7. Hognestad' model for concrete

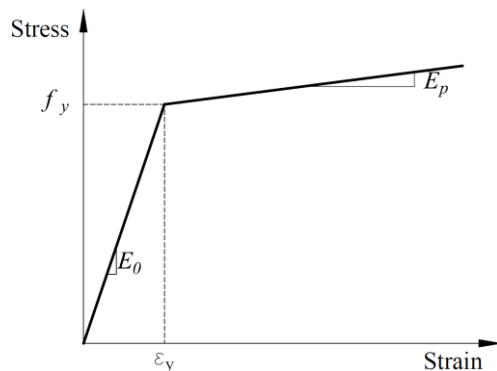


Figure 8. Stress-strain behavior of steel

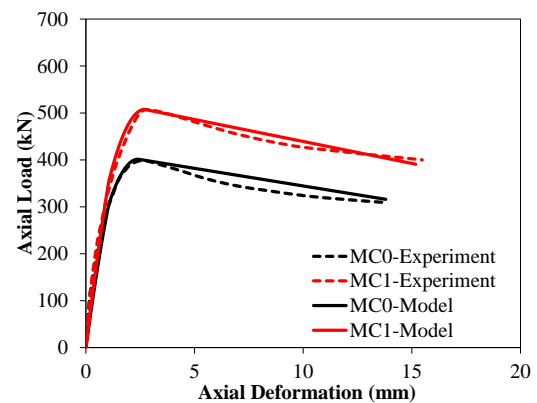


Figure 9. Experimental and numerical axial load-displacement curves for circular columns

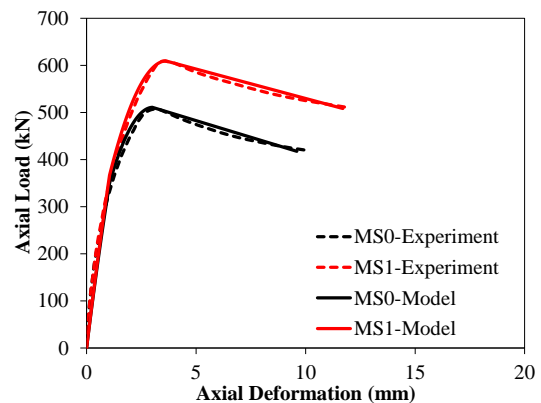


Figure 10. Experimental and numerical axial load-displacement curves for square columns

modeling process. Figures 11 and 12 depict the numerical axial load-deformation relationship for circular and square specimens, respectively, with steel fiber content of (0, 0.5, 1, 2)% along with the experimental curves. It was observed that steel fiber content of 2% increased the axial load capacity by 51 and 38% compared with the control circular and square CFST column, respectively. It also was found that ductility was increased by 22.3 and 20% with the increase of steel fiber content to 2% compared with the control circular and square CFST columns, respectively.

4. 2. Effect of Section Size

Since, in real life applications, CFST columns are much bigger in size than the tested specimens, sectional analysis was utilized to investigate the behavior of large-scale size CFST columns. Section size of 200 mm and wall thickness of 4 mm for both circular and square columns are adopted for that purpose. Figure 13 shows the effect of the selected section size on the axial capacity of CFST columns. The numerical sections were made from regular concrete without steel fibers and compared with the control

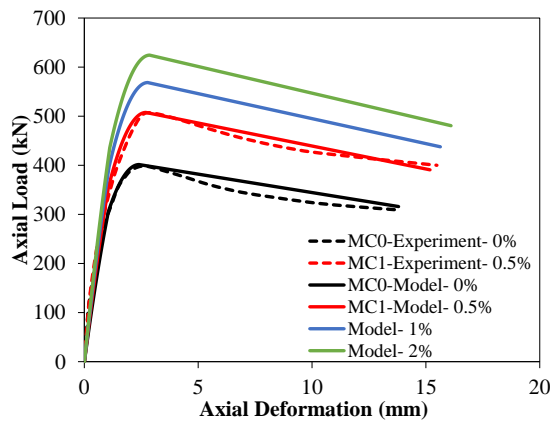


Figure 11. Effect of steel fiber content on axial load-displacement behavior for circular columns

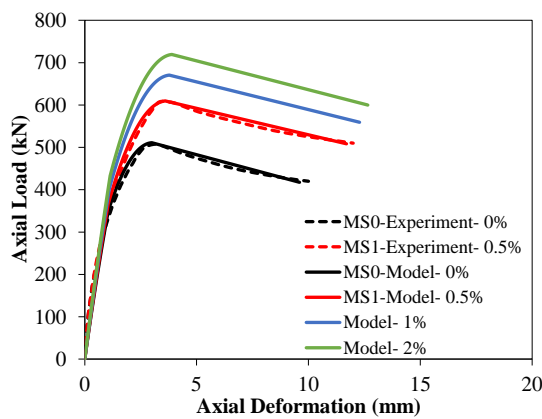


Figure 12. Effect of steel fiber content on axial load-displacement behavior for square columns

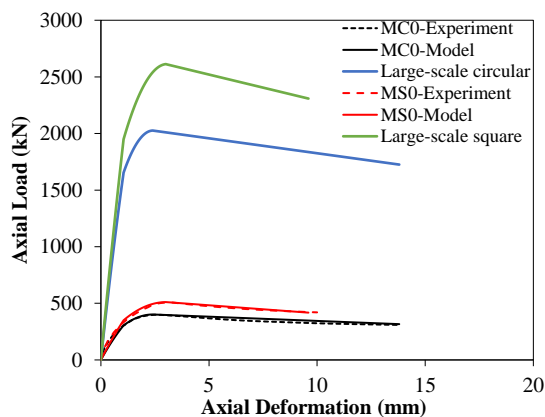


Figure 13. Effect of section size on axial load-displacement behavior for circular and square columns

specimens (MC0 and MS0) that do not have steel fibers. It can be seen that doubling section size increased axial load capacity by approximately 4 and 5 times for circular and square columns, respectively.

5. CONCLUSIONS

Concrete filled steel tube (CFST) columns are gaining more interest in civil engineering applications due to their advantageous structural properties.

This study investigated axial behavior of CFST columns reinforced with steel fibers in comparison with regular CFST columns containing normal concrete. Four specimens were used: two square columns and two circular columns. Ultimate axial load capacity, ductility and failure mode were evaluated in this study. The test results showed that the ultimate axial load capacity of CFST columns reinforced with steel fibers increased by 28 and 20 % for circular and square columns, respectively, compared with the control CFST columns. Also, better ductility was achieved in the circular CFST columns compared with the square CFST columns due to the better uniform concrete confinement that circular shape provides for the infilled concrete.

Circular and square CFST columns reinforced with steel fibers showed improved ductility by 16.3 and 12%, respectively, compared with the control columns without steel fibers. The square CFST columns failed due to local buckling which occurred near the end of columns, while the circular CFST columns failed due to local buckling that occurred near the mid-height.

Also, the study incorporated numerical sectional analysis that was shown to capture the behavior of CFST columns very well. The sectional analysis was used to investigate other factors such as steel fiber content and column section size. It was seen that increasing steel fiber content to 2% increased the axial load capacity by 51 and 38% compared with the control circular and square CFST column, respectively. Furthermore, It was observed that doubling section size increased axial load capacity by approximately 4 and 5 times for circular and square columns, respectively.

6. REFERENCES

1. Alsadey, S., "Review of strengthening rc columns with frp composites fiber reinforced polymer (FRP), LAMBERT Academic Publishing, Germany, (2013).
2. Ozturk, B., Senturk, T. and Yilmaz, C., "Analytical investigation of effect of retrofit application using cfrp on seismic behavior of a monumental building at historical cappadocia region of turkey", in 9th US National and 10th Canadian Conference on Earthquake Engineering, Toronto, Canada., (2010).
3. Öztürk, B., Yilmaz, C. and Şentürk, T., "Effect of frp retrofitting application on seismic behavior of a historical building at nigde, turkey", (2010).
4. Al-Jelawy, H.M. and Mackie, K.R., "Durability and failure modes of concrete beams strengthened with polyurethane or epoxy cfrp", *Journal of Composites for Construction*, Vol. 25, No. 3, (2021), 04021021.
5. Al-Jelawy, H., "Experimental and numerical investigations on bond durability of cfrp strengthened concrete members subjected to environmental exposure", (2013).

6. Naji, A.J., Al-Jelawy, H.M., Saadoon, S.A. and Ejel, A.T., "Rehabilitation and strengthening techniques for reinforced concrete columns", in *Journal of Physics: Conference Series*, IOP Publishing. Vol. 1895, (2021), 012049.
7. Morino, S., Uchikoshi, M. and Yamaguchi, I., "Concrete-filled steel tube column system-its advantages", *Steel Structures*, Vol. 1, No. 1, (2001), 33-44.
8. Haber, Z.B., Mackie, K.R. and Al-Jelawy, H.M., "Testing and analysis of precast columns with grouted sleeve connections and shifted plastic hinging", *Journal of Bridge Engineering*, Vol. 22, No. 10, (2017), 04017078.
9. Al-Jelawy, H.M., Mackie, K.R. and Haber, Z.B., "Shifted plastic hinging for grouted sleeve column connections", *ACI Structural Journal*, Vol. 115, No. 4, (2018), 1101-1114.
10. Al-Jelawy, H., Mackie, K. and Haber, Z., "Experimental and numerical studies on precast bridge columns with shifted plastic hinging", in *Eleventh US national conference on earthquake engineering*. (2018), 25-29.
11. Al-Jelawy, H., Haber, Z. and Mackie, K., "Grouted splice precast column connections with shifted plastic hinging", in *16th World conference on earthquake—16WCEE.*, (2017), 9-13.
12. Al-Jelawy, H., "Shifted plastic hinge column connections using grouted sleeves for accelerated bridge construction", (2017).
13. Al-Jelawy, H., Haber, Z. and Mackie, K., "Seismic performance of grouted splice precast column joints with shifted plastic hinge mechanisms", in *2014 National accelerated bridge construction conference.*, (2014), 3-5.
14. Rahmani, Z., Naghipour, M. and Nematzadeh, M., "Flexural performance of high-strength prestressed concrete-encased concrete-filled steel tube sections", *International Journal of Engineering, Transactions C: Aspects*, , Vol. 32, No. 9, (2019), 1238-1247, doi: 10.5829/ije.2019.32.09c.03.
15. Mohammed, A.H., Khalaf, R.D., Mohammedali, T.K. and Hussin, A.K., "Experimental study on performance of fiber concrete-filled tube columns under axial loading", *International Journal of Engineering, Transactions C: Aspects*, , Vol. 32, No. 12, (2019), 1726-1732, doi: 10.5829/ije.2019.32.12c.05.
16. Naji, A., Mousa, M. and Malik, S., "The production of the sustainable concrete by using different types of plastic waste", *The Journal of Engineering and Applied Science*, Vol. 14, (2019), 5557-5560.
17. Naji, A.J., Al-Yousefi, H.A., Mousa, M.A. and Hussein, M.J., "Optimization of water-cement ratio in concrete contains recycled polypropylene (pp) plastic waste", *Periodicals of Engineering and Natural Sciences*, Vol. 7, No. 4, (2019), 1563-1566.
18. Yu, X., Tao, Z. and Song, T.-Y., "Effect of different types of aggregates on the performance of concrete-filled steel tubular stub columns", *Materials and Structures*, Vol. 49, No. 9, (2016), 3591-3605.
19. Li, P., Zhang, T. and Wang, C., "Behavior of concrete-filled steel tube columns subjected to axial compression", *Advances in Materials Science and Engineering*, Vol. 2018, (2018).
20. Alhatmey, I.A., Ekmekyapar, T. and Ayoob, N.S., "Post-fire resistance of concrete filled steel tube columns", in *IOP Conference Series: Materials Science and Engineering*, IOP Publishing. Vol. 988, (2020), 012036.
21. Tao, Z., Song, T.-Y., Uy, B. and Han, L.-H., "Bond behavior in concrete-filled steel tubes", *Journal of Constructional Steel Research*, Vol. 120, (2016), 81-93.
22. Tao, Z., Han, L.-H. and Wang, D.-Y., "Experimental behaviour of concrete-filled stiffened thin-walled steel tubular columns", *Thin-Walled Structures*, Vol. 45, No. 5, (2007), 517-527.
23. Samman, T.A., Wafa, F.F. and Radain, T.A., "Mechanical properties of normal and high-strength concrete with steel fibers", *Journal of King Abdulaziz University: Engineering Sciences*, Vol. 12, No. 1, (1999), 87-104.
24. Giakoumelis, G. and Lam, D., "Axial capacity of circular concrete-filled tube columns", *Journal of Constructional Steel Research*, Vol. 60, No. 7, (2004), 1049-1068.
25. Wang, W.-H., Han, L.-H., Li, W. and Jia, Y.-H., "Behavior of concrete-filled steel tubular stub columns and beams using dune sand as part of fine aggregate", *Construction and Building Materials*, Vol. 51, (2014), 352-363.
26. Tao, Z., Han, L. and Zhao, X., "Behaviour of square concrete filled steel tubes subjected to axial compression", in *Proceedings of the Fifth International Conference on Structural Engineering for Young Experts*, Shenyang, China., (1998), 61-67.
27. Siqi, L., Tianlai, Y. and Junfeng, J., "Investigation and analysis of empirical field seismic damage to bottom frame seismic wall masonry structure", *International Journal of Engineering, Transactions B: Applications*, , Vol. 32, No. 8, (2019), 1082-1089, doi: 10.5829/ije.2019.32.08b.04.
28. LI, S., Yu, T. and Jia, J., "Empirical seismic vulnerability and damage of bottom frame seismic wall masonry structure: A case study in dujiangyan (china) region", *International Journal of Engineering, Transactions C: Aspects*, , Vol. 32, No. 9, (2019), 1260-1268, doi: 10.5829/ije.2019.32.09c.05.
29. Guler, S., Lale, E. and Aydogan, M., "Non-linear analysis of steel fibre reinforced concrete-filled steel tube columns", *Proceedings of the Institution of Civil Engineers-Structures and Buildings*, Vol. 166, No. 6, (2013), 298-306, <https://doi.org/10.1680/stbu.11.00070>
30. Katwal, U., Tao, Z., Hassan, M.K. and Wang, W.-D., "Simplified numerical modeling of axially loaded circular concrete-filled steel stub columns", *Journal of Structural Engineering*, Vol. 143, No. 12, (2017), 04017169.
31. Nguyen, P.-C., Pham, D., Tran, T. and Nghia-Nguyen, T., "Modified numerical modeling of axially loaded concrete-filled steel circular-tube columns", *Engineering, Technology & Applied Science Research*, Vol. 11, No. 3, (2021), 7094-7099, <https://doi.org/10.48084/etasr.4157>
32. Hognestad, E., *Study of combined bending and axial load in reinforced concrete members*. 1951, University of Illinois at Urbana Champaign, College of Engineering.

Persian Abstract

چکیده

ستون‌های لوله فولادی پرشده بتنی (CFST) به دلیل ویژگی‌های ساختاری برتر در مهندسی عمران محبوب هستند. این مقاله بهبود رفتار محوری ستون‌های CFST را با افزودن الیاف فولادی به بتن ساده که لوله‌های فولادی را پر می‌کند، بررسی می‌کند. چهار نمونه تهیه شد: دو ستون مربعی (۱۰۰ * ۱۰۰ میلی متر) و دو ستون دایره ای (قطر ۱۰۰ میلی متر). تمام ستون ها ۶۰ سانتی متر طول داشتند. مخلوط بتن ساده و بتن تقویت شده با الیاف فولادی برای پر کردن ستون های لوله فولادی استفاده شد. ظرفیت بار محوری نهایی، شکل پذیری و حالت شکست در این مطالعه مورد بحث قرار گرفته است. نتایج نشان داد که ظرفیت بار محوری نهایی ستون‌های CFST تقویت شده با الیاف فولادی به ترتیب ۲۸ و ۲۰ درصد برای ستون‌های دایره‌ای و مربعی افزایش یافت. همچنین، ستون‌های CFST دایره‌ای شکل پذیری بهتری نسبت به ستون‌های CFST مربعی به دلیل محصور شدن بهتر بتن از خود نشان دادند. ستون های CFST دایره ای و مربعی با الیاف فولادی به ترتیب ۱۶.۳٪ و ۱۲٪ شکل پذیری بهبود یافته را نشان دادند. حالت شکست ستون‌های CFST مربعی، کمانش موضعی بود که در نزدیکی انتهای ستون‌ها رخ می‌داد، در حالی که، برای ستون‌های CFST دایره‌ای، کمانش موضعی در نزدیکی ارتفاع وسط رخ داد. همچنین، این مطالعه شامل تجزیه و تحلیل مقطعی بود که رفتار ستون‌های CFST را به خوبی نشان می‌داد. تجزیه و تحلیل مقطعی نشان داد که افزایش محتوای الیاف فولادی به ۲٪ ظرفیت بار محوری را به ترتیب ۵۱ و ۳۸٪ برای ستون های CFST دایره ای و مربعی افزایش داد. علاوه بر این، تجزیه و تحلیل مقطعی نشان داد که دوبرابر کردن اندازه مقطع، ظرفیت بار محوری را به ترتیب تقریباً ۴ و ۵ برابر برای ستون‌های دایره‌ای و مربعی افزایش می‌دهد.



Experimental Evaluation on Palm Oil and Sesame Oil-based Resin Properties as Core Sandwich Material for Lightweight Ship Structure

T. Tuswan^a, E. N. Sari^b, A. Ismail^c, A. R. Prabowo^d

^a Department of Naval Architecture, Universitas Diponegoro, Semarang, Indonesia

^b Departement of Mechanical Engineering, Universitas Billfath, Lamongan, Indonesia

^c Ship Machinery Study Program, Indonesia Defense University, Belu, Indonesia

^d Department of Mechanical Engineering, Universitas Sebelas Maret, Surakarta, Indonesia

PAPER INFO

Paper history:

Received 03 January 2022

Received in revised form 30 March 2022

Accepted 06 April 2022

Keywords:

Bio Resin

Palm Oil

Sesame Oil

Core Sandwich

Ship Structure

ABSTRACT

Research on lightweight material on ship structure has taken giant steps during the last decade. One reason is that shipping activities have increased and, therefore, the possibility of increasing the carrying cargo capacity in a realistic way using advanced lightweight material. This article summarizes a research investigation regarding the experimental tests of vinyl ester bio resin material using palm oil and sesame oil based on Lloyd's Register (LR) standard. Several tests were conducted, including density, water absorption test, Fourier transformed infrared test (FTIR), scanning electron microscope (SEM), and mechanical tests to evaluate the effect of 2-10% addition of vegetable oils on mechanical properties. The influence of the addition of vegetable oils is successfully characterized using physical measurements, which indicate the possible formation of a polymer blend to increase in elongation value. Mechanical testing shows that adding vegetable oils causes a decrease in average density, hardness, bending strength, and tensile strength. The bending strength decreases about 9.20 – 47.06% for 2-10% palm oil addition and 5.33 – 42.40% for sesame oil addition. Moreover, vegetable oil causes a tensile strength decrease of about 5-18.75% on palm oil and 3.75-13.75% on sesame oil. As summarized, bio resin based on sesame oil has better mechanical behavior with the oil addition of 4-8% fulfills all Lloyd's Register criteria.

doi: 10.5829/ije.2022.35.09c.03

1. INTRODUCTION

The lightweight sandwich structure is developed largely in several application engineering disciplines, most notably the shipbuilding sector. Several studies on the development of sandwich material on various ship structural components have revealed benefits. It improves the strength-to-weight ratio [1-3], has good damping properties [4,5], and simplifies production and construction processes.

An intriguing issue is the progression of material types and composition for the faceplate and core sandwich for shipbuilding applications. The experimental testing procedure and acceptance properties criteria of a core sandwich as ship structure are regulated to the Lloyd's Register [6] and DNV GL [7]. In the recent

development of sandwich application in the shipbuilding sector, steel and room temperature curing polyurethane elastomer (RTC-PU) are one of the established material types which are often used as the faceplate and core materials for the sandwich panel [8,9]. However, the RTC-PU material is not cost-effective in practical application, especially for small-scale shipbuilding businesses in a developing country, where the material cost will extremely govern the overall cost of ship production [10,11]. One of the alternative solutions that have been investigated is the use of low-cost polymer and waste material [12-14] for core materials.

Low-cost core material must be tested according to the standard and meet the acceptance criteria value from Lloyd's Register [6] so that the developed material can be used as the core material of the ship sandwich structure.

*Corresponding Author Institutional Email:
tuswan@lecturer.undip.ac.id (T. Tuswan)

Various materials have been developed, but not many have followed the testing standards and met the acceptance criteria value from Lloyd's Register [6]. Several nanocomposites [15,16] have not been tested according to the request of Lloyd's Register to be ship material standard [6]. Various natural fibers [17-19] also do not meet the LR criteria, specifically the elongation at break criteria. The critical point is needed to be addressed, including the material brittleness and elongation threshold. Furthermore, research on the innovation of low-cost core material types with better mechanical properties needs to be conducted.

In order to substitute room temperature curing polyurethane elastomer (RTC-PU) as expensive core material and further investigation to increase the elongation value of resin polymer material, one potential alternative solution to increasing material properties can be achieved by developing a low-cost bio-resin polymer blend of two or more polymers to obtain new polymeric components from vegetable oils with excellent material properties specifically elongation parameter. Even if there are a lot of works completed on developing bio-based resin from vegetable oils to our observation, there are still limited reports on the mechanical testing development of bio-based resin as core sandwich material specifically for ship structure according to the procedure and specification standards have given by Lloyd's Register [6].

To address this issue, vinyl ester bio-based resin combined with palm oil and sesame oil with several compositions is proposed to be developed as the core material of the ship sandwich structure. The proposed core material must meet the Lloyd's Register criteria [6], such as density, hardness, tensile strength, and elongation at break. Physical tests, characterization tests, and mechanical tests were carried out to check the suitability of the proposed bio-based resin against Lloyd's Register criteria [6] and to analyze various compositions of vegetable oils further.

2. METHODS

2. 1. Material Preparation and Processing

EPOXY R-802 EX-1 vinyl ester (VE) resin type was combined with cobalt naphthenate, and Methyl Ethyl Ketone Peroxide (MEKP) were used in this study. The VE has a specific gravity of 1.05 g/cm³ at 25°C, an acid value of 7-13 KOH mg/g, a viscosity of 2-6 poise at 25°C, and styrene composition of 46%. Methyl Ethyl Ketone Peroxide (MEXP) was used as an initiator [13]. The other material used was vegetable oil (VO). In this case, palm oil (PO) was purchased from PT Wilmar Nabati Indonesia, and sesame oil (SO) was purchased from PT Sukanda Djaya Indonesia was used as an addition to the vinyl ester bio-based resin using different compositions.

Sesame oil contains a lot of unsaturated fatty acids, especially oleic acid (C18:1) and linoleic acid (C18:2), omega-6 (35.5–49.5%), omega-9 (37.5–45.4%), and several antioxidant components such as vitamin E, carotene, and lignin components [20]. The chemical structure of sesame and palm oils is depicted in Figure 1.

Because it is biodegradable and safe, vegetable oil (VO) is appropriate for mineral oil. In this case, palm oil (PO) was sesame oil (SO) was used as an addition to the vinyl ester bio-based resin using different compositions. In material development, specimen blend variations are developed based on several procedures. In the first step, all the material components, including vinyl ester, catalyst, and accelerator, are measured specified composition. Then, thermoset blending was formed by using a physical-mechanical mixing process with styrene as the cross-linker diluent, adding sesame and palm oils in 0, 2, 4, 6, 8, and 10 wt % in the vinyl ester (VE).

In the next step, With a catalyst accelerator, Methyl Ethyl Ketone Peroxide was added as a catalyst initiator at 0, 2, 4, 6, 8, and 10% wt. A transparent colorless solution was obtained by blending vinyl ester, vegetable oil, MEKP, and accelerator in a mechanical mixer at room temperature for 2 hours. Next, the specimen is created in the wooden mold with several types according to the corresponding mechanical testing. The mixture was put into wooden molds and cured at room temperature for 24 hours after being placed under a low vacuum (300 kPa) for 2 hours. All the specimens and then removed from the mold after curing in the final step.

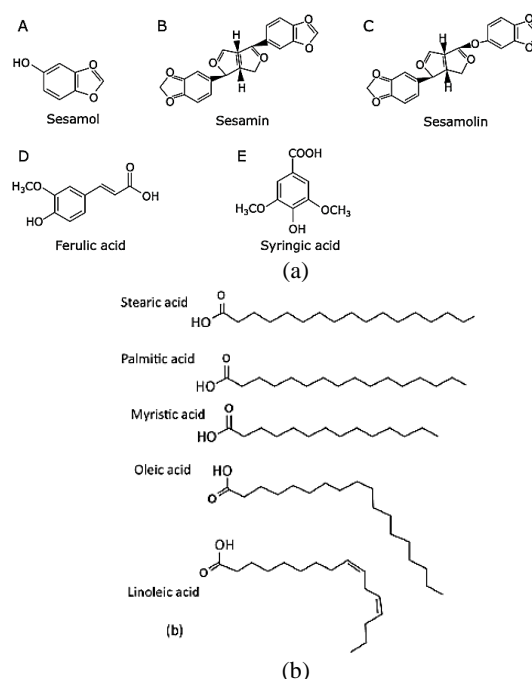


Figure 1. a) chemical structure of sesame oil [20], b) chemical structure of palm oil

2. 2. Experimental Testing and Procedure

Shore D hardness test was conducted using a durometer with the specimen dimensions, and procedures were performed using the ASTM D2240 [21]. In this case, the average hardness test output was obtained by measuring the mean of 3 specimens of each variation with the sample thickness is 6 mm. Further, the tensile test was performed to determine mechanical properties using dumb-bell-shaped samples with Hung Ta HT-2402 at a rate of 0.1 mm/min in accordance with ISO 527-4 [22]. Besides the tensile test, three-point bending testing was carried out to obtain information on the strength of the material using the three-point bending method. Tests were carried out with the WDW-1000 bending test machine. The specimen dimensions and testing procedure used the ASTM D790 standard [23].

Characterization tests were carried out to obtain the microscopic behavior of the material. Their tests are Fourier Transform Infrared test (FTIR) and Scanning Electron Microscopy (SEM). In this test case, both SEM and FTIR test was carried out to analyze the microscopic behavior of several specimens. Thermoscientific Nicolet I S10 spectrophotometer with smart orbit diamond crystal plate sampling technology was used for the FTIR spectroscopic investigation at resolution 4 cm^{-1} in the range of $400\text{--}4000\text{ cm}^{-1}$. Moreover, the SEM test was performed to obtain a morphological image of the sample. The morphology of composites was investigated at the fractured surface of samples using SEM, FEI INSPECT S50 at 20 kV. The cross-section of investigated samples is coated with 100 Å thick C in the sputter coater.

Besides mechanical and characterization tests, physical properties test such as apparent density, water absorption test, and thermogravimetric analysis (TGA) was also conducted. The density test in accordance with ASTM D 70-03 [24] was conducted using a pycnometer and weighing specimens using the FUJITSU FSR-B1200. Water absorption was a test carried out to determine the absorption of material against water at a specific time. The water adsorption test procedure uses the ASTM D570-98 standard [25]. Water absorption was a test carried out to determine the absorption of material against water at a specific time. The procedure used in this test was conducted to prepare a water adsorption specimen and then weigh it when the material is dry and then immersed in a container filled with water with the amount of water that can immerse the entire area of the specimen at a specific time and then weighed again when wet conditions. The difference between the two weighing results will be used as water absorption data [26, 27]. The water absorption specimen is based on ASTM D570-98 standards. Furthermore, thermal analysis of polymers typically involves various techniques, including a well-established thermogravimetric analysis (TGA). The test determined the quantity and frequency of weight

fluctuation of samples versus temperature and time in a controlled atmosphere. A TGA test was used in this case to measure the thermal stability of the material and volatile component percentage by measuring the weight change that occurred while the material was heated at a consistent rate. TGA examines changes in the weight of a sample while it is heated at a regulated temperature, and the changes are continually recorded.

3. RESULT AND DISCUSSION

In this section, the results of experimental testing in all sample variations are reviewed. As the result of physical testing, the comparison result of apparent density due to addition of an epoxidized vegetable oil into vinyl ester bio-resin is shown in Figure 2. It can be found that the results of standard deviation depicted by a vertical line in Figure 2 for VE-palm oil specimen with different volume fractions are in the range of 0.0002-0.001 and for VE-sesame oil in the range of 0.007-0.002. The result of both specimen types experiences a decreasing trend as the fraction volume of vegetable oil increases. It can be found that pure vinyl ester specimens experience the highest density, whereas the lowest one is the specimen with the highest addition of palm and sesame oil. It can be found that the addition of 2-10% palm oil causes a density decrease in the range 10.08-10.61% and 10.43-10.88% decrease for the addition of sesame oil. A similar result was noticed by previous literature [28] that density value decreases due to the addition of vegetable oil (soybean and coconut oils) to vinyl ester specimens. Compared to the two types of material, it can be analyzed that the density of vinyl ester with palm oil is slightly higher than polymer-based sesame oil. Compared to the LR standard, both material types fulfill the minimum standard, except for 10% of VE-sesame oil specimens.

Figure 3 illustrates the comparison of water absorption percentage between polymer based on sesame

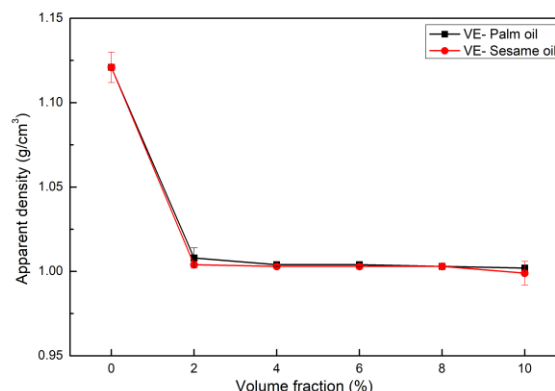


Figure 2. Apparent density between VE-palm oil and VE-sesame oil

and palm oils for 7 days. The results of standard deviation depicted by a vertical line in Figure 3 for VE-Palm oil specimen with different volume fractions is in the range of 0.022-0.050 for palm oil and for VE-sesame oil in the range of 0.03-0.0076. It can be analyzed that the percentage of water absorption increases with an increase in absorption time from day 1 to day 7. It can be found that water absorption on VE-sesame oil increases from 0.285 to 0.611%, which is calculated as about 114.7% increase. Moreover, VE-palm oil experiences a water absorption increase from 0.278 to 0.61%, which calculates 118.8% increase.

Water absorption experiences an increasing trend from day 1 and day 5. However, from day 5 to day 7, it experiences constant water absorption. Water absorption becomes less from day 5 to 7 because the material experiences a state of saturation with water. Therefore, it causes the water absorption of the specimen to decrease. The ability to absorb water in the sample occurs in the surface area. It is due to the basic nature of vegetable oils, which are non-miscible or insoluble in water. It can be seen from the plot that water absorption by bio resin increases monotonically with immersion time until an equilibrium condition is reached after 168 h, where saturation is experienced in all samples [29].

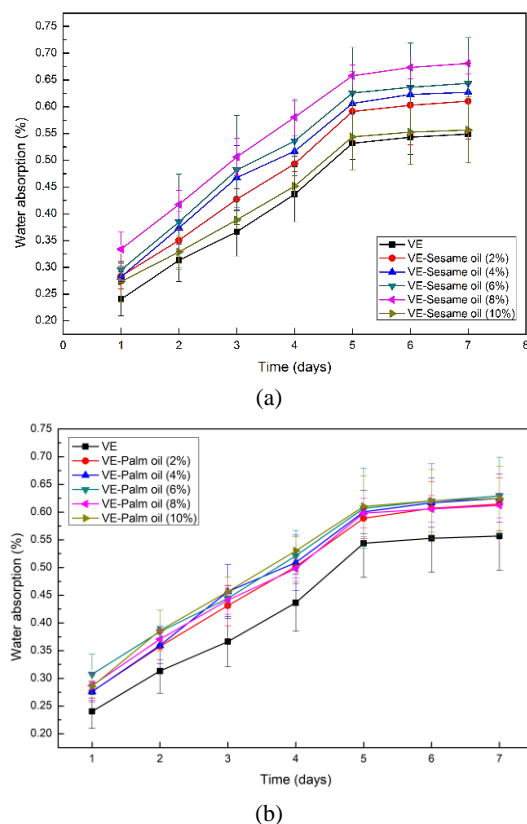


Figure 3. Water absorption a) VE-sesame oil b) VE-palm oil

The result of the thermogravimetric analysis is presented in Figure 4a. TGA test only gives information for substances that show a change in mass for every sample analyzed at the temperature change between 0 - 600°C. It can be found that the mass change in the samples with a higher volume fraction (10%) of sesame and palm oils is greater compared to samples with a lower volume fraction (2%). It can be summarized that the lowest one can be found in the sample with vinyl-ester-sesame oil (2%). In this case, the difference in the weight changes of samples can be caused by decomposition and oxidation reactions and physical processes such as sublimation, vaporization, and desorption.

Figure 5 shows the FTIR result of each variation of the specimen. At the absorption peak of 3392.63 cm^{-1} , the O-H bond is stretched, which is a ketone functional group. Then, C-H bonds stretch at the absorption peaks of 3024.59 cm^{-1} , 2918.77 cm^{-1} , and 2849.48 cm^{-1} . This phenomenon indicates the presence of an alkane functional group (CH_2 or CH_3).

At the absorption peak of 1724.31 cm^{-1} , the C=O bond is stretched, which is the functional group of the ester. Further, there is a C=C bond that vibrates at the absorption peak 1603.40 cm^{-1} and 1507.50 cm^{-1} , which show functional groups of aromatic homocyclic. Then,

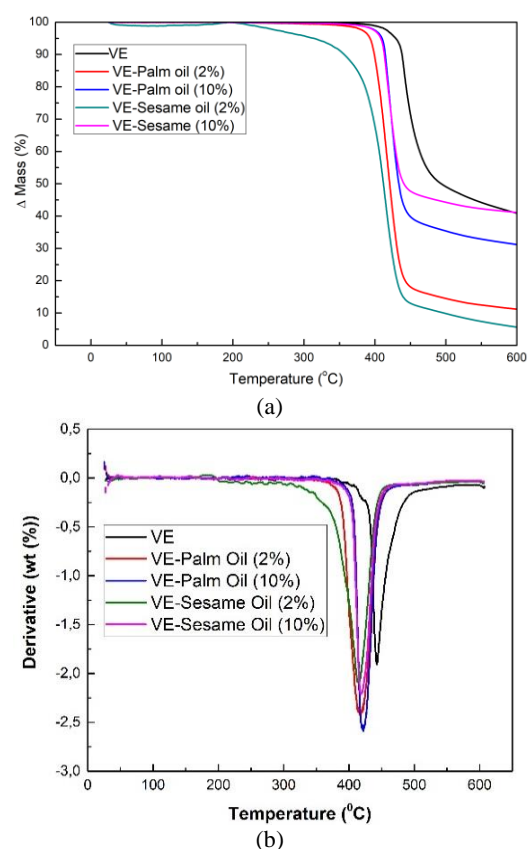


Figure 4. (a) TGA and (b) DTG of different material types

the C-O bond stretching at the absorption peaks of 1179.42 cm^{-1} and 1031.32 cm^{-1} show the ester and alcohol functional groups. At the peak of 826.11 cm^{-1} , the C-H bond is deformed, indicating the presence of an aromatic ring. The FTIR spectrum of vinyl esters can be identified by the dominance of the $-\text{CH}_2$ and $-\text{CH}_3$ alkane groups in the absorption regions of 2960 cm^{-1} , 2923 cm^{-1} , 2871 cm^{-1} , and 2851 cm^{-1} . Then aromatic rings appear in the absorption region of 1604 cm^{-1} and 826 cm^{-1} . The absorption area of 1712 cm^{-1} is identified by the presence of C=O stretching bonds, and there is a $-\text{C-O-C}$ group in the 1220 cm^{-1} region.

The FTIR spectrum in Figure 5 shows a new absorption peak area that appears in vinyl ester bio-resin, at the absorption peak area of $750\text{ cm}^{-1} - 760\text{ cm}^{-1}$ and $690\text{ cm}^{-1} - 700\text{ cm}^{-1}$. The absorption peak region in the range of $735\text{ cm}^{-1} - 770\text{ cm}^{-1}$ is the absorption region of the deflected C-H bond with the benzene ring functional group with 4 free H atoms. The absorption area of $690\text{ cm}^{-1} - 710\text{ cm}^{-1}$ is the absorption region of the deflection C-H bond with the benzene ring functional group with 5 free H atoms.

As expected, the spectra present the same band patterns due to the similar structures of vegetable oils. The spectra presented in Figure 5 show bands corresponding to the stretching vibration of the carbonyl group of the ester linkage (at ca. 1700 cm^{-1} C=O functional group double bonds) from the vinyl ester and the oil structure [30]. The band appearing (at ca. $1600 - 1500\text{ cm}^{-1}$ C=C functional group double bonds) can be ascribed to the stretching vibration of the double bond from maleic anhydride [31]. C=O in the absorption at ca. of 1200 cm^{-1} . It proves that vegetable oil esters form new bonds with pure vinyl esters in the form of a benzene ring with 4 free atoms and a benzene ring with 5 free atoms. Vinyl ester polymer bio-resin with 2% palm oil filler has a steeper wave transmittance than other sample types.

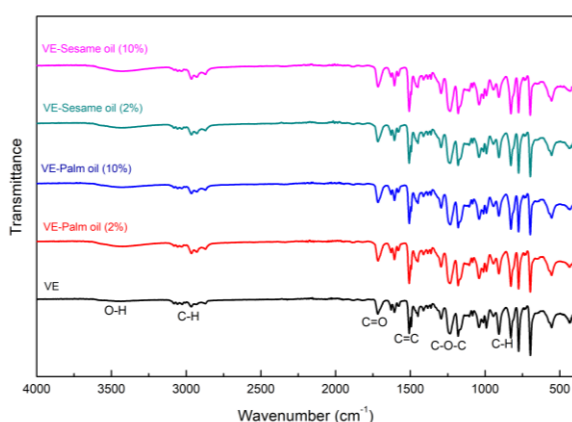


Figure 5. FTIR spectrum of different material types

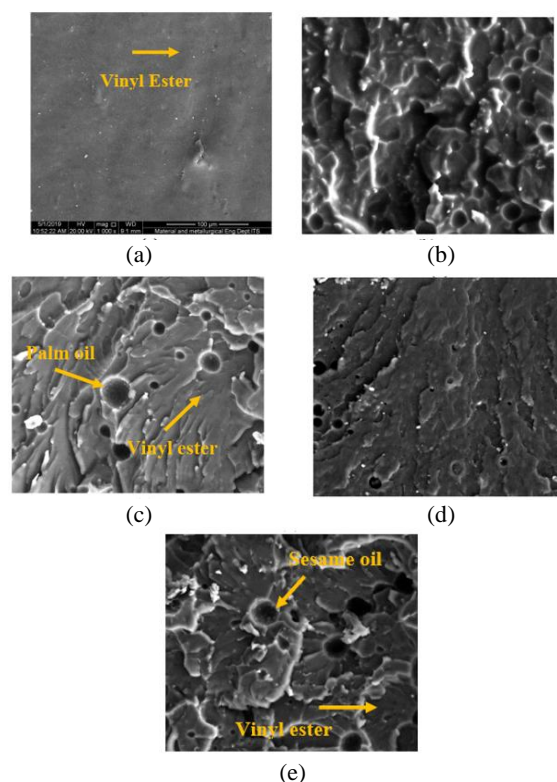


Figure 6. SEM a) VE, b) VE-palm oil (2%), c) VE-palm oil (10%), d) VE-sesame oil (2%), e) VE-sesame oil (10%)

The texture in Figure 6a is smooth and flat because there is no addition of vegetable oil. Figure 6b shows the morphology of VE-palm oil (2%). The effect of the triglyceride bond on the vinyl ester can be seen as rigid and rough-textured. It can be seen from the results that there are several forms of hemispherical basins. This basin is known as a spherical ball. Figure 6c shows a texture that is almost the same as the VE-Palm oil (2%) sample but looks smoother. Moreover, Figure 6d shows the smoothest texture among all specimens. This picture also shows the presence of spherical balls that have a varied distribution. Figure 6e shows a much coarser texture than VE-sesame oil (2%).

Figure 7 compares the average hardness value of pure VE, VE-sesame oil, and VE-palm oil. The hardness value in each specimen variation is the average result of 3 samples with the range of standard deviation 1 - 3.21 for VE-palm oil and 0.58 - 2.52 for VE-sesame oil specimen. It can be analyzed that pure VE has the highest hardness value reaching 80 Shore D. The addition of 2-10% vegetable oil into vinyl ester specimen causes a decrease of about 5.00 - 18.75% for palm oil and 3.75 - 13.75% for sesame oil. The obtained result is linear to the previous findings where the addition of 4.wt% vegetable oil causes a decrease of about 4.92 - 5.97% on hardness value [28].

According to the FTIR data, a polar group (C=O) is not completely attached. It denotes that mixing takes place mechanically rather than chemically. The hardness has dropped because chemical connections between vinyl esters and vegetable oils do not exist. In 10% addition of vegetable oil, it can be found that VE-sesame oil is higher about 6.15% compared to VE-palm oil. Therefore, it can be concluded that VE-sesame oil samples are better resistant to indentation. Compared with the minimum hardness requirement by LR, the hardness value of VE-sesame oil and VE-palm oil in all volume fraction variation is higher than the minimum hardness of 65 Shore D.

Figure 8 presents the comparison result of tensile strength between pure VE, VE-palm oil, and VE-sesame oil samples. The tensile strength value in each specimen variation is the average result of 3 samples with the range of standard deviation for VE-palm oil is 1.4 – 3.46 and 1.41 – 3.16 for VE-sesame oil specimen. From the result of the work, the highest tensile strength can be found in the pure vinyl ester sample, about 47 MPa. The result shows that the addition of vegetable oil causes a tensile strength decrease of about 5-18.75% on VE-palm oil and 3.75-13.75% on VE-sesame oil. The previous report shows that tensile strength decreases in the range 3.5 – 45.6% due to 5-20% palm oil addition into vinyl ester specimens [32]. The decrease in tensile strength is caused by an increase in particle concentration which causes an increase in the agglomeration and the presence of unreacted bonds and molecules.

The more addition of vegetable oil composition, the more triglyceride groups contained in the bio-resin mixture. However, because there is no crosslink, the greater the addition of vegetable oil, the tensile strength value will decrease. Therefore, with an increase in vegetable oil composition, the concentration of polar groups in the bio-resin specimen will decrease, resulting in an increase in the component of vegetable oil, which can reduce the tensile strength value, as can be seen in Figure 8. All tensile strength values fulfill the LR standard.

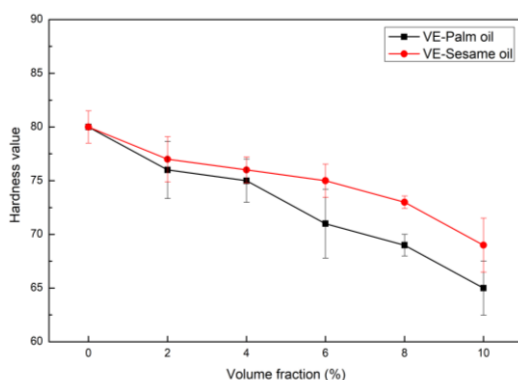


Figure 7. Result of shore D hardness test

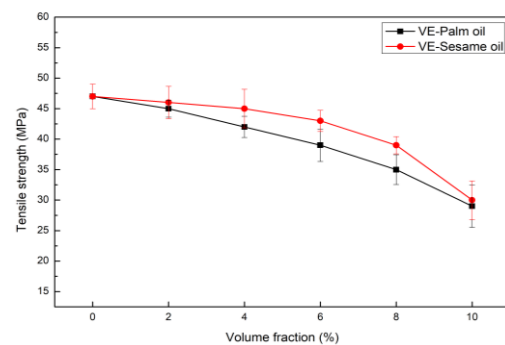


Figure 8. Result of tensile strength of different material types

Figure 9 shows the results of elongation percentage. The elongation value in each specimen variation is the average result of 3 samples with the range of standard deviation for VE-palm oil is 0.4 – 1.0 and 0.3 – 0.8 for VE-sesame oil specimen. It can be shown that adding sesame and palm oils can increase the elongation of the material. It can be found that the addition of 2-10% vegetable oil causes an elongation increase of about 46.6 – 173.3% for VE-palm oil and 33.3 – 140% for VE-sesame oil. The previous study was also noticed a similar result where the addition of vegetable oil (sesame, palm, and coconut oils) causes an increase of elongation value [28,32]. It is caused due to a large number of long-chain polymer chemical structures and the easier movement of molecules [13]. So, with the addition of vegetable oil, the elongation value increases because there are more C chains in the bio-resin. The C chain is getting longer because of the C chain contained in vegetable oil. Compared to the LR standard with a minimum of 20% elongation at break, it can be concluded that adding vegetable oils into bio-resin is the best option and can be used as a recommendation to increase the ductility of the material. Compared to standard, only the addition of 2% sesame oil does not fulfill the minimum elongation given by LR standard.

In the last, the result of the three-point bending test is depicted in Figure 10. The bending test in each specimen variation is the average result of 3 samples with the range of standard deviation for VE-palm oil is 3.67 – 5.88 and 2.44 – 5.87 for VE-sesame oil specimen. A similar result with the tensile test can be found where the VE-sesame oil specimens have better mechanical properties due to higher bending strength than VE-palm oil. From Figure 10, it can be analyzed that the addition of vegetable oil into bio-resin causes a decrease in bending strength. The results show that the bending strength decrease is calculated about 9.20 – 47.06% for VE-palm oil and 5.33 – 42.40% for VE-sesame oil. A similar previous study showed that the flexural strength decreases by 38.9% due to addition of 5-20% palm oil into vinyl ester specimens [32].

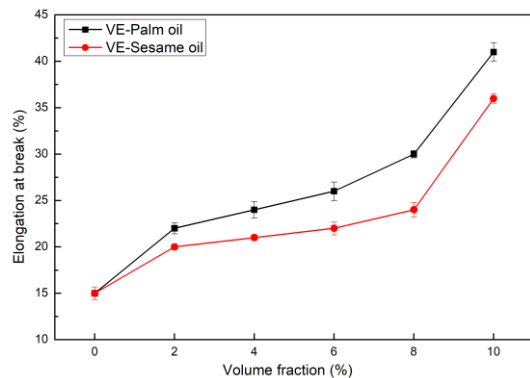


Figure 9. Elongation at break of different material types

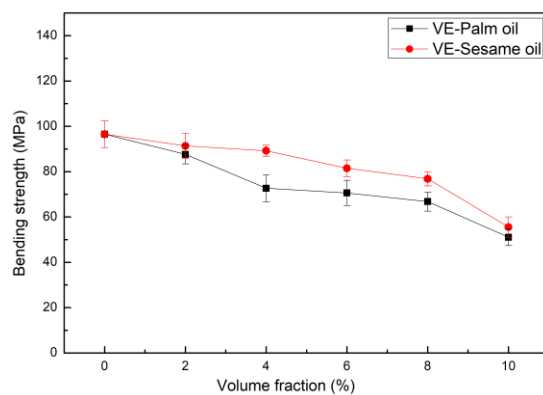


Figure 10. Result of bending of different material types

The decrease in bending strength is caused by the occurrence of porous structure in the material. However, it is found that there is no crosslink, so the greater the addition of vegetable oil, the value of the tensile strength will remain decrease. It is inversely proportional to the elongation value, which increases because there are more C chains in the bio-resin. The C chain is getting longer because of the C chain contained in vegetable oil. The number of C carbon chains in palm oil includes C₁₈, palmitic C₁₆, linoleic C₁₈, while the C carbon chains in sesame oil include sesame C₇, sesamol C₂₀, sesamin C₂₀. The long carbon chain affects the elongation properties of a material. If the C chain of vegetable oil binds with other elements of vinyl ester, it will increase the value of the bending strength of the material. However, based on the results of the FTIR test, there is no crosslink. Therefore, only the elongation value increases without an increase in the bending strength. Although more volume fraction of vegetable oil is added to the vinyl ester mixture, only the elongation value will increase, and there is no increase in bending strength.

Several ship structures have been used to sandwich panels, including the deck [16], hull [33-35], and ramp door [1,10]. Lloyd's Register has suggested other ship

parts that can also be applied to sandwich panels, including double bottom floors and girders, primary structural members, corrugated bulkheads, and any structure directly in contact with the oil cargo [6]. Furthermore, this ductile and non-corrosive composite material can be used as the blade material of the Vertical Axis Hydrokinetic Turbine [36].

4. CONCLUSION

Several experimental tests were carried out in order to measure the optimum composition and mechanical properties of bio-resin based on LR standards. The effect of the addition of volume fraction of sesame and palm oil into bio-resin is investigated. Several conclusions can be stated, as follow:

1. The oil addition indicates the ability to bind to other elements leading to the potential formation of a polymer blend and elongation increment value due to a longer carbon chain.
2. The testings reveal that adding vegetable oil can decrease the density, hardness, and strength properties but increase the elongation.
3. VE-sesame oil has better mechanical behavior than VE-palm oil, with the oil addition of 4-8% is recommended and fulfills the LR standard.

5. REFERENCES

1. Tuswan, T., Zubaydi, A., Piscesa, B. and Ismail, A., Ariesta, R.C., Ilham, M.F, Mualim, F.I., "Influence of Application of Sandwich Panel on Static and Dynamic Behaviour of Ferry Ro-Ro Ramp Door", *Journal of Applied Engineering Science*, Vol. 19, No. 1, (2020), 208-216. doi: 10.5937/jaes0-27708
2. Muniraj, D. and Sreehari, V., "Experimental Damage Evaluation of Honeycomb Sandwich with Composite Face Sheets under Impact Load", *International Journal of Engineering, Transactions A: Basics*, Vol. 34, No. 4, (2021), 999-1007. doi: 10.5829/ije.2021.34.04a.26
3. Khalkhali, A., Narimanzadeh, N., Khakshournia, S. and Amiri, S., "Optimal Design of Sandwich Panels Using Multi-Objective Genetic Algorithm and Finite Element Method", *International Journal of Engineering, Transactions C: Aspects*, Vol. 27, No. 3, (2014), 395-402. doi: 10.5829/idosi.ije.2014.27.03c.06
4. Tuswan, T., Zubaydi, A., Piscesa, B., Ismail, A., Ariesta, R.C. and Prabowo, A.R., "A numerical evaluation on nonlinear dynamic response of sandwich plates with partially rectangular skin/core debonding", *Curved and Layered Structures*, Vol. 9, No. 1, (2022), 25-39. doi: 10.1515/cls-2022-0003
5. Amrane, M. and Bensahal, D., "Effects of Material and Geometrical Parameters on the Free Vibration of Sandwich Beams", *International Journal of Engineering, Transactions B: Applications*, Vol. 29, No. 2, (2016), 222-228. doi: 10.5829/idosi.ije.2016.29.02b.11
6. Register, L., "Rules for the Application of Sandwich Panel Construction to Ship Structure", (2020).
7. DNV-GL, "Steel sandwich panel construction". 2016, Norway. <https://rules.dnv.com/docs/pdf/DNV/CG/2016-04/DNVGL-CG-0154.pdf>

8. Ismail, A., Zubaydi, A., Piscesa, B., Ariesta, R.C. and Tuswan, T., "Vibration-based damage identification for ship sandwich plate using finite element method", *Open Engineering*, Vol. 10, No. 1, (2020), 744-752. doi: 10.1515/eng-2020-0086
9. Prabowo, A.R., Tuswan, T. and Ridwan, R., "Advanced Development of Sensors' Roles in Maritime-Based Industry and Research: From Field Monitoring to High-Risk Phenomenon Measurement", *Applied Sciences*, Vol. 11, No. 9, (2021), 3954. doi: 10.3390/app11093954
10. Tuswan, T., Zubaydi, A., Piscesa, B., Ismail, A. and Ilham, M.F., "Free vibration analysis of interfacial debonded sandwich of ferry Ro-Ro's stern ramp door", *Procedia Structural Integrity*, Vol. 27, (2020), 22–29. doi: 10.1016/j.prostr.2020.07.004
11. Ismail, A., Zubaydi, A. and Budipriyanto, A. "Damage Identification of the Sandwich Plate Having Core from Rice Husk-Epoxy for Ship Deck Structure", in Proceedings of the 3rd International Conference on Marine Technology 2018, Surabaya, Indonesia. doi: 10.5220/0008543301120118
12. Arianto P.Y., Zubaydi, A., Piscesa, B. and Tuswan, T., "Experimental and Numerical Bending Analysis of Steel/Resin-Talk Sandwich Material", *IPTEK The Journal for Technology and Science*, Vol. 30, (2019), 123-128. doi: 10.12962/j20882033.v30i3.5496
13. Ardhyana, H., Sari, E.N., Wicaksono, S.T., Ismail, H., Tuswan, T. and Ismail, A., "Characterization of vinyl ester bio-resin for core material sandwich panel construction of ship structure application: Effect of palm oil and sesame oil", AIP Conference Proceedings, Vol. 2202, (2019), 020051. doi: 10.1063/1.5141664
14. Campanella, A., Rustoy, E., Baldessari, A. and Baltanas, M.A., "Lubricants from chemically modified vegetable oils". *Bioresource Technology*, Vol. 10, No. 1, (2010), 245-254. doi: 10.1016/j.biortech.2009.08.035
15. Nurazzi, N.M., Sabaruddin, F.A., Harussani, M.M., Kamarudin, S.H., Rayung, M., Asyraf, M.R.M., Aisyah, H.A., Norrahim, M.N.F., Ilyas, R.A., Abdullah, N., Zainudin, E.S., Sapuan, S.M. and Khalina, A., "Mechanical Performance and Applications of CNTs Reinforced Polymer Composites-A Review", *Nanomaterials*, Vol. 11, No. 9, (2021). doi: 10.3390/nano11092186
16. Alias, A.H., Norizan, M.N., Sabaruddin, F.A., Asyraf, M.R.M., Norrahim, M.N.F., Ilyas, A.R., Kuzmin, A.M., Rayung, M., Shazleen, S.S., Nazrin, A., Sherwani, S.F.K., Harussani, M.M., Atikah, M.S.N., Ishak, M.R., Sapuan, S.M. and Khalina, A., "Hybridization of MMT/Lignocellulosic Fiber Reinforced Polymer Nanocomposites for Structural Applications: A Review", *Coatings*, Vol. 11, No. 11, (2021). doi: 10.3390/coatings11111355
17. Aisyah, H.A., Paridah, M.T., Sapuan, S.M., Ilyas, R.A., Khalina, A., Nurazzi, N.M., Lee, S.H. and Lee, C.H., "A Comprehensive Review on Advanced Sustainable Woven Natural Fibre Polymer Composites", *Polymers*, Vol. 13, No. 3, (2021). doi: 10.3390/polym13030471
18. Aisyah, H. A., Paridah, M. T., Sapuan, S. M., Khalina, A., Beralp, O. B., Lee, S. H., Lee, C. H., Nurazzi, N.M., Ramli, N., Wahab, M.S. and Ilyas, R. A., "Thermal Properties of Woven Kenaf/Carbon Fibre-Reinforced Epoxy Hybrid Composite Panels", *International Journal of Polymer Science*, Vol. 2019, (2019). doi: 10.1155/2019/5258621
19. Abrial, H., Ariksha, J., Mahardika, M., Handayani, D., Aminah, I., Sandrawati, N., Sapuan, S.M. and Ilyas, R.A., "Highly transparent and antimicrobial PVA based bionanocomposites reinforced by ginger nanofiber", *Polymer Testing*, Vol. 81, No. 106186, (2020). doi: 10.1016/j.polymertesting.2019.106186
20. Handajani, S., Manuhara, G.J. and Anandito, R.B.K. "Pengaruh Suhu Ekstraksi terhadap Karakteristik Fisik, Kimia dan Sensoris Minyak Wijen (*Sesamum Indicum* L.)", *AgriTech*, Vol. 30, No. 2, (2010), 116-122.
21. ASTM D2240-15e1, "Standard Test Method for Rubber Property-Durometer Hardness". ASTM International, West Conshohocken, PA, (2015).
22. ISO 527-4, "Plastics-Determination of tensile properties - Part 4: Test conditions for isotropic and orthotropic fibre-reinforced plastic composites". International Organization for Standardization (ISO), Switzerland, (1997).
23. ASTM D790-17, "Standard Test Methods for Flexural Properties of Unreinforced and Reinforced Plastics and Electrical Insulating Materials". ASTM International, West Conshohocken, PA, (2017).
24. ASTM D70-03, "Standard Test Method for Specific Gravity and Density of Semi-Solid Bituminous Materials (Pycnometer Method)". ASTM International, West Conshohocken, PA, (2003).
25. ASTM D570-98, "Standard Test Method for Water Absorption of Plastics". ASTM International, West Conshohocken, PA, (2018).
26. EL-Wazery, M., EL-Kelity, A. and Elsad, R., "Effect of Water Absorption on the Tensile Characteristics of Natural/ Synthetic Fabrics Reinforced Hybrid Composites", *International Journal of Engineering, Transactions B: Applications*, Vol. 33, No. 11, (2020), 2339-2346. doi: 10.5829/ije.2020.33.11b.24
27. Arief, Y., Makmud, M., Sahari, J., Junian, S. and Wahit, M., "Tensile and Physical Properties of Linear Low Density Polyethylene-natural Rubber Composite: Comparison between Size and Filler Types", *International Journal of Engineering, Transactions C: Aspects*, Vol. 29, No. 9, (2016), 1257-1262. doi: 10.5829/idosi.ije.2016.29.09c.11
28. Tuswan, T., Zubaydi, A., Piscesa, B., Sari, E. N. and Ismail, A. "Core sandwich material development based on vinyl ester bioresin for ship structure application", IOP Conference Series: Materials Science and Engineering, Vol. 1034, No. 1, (2021), 012152. doi: 10.1088/1757-899X/1034/1/012152
29. Daramola, O.O. and Akintayo, O.S., "Water Absorption Characteristic of Epoxy Matrix Composites Reinforced with Green Silica Particles". *Leonardo Electronic Journal of Practices and Technologies*, Vol. 32, (2018), 215-232.
30. Coates, J., "Interpretation of Infrared Spectra, a Practical Approach". Chichester: John Wiley & Sons, (2000).
31. Liu, C., Li, J., Lei, W. and Zhou, Y., "Development of biobased unsaturated polyester resin containing highly functionalized castor oil". *Industrial Crops and Products*, Vol. 52, (2014), 329-337. doi: 10.1016/j.indcrop.2013.11.010
32. Fakhari, A., Rahmat, A. R., Wahit, M. U. and Arjmandi, R., "Bio-Based Hybrid Polymers from Vinyl Ester Resin and Modified Palm Oil: Synthesis and Characterization", *International Polymer Processing*, Vol. 32, No. 1, (2017), 20-25.
33. Ismail, A., Zubaydi, A., Piscesa, B. and Tuswan, T., Ariesta, R.C., "Study of Sandwich Panel Application on Side Hull of Crude Oil Tanker", *Journal of Applied Engineering Science*, Vol. 19, No. 4, (2021), 1090-1098. doi: 10.5937/jaes0-30373
34. Ariesta, R.C., Zubaydi, A., Ismail, A. and Tuswan, T., "Damage Evaluation of Sandwich Material on Side Plate Hull using Experimental Modal Analysis", *Materials Today: Proceedings*, Vol. 47, No. 10, (2021), 2310-2314. doi: 10.1016/j.matpr.2021.04.293
35. Ariesta, R.C., Zubaydi, A., Ismail, A., Tuswan, T., "Identification of Damage Size Effect of Natural Frequency on Sandwich Material using Free Vibration Analysis", *NAŠE MORE: znanstveni časopis za more i pomorstvo*, Vol. 69, No. 1, (2022), 1-8. doi: 10.17818/NM/2022/1.1
36. Hantoro, R., Utama, I.K.A.P., Arief, I.S., Ismail, A. and Manggala, S.W., "Innovation in Vertical Axis Hydrokinetic Turbine-Straight Blade Cascaded (VAHT-SBC) Design and Testing for Low Current Speed Power Generation", *Journal of Physics: Conference Series*, Vol. 1022, No. 1, (2018), 012023. doi: 10.1088/1742-6596/1022/1/012023

Persian Abstract

چکیده

تحقیقات در مورد مواد سبک وزن در ساختار کشتی در دهه گذشته گام های بزرگی برداشته است. یکی از دلایل این است که فعالیت های حمل و نقل افزایش یافته است و بنابراین امکان افزایش ظرفیت حمل بار به روشی واقعی با استفاده از مواد سبک وزن پیشرفته وجود دارد. این مقاله یک بررسی تحقیقاتی در مورد آزمایش های تجربی مواد بیو رزین وینیل استر با استفاده از روغن نخل و روغن کنجد بر اساس استاندارد Lloyd's Register (LR) را خلاصه می کند. آزمایش های متعددی از جمله چگالی، آزمون جذب آب، آزمون مادون قرمز تبدیل فوریه (FTIR)، میکروسکوپ الکترونی روبشی (SEM) و آزمایش های مکانیکی برای ارزیابی اثر افزودن ۲ تا ۱۰ درصد روغن های گیاهی بر خواص مکانیکی انجام شد. تأثیر افزودن روغن های گیاهی با موفقیت با استفاده از اندازه گیری های فیزیکی مشخص می شود، که نشان دهنده احتمال تشکیل یک ترکیب پلیمری برای افزایش مقدار ازدیاد طول است. آزمایشات مکانیکی نشان می دهد که افزودن روغن های گیاهی باعث کاهش چگالی متوسط، سختی، استحکام خمشی و استحکام کششی می شود. استحکام خمشی حدود ۹.۲۰ - ۴۷.۰۶ درصد برای افزودن ۲-۱۰ درصد روغن نخل و ۵.۳۳ - ۴۲.۴۰ درصد برای افزودن روغن کنجد کاهش می یابد. علاوه بر این، روغن نباتی باعث کاهش مقاومت کششی حدود ۵-۱۸.۷۵ درصد در روغن پالم و ۳.۷۵-۱۳.۷۵ درصد در روغن کنجد می شود. همانطور که خلاصه شد، رزین زیستی مبتنی بر روغن کنجد رفتار مکانیکی بهتری با افزودن روغن ۴ تا ۸ درصد دارد که تمام معیارهای ثبت لوید را برآورده می کند.



Effect of Particle Size, Moisture Content and Density on the Hyperbolic Model Parameters for Non-cohesive Soil

G. D. Dhadse*, G. Ramtekkar, G. Bhatt

Department of Civil Engineering, National Institute of Technology, Raipur-492010, C.G., India

PAPER INFO

Paper history:

Received 18 February 2022

Received in revised form 08 April 2022

Accepted 09 April 2022

Keywords:

Hyperbolic Model Parameters

Numerical Modeling

Box Shear Test

Particle Size

Non-cohesive Soil

ABSTRACT

The hyperbolic non-linear elastic constitutive model for idealization of non-cohesive soil has been commonly used by researchers in numerical modeling of geotechnical problems. The hyperbolic model consists of several parameters such as modulus number ' K ', exponent ' n ', angle of internal friction ' ϕ ' and failure ratio ' R_f ', which are evaluated using laboratory shear test. The parameters ' K ', ' n ' and ' R_f ' are evaluated from transformed stress-strain curve whereas ' ϕ ' is directly evaluated from normal and shear stress. The study on ' ϕ ' for various soil samples have been performed by many researchers whereas the variation of ' K ', ' n ' and ' R_f ' for various soil samples have not been much explored in the literatures. In addition to it, the evaluation procedure of hyperbolic model parameters (HMP) is a very tedious task when samples are in large numbers. Therefore it is necessary to study the variation of HMP for various non-cohesive soil conditions and to propose certain correlations for its evaluation. The HMP are highly dependent on particle size, moisture content and density. Thus in order to study the influence of these factors on HMP, coarse, medium and fine sand as well as fine gravels with varying densities have been taken into consideration. The direct shear tests have been conducted in dry and moist conditions. The HMP have been evaluated for every samples and the effect of particle size, moisture content and density have been studied. It has been found that the influence of particle size is more than that of moisture content and density. Further the correlations have been developed for HMP with respect to particle size, moisture content and density. The correlations are useful in evaluation of HMP.

doi: 10.5829/ije.2022.35.09c.04

1. INTRODUCTION

Soil is a complex material having non-linear stress-strain response when subjected to loading [1]. Due to availability of high speed computers and advanced numerical techniques such as finite element method, it is possible to incorporate the non-linearity of soil [2-4]. The non-linearity of soil has been taken into consideration by various constitutive models such as, hypo-elastic models, plasticity models, hyper-elastic models, etc [1, 5, 6]. The performance of these models mainly depends on its parameters [7, 8]. As the numbers of parameter are more, the accuracy of the model is more [9, 10]. Thus every parameter present in the model is having some specific significant contribution on the behavior of soil. These model parameters are depending on many factors such as

type of soil, particle size, water content, density, etc. The influencing factors are varying based on the type of soil. The model parameters are generally showcased strength and stiffness criteria.

In present investigation, the hyperbolic model [11-13] for representation of constitutive behavior of non-cohesive soil has been studied and its parameters have been evaluated. The model is versatile and has been used for many geotechnical applications [14-16]. Hence the appropriate study on its parameters is necessary. This model is helpful in static and quasi-static condition and predicts the load-displacement behavior appropriately [17-19]. The model finds out the tangent modulus ' E_T ' at any stress level using Equation (1). Further, for some specific geotechnical applications, researchers have modified the hyperbolic model [20, 21].

*Corresponding Author Institutional Email: gdhadse@yahoo.com
(G. D. Dhadse)

$$E_T = \left[1 - \frac{R_f(1 - \sin \phi)(\sigma_1 - \sigma_3)}{2(C \cos \phi + \sigma_3 \sin \phi)} \right]^2 K.P_a \left(\frac{\sigma_3}{P_a} \right)^n \quad (1)$$

where, ' P_a ' is atmospheric pressure and ' σ_1 ' & ' σ_3 ' are major and minor principal stresses

The model has several parameters such as modulus number ' K ', exponent ' n ', failure ratio ' R_f ', angle of internal friction ' ϕ ' and cohesion ' C '. These parameters have been evaluated using shear test [22-24]. The parameters ' K ', ' n ' and ' R_f ' have been evaluated from transformed stress-strain curve whereas ' ϕ ' (in degrees) has been directly evaluated from normal and shear stress [16, 25]. The researchers have been focused on the variation of strength parameters for various soil conditions whereas the performance of parameters such as ' K ', ' n ' and ' R_f ' for various soil conditions have not been much explored. Hence there is necessity to study the variation of these parameters with respect to various non-cohesive soil conditions. Also, if the samples are in large numbers, the methodology of evaluation of HMP is a very tedious task. Hence there is need to propose certain correlations which will be helpful in predicting the HMP for non-cohesive soil.

The HMP evaluation procedure has been well explained by various researchers [1, 26, 27]. The hyperbolic model is based on the stress-strain curves of drained triaxial compression tests of sands and clays [25, 28]. Its failure criterion is based on the Mohr-Coulomb model. But as far as non-cohesive samples are considered, the undisturbed sample preparation is very difficult. Hence in order to overcome this difficulty, the HMP has been evaluated from direct shear test by performing few modifications [18, 29, 30]. According to Asadi et al. [29] and other researchers [31, 32], the evaluation of HMP from direct shear test has been found in good agreement as compared to triaxial test.

From the literatures, it has also been reviewed that, the strength parameters of non-cohesive soil depends on particle size, moisture content and density. Thus the stiffness parameters are also vary according to the strength parameters. Hence the same factors have been taken into consideration in present study for studying the variation of ' K ', ' n ' and ' R_f ' for non-cohesive soil samples [22, 33]. The performance of ' K ', ' n ' and ' R_f ' for various soil conditions is a novel contribution of present study. The HMP have been evaluated for coarse, medium and fine sand as well as fine gravels. The tests have been performed for dry and optimum moisture content (OMC) conditions. The density for each sample has also been evaluated. Total 13 no. of direct shear tests have been performed for 04 normal stress conditions. Hence, based on the experimentations, the effect of particle size, density and moisture content on the HMP has been studied in this paper. Also on the basis of analysis result, correlations have been formed for evaluation of HMP.

2. METHODOLOGY

Effect of particle size, density and moisture content on the HMP has been evaluated for the test samples given in Table 1. The HMP has been evaluated for each sample considering dry and moist conditions. After analyzing the samples, correlations are developed to evaluate the HMP directly from particle size, density and moisture content. The methodology has been applied to non-cohesive soil mass only.

2. 1. Materials

The non-cohesive soil samples have been taken into consideration for evaluation of HMP using direct shear test. The sieve analysis, rodded density test and OMC test has been carried out on all the samples under consideration. Table 1 shows the material samples as well as ' D_{50} ' (mean particle size) value, optimum moisture content and rodded density. The material samples have been chosen in such a way that, all gradations of sand and fine gravels will be covered in experimentation. The pictorial representation of samples under consideration is given in Table 2.

2. 2. Evaluation of Hyperbolic Model Parameters

Researchers have suggested the methodology for determination of HMP [26, 29]. In this paper, a similar methodology has been adopted.

The direct shear test has been performed on sand and fine gravel samples. The sand has been tested by small box shear test apparatus whereas the fine gravels have been tested by large box shear test apparatus. In order to get familiar with determination of HMP, an example of normal sand sample has been demonstrated here. The direct shear test on normal sand sample has been performed for four normal stress conditions as shown in Figure 1. The graph between shear stress and tangential displacement is plotted as shown in Figure 1.

The plot in Figure 1 has been transferred to transformed stress-strain curve as shown in Figure 2. In Figure 2, the Y- intercept denotes ' a ' and slope of lines denotes ' b '. Thus from Figure 2, the values for ' a ' and ' b ' are determined. The failure ratio is found as ' $R_f = \tau_f / \tau_{ult}$ ' (whereas ' τ_f ' is shear stress at failure and ' τ_{ult} ' is ultimate shear stress) thus ' $1/b$ ' gives the value of ' τ_{ult} ' (Figure 2 represents as the linear regression of all normal stress values thus the shear stress obtained from it is said as ultimate) and ' τ_f ' is obtained from Figure 1.









From Figure 2, ' $1/a$ ' gives the value of initial tangent modulus. Thus graph between initial tangent modulus Vs normal stress is plotted as shown in Figure 3. The Y-intercept corresponding to unit normal stress gives the value of modulus number ' K ' and slope of the plot gives the value of exponent ' n '.

Finally a graph between shear stress and normal stress is plotted as shown in Figure 4. The slope of plot gives the value of angle of internal friction ' ϕ ' and Y- intercept gives the value of cohesion ' C '.

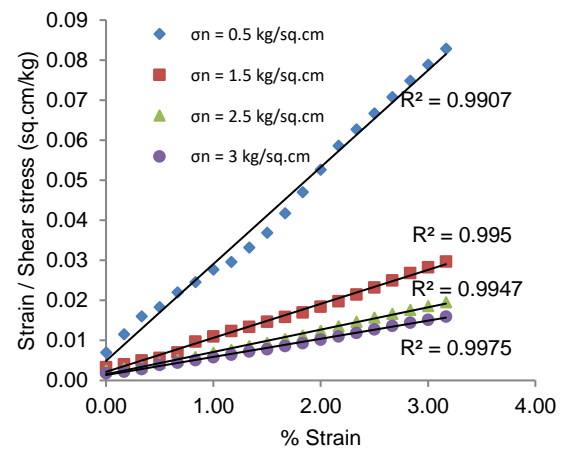
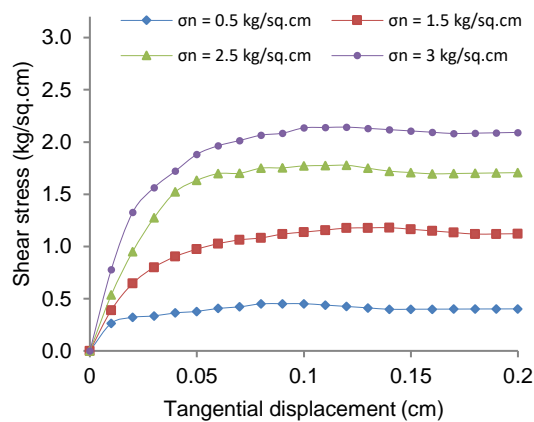
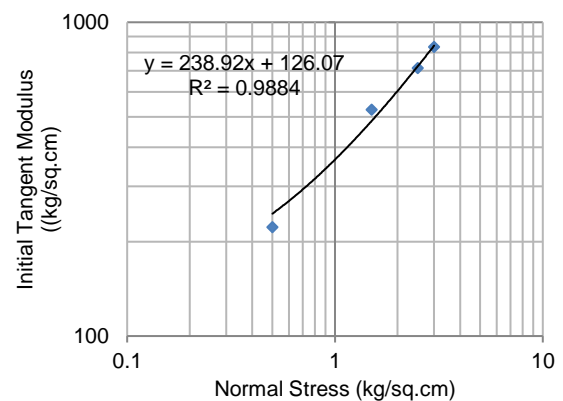
TABLE 1. Material Samples under consideration for evaluation of HMP

Sr. No.	Sample	Abbreviation	Particle Size D_{50} (mm)	Moisture Content (%)	Density (g/cm ³)
1	Fine Sand	A	0.31	0	1.72
2	Sand R 425 u – P 600 u	B	0.51	0	1.69
3	Normal Sand	C	0.68	0	1.78
4	Sand R 600 u – P 1.18mm	D	0.86	0	1.66
5	Sand R 1.18 – P 4.75mm	E	1.76	0	1.61
6	Gravel R 4.75 mm - P 10 mm	F	7.46	0	1.61
7	Gravel R 10 mm – P 12.5 mm	G	11.01	0	1.57
8	Gravel R 12.5 mm – P 20 mm	H	13.52	0	1.54
9	Moist Normal Sand	I	0.68	11.98	1.99
10	Moist Fine Sand	J	0.31	12.35	1.94
11	Moist sand R 425 u – P 600 u	K	0.51	12.72	1.89
12	Moist Sand R 600 u – P 1.18mm	L	0.86	13.05	1.85
13	Moist sand R 1.18 – P 4.75mm	M	1.76	13.48	1.80

TABLE 2. Material Samples Photographs

			
Normal Sand	R 1.18 – P 4.75mm	R 600 u – P 1.18mm	R 425 u – P 600 u
			
Fine R 75 u – P 425 u	R 4.75 mm – P 10 mm	R 10 mm – P 12.5 mm	R 12.5 mm – P 20 mm

P- Passing; R - Retaining

**Figure 2.** Transformed Stress-Strain curve for normal sand**Figure 1.** Shear Stress Vs Tangential displacement plot for normal sand**Figure 3.** Initial Tangent Modulus Vs Normal Stress Plot for normal sand

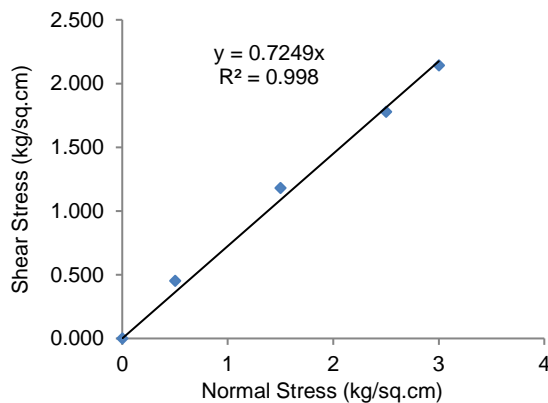


Figure 4. Shear Stress Vs Normal Stress Plot for normal sand

Same methodology has been adopted for evaluation of HMP for all the soil samples.

3. VARIATION OF HYPERBOLIC MODEL PARAMETERS WITH RESPECT TO PARTICLE SIZE, MOISTURE CONTENT AND DENSITY

The HMP has been determined using the procedure discussed in section 2.2. In order to study the variation of particle size (D_{50}), moisture content and density, HMP were plotted against particle size, moisture content and density as shown in Figures 5, 6 and 7, respectively.

From Figure 5, it is observed that, as the ' D_{50} ' value is increasing, the HMP such as ' K ', ' ϕ ', ' n ' are also increasing. Due to increasing in particle size, the friction in between the particles increases; thus, the angle of internal friction also increasing. Similarly, as friction is increased, the initial tangent modulus also tends to increase. Hence the value of ' K ' and ' n ' has increased with an increase in particle size. The variation of ' R_f ' with

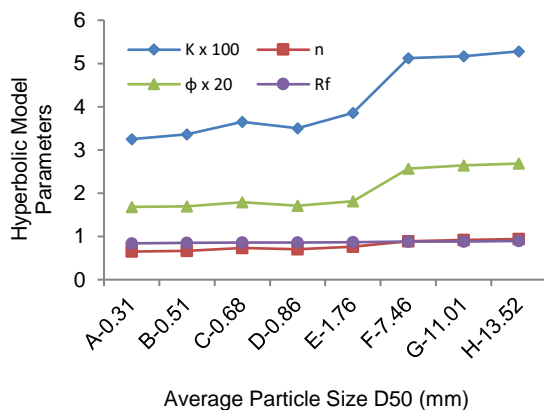


Figure 5. Variation of Particle Size on HMP

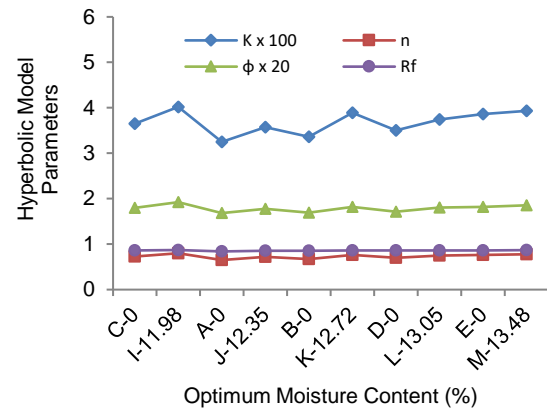


Figure 6. Variation of Moisture Content on HMP

respect to particle size is very insignificant. The parameters ' K ', ' ϕ ', and ' n ' are dependent on each other; thus, the graphical variation is also similar.

From Figure 6, the variation of HMP with respect to dry and moist sand is observed (sample identification is given in Table 1). It is seen that, the sample with OMC slightly gets dense as compared to dry samples. The tests have been carried out on sand samples only because OMC is not feasible for gravel type of samples. As the samples are getting densified due to OMC, the values of ' K ', ' ϕ ' and ' n ' are getting slightly increased as compared to dry samples. Also it is observed that, as particle size increases, the denseness decreases due to lubrication. Thus the ' K ', ' ϕ ' and ' n ' is slightly reduced as compared to fine particles. The variation of ' R_f ' is again very less in spite of variation in moisture content.

Figure 7 illustrates the effect of density on HMP. The density of moist sand is slightly more than that of dry sand, thus the value of parameters such as ' K ', ' ϕ ', and ' n ' are slightly more than that of dry sand. Whereas for fine gravels, the density is less still the HMP are higher than that of the sand. This has happened due to production

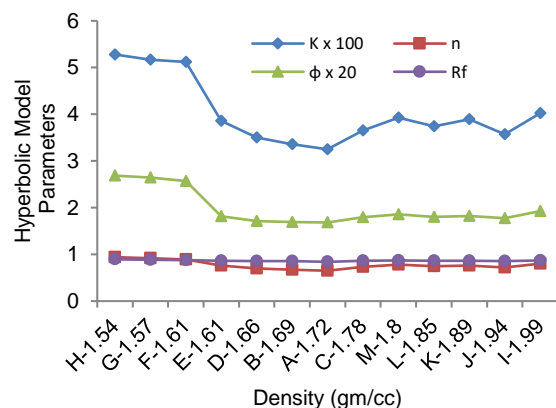


Figure 7. Variation of Density on HMP

of excessive friction between gravel particles. Again ' R_f ' is not much varying as per increase in density. The parameter ' R_f ' is a ratio, thus according to experimentation conditions its value is calculated. Hence ' R_f ' slightly looks independent of particle size, moisture content and density.

3. 1. Sensitivity Analysis The sensitivity analysis has been carried out to study the influence of various input parameters (such as particle size, moisture content and density) on HMP. The analysis is based on the sensitivity index (I). The sensitivity index is a ratio of relative change in the output parameter to relative change in the input parameter [34]. The sensitivity index has been calculated using Lenhart et al. [35] equation. (Equation (2)).

$$I = \frac{X_0(Y_2 - Y_1)}{Y_0(X_2 - X_1)} \quad (2)$$

where, X_0 – central value of input parameter, Y_0 – central value of output parameter at X_0 , $X_1 = X_0 - \Delta X$ (ΔX – difference in input parameter), $X_2 = X_0 + \Delta X$ and Y_1 and Y_2 – corresponding to X_1 and X_2 .

Lenhart et al. [35] has also specified the classification of sensitivity index as stated in Table 3.

Based on Equation (2), the sensitivity index was calculated for every input parameter of every HMP. The sensitivity of the input parameters was assessed as stated in Table 3. Table 4 summarized the sensitivity index of each input parameter for HMP with its significance.

From Table 4 and Figures 5 to 7, it has also been found that, the particle size has the maximum influence on HMP than those of density or moisture content. The parameter ' K ' and ' n ' primarily depend on angle of internal friction for non-cohesive soil. The effect of moisture content and density on HMP is only due to sample densification. The sensitivity of input parameters for ' R_f ' is low.

4. CORRELATIONS FOR EVALUATION OF HYPERBOLIC MODEL PARAMETERS

The HMP was calculated for the given samples and plotted against particle size, moisture content and density in section 3. In order to develop a correlation for HMP based on particle size, moisture content and density, the

TABLE 3. Classification of sensitivity index

Sr. No.	Sensitivity Index (I)	Sensitivity
1	$(I) \geq 1$	Very High
2	$1 \geq (I) \geq 0.2$	High
3	$0.2 \geq (I) \geq 0.05$	Medium
4	$0.05 \geq (I) \geq 0$	Low

TABLE 4. Sensitivity analysis of various input parameters

Sr. No.	HMP	Input parameters	Sensitivity Index (I)	Sensitivity
1	K	Particle size	0.21	High
		Moisture Content	0.07	Medium
		Density	0.16	Medium
2	n	Particle size	0.17	Medium
		Moisture Content	0.08	Medium
		Density	0.14	Medium
3	ϕ	Particle size	0.21	High
		Moisture Content	0.04	Low
		Density	0.16	Medium
4	R_f	Particle size	0.04	Low
		Moisture Content	0.02	Low
		Density	0.03	Low

multivariate regression analysis has been carried out on all set of samples. For regression analysis, HMP is output data whereas particle size, moisture content and density are input data. The 3rd degree polynomial was considered for independent variables with 95% confidence level. Further the regression analysis was carried out on all the independent variables and variables having probability more than 5% were removed. In other way, the insignificant variables were excluded from the equation. The significance of coefficient has also been found out by F -Test and accuracy of input parameters defined with T -Test. In this way, the independent variables were selected in Equations (3) to (6). Equations (3)-(6) show the correlation for ' K ', ' n ', ' ϕ ', and ' R_f ' whereas Figures 8, 9, 10 and Figure 11 show the best fit curves for experimental and predicted values. It has also been observed from Figures 8 to 11 that the values of ' R^2 ' are more than 90%, thus the prediction is very appropriate. (Density is denoted by ' γ ' and OMC is denoted by ' w ' in Equations (3) to (6))

$$K = 330.27 - 159.223D_{50} + 0.79w + 112.82D_{50}\gamma \quad (3)$$

$$n = 0.6723 - 0.81D_{50} + 0.0029w + 0.13D_{50}\gamma \quad (4)$$

$$\phi = 4.6242 - 15.1085D_{50} - 0.2620w + 16.38\gamma + 10.96\gamma D_{50} \quad (5)$$

$$R_f = 11.974 - 0.6817D_{50} + 1.1422w - 12.6578\gamma + 0.04687D_{50}w - 0.3675w\gamma + 0.4009\gamma D_{50} - 0.0285D_{50}w\gamma + 0.0041D_{50}^2 - 0.0353w^2 + 3.5957\gamma^2 \quad (6)$$

Equations (3) to (6) are useful in predicting the HMP values directly. These equations are applicable to all the non-cohesive soil samples which fall under present study area. Also without conducting the shear test, the HMP can be predicted from these correlations. The correlations are reliable based on the statistical analysis. Hence one

must be confident of using it for further analysis with similar scope of study. In similar way, studies on other soil samples can also be carried out and correlations can be proposed. The methodology present in this paper is useful in carrying out further research work.

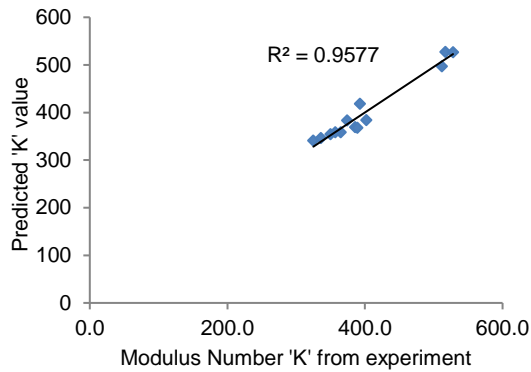


Figure 8. Fitness plot between predicted and experimental values of ' K '

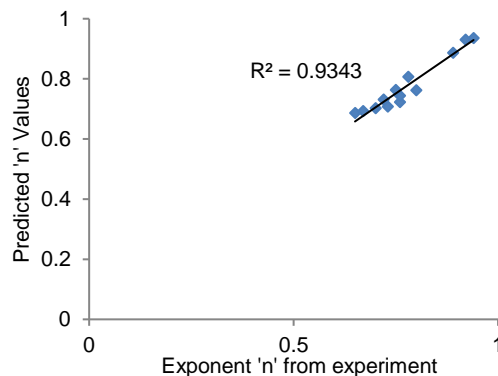


Figure 9. Fitness plot between predicted and experimental values of ' n '

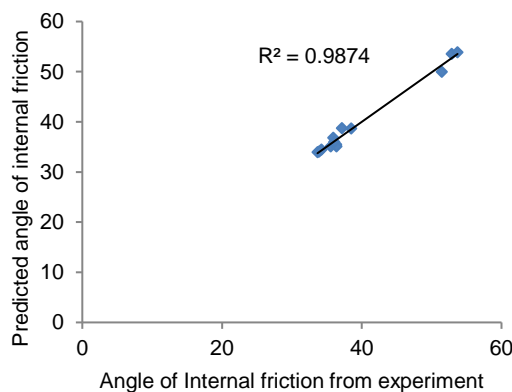


Figure 10. Fitness plot between predicted and experimental values of ' ϕ '

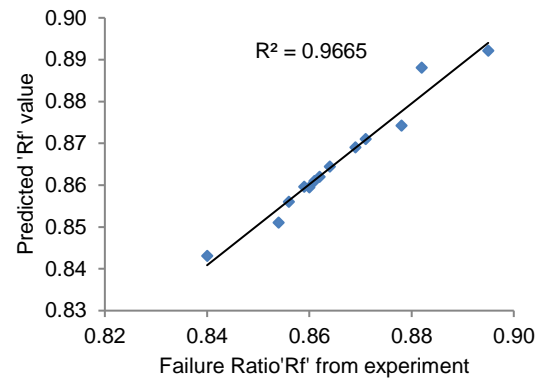


Figure 11. Fitness plot between predicted and experimental values of ' R_f '

4. 1. Error Analysis

The error analysis has also been performed for examining the accuracy of correlations as shown in Table 5. The values of Mean absolute error (MAE), Mean square error (MSE), Root mean square error (RMSE) and Mean absolute percent error (MAPE) show reliable goodness-of-fit.

TABLE 5. Error Analysis

Parameters	n	MAE	MSE	RMSE	MAPE
K	13	11.90	191.73	13.85	3.04
n	13	0.02	0.00	0.02	2.54
ϕ	13	0.64	0.66	0.81	1.61
R_f	13	0.0016	0.0000	0.0024	0.1786
n – total no. of samples					

5. CONCLUSIONS

The experimental investigation has been conducted in the present paper to study the effects of particle size, moisture content and density of non-cohesive soil on HMP. The study on variation of ' K ', ' n ' and ' R_f ' with respect to various non-cohesive soil samples is a novel contribution of present paper. Also looking at the tedious methodology for the evaluation of HMP, the correlations have been proposed. The correlations are generated using multivariate regression analysis. Based on the analysis and correlations presented in this paper, the following conclusions are drawn,

- The direct shear test has been successfully implemented for the evaluation of HMP of non-cohesive soil.
- The values of ' K ', ' n ' and ' ϕ ' are increasing with increase in particle size. This is due to an increase in friction between the particles. The sensitivity index of more than 0.2 is observed which means the particle size is highly sensitive.

- c. The non-cohesive soil samples are getting slightly densified due to OMC. Hence the values of ' K ', ' ϕ ' and ' n ' are getting slightly increased as compared to dry samples. Whereas further increase in water content, reduces the ' K ', ' ϕ ' and ' n ' due to lubrication effect.
- d. The fine gravel is having lesser density than that of sand, still the values of ' K ', ' n ' and ' ϕ ' are increasing with respect to sand samples. This is because of production of excessive friction between the particles.
- e. The variation of failure ratio with respect to particle size, moisture content and density is very less. The sensitivity index of less than 0.05 confirms that.
- f. Particle size is having maximum influence on HMP than that of moisture content and density.
- g. The effect of moisture content and density on HMP is only due to densification of soil.
- h. The proposed correlations are useful in predicting the HMP. The correlations are applicable for non-cohesive soil samples which fall under present scope of the study.
- i. The correlations are reliable based on the statistical analysis (such as R^2 value and error analysis).
- j. The methodology proposed in the present study is applicable to other soil samples as well for further study.

6. REFERENCES

1. Al-Shayea, N., Abduljawwad, S., Bashir, R., Al-Ghamedy, H. and Asi, I., "Determination of parameters for a hyperbolic model of soils", *Proceedings of the Institution of Civil Engineers-Geotechnical Engineering*, Vol. 156, No. 2, (2003), 105-117, doi: 10.1680/jeng.156.2.105.37526.
2. Horpibulsuk, S. and Miura, N., "Modified hyperbolic stress-strain response: Uncemented and cement stabilized clays", *Reports of the Faculty of Science and Engineering, Saga University*, Vol. 30, No., (2001), 39-47, doi.
3. Farhadi, N., Saffari, H. and Torkzadeh, P., "Evaluation of seismic behavior of steel moment resisting frames considering nonlinear soil-structure interaction", *International Journal of Engineering, Transactions A: Basics*, Vol. 31, No. 7, (2018), 1020-1027, doi: 10.5829/ije.2018.32.07a.03.
4. Sarlak, A., Saeedmonir, H. and Gheyretmand, C., "Numerical and experimental study of soil-structure interaction in structures resting on loose soil using laminar shear box", *International Journal of Engineering, Transactions B: Applications*, Vol. 30, No. 11, (2017), 1654-1663, doi: 10.5829/ije.2017.30.11b.05.
5. Wang, Y. and Stokoe, K., "Development of constitutive models for linear and nonlinear shear modulus and material damping ratio of uncemented soils", *Journal of Geotechnical and Geoenvironmental Engineering*, Vol. 148, No. 3, (2022), 04021192, doi: 10.1061/(asce)gt.1943-5606.0002736.
6. Liu, K., Yin, Z.-Y., Chen, W.-B., Feng, W.-Q. and Yin, J.-H., "Nonlinear model for the stress-strain-strength behavior of unsaturated granular materials", *International Journal of Geomechanics*, Vol. 21, No. 7, (2021), 04021103, doi: 10.1061/(asce)gm.1943-5622.0002042.
7. Varga, G. and Czup, Z., "Soil models: Safety factors and settlements", *Periodica Polytechnica Civil Engineering*, Vol. 48, No. 1-2, (2004), 53-63.
8. Rezayibana, B., "The effect of soil type on seismic response of tall telecommunication towers with random vibration analysis", *International Journal of Engineering, Transactions C: Aspects*, Vol. 33, No. 3, (2020), 419-426, doi: 10.5829/ije.2020.33.03c.06.
9. Çakır, Ö. and Coşkun, N., "Theoretical issues with rayleigh surface waves and geoelectrical method used for the inversion of near surface geophysical structure", *Journal of Human, Earth, and Future*, Vol. 2, No. 3, (2021), 183-199, doi: 10.28991/hef-2021-02-03-01.
10. Tarrad, A.H., "3d numerical modeling to evaluate the thermal performance of single and double u-tube ground-coupled heat pump", *HighTech and Innovation Journal*, Vol. 3, No. 2, (2022), 115-129, doi: 10.28991/hij-2022-03-02-01.
11. Brinkgreve, R.B., Selection of soil models and parameters for geotechnical engineering application, in *Soil constitutive models: Evaluation, selection, and calibration*. 2005.69-98.
12. Rahnama, H., "A hyperbolic model for stress-strain behavior of unsaturated soils", in *12th International Conference on Computer Methods and Advances in Geomechanics*, Citeseer. Vol. 2008, (2008).
13. Murugan, R.A. and Stalin, V., "Soil behaviour and hyperbolic model", in *Proc., Indian Geotechnical Conference-2009*, Guntur, India., (2009), 632-636.
14. Banerjee, S. and Malek, S., "Assessment of a hyperbolic model for undrained-cyclic shearing of remolded clay", *Journal of Engineering Mechanics*, Vol. 146, No. 7, (2020), 04020064, doi: 10.1061/(asce)em.1943-7889.0001780.
15. George, T.I. and Dasaka, S.M., "Numerical investigation of soil arching in dense sand", *International Journal of Geomechanics*, Vol. 21, No. 5, (2021), 04021051, doi: 10.1061/(asce)gm.1943-5622.0001971.
16. Viladkar, M., Zedan, A.J. and Saran, S., "Nonlinear elastic analysis of shallow footings subjected to eccentric inclined loads", *Geomechanics and Geoenvironmental Engineering*, Vol. 10, No. 1, (2015), 45-56, doi: 10.1080/17486025.2014.902117.
17. Dong, W., Hu, L., Yu, Y.Z. and Lv, H., "Comparison between duncan and chang's eb model and the generalized plasticity model in the analysis of a high earth-rockfill dam", *Journal of Applied Mathematics*, Vol. 2013, (2013), doi: 10.1155/2013/709430.
18. He, Y. and Chen, X., "The application of improved duncan-chang model in unloading soil", *The Open Civil Engineering Journal*, Vol. 8, No. 1, (2014), doi: 10.2174/1874149501408010410.
19. David, T.K., Krishnamoorthy, R.R. and IB, M.J., "Finite element modelling of soil-structure interaction", *Jurnal Teknologi*, Vol. 76, No. 8, (2015), doi: 10.11113/jt.v76.5625.
20. Gabriel, A.-A., Li, D., Chiocchetti, S., Tavelli, M., Peshkov, I., Romenski, E. and Dumbser, M., "A unified first-order hyperbolic model for nonlinear dynamic rupture processes in diffuse fracture zones", *Philosophical Transactions of the Royal Society A*, Vol. 379, No. 2196, (2021), 20200130, doi: 10.1098/rsta.2020.0130.
21. Jia, P., Khoshghalb, A., Chen, C., Zhao, W., Dong, M. and Alipour Esgandani, G., "Modified duncan-chang constitutive model for modeling supported excavations in granular soils", *International Journal of Geomechanics*, Vol. 20, No. 11, (2020), 04020211, doi: 10.1061/(asce)gm.1943-5622.0001848.
22. Arivazhagan, R., Premalatha, K., K. Sabarishri and B. S. Xavier Vedha Rayan, "Influence of silt content on the hyperbolic model parameters of sand", *Journal of Critical Reviews*, Vol. 7, No. 17, (2020), 1647-1661, doi: 10.31838/jcr.07.17.210.
23. Gens, A., Carol, I. and Alonso, E., "An interface element formulation for the analysis of soil-reinforcement interaction", *Computers and Geotechnics*, Vol. 7, No. 1-2, (1989), 133-151, doi: 10.1016/0266-352X(89)90011-6.
24. Dhadse, G.D., Ramtekkar, G. and Bhatt, G., "Finite element modeling of soil structure interaction system with interface: A review", *Archives of Computational Methods in Engineering*,

- Vol. 28, No. 5, (2021), 3415-3432, doi: 10.1007/s11831-020-09505-2.
25. Viladkar, M., Godbole, P. and Noorzaei, J., "Modelling of interface for soil-structure interaction studies", *Computers & Structures*, Vol. 52, No. 4, (1994), 765-779, doi: 10.1016/0045-7949(94)90358-1.
 26. Abdul-kareem, A.H. and Helal, A., "Estimation of hyperbolic stress-strain parameters for gypseous soils", *International Journal of Civil Engineering*, Vol. 7, (2007), doi: 10.1016/0022-4898(64)90153-3.
 27. Narepalem, S. and Godavarthi, V.R.S.R., "Constitutive behaviour of fine grained soils of vijayawada region", *KSCE Journal of Civil Engineering*, Vol. 23, No. 6, (2019), 2463-2470, doi: 10.1007/s12205-019-0699-5.
 28. Hora, M., "Nonlinear interaction analysis of infilled frame-foundation beam-homogeneous soil system", *Coupled Systems Mechanics*, Vol. 3, No. 3, (2014), 267-289, <http://dx.doi.org/10.12989/csm.2014.3.3.267>
 29. Asadi, M., Shariatmadari, N., Karimpour-Fard, M. and Noorzad, A., "Validation of hyperbolic model by the results of triaxial and direct shear tests of municipal solid waste", *Geotechnical and Geological Engineering*, Vol. 35, No. 5, (2017), 2003-2015, doi: 10.1007/s10706-017-0223-y.
 30. Hormdee, D., Kaikeerati, N. and Angsuwotai, P., "Evaluation on the results of multistage shear test", *Geomate Journal*, Vol. 2, No. 3, (2012), 140-143, doi: 10.21660/2012.3.3m.
 31. Sridharan, A., TG, S.K., Abraham, B.M. and Cyrus, S., "Applicability of hyperbolic method for the prediction of shear strength parameters from multistage direct shear tests".
 32. Adajar, M.A.Q. and Zarco, M.A.H., "Predicting the stress-strain behavior of mine tailing using modified hyperbolic model", *Geomate Journal*, Vol. 10, No. 21, (2016), 1834-1841, doi: 10.21660/2016.21.5127.
 33. Vali, R., "Water table effects on the behaviors of the reinforced marine soil-footing system", *Journal of Human, Earth, and Future*, Vol. 2, No. 3, (2021), 296-305, doi: 10.28991/hef-2021-02-03-09.
 34. Turkane, S.D. and Chouksey, S.K., "Application of response surface method for optimization of stabilizer dosages in soil stabilization", *Innovative Infrastructure Solutions*, Vol. 7, No. 1, (2022), 1-12, doi: 10.1007/s41062-021-00704-9.
 35. Lenhart, T., Eckhardt, K., Fohrer, N. and Frede, H.-G., "Comparison of two different approaches of sensitivity analysis", *Physics and Chemistry of the Earth, Parts A/B/C*, Vol. 27, No. 9-10, (2002), 645-654, doi: 10.1007/BF01743071.

Persian Abstract

چکیده

مدل ساختاری الاستیک غیرخطی هذلولی برای ایده آل سازی خاک غیر چسبنده معمولاً توسط محققان در مدل سازی عددی مسائل ژئوتکنیکی استفاده شده است. مدل هذلولی شامل چندین پارامتر مانند عدد مدول "K"، توان "n"، زاویه اصطکاک داخلی "φ" و نسبت شکست "Rf" است که با استفاده از آزمون برشی آزمایشگاهی ارزیابی می‌شوند. پارامترهای "n, K" و "Rf" از منحنی تنش-کرنش تبدیل شده ارزیابی می‌شوند در حالی که 'φ' به طور مستقیم از تنش نرمال و برشی ارزیابی می‌شود. مطالعه روی «φ» برای نمونه‌های مختلف خاک توسط بسیاری از محققین انجام شده است، در حالی که تغییرات «n, K» و «Rf» برای نمونه‌های مختلف خاک در مقالات چندین مورد بررسی قرار نگرفته است. علاوه بر آن، فرآیند ارزیابی پارامترهای مدل هذلولی (HMP) زمانی که نمونه‌ها در تعداد زیادی هستند، کاری بسیار خسته کننده است. بنابراین بررسی تغییرات HMP برای شرایط مختلف خاک غیر منسجم و پیشنهاد همبستگی‌های خاصی برای ارزیابی آن ضروری است. HMP به شدت به اندازه ذرات، رطوبت و چگالی وابسته است. بنابراین به منظور بررسی تاثیر این عوامل بر HMP، ماسه درشت، متوسط و ریز و همچنین شن‌های ریز با چگالی‌های متفاوت در نظر گرفته شده است. آزمایش برش مستقیم در شرایط خشک و مرطوب انجام شده است. HMP برای هر نمونه ارزیابی شده و اثر اندازه ذرات، میزان رطوبت و چگالی مورد مطالعه قرار گرفته است. مشخص شده است که تأثیر اندازه ذرات بیشتر از میزان رطوبت و چگالی است. علاوه بر این، همبستگی‌ها برای HMP با توجه به اندازه ذرات، محتوای رطوبت و چگالی توسعه داده شده است. همبستگی‌ها در ارزیابی HMP مفید هستند.



Experimental and Numerical Investigation of the Formability of Cross and Accumulative Roll Bonded 1050 Aluminum Alloy Sheets in Single Point Incremental Forming Process

M. Mahmoodi^{a*}, H. Tagimalek^a, M. R. Maraki^b, S. Karimi^a

^a Faculty of Mechanical Engineering, Semnan University, Semnan, Iran

^b Department of Materials and Metallurgy Engineering, Birjand University of Technology, Birjand, Iran

PAPER INFO

Paper history:

Received 08 March 2022

Received in revised form 14 April 2022

Accepted 18 April 2022

Keywords:

Single Point Incremental Forming

Accumulative Roll-bonding

Cross Accumulative Roll-bonding

Thickness Distribution

Formability

Force

ABSTRACT

As one of the methods of Severe Plastic Deformation (SPD), the Accumulative Roll-Bonding (ARB) process leads to the production of high-strength metal sheets and fine-grained structures. In this paper, the Single Point Incremental Forming (SPIF) of Al1050 sheets, processed by the ARB and CARB (Cross-Accumulative Roll-Bonding), is experimentally and numerically investigated. The forming force, thickness distribution, and forming depth in both cases (ARB and CARB) are all determined in this research. The result shows that the formability of CARB samples is higher than ARB samples. Furthermore, the formability of both ARB and Al1050 annealed samples are equal in the initial pass. In addition, the samples' strain is enhanced by increasing the number of rolling passes, and as a result, the formability scales down. The results obtained using the dynamometer reveals that the vertical forming force extent in the CARB samples is higher than the rest of the samples.

doi: 10.5829/ije.2022.35.09c.05

1. INTRODUCTION

Al 1050, due to its high corrosion resistance, good formability, high electrical and thermal conductivity, and high weldability, has been considered [1, 2]. Besides, with an increasing development of the industry, the processes of severe plastic deformation are important as an effective method for the production of high-strength metals and ultra-fine structures [3, 4]. Incremental sheet process is a new process for metal sheet forming in low-volume production without making a die [5]. Advantages of this method include formability, numerical process control capability, and low cost of equipment [6, 7]. The incremental forming is generally divided into two categories: single-point incremental formation (SPIF) and two-point incremental formation (TPIF) [8]. One of the main components in the SPIF is the sheet material and several studies have been conducted in this regard [9, 10]. Najm et al. [11] in order to produce a SPIF component with sufficient quality without defects, selected the

optimal process parameters. In other work [12] they investigated the effects of forming tool characteristics on the accuracy and formability of thin aluminum alloy blanks when using SPIF. Paniti et al. [13] by monitoring servo-motor currents, estimated the forming force in the SPIF and gave a new crack monitoring method based on light sensor.

Suresh et al. [14] examined the effect of the tool path on the incremental sheet process. They found several ways to choose a tool path in the incremental sheet process, and the most important parameters of the tool path were the vertical step, the length of the tool path, and the number of passes that indicate the better formability of the sheet. By reducing the percentage of thinning of the sheet in the direction of the circular tool, the formability will increase. Jackson et al. [15] practically examined the possibility of substituting sheet incremental formwork for sandwich panels. The feasibility of the process was performed by examining the states of thinning, failure, and surface quality after the incremental

*Corresponding author institutional Email: mahmoodi@semnan.ac.ir
(M. Mahmoodi)

forming process for different patterns of sandwich panel. Three groups of panels (metal/metal fiber/metal, metal/polymer/metal and metal/metal foam/metal) were examined. Incremental forming can be used successfully to form sandwich panels with metal foam core. Nikdooz et al. [16] examined the two-step incremental formation of an incomplete 70-degree square pyramid to improve the minimum thickness. They found that using a two-step strategy could double the minimum thickness by a single step. Lu et al. [17] designed a new tool for increasing the shape of aluminum sheets with different alloys. At the tip of the tool, an indirect ball bearing is located. It is possible to prevent the contact of the upper areas of the tip of the tool, which causes the highest friction in the sheet, and improves the formability.

Najm et al. [18] investigated the best results of the final geometry, thickness homogeneity, minimum pillow surface, and maximum forming depth using different shapes and different sizes of the tool.

Neto et al. [19] presented a complete finite element model to examine the stress and strain state near the contact surface. They found that the small contact surface between the tool and the sheet had a positive effect on the stresses under the tool, which delayed the soft failure. It was also concluded, the residual stresses in both circumferential and meridional directions are positive in the inner skin of the cone and negative in the outer skin. Hino et al. [20] studied the effect of grain size on Al 1050 rolled sheets on the vertical forming force. In the results shown, the curvature trend is similar for almost all samples, except that the peak value of the forming force increases with decreasing grain size, which is due to the large displacement density of the coarse grains. Mansouri et al. [21] have investigated the microstructure of the ARB method of sandwich sheets using stainless steel, copper, and aluminum. The analysis showed that in the first and second passes of the ARB, no plastic instability was created in the layers. With the increase in the number of passes of the accumulative roll bonding, plastic instability and eventually fracture will be observed. According to the results of this study, during the ARB process, a proper bonding has been established between the layers. Rahmatabadi et al. [22] studied Young's modulus, the anisotropy coefficient in the rolling direction, and other elastic and plastic parameters of multilayer aluminum/brass composite produced by ARB process. The results showed that a good relation between aluminum /brass mixing in the original sandwich was made and strengthened by increasing the stability pressure. In the other work [23], they examined the effect of the ARB process on the fracture toughness of ultrafine-grained aluminum. Test results showed that by increasing the number of the ARB cycles, fracture toughness was increased and the maximum value of this parameter achieved in the last cycle.

Past Researches in the SPIF process were on single-layer and multilayer sheets. Due to the capabilities of the SPIF process and the properties of the multilayer sheets, it can be used to produce parts with multilayer sheet.

In this paper, the incremental single point forming of Al 1050 sheets processed by the ARB and CARB has been studied experimentally and numerically. The effect of the ARB and CARB process and heat-treatment on the formability of the samples and forming forces were investigated.

2. MATERIALS AND METHODS

2. 1. ARB EXPERIMENTS

The 1050 aluminum sheets were bonded by the ARB and then formed by the SPIF process. The thickness of the sheet used was 1 mm, with dimensions of $130 \times 130 \text{ mm}^2$ and cut according to the size of the die. The chemical composition of the Al 1050 sheet obtained from quantometry analysis, are summarized in Table 1.

The use of rolling in the ARB process is not only as a deformation method but also as a factor for creating bonding between two sheets and producing a completely integrated sheet. To increase the adhesion of the layers, the accumulative roll-bonding process was done in the cold and non-lubricating conditions. In the ARB process, the severe plastic deformation produces a solid-state bonding. According to the Film theory, as a dominant mechanism of low temperature ARB, bonding occurs when metal surfaces are exposed and deformed to a sufficiently large value. The fracture of surface layers and extrusion of virgin metals through the cracks have the main roles in a real contact. The reduction percent at this stage was 50%, and as a result, the thickness of the sheet was equal to the thickness of the original sheet. Then the sheet was cut in two lengthwise, and the steps are repeated. Figure 1 shows a schematic of the ARB and CARB process. The number of layers of sheet bonded by the ARB method was obtained from the relation 2^n (n is the number of passes). The ARB processed sample had 32 layers and the thickness of each layer was $31 \text{ }\mu\text{m}$.

2. 2. SPIF Experiments

In the empirical test of ISF, the rotational speed of the tool was 900 RPM, the forward speed was 700 mm/min, and the vertical step was 0.5 mm.

TABLE 1. Chemical composition of Al 1050

Metal	Al	Zr	V	Sr	Pb
Al 1050	99.54	0.0137	0.0164	0.002	0.0044
Ti	Sn	Ni	Cr	Mn	Fe
0.0044	0.009	0.0019	0.0066	0.010	0.157

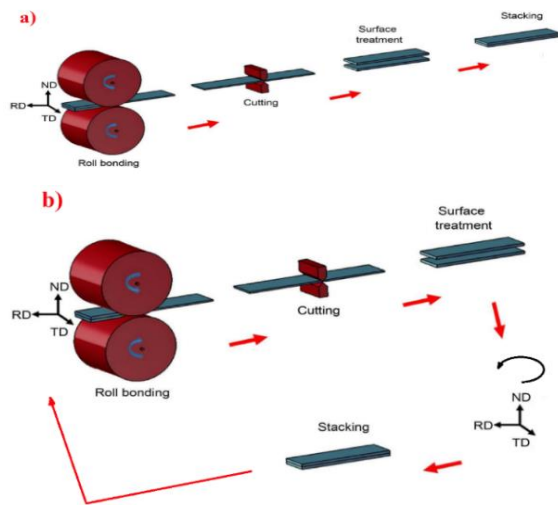


Figure 1. Schematic of the bonding process; a) ARB, and b) CARB

In the SPIF process, it is necessary to control the sheet. Figure 2 shows the tools and fixtures used for the SPIF process. Table 2 shows the specifications of the experimental test samples. According to Table 2, Al 1050, 1ARB, 3ARB, 5ARB and 3CARB samples were annealed at 380°C for 60 minutes.

To perform the tensile tests, samples were prepared according to standard ASTM E8-04 [24].

To apply ISF, a spherical VCN alloy steel head tool with a diameter of 11 mm and hardness of 25 HRC was used. To ensure better performance and prevent sudden failure, and non-corrosion of the tip of the tool, it was heated at a temperature of +950°C and cooled in oil. To perform the SPIF process, it's necessary to move the tool simultaneously in a specific direction in three directions X, Y, and Z. Therefore, the John Ford VMC-850 three-axis CNC milling machine was used for the SPIF process.

Tensile test was performed by the machine SANTAM STM-150 in Semnan University. A dynamometer with piezoelectric b9257 was used to measure the force. The SPIF process and then the measurement of the depth of

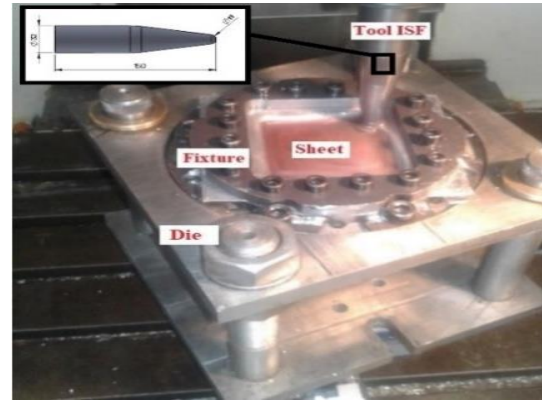


Figure 2. Tools and fixtures used for the SPIF process

tension was done by the CNC machine John Ford VMC-850 three-axis CNC milling made in Taiwan country. According to Figure 3, the path selected in this study is a square path, and the tool must move in a steady direction along the Z-axis and form the sample.

Two common paths have been used in ISF are profile tool path and spiral tool path. Many previous studies proved that the spiral path strategy shows better results than the profile path in formability, geometric accuracy, and surface roughness of ISF components. But in this work, according to the square shape of the sample, the unidirectional profile tool path was designed based on Jadhav's work [25]. He observed twist and dent in parts formed using spiral tool path. The numerical control program to introduce the square path of the process was created by MATLAB. After fixing the sheet on the fixture and preparation of the CNC milling machine, SPIF was done.

To measure the thickness distribution, the part's thickness was determined at different points using an ultrasonic thickness gauge with an accuracy of 0.01 mm in a cross section along the middle plane that for all the forming depth could be different. Song et al. [26] showed there was three different zones along the components wall of ISF (bending/stretching, shear, and stretch/shear). The thickness distribution includes these areas.

TABLE 2. Specifications of experimental samples

Type	Number of passes	Heat-treatment	Code
Al 1050	--	*	Anneal Al 1050
ARB	1	*	1ARBH
ARB	3	*	3ARBH
ARB	5	*	5ARBH
ARB	1	--	1ARB
ARB	3	--	3ARB
CARB	3	--	3CARB
CARB	3	*	3CARBH

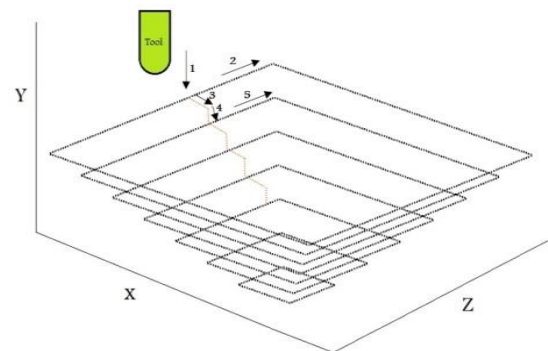


Figure 3. The tool path for the SPIF process

3. FINITE ELEMENT ANALYSIS

To simulate the SPIF process, Abaqus finite element software was used, and the FE model shown in Figure 4. The tools and die were considered to be analytical rigid. The material behavior was considered to be Elastic-Plastic, and assumed that follow the Von-Mises yield criterion. The blank sheet was meshed using for node shell elements with reduced integration (S4R). All surface-to-surface contacts were selected by mechanical contact with tangential behavior in the Columbus friction model. The friction coefficient was 0.1. To simulate the ISF process, Abaqus 2019 software was used. The contact between the backup plate and the sheet was defined as frictionless and wholly constrained. In this modeling, the written code in MATLAB software was used to move the tool. Then the output of this program is defined as a domain in Abaqus software that specifies the tool's movement in all three directions X, Y, and Z at any time. Therefore, due to the large deformation in the cold state process, a dynamic explicit solvent was used. To obtain the optimal mesh size, the effect of mesh size on the equivalent plastic strain (PEEQ) was investigated. Figure 5 shows the effect of the mesh size on PEEQ from the sample center.

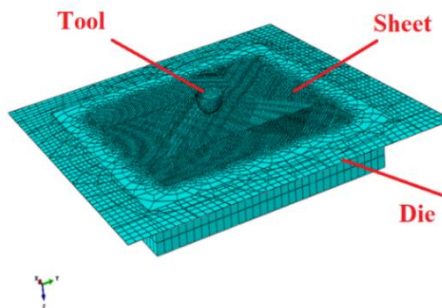


Figure 4. FE model of the SPIF process in Abaqus software

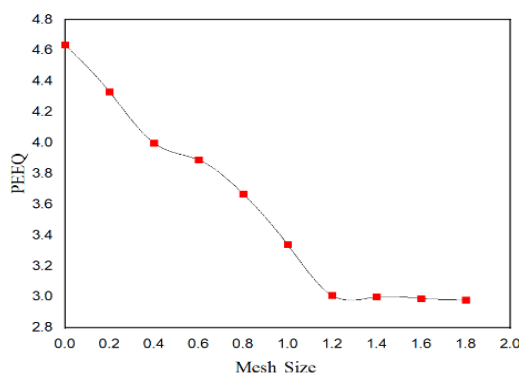


Figure 5. Mesh Sensitivity Diagram: Effect of mesh size on the equivalent plastic strain of Al 1050 sample

So, the mesh size of 1.2 was used to simulate the sheet. In this study, the purpose of the simulation was to investigate the validity of the results in ARB samples that underwent the SPIF process. In FE analysis, only data from existing ARB samples were examined.

4. RESULTS AND DISCUSSION

Because the ARB process is an SPD process, the plane strain rolling process produces different properties in different directions of the sheet. Therefore, due to the anisotropy, different properties are obtained in the directions of RD, TD and 45-degree rolling. Therefore, the tensile test results were evaluated on seven existing samples in three transverse, longitudinal, and 45-degree positions relative to the rolling direction. Figure 6 shows the stress-strain curves of the ARB samples at three different directions 0° , 45° , and 90° angle to the rolling direction. The tensile strength of ARB samples, according to this figure, compared to the annealed sheet has increased, and the formability has decreased. To simulate the finite element and define the properties of materials, it was necessary to have true stress and strain of the material, so the engineering stress-strain obtained from the tensile test must be converted to a true stress-strain. To evaluate the forming forces, a dynamometer with piezoelectric b9257 and amplifier identification number 6019b126 was used to measure the main vertical forces. By putting the die on the dynamometer and performing the SPIF process, the tool's forces could be obtained in three directions. The most significant effect of the force in the SPIF process was in the vertical direction, so only the vertical force was studied. Figure 7 shows the force applied to the tool before filtering. As shown in the figure, the amount of forming force increases until it reaches the necking point, and then due to strain hardening with the thinning defect, a decrease in force was observed.

Because the behavior of materials is different in all samples of experimental designs, their formability is also

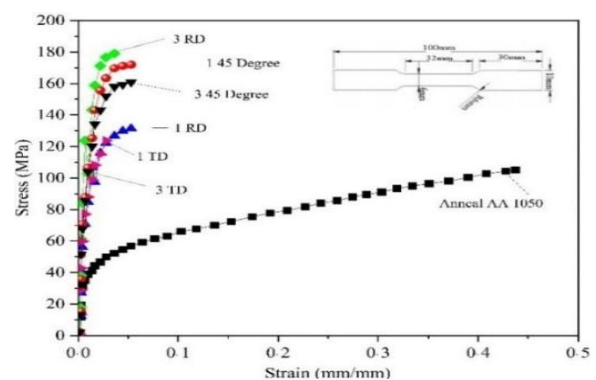


Figure 6. True stress-strain curves after the ARB process

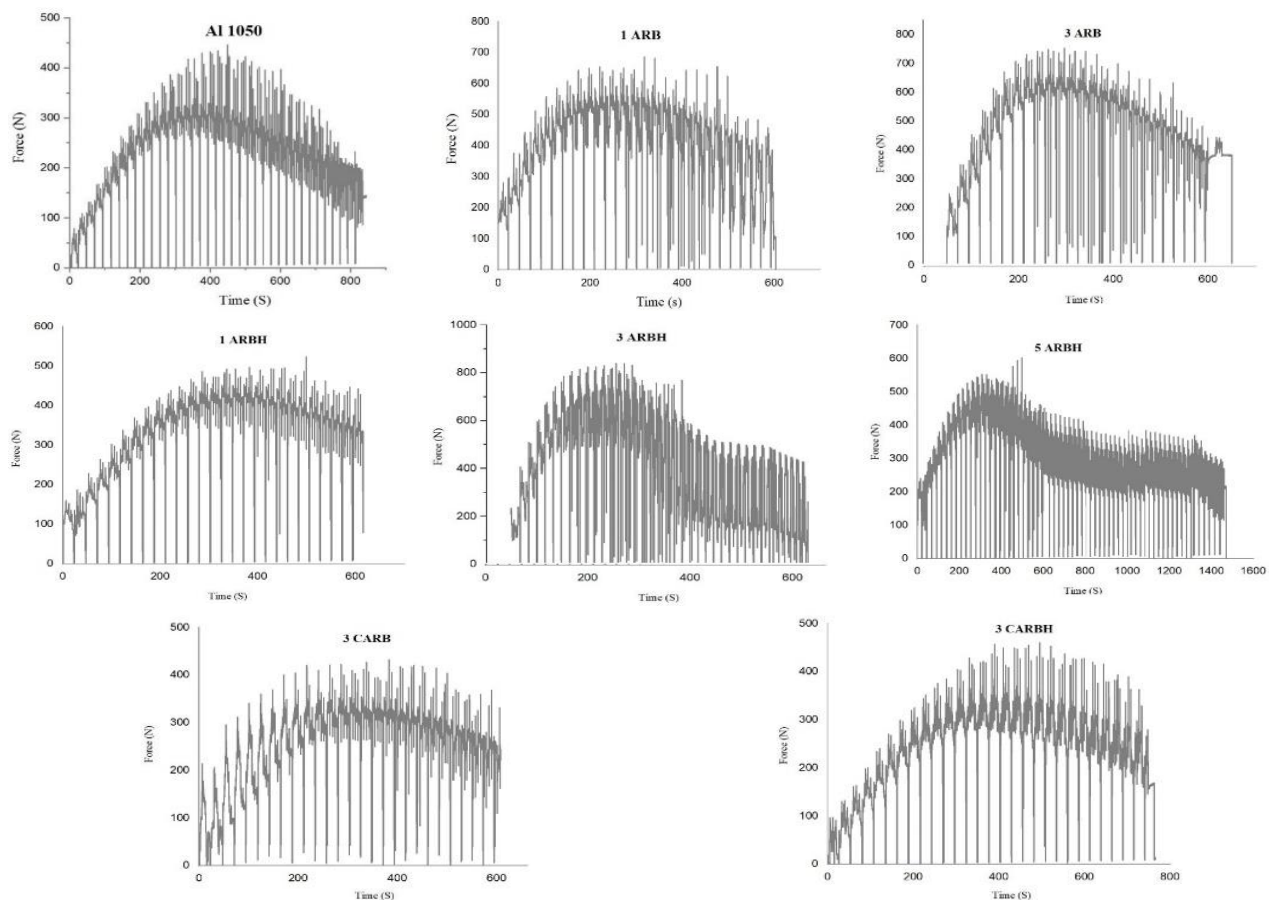


Figure 7. Vertical forming force in the SPIF process (Measured by Dynamometer with piezoelectric b9257 before filtering)

different during the ISF process. As shown in the results, they experience different formability and forming depth. Therefore, the degree of formability and the process continuity affect the time and also the extreme force occurs at different times. The purpose of using a dynamometer is to reach the extreme of force. The ARB process' impact on the forming force is depicted in Figure 8. Increased the number of passes in the ARB process, the tensile strength promotes very rapidly in the first pass. The rise of pass number heightens the sheets' tensile strength, and thus, the forming force in the SPIF process aggravates. The samples' tensile strength is reduced by the annealing heat-treatment, so it devaluates the forming force significantly. In all similar passes, the CARB sheets' tensile strength is higher than ARB sheets', and consequently, the CARB sheets are of greater SPIF forces. As a result, the samples' forming force is declined as compared to the samples without heat-treatment, so that the force in a one-pass ARBH sample is subtracted up to 18% as compared to a one-pass ARB sample. Moreover, a 47% reduction in force is observed in a three-pass ARB sample as compared to its equivalent sample, which imposed to the heat-treatment. In case of

a three-pass CARB sample, a 5% increment has been observed in forming force as compared to a three-pass ARBH sample. As well, in a three-pass CARB sample as compared to a one-pass ARBH sample, the force is increased by 25%. This force augmentation is due to the higher tensile strength of CARB sheets than ARB in each similar cycle [20]. As shown in Figure 8, the simulative results are in a good agreement with the experimental results.

Figure 9 shows the different experimental samples formed by the SPIF process. The localized necking occurs in some processes, such as incremental forming in areas of metal that there is plane stress and also normal stress. In this study, the localized necking criteria were used. The presence of normal stress in the incremental forming process leads to the improvement of the formability of the material and, as a result, the surface of the forming limit curve is higher.

The presence of normal stress reduces the forming loads in the positions of geometric heterogeneity from which failure begins. Figure 10 shows the onset of a localized necking before complete failure.

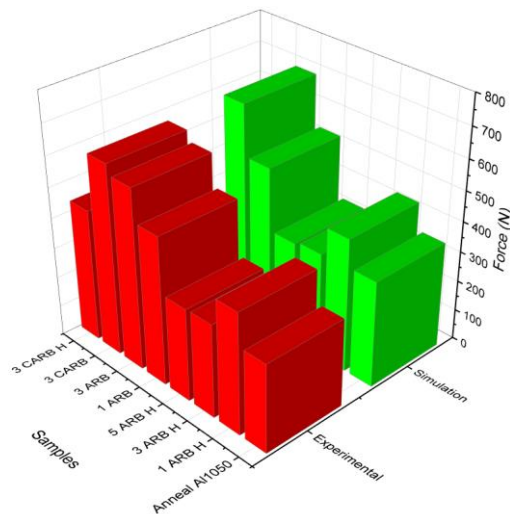


Figure 8. Experimental and numerical comparison of the forming forces in samples



Figure 9. Samples produced by experimental SPIF processes

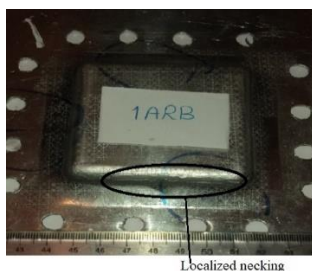


Figure 10. Onset of localized necking

The thickness of the samples produced from the longitudinal section was measured by an ultrasonic thickness gauge. Figure 11 shows the path for measuring the thickness distribution. Thickness measurements in experimental samples and simulation after sheet fracture were performed at maximum forming depth. By applying the mechanical properties of the samples and performing

simulations in ABAQUS finite element software, the results obtained were compared with the experimental results.

The simulation results in the samples are in good agreement with the experimental results. Besides, the simulation results show relatively accurate changes in the location of the thinnest thickness.

In the thickness distribution discussion, the most significant difference between the simulation results and the experimental results was 9.4% (3ARB). Since by applying the ARB process on the Al 1050 sample, a considerable strain is applied to the sample in each pass; therefore, the samples become more brittle. As shown in Figure 12, in the 1ARB sample the thickness of the fracture area was 0.30 mm, which was 0.38 mm thick compared to the 3ARB sample.

Performing heat-treatment on the samples and a significant reduction in sheet thickness at the point of the fracture indicates an improvement in the formability properties of the samples affected by heat-treatment. As shown in Figure 13, the fracture thickness of the 1ARBH sample was 0.38 mm, which was 0.08 mm different from the non-heat treated one. This difference indicates that by applying heat treatment, the percentage of thinning of the sheet increases and also improves the

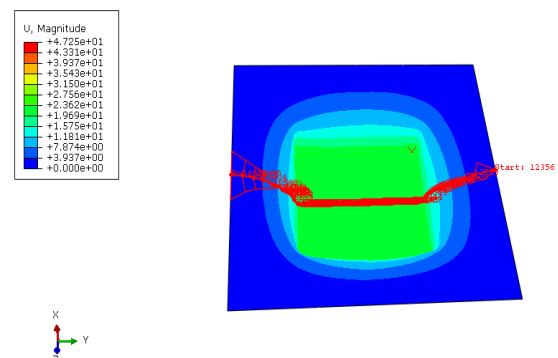


Figure 11. The path of measured thickness in the FE model

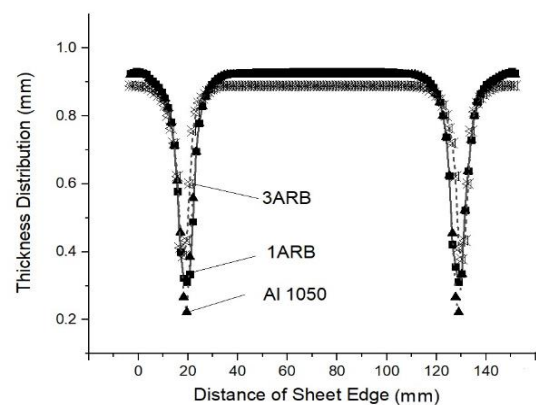


Figure 12. Thickness distribution curve in the ARB samples

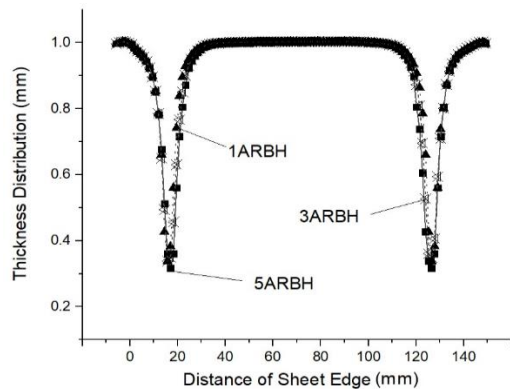


Figure 13. Thickness distribution curves in the heat-treated ARB samples

formability of the samples. Comparing the diagrams shows increasing the number of ARB passes increases the thickness of the sheet at the fracture point.

Figure 14 shows the thickness distribution profile of the sample produced in the CARB process using an ultrasonic thickness gauge. The minimum thickness of the 3CARB sheet was 0.35 mm, which is 0.03 mm different from the 3ARB sheet. The results of the thickness distribution profile show that the amount of thinning was more significant than the ARB samples.

The profile of the wire cut machining sample was determined using a projector profile machines with an accuracy of 0.001 mm. Figure 15 shows the cross-section depth profiles of the samples formed by the SPIF method. At the beginning of the profiles of the samples were curved due to the flow of the sheet, and then due to the Spring back phenomenon, they have an angle of fewer than 80 degrees. The formability of the 3CARBH sample (3 passes CARB with heat-treatment) was higher than other samples. Many grain boundaries acted as a barrier

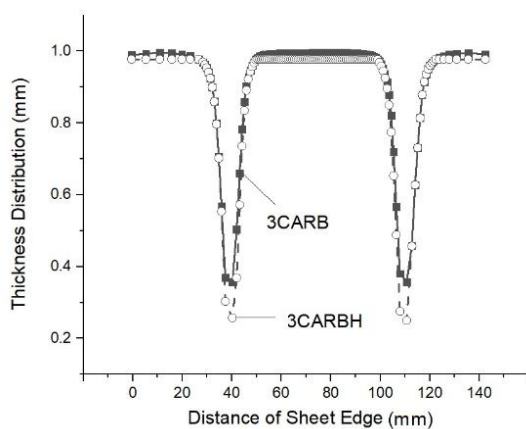


Figure 14. Thickness distribution curves in the heat-treated CARBed sample

to the growth of the main crack and provided better CARB formability. Also, the formability of the 3ARBH sample was higher than the Al 1050 sample. The 3ARB sample also has the lowest formability due to the brittleness of the sheet in the ARB process. It should be noted that the floor thickness of the formed profiles is constant.

To find the height of the breaking point, there are two methods: 1. Position display on the CNC screen, 2. Recording by Dynamometer. After the sheet fractures, the dynamometer was disconnected, and the fracture time was recorded. Using this time, the breaking point height can be obtained in Power mill software. Figure 16 shows the maximum forming depth of the samples at the SPIF process. As can be seen, the formability of the 3CARBH sample is 29 mm, which is significantly different from other samples (Maximum forming depth is 29 mm). Also, the formability of CARB samples is higher than that of ARB samples. The formability of CARB samples is more exorbitant than that of ARB samples. Therefore, a great deal of grain boundaries acts as a barrier to the main crack growth and causes better CARB formability, so that the CARB samples' formability is higher than Al1050 [27].

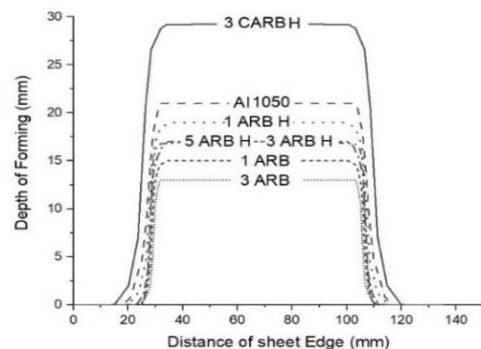


Figure 15. Depth profiles of formed samples by the SPIF process

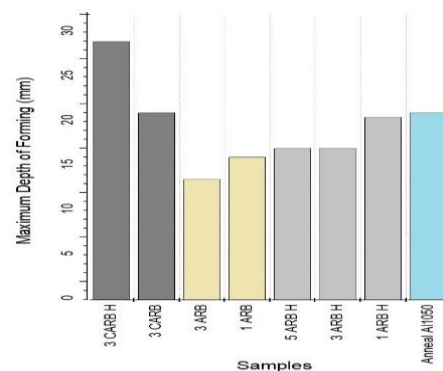


Figure 16. Diagram of the Maximum SPIF depth of the samples

5. CONCLUSIONS

In this paper, the SPIF of Al1050 sheets, processed by both the ARB and CARB, is studied. The results of this study are as follows:

- In the ARB process, the severe strain is applied to the sample: it causes the grains to become finer, and the sample to become more brittle. Therefore, the ARB samples' formability is less than that of Al1050 sheets.
- The samples' formability is improved by the heat-treating of ARB and CARB samples.
- Each pass in the ARB process increases the sheet's tensile strength, because of which the forming force of these sheets in the SPIF process is also intensified.
- The tensile strength of CARB sheets is higher than ARB sheets in any similar pass, so the SPIF force of CARB sheets is more eminent.
- The formability of CARB samples is more exorbitant than that of ARB samples. Therefore, a great deal of grain boundaries acts as a barrier to the main crack growth and causes a better CARB formability, so that the CARB samples' formability is higher than Al1050.
- For further investigation, the DOE technique could be adopted to decrease the sample size, estimate the effect of each parameter and get the better results.

6. REFERENCES

1. Trzepieciniski, T., Najm, S.M., Oleksik, V., Vasilce, D., Paniti, I., and Szpunar, M., "Recent developments and future challenges in incremental sheet forming of aluminium and aluminium alloy sheets", *Metals*, Vol. 12, No. 1, (2022), 124, <https://doi.org/10.3390/met12010124>.
2. Bagherzadeh, S., Abrinia, K. and Han, Q., "Analysis of plastic deformation behavior of ultrafine-grained aluminum processed by the newly developed ultrasonic vibration enhanced ECAP: simulation and experiments", *Journal of Manufacturing Processes*, Vol. 50, (2020), 485-497, <https://doi.org/10.1016/j.jmapro.2020.01.010>.
3. Maraki, M.R., Tagimalek, H. and Pasoodeh, B., "Provide a modeling algorithm for mechanical properties of friction stir welding of 5 series aluminum and pure-copper based on Fuzzy logic," *Iranian (Iranica) Journal of Energy and Environment*, Vol. 13, No. 2, (2022), 169-175, Doi:10.5829/ijee.2022.13. 02.08
4. Lei, W. and Zhang, H., "Analysis of microstructural evolution and compressive properties for pure Mg after room-temperature ECAP," *Materials Letters*, Vol. 271, (2020), 127781, <https://doi.org/10.1016/j.matlet.2020.127781>.
5. Tamimi, S., Gracio, J. J., Lopes, A. B., Ahzi, S. and Barlat, F., "Asymmetric rolling of interstitial free steel sheets: Microstructural evolution and mechanical properties," *Journal of Manufacturing Processes*, Vol. 31, (2018), 583-592, <https://doi.org/10.1016/j.jmapro.2017.12.014>.
6. Kyaw, P.M., Osawa, N., Gadallah, R. and Tanaka, S., "Accurate and efficient method for analyzing mixed-mode SIFs for inclined surface cracks in semi-infinite bodies by using numerical influence function method", *Theoretical and Applied Fracture Mechanics*, Vol. 106, (2020), 102471, <https://doi.org/10.1016/j.tafmec.2019.102471>.
7. Tagimalek, H., Maraki, M.R., and Mahmoodi, M., "A new approach of the constrained groove pressing process on Al5083-O alloy using PMMA polymer, without die non-friction coefficient: nanostructure, mechanical Properties and hardness", *Journal of Engineering Research*, (2021), <https://doi.org/10.36909/jer.12957>.
8. Liavoli, R.P., Gorji, H., Bakhshi-Jooybari, M. and Mirnia, M.J., "Investigation on Formability of Tailor-Welded Blanks in Incremental Forming", *International Journal of Engineering, Transactions B: Applications* Vol. 33, No. 5, (2020), 906-915, doi:10.5829/ije.2020.33. 05b.23.
9. Martínez-Donaire, A.J., Borrego, M., Morales-Palma, D., Centeno, G. and Vallengano, C., "Analysis of the influence of stress triaxiality on formability of hole-flanging by single-stage SPIF", *International Journal of Mechanical Sciences*, Vol. 151, (2019), 76-84, <https://doi.org/10.1016/j.ijmecsci.2018. 11.006>.
10. Wang, Z., Cai, A. and Chen, J., "Experimental investigations on friction stir assisted single point incremental forming of low-formability aluminum alloy sheet for higher formability with reasonable surface quality", *Journal of Materials Processing Technology*, Vol. 277, (2020), 116488, <https://doi.org/10.1016/j.jmatprotec.2019.116488>.
11. Najm, S.M., Paniti, I., Trzepieciniski, T., Nama, S.A., Viharos, Z.J. and Jacso, A., "Parametric effects of single point incremental forming on hardness of AA1100 aluminium alloy sheets", *Materials*, Vol. 14, No. 23, (2021), 7263, <https://doi.org/10.3390/ma14237263>.
12. Najm, S.M. and Paniti, I., "Artificial neural network for modeling and investigating the effects of forming tool characteristics on the accuracy and formability of thin aluminum alloy blanks when using SPIF", *The International Journal of Advanced Manufacturing Technology*, Vol. 114, (2021), 2591-2615, <https://doi.org/10.1007/s00170-021-06712-4>.
13. Paniti, I., Viharos, Z.J., Harangozo, D. and Najm, S.M., "Experimental and numerical investigation of the single point incremental forming of aluminium alloy foils", *Acta Imeko*, Vol. 9, No. 1, (2020), 25-31, http://dx.doi.org/10.21014/acta_imeko.v9i1.750.
14. Suresh, K., Khan, A. and Regalla, S.P., "Tool path definition for numerical simulation of single point incremental forming", *Procedia Engineering*, Vol. 64, (2013), 536-545, <https://doi.org/10.1016/j.proeng.2013.09.128>.
15. Jackson, K., Allwood, J. and Landert, M., "Incremental forming of sandwich panels", *Journal of Materials Processing Technology*, Vol. 204, No. 1, (2008), 290-303, <https://doi.org/10.1016/j.jmatprotec.2007.11.117>.
16. Nikdooz, A. H., Mirnia, M. J. and Baseri, H., "Study of formability of aluminum truncated pyramid in single-stages and two-stage incremental sheet forming," *Modares Mechanical Engineering*, Vol. 16, No. 5, (2016), 210-220, <http://mme.modares.ac.ir/article-15-9274-en.html>.
17. Lu, B., Fang, Y., Xu, D., Chen, J., Ou, H., Moser, N. and Cao, J., "Mechanism investigation of friction- related effects in single point incremental forming using a developed oblique roller-ball tool," *International Journal of Machine Tools and Manufacture*, Vol. 85, (2014), 14-29, <https://doi.org/10.1016/j.ijmachtools.2014.04.007>.
18. Najm, S. M. and Paniti, I., "Study on effecting parameters of flat and hemispherical end tools in SPIF of aluminium foils", *Technical Gazette*, Vol. 27, No. 6, (2020), 1844-1849, <https://doi.org/10.17559/TV-20190513181910>.
19. Neto, D.M., Martins, J.M.P., Oliveria, M.C., Meneses, L.F. and Alves, J. L., "Evaluation of strain and stress states in the single

- point incremental forming process”, *The International Journal of Advanced Manufacturing Technology*, Vol. 85, (2016), 521-534, <https://doi.org/10.1007/s00170-015-7954-9>.
20. Hino, R., Kawabata, K. and Yoshida, F., “Incremental forming with local heating by laser irradiation for magnesium alloy sheet,” *Procedia Engineering*, Vol. 81, (2014), 2330-2335, <https://doi.org/10.1016/j.proeng.2014.10.329>.
 21. Mansouri, M., Eghbali, B. and Afrand, M., “Producing multi-layer composite of stainless steel/aluminum/copper by Accumulative roll-bonding (ARB) process,” *Journal of Manufacturing Processes*, Vol. 46, (2019), 298-303, <https://doi.org/10.1016/j.jmapro.2019.08.025>.
 22. Rahmatabadi, D., Shahmirzaloo, A., Farahani, M., Tayyebi, M. and Hashemi, R., “Characterizing the elastic and plastic properties of the multilayered Al/Brass composite produced by ARB using DIC,” *Materials Science and Engineering: A*, Vol. 753, (2019), 70-78, <https://doi.org/10.1016/j.msea.2019.03.002>.
 23. Rahmatabadi, D., Hashemi, R., Mohammadi, M. and Shojaee, T., “Experimental evaluation of the plane stress fracture toughness for ultra-fine grained aluminum samples prepared by Accumulative roll-bonding process,” *Materials Science and Engineering: A*, Vol. 708, (2017), 301-310, <https://doi.org/10.1016/j.msea.2017.09.085>.
 24. Dargusch, M.S., Pettersen, K., Nogita, K., NAVE, M.D. and DUNLOP, G.L., “ASTM E8-04 Standard Test Methods for Tension Testing of Metallic Materials ASTM International ASTM E8-04 Standard Test Methods for Tension Testing of Metallic Materials ASTM International, 2004.” *Materials Transactions*, Vol. 47, No. 4, (2006), 977-982.
 25. Jadhav, S., “Basic Investigations of the Incremental Sheet Metal Forming Process on a CNC Milling Machine”, Doctorate Thesis, University of Dortmund, Germany, (2004).
 26. Song, X., Zhang, J., Zhai, W., Taureza, M., Castagne, S., Danno, A., “Numerical and Experimental Study of Micro Single Point Incremental Forming Process”, *Procedia Engineering*, Vol. 207, (2017), 825-830, <https://doi.org/10.1016/j.proeng.2017.10.836>.
 27. Roghani, H., Borhani, E., Shams, S.A.A., Lee, C.S. and Jafarian, H.R., “Effect of concurrent accumulative roll bonding (ARB) process and various heat treatment on the microstructure, texture and mechanical properties of AA1050 sheets,” *Journal of Materials Research and Technology*, Vol. 18, (2022), 1295-1306, <https://doi.org/10.1016/j.jmrt.2022.03.001>.

Persian Abstract

به عنوان یکی از روش‌های تغییر شکل شدید پلاستیک، فرآیند نورد تجمعی منجر به تولید ورق‌های فلزی با مقاومت بالا و سازه‌های ریزدانه می‌شود. در این پژوهش، شکل‌دهی افزایشی نقطه‌ای ورق، ورق‌های آلومینیوم ۱۰۵۰ فرآوری شده توسط نورد تجمعی و نورد تجمعی متقاطع به صورت تجربی و عددی بررسی شد. نیروی شکل‌دهی، توزیع ضخامت و عمق شکل‌دهی در هر دو حالت نورد تجمعی و نورد تجمعی متقاطع همگی در این پژوهش تعیین گردید. نتایج نشان می‌دهد که شکل‌پذیری نمونه‌های نورد تجمعی متقاطع بیشتر از نمونه‌های نورد تجمعی است. علاوه بر این، شکل‌پذیری هر دو نمونه آنبیل شده نورد تجمعی و آلومینیوم ۱۰۵۰ در پاس اولیه برابر است. علاوه بر این، کرنش نمونه‌ها با افزایش تعداد عبور نورد افزایش می‌یابد و در نتیجه شکل‌پذیری کاهش می‌یابد. نتایج به دست آمده با استفاده از دینامومتر نشان می‌دهد که میزان نیروی شکل‌دهی عمودی در نمونه‌های نورد تجمعی متقاطع بیشتر از بقیه نمونه‌ها است.



Aspects of Foundation-soil Interaction of Nuclear Structures under Seismic Conditions through the State-of-art Review

B. Thakur*, A. Desai

Department of Civil Engineering, Sardar Vallabhbhai National Institute of Technology, Surat, India

PAPER INFO

Paper history:

Received 21 March 2022

Received in revised form 14 April 2022

Accepted 24 April 2022

Keywords:

Combined Pile Raft Foundation

Failure

Fragility

Nuclear Power Plant

Seismic Resistance

Soil Structure Interaction

ABSTRACT

This state-of-the-art review study emphasized the problem of failure of Nuclear Power Plants (NPP) due to earthquake forces. Soil-NPP interaction may lead to damage to these unique structures of the critical infrastructural system of any nation in demand to fulfill the energy requirement. So, the soil-structure interaction (SSI) is the key motivating factor to review the fundamentals of NPP with its base soil conditions. Moreover, the problems associated with NPP-SSI have been overcome with the application of an advanced foundation system called combined pile raft foundation (CPRF). This study checks the scope of the provision of CPRF to NPP through SSI. The approaches for analyzing the seismic behavior of NPP in CPRF are strategically reviewed in this study. According to the literature findings, SSI is the most significant factor in deciding the seismic resistance of NPP. The fragility analysis demonstrated the importance of SSI in the design of NPP earthquake behavior. CPRF plays an important role in NPP-SSI to minimize structural damage.

doi: 10.5829/ije.2022.35.09c.06

1. INTRODUCTION

The dam sector, chemical sector, nuclear reactors, materials, waste sector etc., are the parts of any countries critical infrastructures (CISs). They are the spine of the development of a nation, and nuclear power industry is one of them. Worldwide, the strenuous growth in the development of the power plants has been observed [1, 2]. Nevertheless, due to the inseparable logic of natural calamities or by chance, these systems are highly susceptible to risky conditions [3-5]. Earthquake is one of the calamities affecting all type of structure, and NPP is no exception. While designing the reactor building (a component of NPP), tremor and break loss of coolant accidents are considered external and internal events [6-8]. Earthquakes of magnitude higher than that of design criteria often occur in the nearby vicinity of NPPs. Jin and Gong [9] studied the Fukushima Daiichi NPP incident (11th March 2011) in great east Japan was one of the example. Due to this Earthquake, Fukushima NPP bore severe destruction [7]. As a result of this situation, significant efforts were being made in many sectors such

as geophysics, structural engineering, and nuclear safety engineering to recognize and assess the danger. Various active and passive approaches have been invented to reduce the seismic impact on the structure. The conventional methods suggest strengthening the structural elements to improve the seismic resistance of the structure. The practical solution is to protect the NPPs by considering the fragility analysis with and without soil structure interaction and combined pile raft foundation (CPRF) of the structure [7, 10]. Fragility analysis as well as SSI should be taken under consideration as it is the governing criteria for the seismic behaviour of the structure. The following sections consist of a preface of past literature and methodology enlightening the fragility analysis, and importance of SSI and CPRF on the response of NPP in earthquake situation.

2. LITERATURE PREFACE

CPRF, a raft supported by piles, is used to achieve desired loading strength. It helps to meet the ability

*Corresponding Author Institutional Email:
bhairavthakur869@gmail.com (B. Thakur)

requirements in an effective pattern than the conventional pile group foundation [11]. The reaction of the isolated piles differs from the piles in the group because of the pile-to-pile interaction factor. The pile-to-pile interaction factor is defined as the ratio of an unloaded receiver pile's displacement or rotations to those of a nearby loaded source pile owing to soil deformation [12]. From the last two decades, CPRF has been proven as a feasible and sustainable foundation as it decreases the settlement of structure, leading to massive financial savings without compromising the capacity of the foundation. Its primary application was for massive facilities. Design and construction guidelines for a vertically loaded piled raft in a range of subsoil conditions have also been established by the International Society for Soil Mechanical and Geotechnical Engineering (ISSMGE) [13]. Although the substructure of the building may face loading from all the sides simultaneously [14], the design of CPRF does not conventionally consider the combination of horizontal (H) and vertical (V) forces and moment (M). Attention is required while designing the CPRF for the load transfer process between the piles and the rafts. As the multi-directional interaction affects the structural response, the soil-structure interaction (SSI) and soil non-linearity must be considered for the design of the facility [15, 16]. The SSI is the interactivity between soil (ground) and a facility erected on it.

The analysis process of the SSI approach is to be done in a deterministic manner. Inertial, kinematic, free-field, and control motion are all stages in the SSI method [17]. The direct and substructure approaches are two general methods of analysis for SSI. The direct method involves assessing the combined soil-structure interaction in one step without superposition [18, 19]. The direct technique solves the SSI problem in both the time and frequency domains. The linear or nonlinear time-history analysis can be used to apply the direct approach. Analysis of SSI by the direct method shall consist of (1) model of structure, (2) model of foundation: geometry, stiffness, and interface, (3) model the soil: a) soil material properties (linear and nonlinear) and b) discretize the soil and locate the bottom and lateral boundaries of the soil structure model, (4) establish input motion to be applied at the boundaries, (5) perform SSI analysis, and (6) perform a second stage analysis for detailed structural response [20]. The substructuring method directly invokes superposition to solve the SSI problem in the frequency domain. Fourier transform techniques applied to the input motion are used to treat time variations in earthquake ground motion. Only linear analysis can be used to implement the substructuring method [20].

SSI is the mechanism through which the soil reaction controls the structure's motion alongside the structure influences the response of the soil. The structural model's fundamental period is determined by building height and the SSI. Raheem et al. [21] conducted a theoretical study on multi-storied frames with varying soil characteristics

beneath the foundation and several stories to demonstrate the impact of SSI on the frames' dynamic properties. The findings were compared to the fixed-base structures. The SSI effect will enhance as the structural stiffness and the soil flexibility increase [21]. The stiffness properties using formulae derived by Gazetas [22] and AERB [23] are described in Table 1. Where ρ , G , ν represent the density of soil, shear modulus and Poisson's ratio, respectively;

L , B , and R denotes the half-length, half-width and R is A_b is the radius of a circular basement, respectively; Area of the base, I_{bx} , I_{by} and I_{bz} are the moment of inertia about x, y and z-direction, respectively.

The CPRF effectively governs the settlements and significantly escalates the strength of the whole structure [16]. In analyzing the CPRF behaviour pattern, a fragility analysis is important. Fragility analysis describes the risk of a specific structure being exposed to a seismic excitation above a damage limit state. Zentner et al. [24] used two types of methods for the fragility analysis of the nuclear industry; the numerical simulation method and the safety factor method. John and Robert [25] developed the safety factor method to develop the element of fragility functions. The ground motion measurements of the design-basis earthquake, several safety factors, and each element's ups and downs have been combined in this safety method. It was utilized to calculate the component's standard deviation and median capacity, which were then included in the fragility functions. At the same time, the numerical simulation method includes regression modelling [26], highest probability estimation [27, 28], and incremental dynamic analysis (IDA) [29], which were also applied to the NPPs case studies [9, 30]. Methodologies for fragility analysis available for CPRF are given in the methodology section.

TABLE 1. Rigid plate stiffness on a semi-infinite homogeneous elastic half-space [18]

Direction	Static stiffness [22]	Spring constant for circular base [24]
Vertical (z)	$K_z = \frac{2GL}{1-\nu} (0.73 + 1.54) \left(\frac{A_b}{4L^2} \right)^{0.75}$	$K_z = \frac{4GR}{1-\nu}$
Horizontal (y) lateral	$K_y = \frac{2GL}{1-\nu} (2.00 + 2.50) \left(\frac{A_b}{4L^2} \right)^{0.85}$	-
Horizontal (x) longitudinal	$K_x = K_y \frac{2GL}{0.75-\nu} \left(1 - \frac{B}{L} \right)$	$K_x = \frac{32(1-\nu)4GR}{7-8\nu}$
Rocking (r_x) about the x-axis	$K_{rx} = \frac{GI_{bx}^{0.75}}{1-\nu} \left(\frac{L}{B} \right)^{0.25} \left(2.4 + 0.5 \frac{B}{L} \right)$	$K_{rx} = \frac{8GR^3}{3(1-\nu)}$
Rocking (r_y) about the y-axis	$K_{ry} = \frac{3GI_{by}^{0.75}}{1-\nu} \left(\frac{L}{B} \right)^{0.15}$	$K_{ry} = \frac{8GR^3}{3(1-\nu)}$
Torsion	$K_t = 3.5GI_{bx}^{0.75} \left(\frac{B}{L} \right)^{0.4} \left(\frac{I_{bz}}{B^4} \right)^{0.2}$	$K_t = \frac{16GR^3}{3}$

Because of the haphazardness and uncertainty of earthquakes, several studies have focused on the seismic response and fragility evaluation of solitary buildings in recent decades. Burland [31] firstly introduced the concept of CPRF with unserviceability. Various numerical [32-35] and analytical research [14, 36, 37] have been performed to have deep insights into the nature of CPRF. The authors presented different ways to address the impacts of non-homogeneity of CPRF on horizontal and vertical response of structure. Choudhury and Kumar [38] have examined CPRF under V-M-H condition in sandy soil using 3D finite element (FE) analysis and evidence the results of improved performance of the structure with the CPRF over the traditional group pile foundation during earthquake loading.

The horizontal load and moment capacities of a piled-raft are determined by a number of factors, including pile-soil relative stiffness, raft-soil relative stiffness, pile spacing to diameter ratio, and foundation and pile head connection with the raft length to width ratio [42]. V-M-H interaction is also considered while developing failure and design envelopes [39]. A hysteresis-based model was utilized to investigate the bi-directional correspondence and the interaction between the soil, pile raft, and structure. The hysteresis model can accurately simulate the deformation in two primary directions. One of the analysis methods, the Square Root Sum Square (SRSS) method, was used for elastic analysis; however, it could not identify the inelastic interaction between both directions. The biaxial model achieves higher accuracy without many complex calculations and has been used for both steel and concrete structures.

Conventionally, one-directional approaches [40] are adopted in analysis that considers the hypothesis of a fixed base; SSI is neglected since it requires complex computing efforts. But studies show that the reflectance of SSI can damage the whole structure. In the seismic SSI of NPP, Abell et al. [41] evaluated the differences in response to 3-D, 3×1-D, and 1-D excitations. Furthermore, as multiple experts have indicated, the interaction between the soil, the pile foundation, and the structure is crucial factor in determining the seismic response of pile-supported buildings in a variety of soil types [40]. Different design standards like NEHRP [42] and ASCE 4-16 [20] have taken into account the relevance of SSI. The detailed methodology for the same has been elaborated in the following section.

2. 1. Methodology Some of the methods that have been experimented with in the past decade are discussed here. Kumar and Chaudhary [43] divided the CPRF system's settlement into two components: settlement caused by load-carrying by the raft and load-carrying by the piles. For stiffness, Fleming [44] solely evaluated the interaction between pile and raft and computed settlement appropriately. Clancy and Randolph [45] studied the small piled raft system, which has a raft width

of 5 to 15 meters and is smaller than the length of the pile, while the large piled raft system has a raft width that is greater than the length of the pile.

The design model of the pile-raft system represents the piles and soil as equivalent constant spring [46, 47]. The ratio of induced load in a pile to the corresponding settlement near the raft pile junction was used to quantify the pile stiffness. Integrating the vertical stress in the top elements of the piles over a pile area yielded the induced load in a pile. The rigidity of the central pile corresponds to the pile in the rafts center. The edge pile stiffness refers to a pile close to the rafts edge. Different interactions regulate the behaviour of the piled raft, including pile-to-pile, pile-to-soil, raft-to-pile, and raft-to-soil interactions [48, 49]. The pile-to-pile contact caused by an adjacent-loaded pile causes more settling in a pile.

Poulos [50] provided a technique for determining the settling of a pile in a pile group by superimposing the additional settlement caused by each pile using the pile-to-pile interaction factor. The interaction factor is influenced by several variables. According to the work of two earlier researchers, Poulos [50] and Lee [51], these parameters are pile spacing, pile stiffness relative to the soil, and pile length to diameter ratio. The pile-to-pile interaction factor depends upon the distance between the two piles. Compared to the edge pile, the central pile is surrounded by piles all around it; hence the interaction impact will be greater for the central piles. As a result, the middle pile has been less stiff than the edge piles.

2. 2. Analysis of CPRF Loading Condition

Pseudo-static load is an equivalent static horizontal load on the foundation unit replaced by the seismically induced load. To get the pseudo-static load, Attar [52] multiplied the seismic coefficient by a vertical load. Mali and Singh [53] considered the initial stage and loading stage for the finite element. Patil et al. [16] approached the analysis of safety related to the NPP structures resting on CPRF, simulating soil-pile interactions using the substructure method under static and dynamic loading conditions. Liu et al. [54] considered dynamic loading with four different types. Initially, the load carried by the piles at a particular displacement level was considered as the weight experienced by the piles at their top node, which was assumed to have transmitted from the raft. This is an example of the raft-soil interface; the raft load was estimated by summing the stresses encountered at all nodes lying on the Pasternak medium, as shown in Figure 1.

2. 3. Pile Dimensions

The length, diameter and spacing of piles play an important role in the behaviour of CPRF. Kumar et al. [55] considered the spacing to diameter ratios of 2, 4 and 6. Kumar and Choudhury [43] computed the dimension of the pile as 0.5 m diameter and 15m length with the help of numerical methodology. Bhaduri and Chaudhury [15] also considered the length

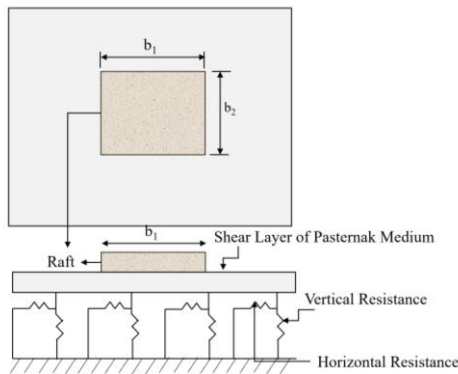


Figure 1. Raft on elastic medium with resistance at the bottom of the plate [15]

to diameter ratios to overcome vertical settlements of the pile. Mali and Singh [53] described the significant effect of the spacing up to 6m.

Unsever [34] and Bhaduri [15] reported how the pile raft elements share structure loading. From both the studies, it was noticed that the highest lateral shear would be borne by the raft initially, but as time permits, piles will resist the higher load. A systematic methodology must be adopted to analyze or simulate the seismic behaviour of the structure. Figure 2. shows the detailed methodology for the static analysis of CPRF.

3. DISCUSSIONS

The combined pile-raft foundation system has been identified as one of the most cost-effective and long-term

foundations system for high-rise buildings, resulting in reduced settlements and provision of smaller piles than the pile group. The combined pile-raft foundation (CPRF) design concept may reduce the number, diameter of piles, and length used in a foundation structure. CPRFs are effective in lowering both average and differential settlement levels. The CPRF can be used for various types of soil. It should be designed according to the soil properties on which the construction is to be done. For that, soil-structure interaction is an important consideration. The SSI impact on the structure increased the fundamental period of vibration by 10.4% while reducing the base shear by 21.7 and 24% in longitudinal and lateral direction [56]. The hard rock foundation can neglect the influence of soil-structure interaction. However, for other soil types, it must not be neglected. For the purpose of determining the number of piles to be installed under the raft, the effect of the soil-pile-raft interaction factor is the most important aspect to be considered. When failure and design envelopes are established for each of the principal three (V-H-M) directions, it has been seen that piled-raft lateral capacity grows more as a result of combined loading than as a result of independent loading when combined and independent loading was considered.

The raft is critical in the distribution of the load, accounting for 23–31% of the total vertical load [58]. It shows the importance of the combined foundation compared to the traditional single raft of pile group foundation. The ISSMGE has developed design and construction guidelines for a vertically loaded pile raft for a variety of subsoil conditions. However, the traditional pile foundation design is still dominant in the engineering practice due to the guidelines and provisions

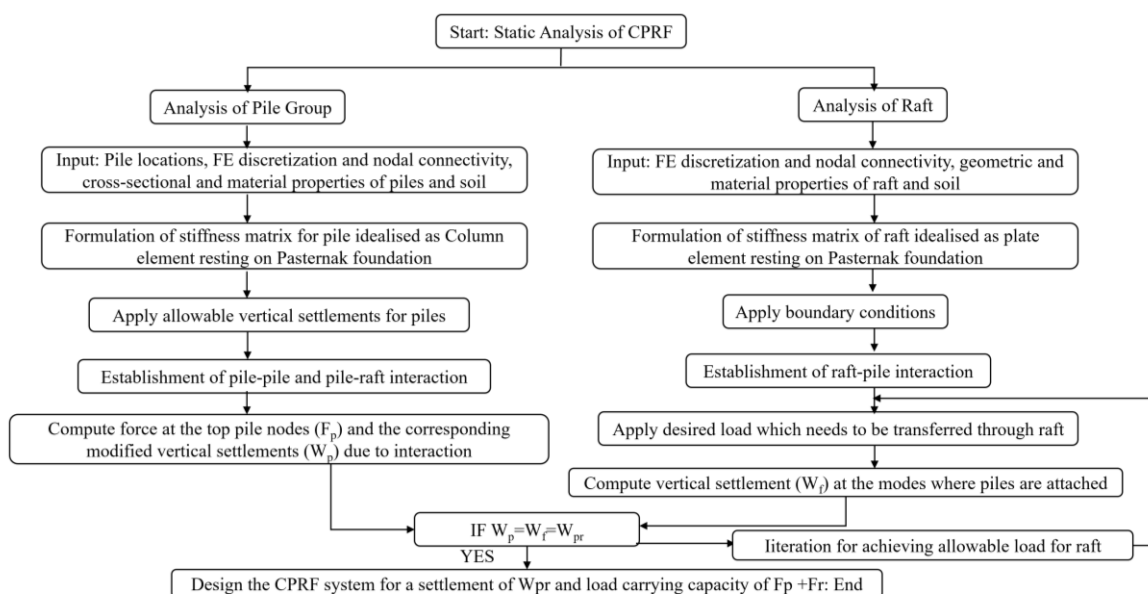


Figure 2. Methodology for static analysis of CPRF [15]

suggested by design codes. The reason may be due to the lack of confidence among the designers for incorporating load sharing advantage between rafts and piles to avoid conservatism through capacity-based design.

4. CONCLUSION

Nuclear energy is the only source to generate a tremendous amount of power with zero carbon footprints. NPP's do not emit the toxic gases that would be definitely generated if fossil fuels were used for power generation. It shows the importance of NPPs for any country. Nuclear reactors have the potential to release radioactive materials into the atmosphere and water that may be harmful to human health. Because of that, while designing and constructing, utmost care should be taken. Such structures are constructed considering the effects of an earthquake. This state-of-the-art review study emphasized the soil-structure interaction of nuclear power plant under the earthquake forces. The review study stated the following conclusions:

- The soil-structure interaction with its base soil conditions is the key factor to be included in the seismic design of NPP.
- The feasibility of an innovative foundation system called combined pile raft foundation (CPRF), which overcomes problems associated with NPP-SSI, is also checked.
- The approaches for analysis of the seismic behavior of NPP in CPRF are strategically reviewed in this study.
- According to the literature findings, compared to the findings obtained by fixed-base structure analysis, the inclusion of soil in the structural analysis yields results, stresses, and deformations that are closest to the real behavior of the structure.
- The fragility analysis demonstrated the importance of SSI in the design of NPP earthquake behavior. CPRF plays an important role in NPP-SSI to minimize structural damage.

5. ACKNOWLEDGEMENTS

The authors would like to acknowledge Department of Civil Engineering, Sardar Vallabhbhai National Institute of Technology, Surat, India for all kinds of support provided to facilitate this research.

6. REFERENCES

1. Norouzi, A., Gerami, M., Vahdani, R. and Sivandi-Pour, A., "Effects of multiple structure-soil-structure interactions considering the earthquake waveform and structures elevation

- effects", *International Journal of Engineering, Transaction B: Application*, Vol. 33, No. 5, (2020), 744-752, doi: 10.5829/ije.2020.33.05b.05.
2. Zhou, Y., Sui, Y., Liu, X. and Gong, T., "Seismic analysis for nuclear power safety related bridge", *KSCE Journal of Civil Engineering*, Vol. 25, No. 2, (2021), 631-645, doi: 10.1007/s12205-20-0718-6.
3. Farhadi, N., Saffari, H. and Torkzadeh, P., "Evaluation of seismic behavior of steel moment resisting frames considering nonlinear soil-structure interaction", *International Journal of Engineering, Transaction A: Basics*, Vol. 31, No. 7, (2018), 1020-1027, doi: 10.5829/ije.2018.32.07a.03.
4. Choi, E., Ha, J.-G., Hahm, D. and Kim, M.K., "A review of multihazard risk assessment: Progress, potential, and challenges in the application to nuclear power plants", *International Journal of Disaster Risk Reduction*, Vol. 53, (2021), 101933, doi: 10.1016/j.IJDRR.2020.101933.
5. Vali, R., "Water table effects on the behaviors of the reinforced marine soil-footing system", *Journal of Human, Earth, and Future*, Vol. 2, No. 3, (2021), 296-305, doi: 10.28991/HEF-2021-02-03-09.
6. Alhanee, S., Yi, Y. and Schiffer, A., "Ultimate pressure capacity of nuclear reactor containment buildings under unaged and aged conditions", *Nuclear Engineering and Design*, Vol. 335, (2018), 128-139, doi: 10.1016/j.nucengdes.2018.05.017.
7. Behnamfar, F. and Fathollahi, A., "Soft soil seismic design spectra including soil-structure interaction", *International Journal of Engineering, Transaction A: Basics*, Vol. 30, No. 10, (2017), 1443-1450, doi: 10.5829/idosi.ije.2017.30.09c.04.
8. Bangia, T. and Raskar, R., "Cohesive methodology in construction of enclosure for 3.6 m devasthal optical telescope", *HighTech and Innovation Journal*, Vol. 3, No. 2, (2022), 162-174, doi: 10.28991/HIJ-2022-03-02-05.
9. Jin, S. and Gong, J., "A simplified method for probabilistic seismic risk evaluation of nuclear containment structure", *International Journal of Pressure Vessels and Piping*, Vol. 189, (2021), 104283, doi: 10.1016/j.ijvp.2020.104283.
10. Hou, G., Liu, Y., Li, M., Sun, M., Sun, F., Zhu, X., Pan, R. and Zhang, D., "Seismic structural responses reduction of double-layered containment nuclear power plant via bis-tmd", *Engineering Computations*, (2020), doi: 10.1108/EC-09-2019-0420.
11. Poulos, H., "Analysis of the settlement of pile groups", *Geotechnique*, Vol. 18, No. 4, (1968), 449-471, doi: 10.1680/geot.1968.18.4.449.
12. Abbas, H.O., Ali, A.H. and Abid Awn, S.H., "Behavior of raft foundation built on layered soil under different earthquake excitation", *International Journal of Engineering, Transaction B: Application*, Vol. 35, No. 8, (2022), doi: 10.5829/ije.2022.35.08b.07.
13. Dutta, S.C., Saha, R. and Haldar, S., "Inelastic seismic behavior of soil-pile raft-structure system under bi-directional ground motion", *Soil Dynamics and Earthquake Engineering*, Vol. 67, (2014), 133-157, doi: 10.1016/j.soildyn.2014.08.012.
14. Bhaduri, A. and Choudhury, D., "Serviceability-based finite-element approach on analyzing combined pile-raft foundation", *International Journal of Geomechanics*, Vol. 20, No. 2, (2020), 04019178, doi: 10.1061/(asce)gm.1943-5622.0001580.
15. Patil, G., Choudhury, D. and Mondal, A., "Estimation of the response of piled raft using nonlinear soil and interface model", *International Journal of Geotechnical Engineering*, Vol. 16, No. 5, (2022), 540-557, doi: 10.1080/19386362.2020.1859250.
16. Çakır, Ö. and Coşkun, N., "Theoretical issues with rayleigh surface waves and geoelectrical method used for the inversion of near surface geophysical structure", *Journal of Human, Earth,*

- and Future*, Vol. 2, No. 3, (2021), 183-199, doi: 10.28991/HEF-2021-02-03-01.
17. Maheshwari, B. and Firoj, M., A state of art: Seismic soil–structure interaction for nuclear power plants, in Latest developments in geotechnical earthquake engineering and soil dynamics. 2021, Springer.393-409.
 18. Raheem, S.E.A., Soil–structure interaction for seismic analysis and design of bridges, in Innovative bridge design handbook. 2022, Elsevier.229-263.
 19. Anand, V. and Kumar, S.S., "Seismic soil-structure interaction: A state-of-the-art review", in Structures, Elsevier. Vol. 16, (2018), 317-326.
 20. Engineers, A.S.o.C., "Seismic analysis of safety-related nuclear structures and commentary, American Society of Civil Engineers. (2014).
 21. Abdel Raheem, S.E., Ahmed, M.M. and Alazrak, T., "Evaluation of soil–foundation–structure interaction effects on seismic response demands of multi-story mrf buildings on raft foundations", *International Journal of Advanced Structural Engineering (IJASE)*, Vol. 7, No. 1, (2015), 11-30, doi: 10.1007/s40091-014-0078-x
 22. Gazetas, G., "Formulas and charts for impedances of surface and embedded foundations", *Journal of geotechnical engineering*, Vol. 117, No. 9, (1991), 1363-1381.
 23. Guide, A.S., *Seismic qualification of structures, systems and components of pressurised heavy water reactors*. 2009, AERB/NPP-PHWR/SG/D-23.
 24. Zentner, I., Humbert, N., Ravet, S. and Viallet, E., "Numerical methods for seismic fragility analysis of structures and components in nuclear industry-application to a reactor coolant system", *Georisk*, Vol. 5, No. 2, (2011), 99-109, doi: 10.1080/17499511003630512.
 25. Reed, J.W. and Kennedy, R.P., "Methodology for developing seismic fragilities", Final Report TR-103959, EPRI, (1994).
 26. Zentner, I., Gündel, M. and Bonfils, N., "Fragility analysis methods: Review of existing approaches and application", *Nuclear Engineering and Design*, Vol. 323, (2017), 245-258, doi: 10.1016/j.nucengdes.2016.12.021.
 27. Dhadse, G.D., Ramtekkar, G. and Bhatt, G., "Effect of particle size, moisture content and density on the hyperbolic model parameters for non-cohesive soil", *International Journal of Engineering, Transaction C: Aspect*, Vol. 35, No. 9, (2022), doi: 10.5829/ije.2022.35.09c.04.
 28. Shinozuka, M., Feng, M.Q., Lee, J. and Naganuma, T., "Statistical analysis of fragility curves", *Journal of Engineering Mechanics*, Vol. 126, No. 12, (2000), 1224-1231, doi: 10.1061/(ASCE)0733-9399(2000)126:12(1224).
 29. Vamvatsikos, D. and Cornell, C.A., "Applied incremental dynamic analysis", *Earthquake Spectra*, Vol. 20, No. 2, (2004), 523-553, doi: 10.1193/1.1737737.
 30. Choun, Y.-S., Choi, I.-K. and Seo, J.-M., "Improvement of the seismic safety of existing nuclear power plants by an increase of the component seismic capacity: A case study", *Nuclear Engineering and Design*, Vol. 238, No. 6, (2008), 1410-1420, doi: 10.1016/j.nucengdes.2007.10.008.
 31. Burland, J.B., Broms, B.B. and De Mello, V.F., "Behaviour of foundations and structures", (1978).
 32. Small, J. and Zhang, H., "Behavior of piled raft foundations under lateral and vertical loading", *The International Journal of Geomechanics*, Vol. 2, No. 1, (2002), 29-45, doi: 10.1061/(asce)1532-3641(2002)2:1(29).
 33. Comodromos, E.M., Papadopolou, M.C. and Laloui, L., "Contribution to the design methodologies of piled raft foundations under combined loadings", *Canadian Geotechnical Journal*, Vol. 53, No. 4, (2016), 559-577, doi: 10.1139/cgj-2015-0251.
 34. Unsever, Y., Matsumoto, T. and Özkan, M.Y., "Numerical analyses of load tests on model foundations in dry sand", *Computers and Geotechnics*, Vol. 63, No., (2015), 255-266, doi: 10.1016/j.compgeo.2014.10.005.
 35. Kumar, A., Choudhury, D. and Katzenbach, R., "Behaviour of combined pile-raft foundation (cprf) under static and pseudo-static conditions using plaxis3d", 6th International Proceedings on Earthquake Geotechnical Engineering. New Zealand, Vol., No., (2015), doi.
 36. Mašin, D., Tamagnini, C., Viggiani, G. and Costanzo, D., "Directional response of a reconstituted fine-grained soil—part ii: Performance of different constitutive models", *International Journal for Numerical and Analytical Methods in Geomechanics*, Vol. 30, No. 13, (2006), 1303-1336, doi: 10.1002/nag.527.
 37. Roy, J., Kumar, A. and Choudhury, D., "Natural frequencies of piled raft foundation including superstructure effect", *Soil Dynamics and Earthquake Engineering*, Vol. 112, (2018), 69-75, doi: 10.1016/j.soildyn.2018.04.048.
 38. Choudhury, D. and Kumar, A., "Seismic response of combined pile-raft foundation-the state of the art review", *Design and Analysis of Piled Raft Foundations-2017*, Vol. 19, (2017), 47, doi.
 39. Chanda, D., Saha, R. and Haldar, S., "Behaviour of piled raft foundation in sand subjected to combined vmh loading", *Ocean Engineering*, Vol. 216, (2020), 107596, doi: 10.1016/j.oceaneng.2020.107596.
 40. Wolf, J.P., Soil-structure-interaction analysis in time domain, in Structural mechanics in reactor technology. 1987.
 41. Abell, J.A., Orbović, N., McCallen, D.B. and Jeremic, B., "Earthquake soil-structure interaction of nuclear power plants, differences in response to 3-d, 3× 1-d, and 1-d excitations", *Earthquake Engineering & Structural Dynamics*, Vol. 47, No. 6, (2018), 1478-1495, doi: 10.1002/eqe.3026.
 42. Program, N.E.H.R. and Council, B.S.S., "Nehrp recommended provisions (national earthquake hazards reduction program) for seismic regulations for new buildings and other structures, Building Seismic Safety Council, (2001).
 43. Kumar, A. and Choudhury, D., "Development of new prediction model for capacity of combined pile-raft foundations", *Computers and Geotechnics*, Vol. 97, (2018), 62-68, doi: 10.1016/j.compgeo.2017.12.008.
 44. Fleming, W., Weltman, A., Randolph, M. and Elson, W., *Piling engineering*, glasgow: Blackie. 1992, Halsted Press.
 45. Clancy, P. and Randolph, M., "An approximate analysis procedure for piled raft foundations", *International Journal for Numerical and Analytical Methods in Geomechanics*, Vol. 17, No. 12, (1993), 849-869, doi: 10.1002/nag.1610171203.
 46. Nguyen, D.D.C., Jo, S.-B. and Kim, D.-S., "Design method of piled-raft foundations under vertical load considering interaction effects", *Computers and Geotechnics*, Vol. 47, (2013), 16-27, doi: 10.1016/j.compgeo.2012.06.007.
 47. Poulos, H.G., "Tall building foundations: Design methods and applications", *Innovative Infrastructure Solutions*, Vol. 1, No. 1, (2016), 1-51, doi: 10.1007/s41062-016-0010-2.
 48. Lee, J., Park, D., Park, D. and Park, K., "Estimation of load-sharing ratios for piled rafts in sands that includes interaction effects", *Computers and Geotechnics*, Vol. 63, (2015), 306-314, doi: 10.1016/j.compgeo.2014.10.014.
 49. Katzenbach, R., Leppla, S. and Choudhury, D., "Foundation systems for high-rise structures, CRC press, (2016).

50. Poulos, H., "Piled raft foundations: Design and applications", *Geotechnique*, Vol. 51, No. 2, (2001), 95-113, doi: 10.1680/geot.2001.51.2.95.
51. Lee, C., "Settlement of pile groups—practical approach", *Journal of Geotechnical Engineering*, Vol. 119, No. 9, (1993), 1449-1461, doi: 10.1061/(ASCE)0733-9410(1993)119:9(1449).
52. El-Attar, A., "Dynamic analysis of combined piled raft system (cprs)", *Ain Shams Engineering Journal*, Vol. 12, No. 3, (2021), 2533-2547, doi: 10.1016/j.asej.2020.12.014.
53. Mali, S. and Singh, B., "Behavior of large piled raft foundation on different soil profiles for different loadings and different pile raft configurations", *Innovative Infrastructure Solutions*, Vol. 4, No. 1, (2019), 1-16, doi: 10.1007/s41062-018-0193-9.
54. Liu, Z., Bishop, J.A. and Lindsey, J.K., "Study of combined pile raft foundations for heavy dynamic equipment", in *Geotechnical and Structural Engineering Congress 2016*. (2016), 829-840.
55. Kumar, A., Patil, M. and Choudhury, D., "Soil–structure interaction in a combined pile–raft foundation—a case study", *Proceedings of the Institution of Civil Engineers-Geotechnical Engineering*, Vol. 170, No. 2, (2017), 117-128, doi: 10.1680/jgeen.16.00075.
56. Bandyopadhyay, S., Sengupta, A. and Parulekar, Y., "Behavior of a combined piled raft foundation in a multi-layered soil subjected to vertical loading", *Geomechanics and Engineering*, Vol. 21, No. 4, (2020), 379-390, doi: 10.12989/gae.2020.21.4.379.

Persian Abstract

چکیده

این مطالعه مروری پیشرفته بر مشکل خرابی نیروگاه‌های هسته‌ای (NPP) در اثر نیروهای زلزله تأکید دارد. تعامل خاک و NPP ممکن است منجر به آسیب به این ساختارهای منحصر به فرد سیستم زیرساختی حیاتی هر کشوری شود که برای برآورده کردن نیاز انرژی مورد نیاز است. بنابراین، اندرکنش خاک-ساختار (SSI) عامل انگیزشی کلیدی برای بررسی اصول NPP با شرایط خاک پایه آن است. علاوه بر این، مشکلات مربوط به NPP-SSI با استفاده از یک سیستم فونداسیون پیشرفته به نام پایه رافت ترکیبی (CPRF) برطرف شده است. این مطالعه دامنه ارائه CPRF به NPP را از طریق SSI بررسی می‌کند. رویکردهای تجزیه و تحلیل رفتار لرزه ای NPP در CPRF به صورت استراتژیک در این مطالعه بررسی می‌شود. با توجه به یافته‌های ادبیات، SSI مهم ترین عامل در تصمیم گیری مقاومت لرزه ای NPP است. تجزیه و تحلیل شکنندگی اهمیت SSI را در طراحی رفتار زلزله NPP نشان داد. CPRF نقش مهمی در NPP-SSI برای به حداقل رساندن آسیب ساختاری ایفا می‌کند.



Diagnostics Devices for Improving the World: μ PADs Integrated with Smartphone for Colorimetric Detection of Dopamine

F. Ghorbani Valikhali^a, M. Rahimnejad^{*a}, A. Ramiar^b, M. Ezoji^c

^a Biofuels and Renewable Energy Research Center, Department of Biotechnology, Faculty of Chemical Engineering, Noshirvani University of Technology, Babol, Iran

^b Department of Mechanics, Faculty of Mechanical Engineering, Noshirvani University of Technology, Babol, Iran

^c Department of Electronics, Faculty of Electrical and Computer Engineering, Noshirvani University of Technology, Babol, Iran

PAPER INFO

Paper history:

Received 19 March 2022

Received in revised form 17 May 2022

Accepted 20 May 2022

Keywords:

Microfluidic Systems

Dopamine

Colorimetric Detection

μ PADs

Smartphone

Oxidation-reduction

ABSTRACT

In recent years, microfluidic paper-based analytical devices (μ PADs) were used; because of their low cost, ease of use, low sample consumption and reagent, and portability, specially in developing countries. In this research, colorimetric detection of dopamine (DA) was proposed on fast, simple, sensitive and low-cost μ PADs, which is fabricated by using laser cutting technique. In paper-based microfluidic systems, wax printing is commonly used to create a hydrophobic barrier, but in this study, labels were used for the first time to create hydrophobic barriers due to their cost-effectiveness and easy access. Also in this study, the effect of various parameters on the performance improvement of developed μ PADs such as DA volume, reaction time, drying time and volume ratio of ferric ion to DA was investigated. The results showed that the presence of DA made the red color bolder and a quantitative amount of DA was obtained by taking pictures of colored areas with a smartphone. Finally, after drawing the calibration curve, the limit of detection value 0.1 μ M was defined.

doi: 10.5829/ije.2022.35.09.c.07

1. INTRODUCTION

μ PADs offer lower fabricating cost than traditional microfluidic devices, do not need microstructure equipment, and they are using for Point-of-care (POC) diagnostics in limited resource environments [1-3]. So far, several detection methods have been used for μ PADs, for example: fluorescence, colorimetry, electrochemistry, and chemiluminescence [4-11]. Between these techniques, colorimetric detection is the most widely used for integrating with μ PADs because it is easy to perform, does not require complex equipment and suitable for integrating with partly cheap devices, like scanners and smartphones [12-14].

DA related to a group of catecholamine that play a very important role in the mammals central nervous, cardiovascular and endocrine systems. Most importantly, an imbalance of DA levels can lead to neurological

disorders including Huntington's disease, immunosuppressive diseases and addiction problems, schizophrenia, depression, and Parkinson's [15-18]. Hence, detection of DA in biological fluids including serum and blood plasma is very important for clinical objects [13].

In recent years, various researches have been done in this field. For example, Liu et al. [19], in 2020, Provided an engineering insight that focuses on practical strategies for enhancing the analytical performance of μ PADs while maintaining the desired simplicity and performance. Teepoo et al. [20], in 2019, reported a one-step approach for fabricating screened printed microfluidic paper-based analytical devices (μ PADs) using polylactic acid as a new hydrophobic material.

In 2019, Liu et al. [21], reported the colorimetric detection of DA in μ PADs using the redox method. In the present study, similar to the method proposed by Liu et

*Corresponding Author Institutional Email: rahimnejad@nit.ac.ir (M. Rahimnejad)

al. [21], colorimetric measurements of DA were developed in simple and low-cost μ PADs, except that the label because of its cheapness and availability was used for the first time as a hydrophobic barrier. In addition, for the first time in recent studies, the influence of different geometries and the presence of microfluidic channels were discussed.

In this study, first, a suitable hydrophobic material was selected from the publicly available materials and then the effect of various factors on the detection of DA was investigated. In the next step, these factors were optimized to create the best paper-based microfluidic device. Finally, the effect of microfluidic channel on improving the results was discussed and analyzed.

2. MATERIALS AND METHODS

2.1. Chemicals and Materials

Dopamine hydrochloride powder (Sigma-Aldrich, USA) was obtained from Safir Azma Company (Tehran, Iran). Iron (III) chloride, Phenanthroline, K_2HPO_4 and KH_2PO_4 were purchased from Merck (Germany). Whatman® Filter paper No.1 was obtained from Azmiran Company (Tehran, Iran). DA solution and ferric chloride solution were prepared with a certain amount of deionized water. Na_2HPO_4 and NaH_2PO_4 solutions were used to construct phosphate buffer solution with different pH. Phenanthroline solution was obtained by adding a certain amount of phosphate buffer.

2.2. Construction of μ PADs

μ PADs Structure were designed by Microsoft PowerPoint software 2013. Then Whatman filter paper No.1 was cut according to the desired design by a laser cutting machine. At the first step, we were trying to use wax printing for hydrophobic barriers, but unfortunately we could not find 3-D wax printer. Because of that we were looked for some materials that had the same function as wax to manually create hydrophobic barriers.

Various materials and compounds available were used. However, each of the materials and compounds have been used had disadvantages that were not suitable for selection as a hydrophobic barrier. Finally, we got the label using trial and error. After assembly, a colorimetric test was performed and obtain the best result among the other options. Because the label cutting was done with a laser cutting machine, it had a very high accuracy and delicacy compared to other methods. At the same time, it was very economical. At the end, the results showed the suitability of using label as a hydrophobic barrier and then the potential of our proposed method as a simple and economical method.

2.3. Analysis Technique

A similar analysis technique was performed by Liu et al. [21] (Figure 1).

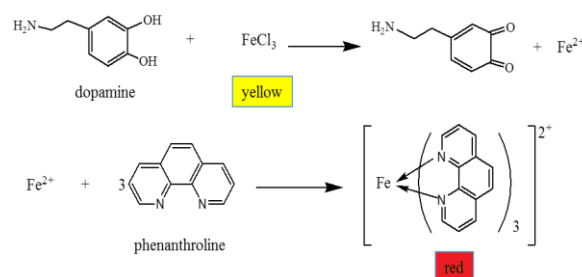


Figure 1. Schematic of DA assay reaction [21]

According to these reactions, ferric ions oxidize DA is reduced to ferrous ion. In the next step, the ferrous ion reacts with phenanthroline to form the red iron (II) tris complex (1 -10-phenanthroline).

2.4. Sample Preparation

4.2 μ l of DA solution and 8.4 μ l of ferric chloride solution were reacted for 6 minutes, then the mixture was poured into uptake zone 1 and 12.6 μ l phenanthroline was poured into uptake zone 2. After the solutions flowed through the capillary adsorption process, a red complex was formed in the detection area. After drying for 10 minutes, photos of the colored areas were taken using a smartphone camera in a light box. The images were then transferred to Photoshop software and the average red color intensity generated on the device was obtained (all the above steps were performed according to the instructions proposed by Liu et al. [21]).

3. RESULT AND DISCUSSION

3.1. Construction of μ PADs

To use the label in the structure of the paper-based microfluidic systems, we designed a label border for the paper substrate and then distributed the filter paper in the middle of layer and fixed it completely (Figure 2).

3.2. The Effect of Different Parameters on Color Intensity

Many parameters can affect the color intensity created in the colorimetric assay. For example, in the study conducted by Gash et al. [22], Paper

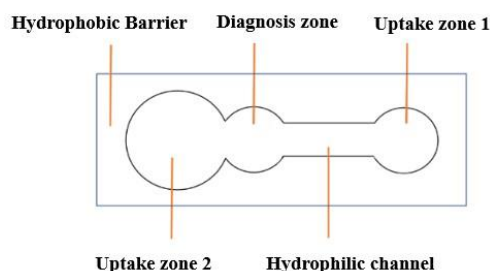


Figure 2. Schematic of the fabricated μ PADs

Topography, μ PAD capability in liquid confinement, channel resolution and minimum barrier width, as well as stability against surfactants and solvents were investigated. In the study of Lin et al. [23], UV exposure time, resolution of hydrophobic-hydrophilic patterns, concentration of polyurethane acrylate (PUA) and chemical resistance of PUA-based barriers were evaluated. Aksoren et al. [24], Studied the effects of reagent volume in the detection area, the concentration of reagents and solutions, and the reaction time of the analytes. Based on the researches, in the present study, the parameters of DA volume, reaction time, drying time, and volume ratio of ferric ion/DA, etc. have been investigated. In the following sections, we examined these parameters in more details.

3. 2. 1. Volume of DA To evaluate the effect of sample volume on color intensity, first different volumes of DA, ferric chloride and phenanthroline solutions were prepared. Then, for DA detection test, other parameters were fixed. After that, the colorimetric detection test was performed according to the mentioned steps. Finally, using the obtained data, a graph of sample volume changes in terms of average color intensity was drawn. According to Figure 3, as the sample size increases, the color intensity increases. But when the sample size exceeds a certain limit, a little solution leaks from the detection area, which is not desirable for us. So that, optimizing the sample volume, in addition to affecting the color intensity, can also reduce the sample consumption and thus reduce the cost.

3. 2. 2. Ferric Chloride/DA Reaction Time The reaction times varied from 2 - 10 minutes with an interval of 2 minutes and other parameters were fixed. Ferric chloride / DA reaction time affected the color intensity as shown in Figure 4. As you can see, as the reaction time is greater, the average color intensity gets higher and then its value is fixed. We can see the highest color intensity during the reaction time of 4 minutes. Therefore, it can be said that the time required to perform the oxidation-reduction reaction in this study is 4 minutes.

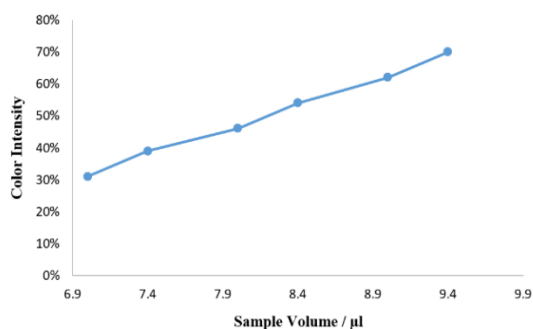


Figure 3. Effect of DA volume on the average color intensity

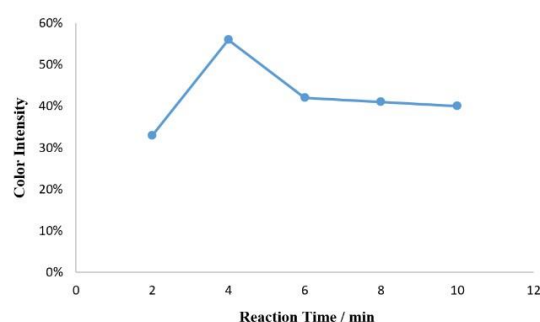


Figure 4. Effects of ferric chloride / DA reaction time on color intensity

3. 2. 3. Drying Time Drying time varied between 6-14 minutes and ferric chloride / DA reaction time, sample volume, and DA/ferric ratio were fixed. The graph shows that over time the color intensity goes up and for a longer time, the color intensity had decrease. The reason for the upward trend can be attributed to the slow drying of the paper substrate, followed by a gradual increase in color intensity (Figure 5).

3. 2. 4. Volume Ratio of Ferric Ion / DA The results showed that with increasing the ratio of Ferric ion / DA, the color intensity increases and reaches a peak value in 2 / 1 and a little reduced in ratios higher than that (Figure 6). According to the obtained results, since the highest color intensity was obtained in the ratio of 2 / 1 for the volume ratio of ferric chloride to dopamine, then the volume ratio of 2 / 1 will be considered as the optimal volume ratio.

3. 3. μ PAD Dimension Optimization To achieve optimal geometry and also to prove the superiority of the presence of microfluidic channel in the system structure, 4 different geometries were designed and fabricated (Figure 7). Designs 1 and 2 were with microfluidic channel, designs 3 and 4 were without microfluidic channel. Then, the effect of DA / ferric chloride reaction time was performed for each geometries and the results were obtained.

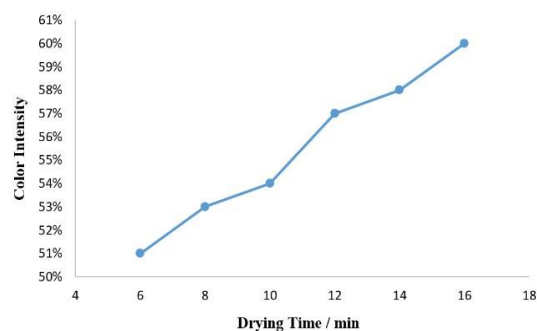


Figure 5. Effect of drying time on the average color intensity

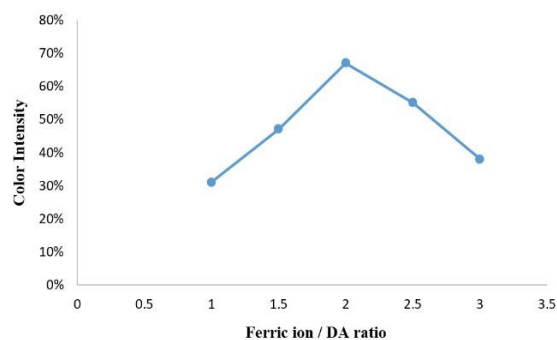


Figure 6. Effect of Ferric ion / DA ratio on the average color intensity

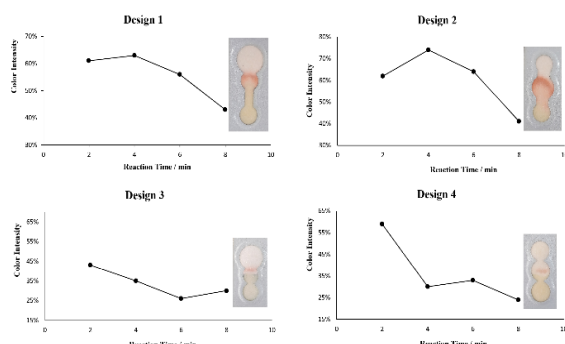


Figure 7. Effect of reaction time for 4 different geometries

The results show that, in geometries with microfluidic channels, it was observed that as the reaction progressed, the intensity of the color obtained increased and reached its peak in 4 minutes, and after that declining. For geometries without microfluidic channels, the trend of color intensity changes did not follow a specific rule and there was no peak in the diagrams. The cause of this phenomenon can be attributed to the random movements of the fluid along the paper because the presence of a microfluidic channel determines the path of movement and prevents such a problem. Therefore, it can be concluded that the presence of microfluidic channel causes proper guidance of the solution in the system and prevents additional movements of the solutions. At the end, among the two geometries with microfluidic channels, the geometry with the highest color intensity (design 2) was selected as the optimal geometry.

3.4. Calibration Curve In order to determine the concentration of DA in the samples, the calibration curve was obtained. To reach the calibration curve, different solutions of DA with different concentrations in the range of 1-6 μM were prepared. As a result, a linear relationship was obtained between the color intensity and the concentration of DA (Figure 8). The mathematical relation is expressed as $y = 23.4x + 189.38$ and the linear

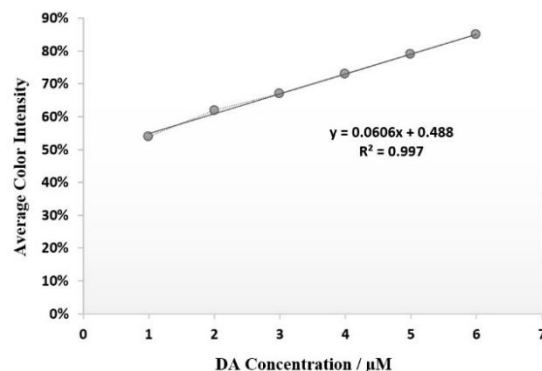


Figure 8. Analytical calibration curve for different concentration of DA from 1×10^{-6} – 6×10^{-6} M

correlation coefficient were $R^2 = 0.997$. This calibration curve allowed determining an experimental limit of detection of $0.1 \mu\text{M}$.

4. CONCLUSIONS

A simple, inexpensive, portable, and environmentally friendly colorimetric method was developed to determine DA concentrations. The analytical platform is made of cellulosic material that is compatible with many chemicals. The developed method is easy to use and can be easily stored. Therefore, these devices can be used for other chemical reactions that include analytical methods. In this study, the LOD value was $0.1 \mu\text{M}$, which is an acceptable number compared to the LOD obtained and reported in literature ($0.37 \mu\text{M}$).

5. REFERENCES

- Martinez, A.W., Phillips, S.T., Nie, Z., Cheng, C.-M., Carrilho, E., Wiley, B.J. and Whitesides, G.M., "Programmable diagnostic devices made from paper and tape", *Lab on a Chip*, Vol. 10, No. 19, (2010), 2499-2504, doi: 10.1039/C0LC00021C.
- Mao, X. and Huang, T.J., "Microfluidic diagnostics for the developing world", *Lab on a Chip*, Vol. 12, No. 8, (2012), 1412-1416, doi: 10.1039/C2LC90022J.
- Bhakta, S.A., Borba, R., Taba Jr, M., Garcia, C.D. and Carrilho, E., "Determination of nitrite in saliva using microfluidic paper-based analytical devices", *Analytica Chimica Acta*, Vol. 809, (2014), 117-122, https://doi.org/10.1016/j.aca.2013.11.044.
- Taudte, R.V., Beavis, A., Wilson-Wilde, L., Roux, C., Doble, P. and Blanes, L., "A portable explosive detector based on fluorescence quenching of pyrene deposited on coloured wax-printed μpads ", *Lab on a Chip*, Vol. 13, No. 21, (2013), 4164-4172, https://doi.org/10.1039/C3LC50609F.
- Li, L., Li, W., Yang, H., Ma, C., Yu, J., Yan, M. and Song, X., "Sensitive origami dual-analyte electrochemical immunodevice based on polyaniline/au-paper electrode and multi-labeled 3d graphene sheets", *Electrochimica Acta*, Vol. 120, (2014), 102-109, https://doi.org/10.1016/j.electacta.2013.12.076.

6. Zhou, F., Noor, M.O. and Krull, U.J., "Luminescence resonance energy transfer-based nucleic acid hybridization assay on cellulose paper with upconverting phosphor as donors", *Analytical Chemistry*, Vol. 86, No. 5, (2014), 2719-2726, <https://doi.org/10.1021/ac404129t>.
7. Mahato, K. and Chandra, P., "Based miniaturized immunosensor for naked eye alp detection based on digital image colorimetry integrated with smartphone", *Biosensors and Bioelectronics*, Vol. 128, (2019), 9-16, <https://doi.org/10.1016/j.bios.2018.12.006>.
8. Wang, F., Fu, C., Huang, C., Li, N., Wang, Y., Ge, S. and Yu, J., "Based closed au-bipolar electrode electrochemiluminescence sensing platform for the detection of mirna-155", *Biosensors and Bioelectronics*, Vol. 150, (2020), 111917, <https://doi.org/10.1016/j.bios.2019.111917>.
9. Nourbakhsh, A., Rahimnejad, M., Asghary, M. and Younesi, H., "Simultaneous electro-determination of trace copper, lead, and cadmium in tap water by using silver nanoparticles and graphene nanoplates as nanocomposite modified graphite electrode", *Microchemical Journal*, (2022), 107137, <https://doi.org/10.1016/j.micro.2021.107137>.
10. Ezoji, H., Rahimnejad, M. and Najafpour-Darzi, G., "Advanced sensing platform for electrochemical monitoring of the environmental toxin; bisphenol a", *Ecotoxicology and Environmental Safety*, Vol. 190, (2020), 110088, <https://doi.org/10.1016/j.ecoenv.2019.110088>.
11. Zabiollahpoor, A., Rahimnejad, M. and Najafpour-Darzi, G., "Recent advances in electroanalytical methods for the therapeutic monitoring of antiepileptic drugs: A comprehensive review", *Journal of Pharmaceutical and Biomedical Analysis*, Vol. 188, (2020), 113394, <https://doi.org/10.1016/j.jpba.2020.113394>.
12. Nuchtavorn, N. and Macka, M., "A novel highly flexible, simple, rapid and low-cost fabrication tool for paper-based microfluidic devices (μ pads) using technical drawing pens and in-house formulated aqueous inks", *Analytica Chimica Acta*, Vol. 919, (2016), 70-77, <https://doi.org/10.1016/j.aca.2016.03.018>.
13. Manmana, Y., Chutvirasakul, B., Suntornsuk, L. and Nuchtavorn, N., "Cost effective paper-based colorimetric devices for a simple assay of dopamine in pharmaceutical formulations using 3, 3', 5, 5'-tetramethylbenzidine-silver nitrate as a chromogenic reagent", *Pharm. Sci. Asia*, Vol. 46, (2019), 270-277, doi: 10.29090/psa.2019.04.018.0037.
14. Morbioli, G.G., Mazzu-Nascimento, T., Stockton, A.M. and Carrilho, E., "Technical aspects and challenges of colorimetric detection with microfluidic paper-based analytical devices (μ pads)-a review", *Analytica Chimica Acta*, Vol. 970, (2017), 1-22, <https://doi.org/10.1016/j.aca.2017.03.037>.
15. de Fatima Ulbrich, K., Winiarski, J.P., Jost, C.L. and de Campos, C.E.M., "Mechanochemical synthesis of a ni3-xte2 nanocrystalline composite and its application for simultaneous electrochemical detection of dopamine and adrenaline", *Composites Part B: Engineering*, Vol. 183, (2020), 107649, <https://doi.org/10.1016/j.compositesb.2019.107649>.
16. Ozoemena, O.C., Shai, L.J., Maphumulo, T. and Ozoemena, K.I., "Electrochemical sensing of dopamine using onion-like carbons and their carbon nanofiber composites", *Electrocatalysis*, Vol. 10, No. 4, (2019), 381-391, <https://doi.org/10.1007/s12678-019-00520-x>.
17. Thamilselvan, A., Manivel, P., Rajagopal, V., Nesakumar, N. and Suryanarayanan, V., "Improved electrocatalytic activity of au@ fe3o4 magnetic nanoparticles for sensitive dopamine detection", *Colloids and Surfaces B: Biointerfaces*, Vol. 180, (2019), 1-8, <https://doi.org/10.1016/j.colsurfb.2019.04.034>.
18. Tyszczyk-Rotko, K., Jaworska, I. and Jędruchiewicz, K., "Application of unmodified boron-doped diamond electrode for determination of dopamine and paracetamol", *Microchemical Journal*, Vol. 146, (2019), 664-672, <https://doi.org/10.1016/j.micro.2019.01.064>.
19. Baharfar, M., Rahbar, M., Tajik, M. and Liu, G., "Engineering strategies for enhancing the performance of electrochemical paper-based analytical devices", *Biosensors and Bioelectronics*, Vol. 167, (2020), 112506, <https://doi.org/10.1016/j.bios.2020.112506>.
20. Teepoo, S., Arsawiset, S. and Chanayota, P., "One-step polylactic acid screen-printing microfluidic paper-based analytical device: Application for simultaneous detection of nitrite and nitrate in food samples", *Chemosensors*, Vol. 7, No. 3, (2019), 44, <https://doi.org/10.3390/chemosensors7030044>.
21. Liu, C., Gomez, F.A., Miao, Y., Cui, P. and Lee, W., "A colorimetric assay system for dopamine using microfluidic paper-based analytical devices", *Talanta*, Vol. 194, (2019), 171-176, <https://doi.org/10.1016/j.talanta.2018.10.039>.
22. Ghosh, R., Gopalakrishnan, S., Savitha, R., Renganathan, T. and Pushpavanam, S., "Fabrication of laser printed microfluidic paper-based analytical devices (lp- μ pads) for point-of-care applications", *Scientific Reports*, Vol. 9, No. 1, (2019), 1-11, <https://doi.org/10.1038/s41598-019-44455-1>.
23. Lin, D., Li, B., Qi, J., Ji, X., Yang, S., Wang, W. and Chen, L., "Low cost fabrication of microfluidic paper-based analytical devices with water-based polyurethane acrylate and their application for bacterial detection", *Sensors and Actuators B: Chemical*, Vol. 303, (2020), 127213, <https://doi.org/10.1016/j.snb.2019.127213>.
24. Aksorn, J. and Teepoo, S., "Development of the simultaneous colorimetric enzymatic detection of sucrose, fructose and glucose using a microfluidic paper-based analytical device", *Talanta*, Vol. 207, (2020), 120302, <https://doi.org/10.1016/j.talanta.2019.120302>.

Persian Abstract

چکیده

در سال‌های اخیر، دستگاه‌های تحلیلی مبتنی بر کاغذ میکروسیال (μ PADs) به دلیل هزینه کم، سهولت استفاده، مصرف نمونه و معرف کم و قابلیت حمل، به‌ویژه در کشورهای در حال توسعه مورد استفاده قرار گرفته‌اند. در این تحقیق، تشخیص رنگ سنجی دوپامین بر روی μ PADهای سریع، ساده، حساس و کم‌هزینه پیشنهاد شد که با استفاده از تکنیک برش لیزر ساخته شده است. در سیستم‌های میکروسیالی مبتنی بر کاغذ، معمولاً از چاپ موم برای ایجاد مانع آبگریز استفاده می‌شود، اما در این مطالعه برای اولین بار از برچسب‌ها به دلیل مقرون به صرفه بودن و دسترسی آسان استفاده شد. همچنین تأثیر پارامترهای مختلف بر بهبود عملکرد μ PADهای توسعه‌یافته مانند حجم دوپامین، زمان واکنش، زمان خشک شدن و نسبت حجمی یون آهن به دوپامین مورد بررسی قرار گرفت. نتایج نشان داد که وجود دوپامین سبب پررنگ تر شدن رنگ قرمز شده و مقدار کمی آن با گرفتن عکس از مناطق رنگی توسط تلفن هوشمند به‌دست آمد. در نهایت پس از رسم منحنی کالیبراسیون، مقدار LOD $0.1 \mu\text{g/L}$ میکرومولار محاسبه شد.



Testable MUXED-D Scan Cell in Quantum-dot Cellular Technology

M. Gholami^{*a}, S. Zarei^b

^a Department of Electrical Engineering, Faculty of Engineering and Technology, University of Mazandaran, Babolsar, Iran

^b Department of Computer Engineering, Faculty of Engineering and Technology, University of Mazandaran, Babolsar, Iran

PAPER INFO

Paper history:

Received 04 April 2022

Received in revised form 17 May 2022

Accepted 19 May 2022

Keywords:

MUXED-D Scan Cell

Nanotechnology

Quantum-dot Cellular Automata

Shift Register

ABSTRACT

Quantum-dot Cellular Automata (QCA) is one of the new nanoscale technologies which proposed for future circuits. This technology has been remarkable due to its faster speed, lower size and reduction in power consumption compared to CMOS technology. Many circuits have been implemented in this technology including shift registers, they are one of the most important digital circuits for many applications. With the development of QCA technology, it is important to provide testing methods for testing these circuits. 4-Bit serial shift registers designed in previous research were not capable of testing their output. In this paper, MUXED-D scan cell concept helps to detect the errors before fabrication and reduce time and cost. The MUXED-D scan consists of a D flip-flop and a 2 to 1 multiplexer. Compared to the latest scan cell, we have seen a 25 % decrease in occupied area and 15.62 % decrease in the number of cells and latency from 1 to 0.75 clock cycle. In general, this scan cell circuit is made of 27 cells with an area of $0.03 \mu\text{m}^2$ and a latency of 3 clock cycles. The proposed shift register includes four scan cells with two inputs which includes main and test signals. In fact, the number of cells used for the last 4-bit serial testable shift register in this design is 324, $0.39 \mu\text{m}^2$ occupied area and the corresponding delay is 6.75 clock cycles. In order to verify this performance, QCA simulator is used.

doi: 10.5829/ije.2022.35.09c.08

1. INTRODUCTION

According to the Moore's law, the trend of doubling the number of transistors used in each chip with time has become a major challenge for CMOS technology. Physical limitations on the CMOS prevents the transistor from shrinking. It can be said that emerging Quantum-dot Cellular Automata (QCA) technology has partially compensated for the constraints of CMOS [1]. Due to the structure of the cells in the QCA, one of the suitable alternatives for CMOS is QCA technology [2]. What is clear is that registers are needful components for storing binary information [3]. So, designing circuits specially registers, without detects is something that needs to be addressed. One of the steps to complete the design is to test, obviously if the test is done in the last step of the design, it will take a lot of effort [4]. One such solution is using scan flip-flop. A scan flip-flop is one of the tools that is widely used to test the correct operation of the

circuit, it consist of multiplexer and D flip-flop [5]. It has a control line for selecting data or scanning input. By checking the current status of the flip-flop, it ensures that the flip-flop output is correct, that we can troubleshoot the circuit in larger-scale, and locate the fault [6].

Apparently, not much research has been done on this issue, some of them have tried to improve the efficiency of scan cells. In these papers, they described how they could improve circuits such as scan cells by making multiplexers more efficient [5, 7, 8]. The scan circuit proposed by Goswami et al. [7] occupied a large area due to the large number of its cells. Harshitha et al. [5] and Shantala and Karthik [8] tried as much as possible to reduce the size of the circuit and use fewer cells, but they did not make any progress in terms of latency and it remained 4 clock cycles. In this paper, the scan cell is optimized and testing of QCA based shift register is studied. Eventually the proposed design is defined. In other words, by replacing the scanning cell, the function

*Corresponding Author Institutional Email: m.gholami@umz.ac.ir
(M. Gholami)

of the shift register can be checked. This means that by selecting the test input line of the shift register, we can change its status to test mode and check its output, and then the circuit can continue to operate normally. This article is divided into sections to make it easier to understand the essence of the case. It has been discussed in the second section about the structure and logic of QCA design. The main gates and the concept of clock are examined in QCA technology. Then, in the third part, the designed circuits that are used for the final simulation are introduced. In the next part, the recommended test shift register is introduced and its implementation and performance are examined. At the last part, the conclusion of the work has been done.

2. BACKGROUND

The technology is based on a quantum cell which has a square shape and has four quantum dots in its corners. Each cell has two electrons that can move between the quantum dots. These electrons tend to minimize their mutual Coulomb interaction, for this reason, they placed in opposite corners of the cell [9]. This act causes two polarizations in the form of +1 and -1. The polarization of the cell in the $P=+1$ represents logic "1" and $P = -1$ represents logic "0" (Figure 1) [10]. Basic implementations in QCA are wire, inverter, and majority gate. A line of cells can be used as a QCA wire to propagate information [11]. Due to the Coulomb interactions between cells, binary information transmit from input to output (Figure 2) [12]. Also, the majority gate consists of 5 cells. As shown in Figure 3 cells are used as input and the middle cell is used as a voter and the other cell is the output of this gate. In fact, the voting cell performs the main operation. The logic of the majority voting can be demonstrated by Boolean operators in this way:

$$M(A,B,C)=AB+BC+AC \quad (1)$$

The said system can perform AND/OR operations. To convert the majority gate to the AND/OR gates, one of the input cells must consider as a program line. When program line is equal to 1, OR gate is performed and when the line is equal to 0, the AND gate is performed [13].

Moreover, the not gate is another one of the fundamental gates of QCA circuits. The position of the

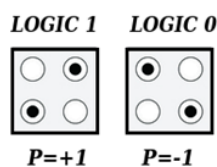


Figure 1. QCA cell [12]

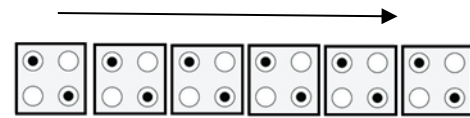


Figure 2. QCA wire [12]

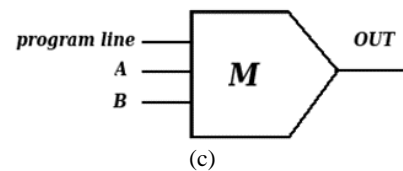
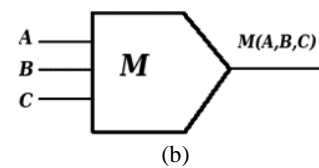
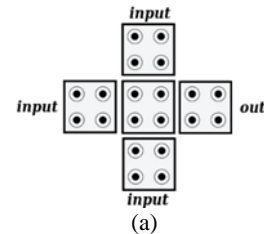


Figure 3. (a) The QCA majority gate; (b) The schematic of majority gate; (c) The schematic of programmable AND/OR gate [12]

cells makes them try to reach a stable state. Eventually, the input and output are reversed. Two types of implementation of this gate are shown in Figure 4.

In addition to controlling the flow of information throughout the circuit, clocking provides the true power of the QCA circuit [9]. QCA cells have 4 clock states, including switch, hold and release and relax (Figure 5) [14]. In fact, increasing or decreasing the potential barrier between neighboring cells changes the status of the cells. As the potential barrier rises, the tunneling rate decreases and the electrons are placed in the right place, and the

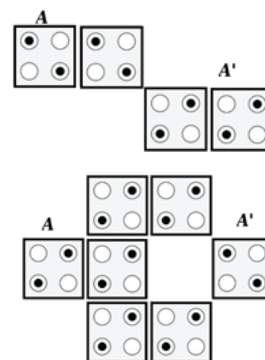


Figure 4. QCA inverter [12]

cell becomes definitively polarized [15]. In the first phase that it called switch, the polarization of the cell is done and reaches its final binary state. In the hold phase, the cell retains its polarity and is not affected by the surrounding cells. In the next phase potential barrier is decreases, as a result it gradually loses its polarity. In the following, there is no potential barrier and the cell does not affect other cells in relax phase.

3. RELATED WORKS

In this section related works which can prove the better performance of proposed designs will be introduced.

3.1. QCA Multiplexer Multiplexer receives data from input lines, with one of the inputs sending data to the output at a time, based on selector signals [16]. The output of this combinational logic circuit for 2-input line is confirmed by following simplified Boolean expression

$$Q = \bar{S} I_1 + S I_0 \quad (2)$$

when $S=0$ the Q is equal to I_1 and when $S=1$ the Q is equal to I_0 . This design has 12 cells and 1 clock zones latency. The schematic and QCA layout of the recent previous 2:1 multiplexer is shown in Figure 6 [17].

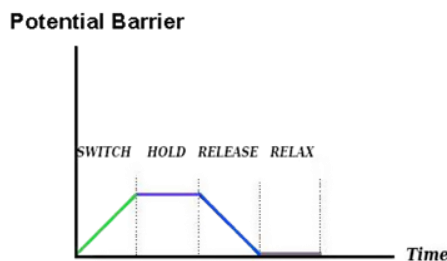


Figure 5. QCA clock phases [18]

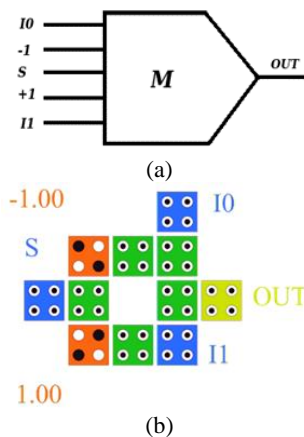


Figure 6. 2:1 multiplexer, (a) Schematic; (b) QCA layout [17]

3.2. QCA D Flip-flop

The D storage element is one of the most widely used in the structure of logic circuits design. A flip-flop called a 'Delay flip-flop' or 'data flip-flop' and latch is a circuit that stores one bit [19]. The main difference between the two circuits is that the latch is level-sensitive while the flip-flop is edge-triggered. Figure 7 shows the structure of D latch which consists of two input: a data line and a control line for the clock signal. The Q represents output state of the latch. The remarkable point about performance of latch is that the input can change the output state when the clock is not low. D latch layout which is implemented with multiplexer, involves 18 cells and input-output delay takes 0.5 clock cycle (Figure 8) [20].

It is possible to use the structure that mentioned by Hashemi and Navi [21] to convert the latch to a flip-flop. By performing the AND operation between the current and reverse clock pulses, the required output clock is generated. The corresponding layout and diagram of D flip-flop are shown in Figure 9.

4. PROPOSED SHIFT REGISTER WITH TEST ABILITY

Shift registers are sequential logic circuits, usable for storing and transferring data, this device shifts the input data to the output with each clock [18]. A shift register is created by connecting the output of one flip-flop to the input of the next flip-flop in the chain using a cascade of flip-flops with the same clock [19]. (Shown in Figure 10). Test capability is provided by having a scanning cells in desired circuit. As we can see in the Figure 11, this

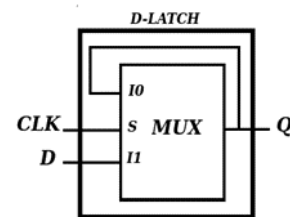


Figure7. D latch diagram

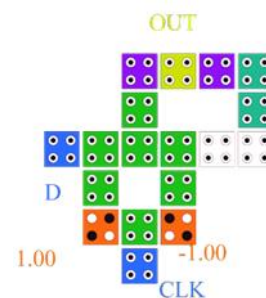


Figure 8. QCA layout of D latch [20]

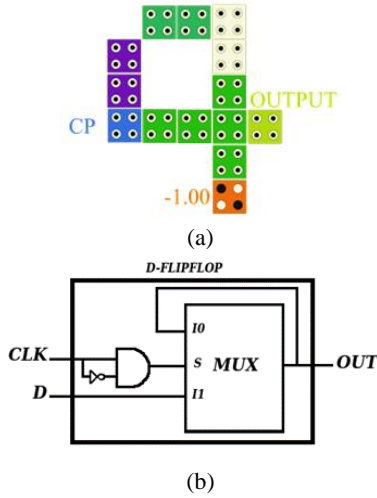


Figure 9. (a) layout of the edge to level converter [22]; (b) diagram of the D flip-flop [23]

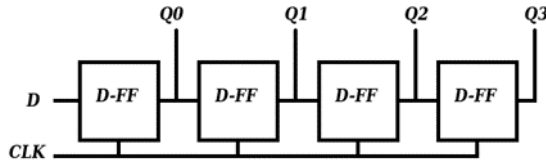


Figure 10. Diagram of 4-bit series shift register [20]

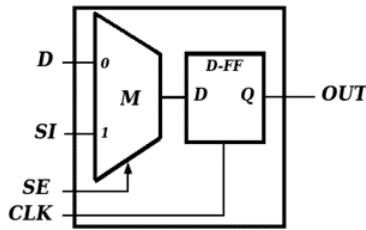


Figure 11. Scan cell diagram [8]

element consists of a multiplexer and a D flip-flop. The selector of multiplexer puts SI on the input line of the flip-flop when it has a '1' value and DI when it has a value of '0'. It contains 27 cells and takes 0.75 cycles that results get correct output [4]. Figure 12 shows the layout of scan cell that described. Suggested scan cell is more efficient than designed scan cells. Table 1 gives a brief overview of designed scan cells during past research.

Each of the flip-flops has been replaced with scan cells to add testability to the proposed SISO shift register circuit. The proposed shift register can be seen in the Figure 13. To form the shift register, the output of the first scan cell is connected to the inputs of the second scan cell, and each output is still connected to the SI and DI of the next scan cell. Also, the selector and clock inputs are connected to all scan cells simultaneously. As a result, a

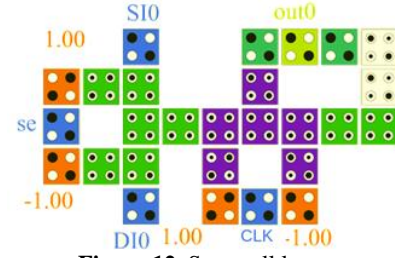


Figure 12. Scan cell layout

TABLE 1. Performance analysis of scan flip-flop

Sff	Number of Cells	Area (μm^2)	Latency
[7]	72	0.12	4
[8]	40	0.06	4
[5]	32	0.04	4
Proposed	27	0.03	3

chain of scan has emerged. By placing the converter for the clock, we actually sensitized the D latches, which we have used in the scan cells structure, to the rising edge. Based on the simulation, the delay is equal to 6.75 cycles and its area is $0.39\mu\text{m}^2$ with number of 324 cells. Figure 14 shows the proposed shift register which is made by joining 4 scan cells.

5. SIMULATION RESULTS

The designs of the proposed circuit have been performed on QCA Designer software. The result of the simulation is shown in Figure 15. In addition, the scan cell simulation result, which is an important component of the proposed shift register structure, is shown in Figure 16.

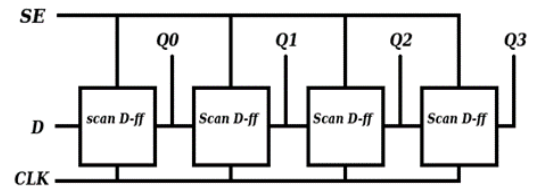


Figure 13. Proposed 4-bit SISO shift register

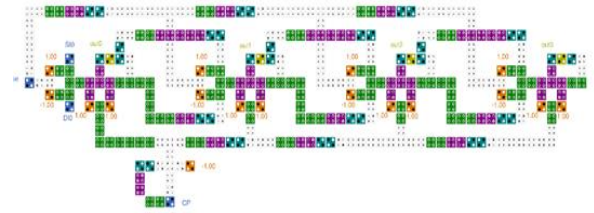


Figure 14. Layout of proposed testable shift register

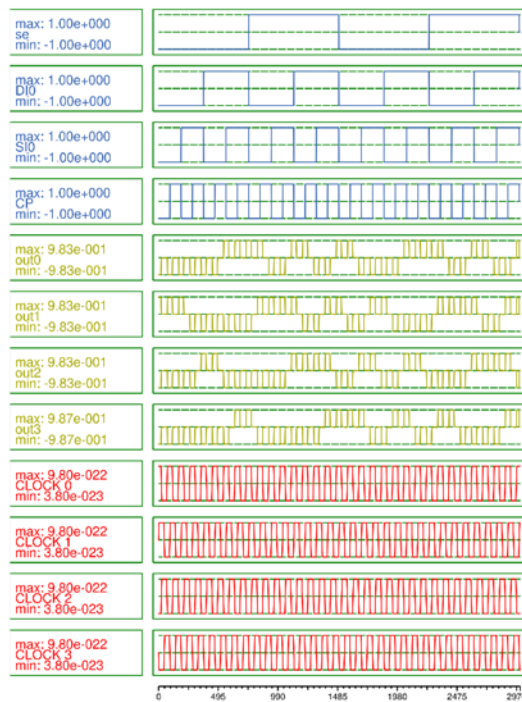


Figure 15. Simulation result of proposed 4-bit testable shift register

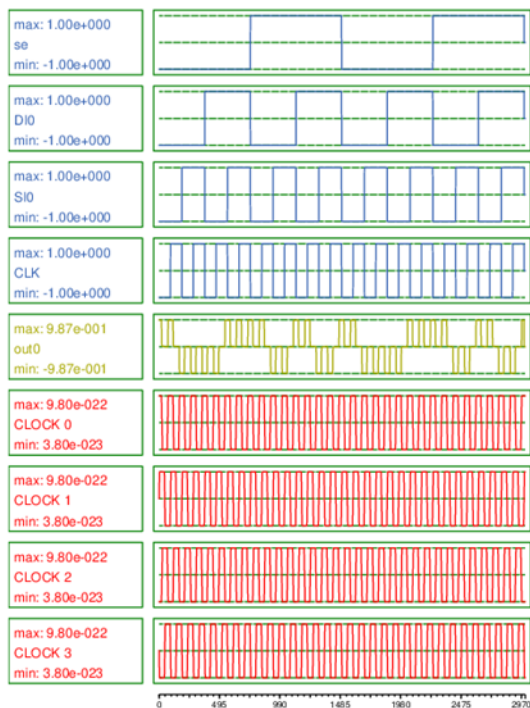


Figure 16. simulation result of scan cell

The output of the scan cell simulation shows the correct operation of this design. This circuit is made of a multiplexer and D latch. According to this, output is the

result of changes in the clock and selector level. The multiplexer used in the scan cell allows us to choose between SI and D by SE. As it is known, if the clock is in the enable state and SE is zero, D will appear in the output and if its value is one, SI will be displayed. In the opposite case, if the clock is not enabled, the previous values of the circuit will be displayed again without considering the inputs and SE.

The proposed structure consists of positive edge-triggered flip-flops, so output changes only at the point in time when the clock changes from 0 to 1. When the clock pulse is applied, depending on the value of SE, one or two input values are enter the shift register. Applying the next clock will transfer the output of each scan cell to the input of the next scan cell. The result of this simulation is shown in Figure 15 represents that when SE is zero, D is selected as the input, and when the clock becomes one after a delay of 0.75 cycles, the first input is placed on output0. In the next cycle, the new input is placed at output0. Of course, this new input can be D or S depending on the SE value. So the previous value of output0 is stored in output1 and continues to reach output3.

The thermal hotspots in the average power dissipation map of proposed 4-bit testable shift register with $0.5 E_k$ is shown in Figure 17. We obtained this diagram with the QCAPro tool to estimate the average, maximum, and minimum power dissipation in a QCA circuit while the input is being switched [24]. In this diagram, the darker color indicates the high level of energy loss whereas the input cells are shown as white cells.



Figure 17. Energy diagram of proposed 4-bit testable shift register

6. CONCLUSION

With the complexity and increasing number of inputs in designed circuits, the ability to test different parts of the circuit has become very important. Therefore, by adding a test cells to the desired circuit, the output of different parts can be controlled. Necessity of presence of shift registers in the memory structure is not hidden from anyone, In addition, the test capability hasn't been implemented in previous shift registers. Though, in this

work, we have proposed a design and layout for QCA testable SISO shift register. In this proposed design, the efficiency of the shift register has been improved by reducing the size and latency of the test cells.

7. REFERENCES

1. Lim, L.A., Ghazali, A., Yan, S.C.T. and Fat, C.C., "Sequential circuit design using quantum-dot cellular automata (QCA)", in 2012 IEEE International Conference on Circuits and Systems (ICCAS), IEEE. (2012), 162-167.
2. Lent, C.S., Tougaw, P.D., Porod, W. and Bernstein, G.H., "Quantum cellular automata", *Nanotechnology*, Vol. 4, No. 1, (1993), 49, doi: 10.1088/0957-4484/4/1/004.
3. Sabbaghi-Nadooshan, R. and Kianpour, M., "A novel qca implementation of mux-based universal shift register", *Journal of Computational Electronics*, Vol. 13, No. 1, (2014), 198-210, doi: 10.1007/s10825-013-0500-9.
4. Wang, L.-T., Wu, C.-W. and Wen, X., "Vlsi test principles and architectures: Design for testability, Elsevier, (2006).
5. Harshitha, S., Dhanush, T. and Premananda, B., "A novel qca based compact scan flip-flop for digital design testing", *International Journal of Engineering and Advanced Technology*, Vol. 9, No. 1, (2019), 6681-6686, doi: 10.35940/ijeat.A1973.109119.
6. Pooja, M., Shetty, G.S., Datta, V.S. and Suchitra, M., Design of set d flip-flop and scannable set d flip-flop with optimized area, in Advances in communication, signal processing, vlsi, and embedded systems. 2020, Springer.239-245.
7. Goswami, M., Kumar, B., Tibrewal, H. and Mazumdar, S., "Efficient realization of digital logic circuit using qca multiplexer", in 2014 2nd International Conference on Business and Information Management (ICBIM), IEEE., (2014), 165-170.
8. Shantala, G. and Karthik, P., "Design and implementation of scan flip-flop for processor using qca technology", *International Journal of Control and Automation*, Vol. 10, No. 8, (2017), 41-52, doi: 10.14257/ijca.2017.10.8.04.
9. Lent, C.S., Liu, M. and Lu, Y., "Bennett clocking of quantum-dot cellular automata and the limits to binary logic scaling", *Nanotechnology*, Vol. 17, No. 16, (2006), 4240, doi: 10.1088/0957-4484/18/29/298001.
10. Ahmad, F. and Bhat, G., "Novel code converters based on quantum-dot cellular automata (QCA)", *International Journal of Science and Research*, Vol. 3, No. 5, (2014), doi.
11. Kong, K., Shang, Y. and Lu, R., "An optimized majority logic synthesis methodology for quantum-dot cellular automata", *IEEE Transactions on Nanotechnology*, Vol. 9, No. 2, (2009), 170-183, doi: 10.1109/TNANO.2009.2028609.
12. Wang, W., Walus, K. and Jullien, G.A., "Quantum-dot cellular automata adders", in 2003 Third IEEE Conference on Nanotechnology, 2003. IEEE-NANO 2003., IEEE. Vol. 1, (2003), 461-464.
13. Tougaw, P.D. and Lent, C.S., "Logical devices implemented using quantum cellular automata", *Journal of Applied Physics*, Vol. 75, No. 3, (1994), 1818-1825, doi: 10.1063/1.356375.
14. Abutaleb, M., "Robust and efficient quantum-dot cellular automata synchronous counters", *Microelectronics Journal*, Vol. 61, (2017), 6-14, doi: 10.1016/j.mejo.2016.12.013.
15. Vetteth, A., Walus, K., Dimitrov, V.S. and Jullien, G.A., "Quantum-dot cellular automata of flip-flops", *ATIPS Laboratory*, Vol. 2500, (2003), 1-5, doi.
16. AlKaldy, E., Majeed, A.H., Zainal, M.S. and Nor, D.M., "Optimum multiplexer design in quantum-dot cellular automata", arXiv preprint arXiv:2002.00360, (2020), doi: 10.48550/arXiv.2002.00360.
17. Asfestani, M.N. and Heikalabad, S.R., "A unique structure for the multiplexer in quantum-dot cellular automata to create a revolution in design of nanostructures", *Physica B: Condensed Matter*, Vol. 512, (2017), 91-99, doi: 10.1016/j.physb.2017.02.028.
18. Ahmad, F., Mustafa, M., Wani, N.A. and Mir, F.A., "A novel idea of pseudo-code generator in quantum-dot cellular automata (QCA)", *International Journal for Simulation and Multidisciplinary Design Optimization*, Vol. 5, No., (2014), A04, doi: 10.1051/smdo/2013012.
19. Yaqoob, S., Ahmed, S., Naz, S.F., Bashir, S. and Sharma, S., "Design of efficient n-bit shift register using optimized d flip flop in quantum dot cellular automata technology", *IET Quantum Communication*, Vol. 2, No. 2, (2021), 32-41, doi: 10.1049/qtc2.12008.
20. Roshan, M.G. and Gholami, M., "4-bit serial shift register with reset ability and 4-bit lfsr in qca technology using minimum number of cells and delay", *Computers & Electrical Engineering*, Vol. 78, (2019), 449-462, doi: 10.1016/j.compeleceng.2019.08.002.
21. Hashemi, S. and Navi, K., "New robust qca d flip flop and memory structures", *Microelectronics Journal*, Vol. 43, No. 12, (2012), 929-940, doi: 10.1016/j.mejo.2012.10.007.
22. Gholamnia Roshan, M. and Gholami, M., "Novel d latches and d flip-flops with set and reset ability in qca nanotechnology using minimum cells and area", *International Journal of Theoretical Physics*, Vol. 57, No. 10, (2018), 3223-3241, doi: 10.1007/s10773-018-3840-1.
23. Shamsabadi, A.S., Ghahfarokhi, B.S., Zamanifar, K. and Movahedinia, N., "Applying inherent capabilities of quantum-dot cellular automata to design: D flip-flop case study", *Journal of Systems Architecture*, Vol. 55, No. 3, (2009), 180-187, doi: 10.1016/j.sysarc.2008.11.001.
24. Srivastava, S., Asthana, A., Bhanja, S. and Sarkar, S., "Qcapro-an error-power estimation tool for qca circuit design", in 2011 IEEE international symposium of circuits and systems (ISCAS), IEEE. (2011), 2377-2380.

Persian Abstract

چکیده

اتوماتای سلولی - نقطه‌ای کوانتومی (QCA) یکی از تکنولوژی‌های نوین در مقیاس نانو است که برای مدارهای آینده پیشنهاد شده است. این تکنولوژی به دلیل سرعت بالاتر، اندازه کوچک تر و کمتر بودن توان مصرفی در مقایسه با تکنولوژی CMOS قابل توجه بوده است. مدارات زیادی از جمله شیفت رجیسترها با این تکنولوژی پیاده‌سازی شده‌اند. شیفت رجیسترها از مهم ترین و پرکاربردترین مدارات دیجیتال هستند. با توسعه تکنولوژی QCA، ارائه روش‌هایی برای تست این مدارات بسیار مهم و حیاتی است. شیفت رجیسترهای سری بیتی که در تحقیقات قبلی طراحی شده‌اند، قادر به آزمایش خروجی خود نبوده‌اند. در این مقاله مفهوم سلول اسکن MUXED-D به شناسایی خطا قبل از ساخت، کاهش زمان و هزینه کمک می‌کند. اسکن MUXED-D از یک فلیپ فلاپ D و یک مالتی پلکسر ۲ به ۱ تشکیل شده است. در مقایسه با آخرین سلول اسکن طراحی شده، شاهد ۲۵٪ کاهش در مساحت اشغالی و ۱۵.۶۲٪ کاهش در تعداد سلول‌ها و کم شدن تاخیر از ۱ به ۰.۷۵ هستیم. به طور کلی، این مدار سلول اسکن از ۲۷ سلول با مساحت $0.03 \mu m^2$ و تاخیر ۳ سیکل کلاک ساخته شده است. شیفت رجیستر پیشنهادی شامل چهار سلول اسکن با دو ورودی است که شامل سیگنال‌های اصلی و آزمایشی می‌باشد. در حقیقت، تعداد سلول‌های مورد استفاده برای شیفت رجیستر سری ۴ بیتی طراحی شده ۳۲۴ بوده و $0.39 \mu m^2$ مساحت اشغال شده و تاخیر مربوطه $6.75 \mu m^2$ سیکل کلاک می‌باشد. به منظور تایید این عملکرد، شبیه‌ساز QCA مورد استفاده قرار گرفته است.



Effect of Friction Stir Processing on Fusion Welded Joint of Al-5083

K. D. Tandel*, J. V. Menghani

Sardar Vallabhbhai National Institute of Technology, Surat, India

PAPER INFO

Paper history:

Received 07 April 2022

Received in revised form 18 May 2022

Accepted 26 May 2022

Keywords:

Friction Stir Processing

Surface Modification

Autogenous TIG Welding

Grain Refinement

ABSTRACT

Tungsten Inert Gas Welding (TIG) is the most preferred joining process for aluminum alloys, but it produces weld joint having inferior mechanical property in comparison with base metal because of inherent limitations of the process. To improve the mechanical properties, the weld is post processed by friction stir processing (FSP) upto depth of 2mm. This paper presents the effect of performing FSP on autogenous TIG welded butt joint of Al-5083, 6mm thick plate. Mechanical and metallurgical properties of both processed and unprocessed autogenous TIG weld are compared. Characterisation techniques adopted to evaluate weld joint are tensile test, microhardness measurement, microstructural examinations and SEM analysis. Tensile strength of autogenous TIG weld joint is lowered by 6.5% compared to base metal because of presence of micro porosities in the weld metal. Friction stir processing produces the fine grain refined structure, marginally improves the tensile strength of the autogenous TIG weld joint by 2.7%. Microhardness of the autogenous TIG weld metal of the surface is raised from 163.6 HV to 298 HV after performing FSP. However, SEM images of fractured surface of friction stir processed specimen reveals fine dimpled structure which indicates that ductility of the weld joint remain unaffected after performing FSP on autogenous TIG weld joint.

doi: 10.5829/ije.2022.35.09c.09

1. INTRODUCTION

Recent advancements in the field of marine, automobile, defence and aerospace propel the usage of light metals such as aluminum, titanium and magnesium against the conventional materials. 5xxx, 6xxx and 7xxx series of aluminum alloys possesses excellent mechanical and physical properties such as high strength to weight ratio, good corrosion resistance in extreme conditions, low density, good formability and high thermal conductivity. That is why they have been the prime choice for manufacturing various components used in interceptor boat structure, car frame and bodies, axles, shafts, air craft, missile, rocket and rocket launcher [1].

Tungsten Inert Gas Welding (TIG) has been the preferred fusion welding technique over Shielded Metal Arc Welding (SMAW), and Metal Inert Gas Welding (MIG) for manufacturing of aluminium alloy structures and components because of its ability to produce deeper penetration and cleaner weld joint [2]. As the aluminum alloys are having high heat conductivity, high thermal expansion coefficient, and inclination for refractory

aluminium oxide (Al_2O_3) generation, fusion welding of aluminium alloys is challenging [3]. Furthermore, welding flaws associated with fusion welding of aluminum alloy such as porosity, low wetting, hot cracking, lack of fusion, residual stresses, and distortion are responsible for decrease in strength, and poor joint efficiency [4, 5]. However, the rising use of aluminium alloys in practically every industry is forcing researchers to create practicable and effective technologies to weld aluminium alloys without compromising their mechanical, chemical, or metallurgical properties, which are required for longer service life.

Being a green technology by nature, friction based welding and surface processing techniques have been very popular since last two decades and best suited for welding and processing of aluminum alloys as it does not melt the base metal [6]. The Welding Institute (TWI) in the UK first invented and patented the novel Friction Stir Welding (FSW) process in the year 1991. The process involves generation of frictional heat using non-consumable spinning tool with a probe/pin and a collar plunged in to the metals to be joined and traverse along

*Corresponding Author Email: kdtandel.gecd@gmail.com
(K. D. Tandel)

the intended welding path [7]. The material around the tool probe softens due to frictional heating generated due to rubbing action of tool and base metal. Extreme plastic deformation and plastic material flow all around the tool probe are caused by the combined impact of tool rotational and transverse movement. The churning of two base metals in a plastic state around the tool produces a permanent weld joint upon cooling to room temperature [8]. FSW-produced joint possesses superior mechanical property compared to fusion welded joints of aluminum alloys because in FSW process, weld metal experiences an excessive plastic deformation at elevated temperature, breaks dendritic coarse grain structure, and produces fine and equiaxed recrystallized structure [6]. However, the mechanical characteristics of the weld joint is greatly affected by the FSW operating parameters and tool geometry [9]. As the heat produced by friction is directly proportional to the tool rotation speed, the tensile strength increases as tool rotation speed increases and decreases as tool traverse feed increases [10].

A newer welding approach of surface modification by Friction Stir Processing (FSP) has been successfully demonstrated by many researchers. FSP is a novel variant of FSW, introduced by Mishra et al. [11], having the same working principle as that of FSW, in that a rotating tool is inserted into the material surface up to a specific targeted depth and travelled along the required path to cover the material's intended surface area with the purpose of modifying the microstructure and consequently changing the material's surface mechanical characteristics [12]. Later on fabrication of composite of SiC reinforcement in the Al-5083 metal matrix was successfully demonstrated by Mishra et al. [11]. The experimental results show substantial increase in the hardness of the FSPed segment in comparison with the base metal. The SiC particles were well dispersed throughout the aluminium matrix, demonstrating good bonding with the aluminium alloy substrate. Factors like tool geometry, number of FSP passes, FSP operating parameters (tool rpm and travel speed), and the type and volume fraction of metal matrix composite fabrication are responsible for the desired change in surface properties [13]. Wang et al. had successfully fabricated SiCp reinforced Al metal matrix composites (MMCs) up to the depth of 100 μm using FSP technique. Increase in top surface micro hardness value of about 10% compared to base metal was reported by addition of SiCp (1.5%) to aluminum matrix [14]. Kaushik and Singhal [15] studied effect of FSP on microstructural and mechanical behavior of friction stir welded aluminum alloy 6063 matrix reinforced with 7 wt% SiC particles. Uniform distribution of SiC particles in Al-6063 matrix was observed after FSP. Significant improvement in wear resistance property of Al-TiC composite using FSP was reported by Akinlabi et al. [16]. Wear resistance property was found to be influenced by tool rotation speed and processing feed rate. Multipass FSP was used by Bauri et

al. [17] to homogenise the TiC particle dispersed in an aluminium matrix. After each FSP pass, the grain size was refined which significantly improved mechanical property without compromising ductility. Sharma et al. [18] had employed variety of FSP methods including varying process parameters, dual-tool processing and tool offset overlapping to produce SiC reinforced AA5083 alloy surface. Success of the FSP as a surface modification technique has been a driving force for many researchers to execute the same on welded surface. To enhance fatigue characteristics of the weld joint, Costa et al. [19] and Borrego et al. [20] had performed FSP on the toe of the T-joint and butt joint of Al-5083 welded by Metal Inert Gas (MIG) welding process respectively. Xu and Bao [21] claimed that mechanical properties of weld joint of AZ31 magnesium alloy performed by TIG welding process was improved after performing rapid cooled FSP on it. Friction Stir Processed (FSPed) TIG and Friction Stir Welded joints were tested by Mabuwa and Msomi [22]. In the work, full depth FSP showed significant improvement in tensile strength while hardness was marginally affected [22]. Al-5052 alloy weldment produced by TIG welding process, which was post processed by a newer method called friction stir vibration processing (FSVP) showed greater grain refinement in the stir zone which leads to increase in tensile strength by 17% and improvement in ductility by 33% compared to unprocessed TIG weld joint [23]. Mehdi and Mishra [24] studied effect of FSP on mechanical property and heat transfer of TIG weld joint of dissimilar aluminum alloy AA-6061 and AA-7075. The calculated maximum temperature using ANSYS software was around 515°C tool rotation speed of 1600 RPM whereas maximum rate of heat flux was calculated about $5.33 \times 10^6 \text{ W/m}^2$ observed at tool rotation speed of 1600 RPM.

In the present investigation, Al-5083 plate of 6mm thickness was butt welded by TIG welding technique without addition of filler wire (autogenous welding). The weld was then friction stir processed (FSPed) with a solid tool having a pin. The processing was achieved upto depth of 2mm on both sides. Characterisation of the weld joint produced was performed by macro observation, micro examination, tensile testing, and microhardness mapping. The nature of weld failure was investigated via fractographic examinations using scanning electron microscope (SEM). As per the reviewed literature, FSP upto depth of 2mm on both sides of autogenous TIG weld of Al-5083 is not observed. The present work is a step towards it.

2. MATERIALS AND METHODS

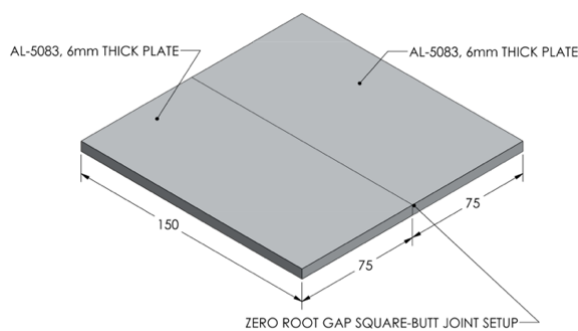
2.1. Base Metal The base metal in this experiment was Al-5083, a 6mm thick plate. Aluminum alloy 5083 is an Al-Mg alloy which has the highest strength amongst

TABLE 1. Chemical composition of Al-5083

Mg	Mn	Fe	Si	Cr	Cu	Zn	Al
5	0.57	0.35	0.15	0.05	0.05	0.02	Rest

TABLE 2. Mechanical Properties of Al-5083

Property	Value
Tensile Yield Strength	228 MPa
Ultimate Tensile Strength	317 MPa
Elongation at Break	16%
Hardness	85 BHN

**Figure 1.** Weld setup for autogenous TIG welding

non-heat treatable alloys as well as it possesses excellent corrosion resistance in salt water which make it an ideal choice for chemical industry and marine applications [2]. According to ASTM B209/B928M, the chemical composition and typical mechanical properties of Al-5083 are presented in Table 1. Mechanical properties of Al-5083 collected from ASM data sheet is summarized in Table 2. Using a cutting wheel, the plate was cut into pieces of 150mm x 75mm. The plate's edges were flat ground to create a zero root gap, Square-butt joint configuration for the autogenous TIG welding process is shown in Figure 1.

2. 2. Autogenous TIG Welding Aluminium-Mg alloy with Mg in the range of 1 to 2.5 percent may be prone to hot cracking if welded without filler wire or with a filler wire having matching chemical composition with base metal. To avoid hot cracking while welding of Al-Mg alloy, filler metal having Mg content greater than 3.5% is used [25]. Autogenous TIG welding arrangements are illustrated in Figure 1. The Lincoln Electric made Aspect-300 TIG welding equipment was used to execute TIG welding on square-butt joint. To accomplish a full penetration joint, single pass on each sides was deposited by TIG welding. Argon (99.998% purity) was used as the shielding gas, and a 3mm diameter Thoriated Tungsten rod was used as electrode.

The electrode tip had a blunt conical form. The pointed tungsten electrode tip deteriorates quickly, causing the arc to wander during AC welding, resulting in a welding defect. The arc becomes steady when using a blunt electrode tip. Welding parameters to achieve full penetration joint by autogenous TIG welding process are 150 amp current, 15-16 V voltage, 120-130 mm/min travelspeed and 13-14 lpm shielding gas flow rate.

2. 3. Friction Stir Processing Autogenous TIG welded plate was friction stir processed (FSPed) on both side upto a depth of 2mm from the top surface by using a tool having a pin. Tool used in FSP is shown in Figure 2. Pin geometry was cylindrical and having a height of 2 mm. FSP was performed on Batiboi made milling machine. Figure 3 shows setup of FSP on milling machine. For FSP of TIG welded plate, different combination of tool rotation speed (500, 710, 1000 and 1400 rpm) and tool travel speed (40, 56 and 80 mm/min) are used. FSP parameters used for processing of TIG weld is shown in Table 3.

2. 4. Metallurgical and Mechanical Examination Macro examination of the TIG weld and FSPed sample was performed to ensure absence of macro flaws such as tunnel, pin hole, undercut, and porosity. Microstructural examination was performed using Carl Zeiss, Jena, Model-EPY Type-2 optical microscope. Specimen for micro examination was taken across the weld in order to

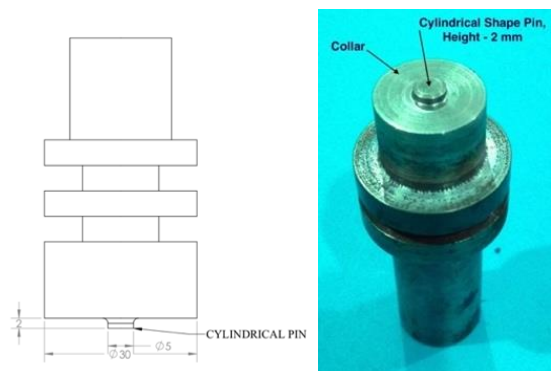
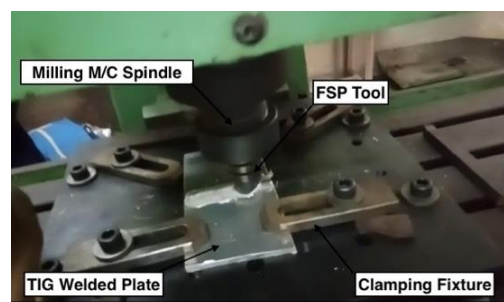
**Figure 2.** FSP Tool Having Cylindrical Pin Profile**Figure 3.** FSP setup on milling machine

TABLE 3. FSP Parameters and Tensile strength of autogenous TIG + FSP plate

Sample ID	Tool Rotation (RPM)	Feed Rate (mm/min)	Tensile Strength (MPa)	% Elongation	Remark
B1	-	-	298.3	22	Unaffected Base Metal
T2	-	-	278.5	20	Autogenous TIG Weld
TF13	500	40	286.1	22	-
TF14	500	56	279.7	22	-
TF15	500	80	-	-	Tunnel defect
TF3	710	40	273.1	20	-
TF2	710	56	173.3	8	Tunnel defect
TF8	710	80	268.7	16	Tunnel defect
TF6	1000	40	207.6	12	-
TF9	1000	56	195.1	10	-
TF7	1000	80	154.6	6	Tunnel defect
TF10	1400	40	196	10	-
TF11	1400	56	177.7	10	Tunnel defect
TF12	1400	80	-	-	Tunnel defect

observe base metal, heat affected zone (HAZ), thermo mechanically affected zone (TMAZ), stir zone (SZ), and weld metal microstructure. Etchant used for macro and micro examinations was Keller's reagent composed of 192ml distilled water, 5ml nitric acid, 3ml hydrochloric acid, 2ml hydrofluoric acid. Grain size (diameter) was digitally measured using ImageJ software.

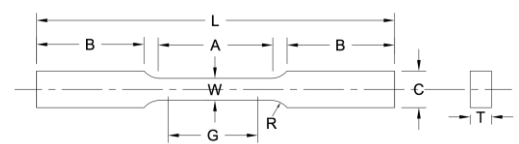
Tensile test samples were collected from welded plate as well as unaffected base metal. Dimensions of the samples were kept as per ASTM B557. Dimensions of a sub-size flat tensile specimen is illustrated in Figure 4. Tensile test samples were sectioned across the weld axis. Tensile test was performed on a computerised tensometer, having 2T loading capacity. Test was performed at the speed of 10 mm/min. Change in hardness due to autogenous TIG welding and FSP was evaluated.

Microhardness was measured across the weld in FSPed and autogenous TIG weld region using a diamond indenter. Load applied during the test was 200gm for 20 second dwell time. The indentations were evaluated microscopically at the 100X magnification. Microhardness values were plotted against distance from weld center for all test specimens. Fracture surface of tensile test specimens were examined using Hitachi Made, Model - S-3400N scanning electron microscope at 1000X magnification. Fractured surface topography of tensile test specimens of autogenous TIG and FSPed specimens were thoroughly examined to understand the nature of failure.

3. RESULT AND DISCUSSION

3. 1. Macro and Micro Examination Photographs

shown in Figure 5 illustrates the as-welded appearance of autogenous TIG weld and FSPed TIG weld samples. Autogenous TIG welded plate using welding current of 150 amp and travel speed of 120 mm/min, displayed excellent bead finish in as welded condition, which does not demand for any post processing treatment. Furthermore, the surface macro flaws such as pin holes and undercut were also not observed on the weld surface (Figure 5(a)). Surface finish of FSPed plate was also good and no sign of tunnel defect was seen in the stir zone (SZ) (Figure 5(b)). Specimen shown in Figure 5(b) was FSPed at tool rotation and feed rate of 500 rpm and 40 mm/min, respectively. Autogenous TIG welded plate which was FSPed at higher feed rate (56 mm/min and 80 mm/min) showed tunnel defect as depicted in Figure 6. At faster feed rate material flow is insufficient to fill the void created by movement of FSP tool leads to tunnel defect in the SZ [28]. Autogenous TIG weld cross-



Nomenclature	Dimension in mm
Gauge length, G	25.00 ± 0.10
Width, W	6.01 ± 0.05
Thickness, T	Thickness of material (6mm)
Radius of fillet, R	6
Overall Length, L	100
Length of reduced section, A	32
Length of grip section, B	30
Width of Grip Section, C	10

Figure 4. Tensile Test Specimen Details as per ASTM B557

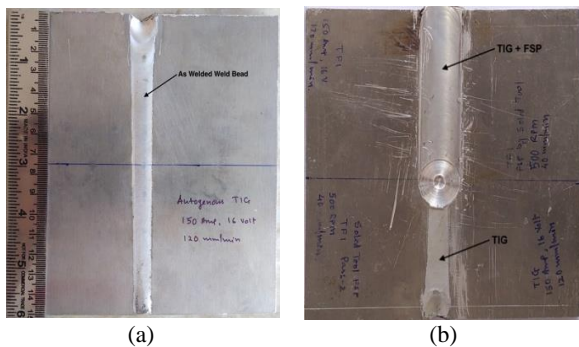


Figure 5. As welded appearance of (a) Autogenous TIG welded plate, (b) TIG + FSP plate

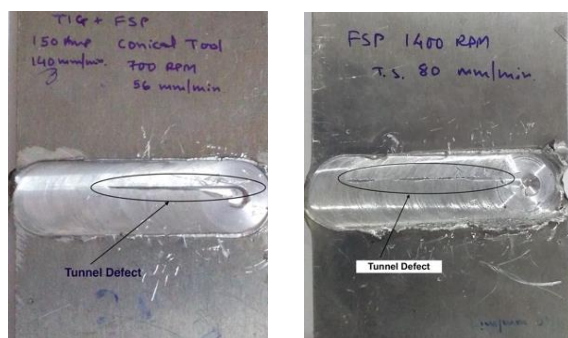


Figure 6. Tunnel Defect in FSP at Higher Travel Speed

According to the microstructural observation of autogenous TIG welded specimen, the weld and near vicinity regions are free from welding defects like void, crack and lack of fusion. However, small amount of micropores were observed in the weld region (Figure 7(b)). Elongated and distorted grains in the aluminum solid solution are observed in the microstructure of unaffected base metal mainly due to cold plate rolling (Figure 7 (d)). Weld metal microstructure reveals fine grain columnar structure (average grain size $22 \mu\text{m}$) in aluminum solid solution. This is attributed to instant heating and cooling experienced by weld metal in welding process (Figure 7b). The HAZ, on the other hand, does not exhibit columnar grain structure but shows coarse grain and recrystallized structure (average grain size $35 \mu\text{m}$) in aluminum solid solution as shown in Figure 7(c). The main reason behind grain coarsening in HAZ region is the welding heat input. Microstructural examination of FSPed specimen shows significant improvement in weld microstructure and will leads to enhanced mechanical property. Figure 8 shows microstructures of various zones of TIG + friction stir processed weld. Microstructure of stir zone depicts that coarse grained structure produced by autogenous TIG weld is well refined due to vigorous stirring effect produced by friction stir processing tool. Although temperature in the SZ is lower than the base metal's melting point but it is high enough to promote recrystallisation and produce fine grain equiaxed

structure (average grain size $4.6 \mu\text{m}$) in the SZ of FSPed region. Micro-pores present in autogenous TIG weld structure disappears from the stir zone of FSPed weldment due to stirring effect produced by FSP tool, which results in better mechanical property (Figure 8(b)). Microstructure of TMAZ reveals coarse grain dendritic structure (average grain size $30 \mu\text{m}$) as shown in Figure 8(c). Microstructure of unprocessed TIG weld + FSP specimen shows coarser grain structure compared to autogenous TIG weld specimen without FSP as shown in Figure 8(d) (average grain size $57 \mu\text{m}$). Heat input from the friction stir processing method is the reason behind grain coarsening.

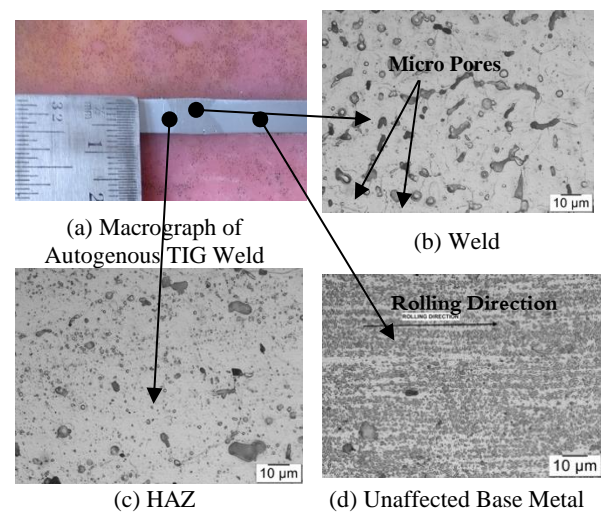


Figure 7. Macrograph and Microstructure of Autogenous TIG Weld at Different Locations: (a) Macrograph of Autogenous TIG Weld; (b) Weld (c) HAZ; (d) Base Metal, Magnification 500x

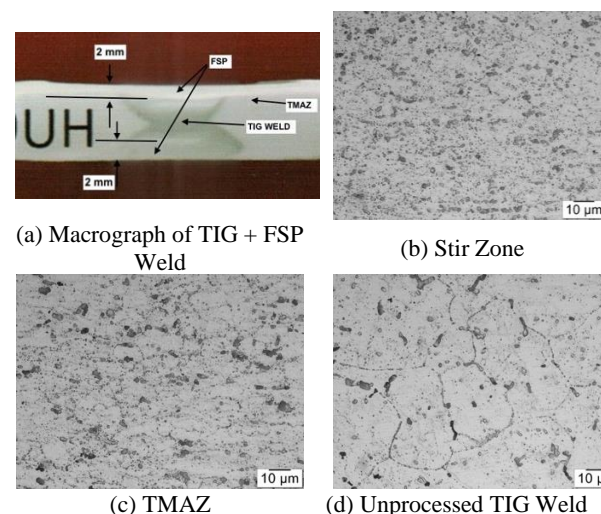


Figure 8. Macrograph and Microstructure of Autogenous TIG + FSP Weld at Different Locations: (a) Macrograph of TIG + FSP Weld; (b) Stir Zone; (c) TMAZ; (d) Unprocessed TIG Weld, Magnification 500x

3. 2. Tensile Test

Tensile strength and % elongation values of FSPed weld specimens are compiled in Table 3. Ultimate tensile strength values of unaffected parent metal and unprocessed autogenous TIG weld were also derived for comparison by performing tensile test. Figure 9 shows comparison of stress vs strain curve of parent metal, autogenous TIG welded plate (Sample T2, corresponding to maximum tensile strength among all autogenous TIG welded plates) and autogenous TIG + FSP plate (Sample TF13). Ultimate tensile strength of base metal (Sample B1), autogenous TIG (Sample T2) weld and TIG + FSP weld (Sample ID TF13) were found to be 298.3 MPa, 286.1 MPa and 278.5 MPa, respectively. It was observed that UTS of all the processed and unprocessed welded specimens were lower than UTS of unaffected base metal. This is because of the adverse effect of welding heat input on microstructure of Al-5083 alloy [26]. In addition to that, Al-5083 is a work hardened alloy possessing an unequiaxed grain structure in which grains are elongated in line with the direction of rolling as shown in Figure 7(d). During performing autogenous TIG welding process, due to welding heat input, effect of work hardening is destroyed, that leads to weakening of mechanical properties. During subsequent application of FSP on TIG weld recrystallisation reformed the microstructure resulting in improved mechanical properties [27]. Specimens processed at 80 mm/min feed rate (TF15, TF12) show full length tunnel defect hence tensile test can not be performed. Specimen processed at 500 rpm tool rotation speed and 40 mm/min feed rate (TF13) showed maximum ultimate tensile strength of 286.1 MPa and % elongation of 22% among all specimens processed at different tool rotation speed and feed rate. FSP displays marginal increase in tensile strength of around 2.7% compared to tensile strength of autogenous TIG welded specimen (278.5 MPa). This rise in the tensile strength is because of grain refinement and elimination of defects like micro porosity from the FSP region. However, all the welded specimens (autogenous TIG weld and autogenous TIG + FSP) display lower

tensile strength as compared to parent metal. This is primarily due to reduction in strain hardening effect due to heat input given to the base metal during fusion welding and FSP [29].

3. 3. Microhardness Measurement

Trend of microhardness variation across the weld for autogenous TIG and autogenous TIG followed by FSP samples are depicted in Figure 10. The weld zone of an autogenous

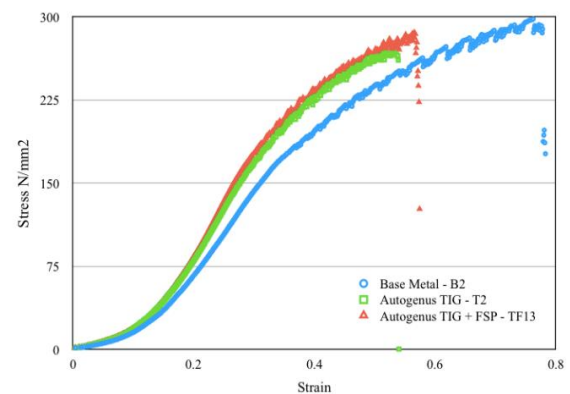


Figure 9. Tensile test curves for base metal, autogenous TIG (T2), and autogenous TIG+FSP (TF13)

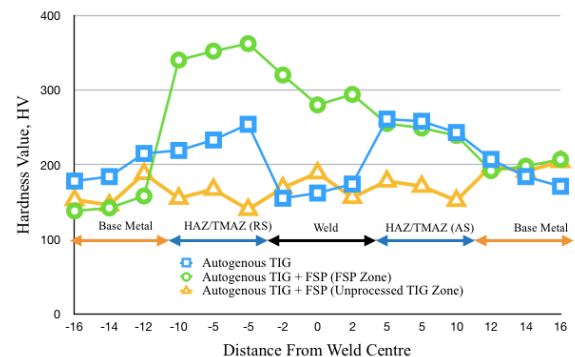
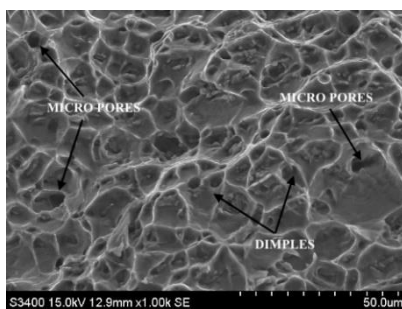
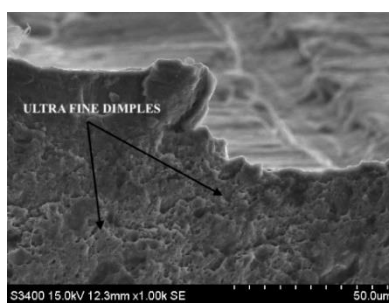


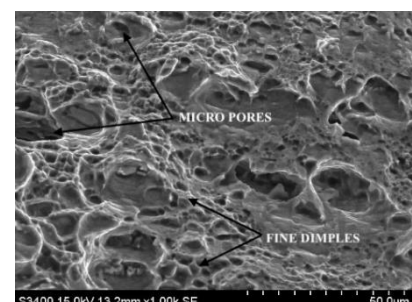
Figure 10. Microhardness profile across the weld



(a) Autogenous TIG Weld



(b) Autogenous TIG + FSP – Stir Zone



(c) Autogenous TIG + FSP – TIG Weld Center

Figure 11. SEM fractograph of: (a) Autogenous TIG Weld; (b) Autogenous TIG + FSP - SZ, (c) Autogenous TIG + FSP – TIG Weld Center; Magnification 1000x

TIG welded specimen has a lower microhardness value than the base metal and HAZ/TMAZ. This could be due to re-precipitation of the β -phase Mg_2Al_3 during welding [30]. Because Al-5083 is a non-heat treatable alloy, lowering of hardness value as a result of welding heat input is not expected as plastic deformation is the primary hardening mechanism in this alloy [20]. Notable rise in hardness is reported in the SZ of FSP compared to autogenous TIG weld hardness. FSP causes excessive plastic deformation and promotes well refined grain structure in the SZ. Also, Compressive stresses produced in the SZ during FSP minimizes the presence of micro-pores in the SZ leading to the increase in hardness in the SZ of FSP [15]. Microhardness of unprocessed TIG weld of FSPed specimen is almost unchanged in weld zone whereas HAZ microhardness is reduced due to added heat input during FSP [31]. Decrease in TMAZ hardness value away from the weld center towards advancing side is observed for TIG+FSP specimen. In FSP, the advancing side is the point at which a solid material begins to transform into a semi-solid phase and swirls about a tool pin which is inserted into the material. In the retreating side, the semi-solid phase retreated and cooled. As a result, during the FSW process, the advancing side, which has a more solid state nature at any point in time/location than the retreating side, should generate more frictional stresses, which generates more heat and elevates the peak temperature. This is attributed to the lower hardness value in the advancing side of FSP [11, 32].

3. 4 SEM Fractoscopy Scanning Electron Microscopy (SEM) was performed on the broken surface of tensile test samples of autogenous TIG and autogenous TIG + FSP weldment to analyse the nature of failure. The fractographs shown in Figure 11 reveals network of dimples in both specimens which indicates ductile failure. However, dimples observed in autogenous TIG + FSP weldment are much finer than that observed in autogenous TIG weld specimen. This is again due to the fact that FSP produces better refined structure compared to as welded autogenous TIG weld. Traces of micro porosities are also observed in SEM fractograph of autogenous TIG weld as shown in Figure 11(a). SEM fractograph of unprocessed TIG weld region of FSPed specimen shown in Figure 11(c) confirms the presence of micro-porosities and voids in the matrix of finer dimples compared to autogenous TIG weld specimen without FSP.

4. CONCLUSION

Friction Stir Processing (FSP) was performed on autogenous TIG weld surface to achieve structural modification and thus improving mechanical property of

the weld joint. Conclusions derived from the present experimental work are as follows:

Full fusion butt weld joint of 6mm thickness is achieved through autogenous TIG welding process. Weld joint produced by autogenous TIG welding process exhibit lower tensile strength compared to base metal by 6.5%. The existence of micro-porosities in the TIG weld metal contributes to the decrease in weld joint's tensile strength.

Marginally increase (2.7%) in the tensile strength of autogenous TIG weld joint is observed after performing FSP on it. The grain refinement achieved by the FSP process is the reason behind improved tensile strength. Microhardness of autogenous TIG weld metal and HAZ region is substantially increased due to friction stir processing method. Percentage elongation value indicate that weld joint possesses good ductility in both autogenous TIG weld (20% elongation) and friction stir processed TIG weld (22% elongation). The SEM images of fractured surface of all tensile test specimens show series of dimple structure having different degree of fineness. Out of which, the FSPed specimen shows the most fine dimple structure.

Weldment which are friction stir processed at higher feed rates (56 mm/min and 80 mm/min) produces tunnel defect in the SZ due to insufficient heat input resulting in limited metal flow in the SZ.

Macroscopic and microstructural examination confirms that FSP can be used as weld joint surface modification technique. Churning and reheating of weld metal in the SZ during FSP causes grain refinement and recrystallisation leads to notable improvement in the weldment's surface characteristics.

5. REFERENCES

1. Miller, W. S., Zhuang, L., Bottema, J., Wittebrood, A., De Smet, P., Haszler, A. and Vieregge, A., "Recent development in aluminium alloys for the automotive industry", *Materials Science and Engineering: A*, Vol. 280, No. 1, (2000), 37-49, doi: 10.1016/S0921-5093(99)00653-X.
2. Mabuwa, S. and Msomi, V., "Effect of Friction Stir Processing on Gas Tungsten Arc-Welded and Friction Stir-Welded 5083-H111 Aluminium Alloy Joints", *Advances in Materials Science and Engineering*, Vol. 2019, (2019), 1-14, doi: 10.1155/2019/3510236.
3. Doshi, S., Gohil, A., Mehta, N. And Vaghasiya, S. "Challenges in Fusion Welding of Al alloy for Body in White", *Materials Today: Proceedings*, Vol. 5, No. 2, Part 1, (2018), 6370-6375, doi: 10.1016/j.matpr.2017.12.247.
4. Ardika, R.D., Triyono, T. and Muhayat, N., "A review porosity in aluminum welding", *Procedia Structural Integrity*, Vol. 33, (2021), 171-180, doi.org/10.1016/j.prostr.2021.10.021.
5. Mathers, G., "The welding of aluminium and its alloys", 1st ed. Woodhead Publishing Limited, 2002.
6. Wang, X., Wang, K., Shen, Y. and Hu, K. "Comparison of fatigue property between friction stir and TIG welds", *Journal of*

- University of Science and Technology Beijing, Mineral, Metallurgy, Material*, Vol. 15, No. 3, (2008), 280-284, doi: 10.1016/S1005-8850(08)60053-5
7. Thomas, W. M., and R. E. Dolby. "Friction stir welding developments", Proceedings of the sixth international trends in welding research, (2003), 203-211.
 8. Mishra, R. S., and Ma, Z. Y., "Friction stir welding and processing", *Materials Science and Engineering: R: Reports*, Vol. 50, No. 1, (2005), 1-78, doi: 10.1016/j.mser.2005.07.001.
 9. Fabregas Villegas, J., Martínez Guarín, A. and Unfried-Silgado, J., "A Coupled Rigid-viscoplastic Numerical Modeling for Evaluating Effects of Shoulder Geometry on Friction Stir-welded Aluminum Alloys", *International Journal of Engineering Transactions B: Applications*, Vol. 32, No. 2, (2019), 313-321, doi: 10.5829/ije.2019.32.02b.17
 10. Singh, R., Rizvi, S. A. and Tewari, S. P., "Effect of Friction Stir Welding on the Tensile Properties of AA6063 under Different Conditions", *International Journal of Engineering Transactions A: Basics*, Vol. 30, No. 4, (2017), 597-603, doi: 10.5829/idosi.ije.2017.30.04a.19.
 11. R. S. Mishra, Z. Y. Ma, and I. Charit, "Friction stir processing: a novel technique for fabrication of surface composite", *Materials Science and Engineering: A*, Vol. 341, No. 1, (2003), 307-310, doi: 10.1016/S0921-5093(02)00199-5.
 12. Su, J. Q., Nelson, T. W., and Sterling, C. J., "Microstructure evolution during FSW/FSP of high strength aluminum alloys", *Materials Science and Engineering: A*, Vol. 405, No. 1, (2005), 277-286, doi: 10.1016/j.msea.2005.06.009.
 13. Rao, D. S. and Ramanaiah, N., "Evaluation of Wear and Corrosion Properties of AA6061/TiB₂ Composites Produced by FSP Technique", *Journal of Minerals and Materials Characterization and Engineering*, Vol. 5, No. 6, (2017), 353-361, doi:10.4236/jmmce.2017.56029.
 14. Wang, W., Shi, Q.Y., Liu, P., Li, H.K. and Li, T., "A novel way to produce bulk SiCp reinforced aluminum metal matrix composites by friction stir processing", *Journal of Materials Processing Technology*, Vol. 209, No. 4, (2009), 2099-2103, doi: 10.1016/j.jmatprotec.2008.05.001.
 15. Kaushik, N. and Singhal, S., "Experimental Investigations on Microstructural and Mechanical Behavior of Friction Stir Welded Aluminum Matrix Composite", *International Journal of Engineering Transactions A: Basics*, Vol. 32, No. 1, (2019), 162-170, doi: 10.5829/ije.2019.32.01a.21
 16. Akinlabi, E.T., Mahamood, R.M., Akinlabi, S.A. and Ogunmuyiwa, E., "Processing parameters influence on wear resistance behaviour of friction stir processed Al-TiC composites", *Advances in Materials Science and Engineering*, Vol. 2014, (2014), 1-12, doi: 10.1155/2014/724590
 17. Bauri, R., Yadav, D. and Suhas, G., "Effect of friction stir processing (FSP) on microstructure and properties of Al-TiC in situ composite", *Materials Science and Engineering: A*, Vol. 528, No. 13, (2011), 4732-4739, doi: 10.1016/j.msea.2011.02.085.
 18. Sharma, V., Gupta, Y., Kumar, B.M. and Prakash, U., "Friction Stir Processing Strategies for Uniform Distribution of Reinforcement in a Surface Composite", *Materials and Manufacturing Processes*, Vol. 31, No. 10, (2016), 1384-1392, doi: 10.1080/10426914.2015.1103869.
 19. Costa, J.D.M., Jesus, J.S., Loureiro, A., Ferreira, J.A.M. and Borrego, L.P., "Fatigue life improvement of mig welded aluminium T-joints by friction stir processing", *International Journal of Fatigue*, Vol. 61, (2014), 244-254, doi: 10.1016/j.ijfatigue.2013.11.004.
 20. Borrego, L.P., Costa, J.D., Jesus, J.S., Loureiro, A.R. and Ferreira, J.M., "Fatigue life improvement by friction stir processing of 5083 aluminium alloy MIG butt welds", *Theoretical and Applied Fracture Mechanics*, Vol. 70, (2014) 68-74, doi: 10.1016/j.tafmec.2014.02.002.
 21. Xu, N. and Bao, Y., "Enhanced mechanical properties of tungsten inert gas welded AZ31 magnesium alloy joint using two-pass friction stir processing with rapid cooling", *Materials Science and Engineering: A*, Vol. 655, (2016), 292-299, doi: 10.1016/j.msea.2016.01.009.
 22. S. Mabuwa and V. Msomi, "Friction Stir Processing Of TIG And Friction Stir Welded Dissimilar Alloy Joints: A Review", (2019), doi: 10.20944/preprints201910.0226.v1.
 23. Abbasi, M., Givi, M. and Bagheri, B., "New method to enhance the mechanical characteristics of Al-5052 alloy weldment produced by tungsten inert gas", *Proceedings of the Institution of Mechanical Engineers, Part B: Journal of Engineering Manufacture*, (2020), doi: 10.1177/0954405420929777.
 24. Mehdi, H. and Mishra, R.S., "Effect of friction stir processing on mechanical properties and heat transfer of TIG welded joint of AA6061 and AA7075", *Defence Technology*, Vol. 17, No. 3, (2020), 715-727, doi:10.1016/j.dt.2020.04.014.
 25. Tandel, K.D. and Menghani, J.V., "Autogenous TIG Welding of Al-5083-H111 Butt Joint", *In Advances in Manufacturing Processes*, (2021), 205-219, doi: 10.1007/978-981-15-9117-4_16.
 26. Rezaei, G. and Arab, N. B. M. "Investigation on Tensile Strength of Friction Stir Welded Joints in PP/EPDM/Clay Nanocomposites", *International Journal of Engineering Transactions C: Aspects*, Vol. 28, (2015), 1382-1391, doi: 10.5829/idosi.ije.2015.28.09c.17.
 27. Zhao, H., Pan, Q., Qin, Q., Wu, Y. and Su, X., "Effect of the processing parameters of friction stir processing on the microstructure and mechanical properties of 6063 aluminum alloy", *Materials Science and Engineering: A*, Vol. 751, (2019), 70-79, doi: 10.1016/j.msea.2019.02.064.
 28. Hasanazadeh R. and Azdast, T., "Welding Properties of Polymeric Nanocomposite Parts Containing Alumina Nanoparticles in Friction Stir Welding Process", *International Journal of Engineering Transactions A: Basics*, Vol. 30, (2017), 143-151, doi: 10.5829/idosi.ije.2017.30.01a.18.
 29. Fuller, C.B. and Mahoney, M.W., "The effect of friction stir processing on 5083-H321/5356 Al arc welds: Microstructural and mechanical analysis", *Metallurgical and Materials Transactions A*, Vol. 37, No. 12, (2006), 3605-3615, doi:10.1007/s11661-006-1055-1.
 30. Jiang, Z., Hua, X., Huang, L., Wu, D. and Li, F., "Effect of multiple thermal cycles on metallurgical and mechanical properties during multi-pass gas metal arc welding of Al 5083 alloy", *The International Journal of Advanced Manufacturing Technology*, Vol. 93, No. 9-12, (2017), 3799-3811, doi: 10.1007/s00170-017-0771-6.
 31. Chaurasia, P.K., Pandey, C., Giri, A., Saini, N. and Mahapatra, M.M., "A comparative study of residual stress and mechanical properties for FSW and TIG weld on structural steel", *Archives of Metallurgy and Materials*, Vol. 63, (2017), 1019-1029, doi: 10.24425/122437.
 32. Węglowski, M.S., "Friction stir processing -- State of the art", *Archives of civil and Mechanical Engineering*, Vol. 18, No. 1, (2018), 114-129, doi: 10.1016/j.acme.2017.06.002.

Persian Abstract

چکیده

جوشکاری با گاز خنثی تنگستن (TIG) ترجیح داده شده ترین فرآیند اتصال برای آلیاژهای آلومینیوم است، اما به دلیل محدودیت های ذاتی فرآیند، اتصال جوشی را تولید می کند که دارای خواص مکانیکی پایین تری در مقایسه با فلز پایه است. برای بهبود خواص مکانیکی، جوش توسط پردازش اغتشاشی اصطکاکی (FSP) تا عمق ۲ میلی متر پس از پردازش می شود. این مقاله تاثیر اجرای FSP را بر روی اتصال لب به لب جوش داده شده خودبخود TIG صفحه Al-5083 با ضخامت ۶ میلی متر ارائه می دهد. خواص مکانیکی و متالورژیکی جوش TIG خودزای فرآوری شده و فرآوری نشده مقایسه شده است. تکنیک های مشخصه ای که برای ارزیابی اتصال جوش اتخاذ شده اند عبارتند از: تست کششی، اندازه گیری ریزسختی، بررسی های ریزساختاری و آنالیز SEM. استحکام کششی اتصال جوش TIG 6.5 درصد نسبت به فلز پایه به دلیل وجود تخلخل های ریز در فلز جوش کاهش می یابد. پردازش اغتشاشی اصطکاکی ساختار تصفیه شده دانه ریز را تولید می کند، استحکام کششی اتصال جوش TIG خودزا را تا ۲.۷ درصد بهبود می بخشد. ریزسختی فلز جوش TIG خودزا از ۱۶۳.۶ HV به ۲۹۸ HV پس از انجام FSP افزایش می یابد. با این حال، تصاویر SEM از سطح شکسته نمونه پردازش شده با اغتشاش اصطکاکی، ساختار فرورفتگی ظریفی را نشان می دهد که نشان می دهد شکل پذیری اتصال جوش پس از انجام FSP روی اتصال جوش TIG خودزا، بی تأثیر باقی می ماند.



Mechanical and Dynamical Properties of Structural Rubcrete Mixes

O. M. Makki*, H. M. K. Al-Mutairee

Department of Civil Engineering, College of Engineering, University of Babylon, Babylon, Iraq

PAPER INFO

Paper history:

Received 25 May 2022

Received in revised form 10 June 2022

Accepted 12 June 2022

Keywords:

Rubberized Concrete

Sustainable Concrete

Rubcrete

Green Concrete

Structural Rubcrete

ABSTRACT

In most civil constructions, concrete members need to gain some ductility to resist the dynamic loads which it suffered. For sustainability and economical reasons, scrapped tires rubbers are the most cheap material able to achieve this goal. The bad manner in such replacement is that, the high replacing percentages cause a large drop in concrete mechanical properties till becomes unstructural. This paper offers six structural rubcrete mixes and discuss its properties after replacement. Slump, density, water absorption, compressive strength for cubes and cylinders, impact resistance, flexural strength, splitting, ultrasonic and stress versus strain curves were tested and discussed. It can be concluded that, the sustainable rubcrete mixes still structural in spite of the dropping in strength due to the replacing process. Concrete tensile, compressive and flexural strength minimized for every incrementing in rubber amounts due to the loss of bond between mortar and the rubbers.

doi: 10.5829/ije.2022.35.09C.10

NOMENCLATURE

RF	Reference conventional concrete	G30	30 % gravel – chip replacing percent
S10	10% sand – crumb replacement	Sp.I	Specimen one
S20	20% sand – crumb replacement	Sp.II	Specimen two
S30	30% sand – crumb replacement	Sp.III	Specimen three
G10	10 % gravel – chip replacing percent	MOR	Modulus of rupture
G20	20 % gravel – chip replacing percent		

1. INTRODUCTION

Constructions in usual highly exposed to dynamic loads in addition to monotonic loads. It is well known that, concrete is a brittle material that cannot resist dynamic loads. Enhancing dynamic properties of concrete investigated by researchers using different ways like adding steel fibers or rubbers or even both [1-4]. Since rubber is not a biodegradable material and for its low cost against the high cost of steel fiber and for sustainability, it can be used as a percentage replacement from mix aggregate. The total recovery of scraped tires in civil engineering works reached to 89, 94, 91 and 90% in each of the United States, Europe, Japan and Mexico, respectively [5]. Entering scraped tire rubber into constructions helps the nature to get rid of it as a waste material and avoid the pollution which results in if the factories fired it. Rubber has to be replaced as a

volumetric percentage of sand or gravel or even both, some replaced it from aggregate weight or even as an additives. It is important to expect that, the replacement will deteriorate the mechanical properties of concrete if it is done by a big amounts [3, 6-14]. Weakened bond between cement past and rubber particles is the most effective reason for that deterioration in addition to the low unit weight of the mix after replacement [15-20]. The big difference in elastic modulus between the two replaced materials is also a cause [9].

The energy absorption was proved to be enhanced for 5, 10, 15 and 20 % sand replacement by 138, 185, 300, and 396 % while incrementing equals 150, 204, 326 and 426% for the same percentages of gravel replacing [14]. The dynamic modulus of elasticity found to be minimized after replacement [21, 22]. The damping ratio enhanced by 230% of 15% coarse weight replacement [21]. This paper investigated the effect of three replacing

*Corresponding Author Institutional Email:
sth.ola.ali@student.uobabylon.edu.iq (O. M. Makki)

percentages for fine aggregate and the same for course aggregate on the mechanical properties of concrete. Workability, unit weight, water absorption, cubes compressive strength, cylinder compressive strength, stress strain curve, tensile strength, flexural strength, ultra-sonic, and impact load of concrete were investigated.

2. MATERIALS, MIXES AND SPECIMENS

Normal Portland cement was used, along with natural quartzite sand of specific gravity equals 2.65 and 2.6 for gravel. As a full graded replacement was made for both fine and course aggregates for 14 mm maximum gravel-chip size which are matched with the ASTM C33-78, so as for sand crumb replacement. Physical and chemical properties of sand, gravel and rubber are summarized in Tables 1-3.

Seven mixes were casted to investigate the effect of rubber-aggregate replacing. The first group consist of three mixes of sand- Crumb rubber replacement as 10, 20 and 30% replacement. The second group is of gravel versus chips replacing for the same pervious percentages. While the seventh mix was a normal concrete to be used as a reference. All mixes were prepared with (1:1.4:2) percentages and of w/c ratio equals 0.365. Supperplasticsizer Gelimum G54 also utilized. Figures 1 and 2 show the mixing processes, curing, and specimens before tests. A rotating mixer of 250 kg total capacity was utilized. Specimens was cured by sinking into water for 28 days. Mixes percentages per one cubic meter were listed in Table 4. The following section investigated the properties of the seven mixes.

TABLE 1. Chemical and physical properties of rubber

Composition	Value
Chip density	650 kg/m ³
Crumb density	720 kg/m ³
Carbon black	20%
steel	4 %
Water absorption	0.01
Specific gravity	1.09

TABLE 2. Chemical and physical properties of fine aggregate

Properties Test results Limits of	Magnitude
Sulfate content (SO ₃)	0.01 %
Specific gravity	2.65
Fineness modulus	3.19
absorption	0.1

TABLE 3. Chemical and physical properties of course aggregates

Properties	Magnitude
Sulfate content (SO ₃)	0.08 %
Specific gravity	2.6
absorption	0.15

TABLE 4. Mixes weights (kg/m³)

Mix	Cement	Sand	Gravel	Rubber	Water	G54
RF	475	760	1119	0	124	2.33
S10	475	684	1119	34	124	2.33
S20	475	608	1119	68	124	2.33
S30	475	532	1119	103	124	2.33
G10	475	760	1008	44	124	2.33
G20	475	760	896	88	124	2.33
G30	475	760	784	132	124	2.33



Figure 1. Casting and curing process



Figure 2. Specimens before test

3. PROPERTIES RESULTS AND DISCUSSIONS

The average of three specimens' values at 28 day of curing was investigated for each single mix of the following.

3.1. Workability The workability of concrete mixes were investigated using slump test in accordance to ASTM 143M-12 [23]. It can be concluded from Figures 3 and 4, which are shown in the results of slump test that, the replacement working on decreasing concrete workability in amounts depend on replacement percentages. It can be also noting that, the mix has an excellent workability for civil engineering works. The unrounded rubber particles (in comparing with the aggregate) will bound the water particles into their irregular shapes, that what causes the low slumps for rubcrete. From Figure 4 it can be concluded that and in accordance to UNI EN 12350-2 [24] the form of all rubcrete mixes was true slump.

3.2. Unit Weight The unit weight of rubcrete is lower than concrete due to replacing the heavier aggregate by the lighter rubber, and that what proved in Table 5. The results based on the mean of three samples for each single mix. The unit weight of rubcrete decreases for each incrementing in rubber percentages for either sand or gravel replacement. Sand replacement specimens lighter than the gravel for the same replacing percents. It is due to that, the crumb is denser than chip for the same cubic meter as explain in Table 5. But, for such replacements, it impossible to consider rubcrete as a light weight material.

3.3. Water Absorption It is the ability of material to absorb water. It can be stated that, replacement increases water absorption of concrete mixes since rubber is a hydrophobic material. All obtained results are summarized in Table 6. and such results were confirmed with the reported data in literature [18, 25, 26].

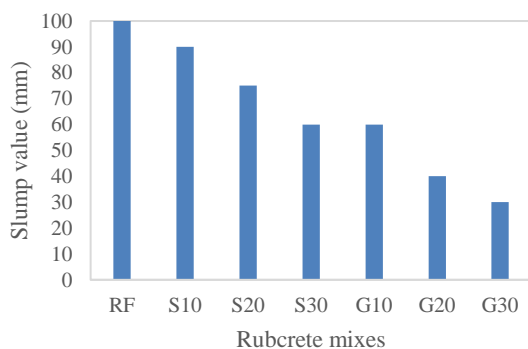


Figure 3. Slump test values



Figure 4. Workability test

TABLE 5. Rubcrete unit weight (All weight in kg)

Mix	SP.I	Sp.II	SP.III	mean	Redaction %
RF	8.03	8.025	8.034	8.03	
S10	7.67	7.665	7.625	7.653	4.69
S20	7.445	7.393	7.375	7.403	7.8
S30	7.09	7.065	7.16	7.105	11.5
G10	7.905	7.87	7.85	7.875	1.93
G20	7.705	7.705	7.66	7.69	4.23
G30	7.325	7.31	7.345	7.327	8.76

TABLE 6. Water absorption details

Mix	Water absorption (%)	Increment (%)
RF	0.024	
S10	0.027	11.41
S20	0.037	53.45
S30	0.041	69.44
G10	0.027	12.96
G20	0.030	24.25
G30	0.03	37.85

3. 4. Compressive Strength The average of three cubes in accordance to BS 1881 -116 [27] to get the British compressive strength F_{cu} . Furthermore, the average of three cylinders of 150*300 mm² (diameter * height) was also tested to get the American compressive strength f'_c . The converting factor from British to American compressive strength was also checked out for rubcrete. Table 7 shows the results of the three cubes specimens, the means of them, the difference in accordance to reference mix and the converting factor from cylinder to cube. It can be noting that, compressive strength drops for each incrementing in rubber percents but still structural for this suggested rubcrete mix. Also, since the replacement was from the volume of aggregates, the weight of rubber in cubic meter is more than the gravel, that which made the gravel replacement specimens stronger than the sand replacing. The failure of the RF mix was as a fully sudden explosion due to its strength in contrast to other rubcrete mixes.

Relenting on the results, the converting factor from cubes to cylinders was found to be ranged from 0.8 to 0.83 which is matched with the normal converting factor.

To discuss the converting factor from 100*200 mm cylinder into a 150*300 mm specimen, an average of 3 specimens were tested and compared with the bigger cylinders results. All details are listed in Table 8. It can be concluded that, the reconverting factor from bigger to smaller cylinder is ranged from 0.08 to 0.88 for rubcrete mixes.

TABLE 7. Cubes compressive strength

Mix	SP.I (MPa)	SP.II (MPa)	SP.III (MPa)	Mean (MPa)	Redaction (%)	Convert to f'c
RF	52.92	53.28	52.9	53.06		0.814139
S10	34.27	34.34	34.42	34.35	35.27	0.8297
S20	26.49	25.05	26.34	25.97	51.06	0.808692
S30	22.74	22.64	22.8	22.74	57.14	0.835396
G10	37.93	37.67	38.16	37.92	28.53	0.804221
G20	34.39	34.2	34.23	34.3	35.36	0.810464
G30	27.54	27.4	27.41	27.48	48.22	0.800703

TABLE 8. Small cylinders compressive strength

Mix	SP.I (MPa)	SP.II (MPa)	SP.III (MPa)	Aver. (MPa)	Redaction (%)	Convert factor
RF	34.47	34.73	35.08	34.76	----	0.80
S10	23.1	22.6	22.96	22.88	34.1	0.803
S20	18.04	18.27	18.57	18.29	47.3	0.871
S30	15.48	15.39	16.26	15.7	54.8	0.82
G10	25.59	26.14	26.52	26.08	24.9	0.85
G20	24.27	24.56	24.79	24.53	29.40	0.88
G30	18.17	18.71	19.17	18.6	46.24	0.84

3. 5. Stress Strain Curve

Stress versus strain curves are one of the best behavior viewers to the concrete mixes. It shows the linear, and nonlinear stages under loading conditions. It was tested through evaluating the average of three cylinders of 100*200 mm (diameter * height) for all seven mixes. From Figure 5, one may conclude that, rubcrete mixes have a strain values much more than the conventional concrete mixes due to its elasticity under loading with lower compressive strengths. The intensity of this behavior becomes more visible at high replacement rates. The brittle exploded failure of the reference mix was less gradually after every incrementing in rubber percentages and becomes as a ductile failure. All cylinders failed within the standard expected failure types listed in ASTM VC39/C39M- 15a [28] specification for type 3 (i.e. columnar vertical cracks from both ends) as shown in Figure 6 which illustrated the failure mode of three different mixes.

3. 6. Tensile Strength

Three samples of 100*200 mm cylinders were tested to investigate the splitting tensile strength of the seven mixes in accordance to the ASTM C496 specifications [29]. Table 9 listed the tensile strengths at 28 day age in which deduced that, the tensile strength of rubcrete decreases for every rising in replacement amount due to loss of bonding, less density

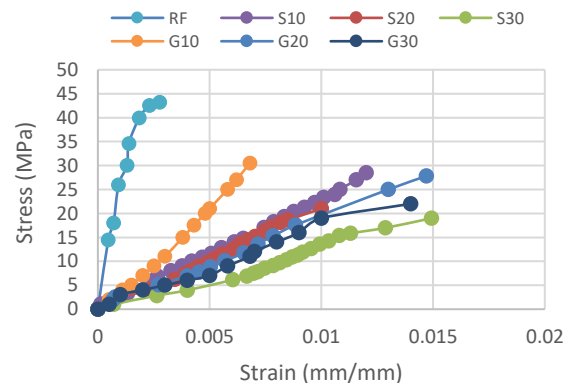


Figure 5. Stress vs strain curves for all mixes



Figure 6. Failure mode of cylinders

of rubcrete or due to the micro cracks of mortar which will multiple due to the difference between the rubber elastic modulus and the mortar. Specimens after failure can be seen at Figure 7.

3. 7. Rupture Strength

A prisms of (100*100*300 mm) dimensions were casted for the seven mixes to test the modulus of rupture at 28 days in accordance to the ASTM C133-97 [30]. The tested specimens results' were clarified at Figure 8, and accordingly the rupture strength of rubcrete reduced due to the reduction in bending strength. It possible to conclude that, a dropping in MOR noted since the flexural strength effected in the first design on

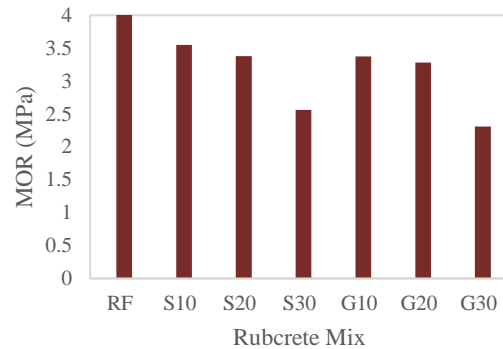


Figure 8. Flextural strength

TABLE 9. Tensile splitting test details

Mix	SP.I (kN)	SP.II (kN)	SP.III (kN)	Ft (MPa)	Redaction (%)
RF	344.8	245	341.12	4.941	
S10	220.86	297.14	224.78	3.942	20.210
S20	200.24	203.68	200.88	3.210	35.032
S30	163.78	164.52	162.74	2.606	47.252
G10	262.3	257.6	260.94	4.144	16.121
G20	209.7	208.6	211.6	3.343	32.335
G30	182.55	183.94	185.08	2.927	40.75

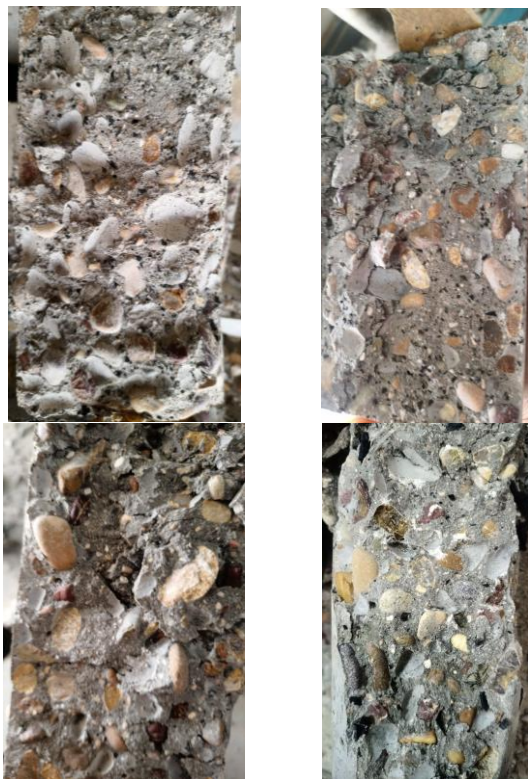


Figure 7. Failure splitting

compressive strength. Results also showed that, the flexural strengths of sand replacement are slightly higher than the gravel replacement, which is due to the sand provides higher ductility than gravel. Rupture test for rubcrete also investigated widely by Mohammed and Breesem [31]. Failure shape of all specimens was similar so one specimen was considered as shown the failure (Figure 9).

3. 8. Ultrasonic Test

It is used for investigating the velocity of passing sound waves through concrete mixes to show its deterioration against loads and its cracks. It can also view how the sound wave effected by aggregates-scraped rubbers replacements. A non-destructive test was made for disk specimens (65*152 mm (diameter * length)) for the seven concrete mixes. The specimens' centers were identified in order to achieve the extremely direct wave path passing through them (Figure 10). From the obtained results which are summarized in Table 10; it can be noting that, the replacements slowed down the sound wave which crossed within due to the high energy absorb of rubber. Gravel replacement showed more slowly velocity when compared with the same percent of replacement of sand due to the larger rubber particles.

3. 9. Impact Test

In accordance to Tonon [32] and ASTM D5607, the impact resistance of concrete may be gotten by casting a cylindrical specimens of 65*152 mm (diameter * length) and applying a drop weight simulated of 4.54 kg. Number of hits which caused the first crack were recorded besides the total number of hits to final failure. The impact test showed that, replacing causes to higher impact resistance for rubcrete mixes comparing with concrete as detailed in Table 11. Gravel replacement mixes shows more impact resistance when comparing with sand replacement. The reason was visible and sensible during the test, it is due to that, the chips particles bigger than sand which will collect the cracks and prevent them to be developed during the test. Failure shapes of the mixes were listed in Figure 11.



Figure 9. Specimen G10 for example after failure



Figure 10. Ultra sonic test

TABLE 10. Sound velocities through rubcrete

Mixes	Velocity (m/s)	Decrement (%)
RF	5191	-----
S10	4928	5.066
S20	4304	17.09
S30	4224	18.63
G10	4444	14.39
G20	4201	19.07
G30	4172	19.63

TABLE 11. Impact test results

	Number of hits till 1st crack	Number of hits till failure	Energy at first crack	Energy at failure	Increment due to replacement %
RF	6	8	122.1	162.8	-----
S10	4	17	81.41	346.0	112.5
S20	7	35	142.4	712.3	337.5

S30	12	61	244.2	1241.5	662.5
G10	5	24	101.7	488.4	200
G20	8	38	162.8	773.4	375
G30	15	116	305.3	2361	1350

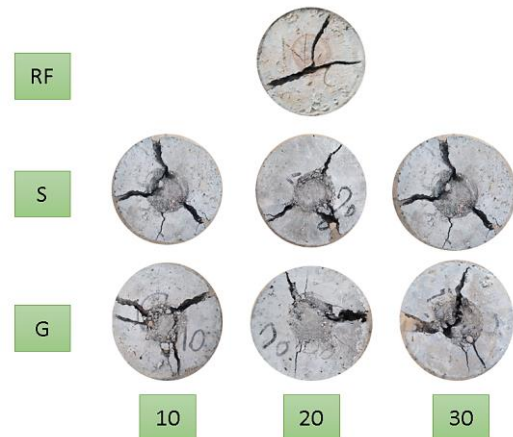


Figure 11. Specimens after failure

4. CONCLUSIONS

1. Rubcrete workability deteriorated for every increment in replacement percentage.
2. Partial rubber versus aggregate replacement means replacing heavier by lighter material which will make the rubcrete a lighter material than conventional concrete.
3. The capability of sand to absorb free water mix is more than the gravel capacity so that the water absorption of sand replacement becomes larger, especially after knowing that, the weight of crumb in the one cubic meter is larger than the chips.
4. Concrete compressive strength does not matter it was British or American compressive strength-drops after any replacement in amounts depends on the replacement type, percentages and kind.
5. Converting factors from F_{cu} to f'_c as well as converting factor from 100*200 cylinder size to 150*300 size are the same of conventional mixes for rubcrete.
6. Mixes percentages offers a sustainable structural rubcrete so suitable for the dynamic constructions.
7. Rubcrete mixes has a high straining rates due to the elastic behaviour of rubber, and that strain depends for the first degree on rubber amounts.
8. Splitting tensile effected by the concrete compressive strength so it is logically drops after any replacement especially it depends on the bond strength between mortar and gravel particles which it weaken for rubbers, so as for flexural property.

9. Involving rubber into concrete mixes deteriorate the velocity of sound wave passing through the mix because the ability of rubber to absorb energy.

5. REFERENCES

1. Liu, F., Chen, G., Li, L., and Guo, Y. "Study of impact performance of rubber reinforced concrete." *Construction and Building Materials*, Vol. 36, (2012), 604-616. <https://doi.org/10.1016/j.conbuildmat.2012.06.014>
2. Noaman, A. T., Bakar, B. H. A., and Akil, H. M. "The effect of combination between crumb rubber and steel fiber on impact energy of concrete beams." *Procedia Engineering*, Vol. 125, (2015), 825-831. <https://doi.org/10.1016/j.proeng.2015.11.148>
3. Wang, J., Dai, Q., Guo, S., and Si, R. "Study on rubberized concrete reinforced with different fibers." *ACI Materials Journal*, Vol. 116, No. 2, (2019), 21-31. <https://doi.org/10.14359/51712266>
4. Makki, O. M. and H. M. K. A.-M. "Response of Rubcrete Continuous Deep Beams under Sinusoidal loads." *International Journal of Engineering*, Vol. 35, No. 7, (2022), 1307-1316. doi: 10.5829/IJE.2022.35.07A.10
5. S. Kumar, N. Manodeepan, S. Arulkesavan, S. P. "An Experimental Investigation on Rubberized Concrete." *International Journal for Innovative Research in Science & Technology*, Vol. 2, No. 07/013, (2015), 82-88.
6. Youssf, O., Hassanli, R., Mills, J. E., and Abd Elrahman, M. "An experimental investigation of the mechanical performance and structural application of LECA-Rubcrete." *Construction and Building Materials*, Vol. 175, (2018), 239-253. <https://doi.org/10.1016/j.conbuildmat.2018.04.184>
7. Sukontasukkul P, C. C. "Properties of concrete pedestrain block mixed with crumb rubber." *Construction and Building Materials*, Vol. 20, No. 7 (2006), 450-457. <https://doi.org/10.1016/j.conbuildmat.2005.01.040>
8. Batayneh, M. K., Marie, I., and Asi, I. "Promoting the use of crumb rubber concrete in developing countries." *Waste Management*, Vol. 28, No. 11, (2008), 2171-2176. <https://doi.org/10.1016/j.wasman.2007.09.035>
9. . S. K. G. "Fundamental Properties of Self-Compacting Concrete Utilizing Waste Rubber Tires-a Review." *International Journal of Research in Engineering and Technology*. Vol. 5, No. 1 (2016), 254-261. <https://doi.org/10.15623/ijret.2016.0501051>
10. Yung, W. H., Yung, L. C., and Hua, L. H. "A study of the durability properties of waste tire rubber applied to self-compacting concrete." *Construction and Building Materials*, Vol. 41, (2013), 665-672. <https://doi.org/10.1016/j.conbuildmat.2012.11.019>
11. Ganjian, E., Khorami, M., and Maghsoudi, A. A. "Scrap-tyre-rubber replacement for aggregate and filler in concrete." *Construction and Building Materials*, Vol. 23, No. 5, (2009), 1828-1836. <https://doi.org/10.1016/j.conbuildmat.2008.09.020>
12. Al-mutairee, H. M. K., and Makki, O. M. "Rubberized concrete mix – discussions for literature review," Vol. 1895, No. 1, (2021), 012011. IOP Publishing.. <https://doi.org/10.1088/1742-6596/1895/1/012011>
13. Beiram, A. A. H., and Al-Mutairee, H. M. K. "Effect of using Waste Rubber as Partial Replacement of Coarse Aggregate on Torsional Strength of Square Reinforced Concrete Beam." *International Journal of Engineering, Transactions B: Applications*, Vol. 35, No. 2, (2022), 397-405. <https://doi.org/10.5829/ije.2022.35.02b.16>
14. Abdulameer, A., and Al-mutairee, H. M. K. "An Experimental Study on Behavior of Sustainable Rubberized Concrete Mixes," *Civil Engineering Journal*, Vol. 6, No. 7, (2020), 1273-1285. <http://dx.doi.org/10.28991/cej-2020-03091547>
15. Khan, S., and Singh, A. "Behavior of Crumb Rubber Concrete." *International Journal of Research in Engineering, IT and Social Sciences*, Vol. 08, No. 2, (2018), 86-92. Retrieved from https://www.researchgate.net/publication/333044437_Behavior_of_Crumb_Rubber_Concrete
16. Topçu, I. B. "The properties of rubberized concretes." *Cement and Concrete Research*, Vol. 25, No. 2, (1995), 304-310. [https://doi.org/10.1016/0008-8846\(95\)00014-3](https://doi.org/10.1016/0008-8846(95)00014-3)
17. Liu, F., Zheng, W., Li, L., Feng, W., and Ning, G. "Mechanical and fatigue performance of rubber concrete." *Construction and Building Materials*, Vol. 47, (2013), 711-719. <https://doi.org/10.1016/j.conbuildmat.2013.05.055>
18. Bisht, K., and Ramana, P. V. "Evaluation of mechanical and durability properties of crumb rubber concrete." *Construction and Building Materials*, Vol. 155, (2017), 811-817. <https://doi.org/10.1016/j.conbuildmat.2017.08.131>
19. Sahib, F.N. and Al-Mutairee, H.M., "Punching strength behavior of reinforced concrete slabs with chips waste tire rubber." *Periodicals of Engineering and Natural Sciences*, Vol. 8, No. 4, (2020), 2389-2404. <http://dx.doi.org/10.21533/pen.v8i4.1735>
20. Hasan, Z.A., Nasr, M.S. and Abed, M.K., "Properties of reactive powder concrete containing different combinations of fly ash and metakaolin." *Materials Today: Proceedings*, Vol. 42, (2021), 2436-2440. <https://doi.org/10.1016/j.matpr.2020.12.556>
21. Najim, K. B., and Hall, M. R. "Mechanical and dynamic properties of self-compacting crumb rubber modified concrete." *Construction and Building Materials*, Vol. 27, No. 1, (2012), 521-530. <https://doi.org/10.1016/j.conbuildmat.2011.07.013>
22. Skripkiunas, G., Grinys, A., and Miškinis, K. "Damping properties of concrete with rubber waste additives." *Medžiagotyra*, Vol. 15, No. 3, (2009), 266-272.
23. ASTM C143M. "Standard test method for slump of hydraulic-cement concrete." ASTM Int. i(Reapproved), (2012). https://doi.org/10.1520/C0143_C0143M-12
24. BS EN 12350-9, and :2010. "BSI Standards Publication Testing fresh concrete." *British Standard*, (2010), 18.
25. Girskas, G., and Nagrockienė, D. "Crushed rubber waste impact of concrete basic properties." *Construction and Building Materials*, Vol. 140, (2017), 36-42. <https://doi.org/10.1016/j.conbuildmat.2017.02.107>
26. binti Salehuddin, S., Rahim, N. L., Mohamad Ibrahim, N., Tajri, S. A. N., and Zainol Abidin, M. Z. "The Behaviour of Rubber Tyre as Fine Aggregate in Concrete Mix." *Applied Mechanics and Materials*, Vol. 754-755, (2015), 427-431. <https://doi.org/10.4028/www.scientific.net/amm.754-755.427>
27. BS 1881-116. "Testing concrete - Part 116: Method for determination of compressive strength of concrete cubes." *British Standard*, Vol. 2, No. 2, (2010), 1-14.
28. ASTM International. "Standard Test Method for Compressive Strength of Cylindrical Concrete Specimens 1 This standard is for EDUCATIONAL USE ONLY ." Annual Book of ASTM Standards, No. C, (2010), 1-7. <https://doi.org/10.1520/C0039>
29. ASTM C469-11. "Standard Test Method for Splitting Tensile Strength of Cylindrical Concrete Specimens." *Manual on Hydrocarbon Analysis, 6th Edition*, Vol. i, (2008), 545-548. <https://doi.org/10.1520/C0496>
30. C133-97. "Standard test methods for cold crushing strength and modulus of rupture of refractories (C133-97)." Annual B. ASTM Standard, Vol. 97, No. Reapproved 2008, (2015), 1-6. <https://doi.org/10.1520/C0133-97R15.2>
31. Mohammed, T. J., and Breesem, K. M. "Enhancement of the Shear-flexural Strength of the Rubberized Concrete Prism Beam

by External Reinforcement.” *International Journal of Engineering, Transactions B: Applications*, Vol. 35, No. 5, (2022), 1017-1023. <https://doi.org/10.5829/ije.2022.35.05b.17>

32. Tonon, F. "JSCE-SF6 Limitations for Shear Tests and ASTM D5607 Shear Tests on Fiber-Reinforced Concrete." *ACI Materials Journal*, Vol. 118, No. 3 (2021), 91-100, doi: 10.14359/51732599.

Persian Abstract

چکیده

در اکثر انقباضات عمرانی، اعضای بتنی برای مقاومت در برابر بارهای دینامیکی که متحمل می‌شوند باید مقداری شکل‌پذیری به دست آورند و راه‌های زیادی مانند افزودن الیاف فولادی به مخلوط بتن یا جایگزینی سنگدانه‌ها با لاستیک وجود دارد. به دلایل پایداری و اقتصادی، لاستیک‌های لاستیک اسفاط شده ارزان‌ترین مواد برای دستیابی به این هدف هستند. روش بد در چنین جایگزینی این است که درصد جایگزینی بالا باعث افت زیادی در خصوصیات مکانیکی بتن می‌شود تا اینکه غیر سازه ای شود. این مقاله شش مخلوط روبکریت ساختاری را بررسی می‌کند و خواص آن را پس از جایگزینی مورد بحث قرار می‌دهد. اسلامپ، چگالی، جذب آب، مقاومت فشاری برای مکعب‌ها و سیلندرها، ضریب ضربه، مقاومت خمشی، شکاف، مدول الاستیک و تنش در مقابل منحنی‌های کرنش آزمایش و مورد بحث قرار گرفتند. می‌توان نتیجه گرفت که اختلاط rubcrete پایدار علیرغم افت استحکام ناشی از فرآیند جایگزینی همچنان ساختاری دارند. استحکام کششی، فشاری و خمشی بتن به دلیل از بین رفتن پیوند بین ملات و لاستیک‌ها به ازای هر افزایش در مقادیر لاستیک به حداقل می‌رسد.



Relationship Between Compressive Strength and Non-destructive Tests of Colored Geopolymer Concrete Based on Fly Ash

M. Q. Mutair, M. A. Abdulrehman*, K. M. Eweed

Materials Engineering Department, Faculty of Engineering, Mustansiriyah University, Baghdad, Iraq

PAPER INFO

Paper history:

Received 16 May 2022

Received in revised form 14 June 2022

Accepted 15 June 2022

Keywords:

Concrete

Fly Ash

Geopolymer

Non-destructive

Pigments

ABSTRACT

In this work, some physical and mechanical properties of colored geopolymer concrete based on fly ash were studied. Geopolymer concrete was colored using two types of dyes (chromium oxide which gives green color and iron oxide hydroxide which gives yellow color). The geopolymer concrete samples were subjected to controlled curing conditions at 30°C. At the age of 28 days, all samples were tested under compressive loading and non-destructive tests (NDTs) were also performed such as ultrasonic pulse velocity, Schmidt hammer, dynamic elastic modulus, and dynamic shear modulus. The test results were used to obtain a mathematical relationship between the compressive strength on the one side and the NDTs tests on the other side. This relationship can be used to estimate the compressive strength of the colored geopolymer concrete by the means of NDTs. In addition, the results proved that the percentage of adding 2% of the dye (for the green color) and 1% of the dye (for the yellow color) is the optimum percentage of the addition.

doi: 10.5829/ije.2022.35.09c.11

1. INTRODUCTION

Geopolymer consists of a natural or a by-product materials that contains alumina and silica in different proportions depending on the type of the raw material, as well as other oxides in small proportions. These materials are chemically activated by mixing with alkaline solutions and can be used as an alternative to ordinary cement [1]. Davidovits [2] found that aluminum (Al) and silicon (Si) in residues such as fly ash, metakaolin, slag, or rice husk ash can react in a process similar to the polymerization process if mixed with alkaline liquids. Thus, Davidovits [2] developed the term geopolymer to explain this reaction.

The geopolymer studies had shown the possibility of reducing CO₂ significantly by up to 80% when compared to the emissions resulting from the use of regular cement [3, 4]. This is one of the modern solutions proposed to address the issue of global warming [5].

Das [6] studied the effect of various factors, namely the ratio of sodium silicate to sodium hydroxide, curing

temperature, type of curing, and molarity of sodium hydroxide on the properties of a fly ash-based geopolymer. Lavanya and Jegan [7] studied the durability of geopolymer concrete made from high calcium fly ash and alkaline activators when exposed to a solution of 2% sulfuric acid and 5% magnesium sulfate for up to 45 days. Yahya et al. [8] have studied the feasibility of a fly ash-based geopolymer concrete to which kaolin has been added. Noori et al. [9] studied the relationship between destructive and NDTs for geopolymers based on metakaolin and others based on fly ash and found a relationship between the results of these tests.

Other researchers focused on colored concrete such as Craeye et al. [10] discussed the effect of red pigment on the frostiness resistance of concrete, as well as improvement steps such as adding super absorbent polymers (SAPs) to the fresh mixture. Huang et al. [11] studied the possibility of adding inorganic color paste with proportions of 5%, 10%, and 20% of polyacrylic emulsion to cement mortar. Awadly et al. [12] discussed the effect of adding colored pigments on the different

*Corresponding Author Institutional Email:
mohammed.ali.mat@uomustansiriyah.edu.iq (M. A. Abdulrehman)

properties of concrete, as they used a different group of colored pigments found in the local markets in Egypt.

Accordingly, colored geopolymer concrete could be widely used in some construction applications such as interlocking pavement bricks. For this reason, many researchers had studied the using of fly ash as an alternative to cement, and others have studied the compatibility of using color cement and pigments with geopolymer concrete. The aim of this work is focus on assessing the quality of colored geopolymer concrete by means of nondestructive tests. Also, the current study aims to find a relationship between the compressive strength and the nondestructive NDTs (rebound hammer and ultrasonic pulse velocity UPV) of colored geopolymer concrete fly ash based [13].

2. MATERIALS

2. 1. Fly Ash The Type C fly ash used in this work was imported from UAE origin by Eurobuild company. Tables 1 and 2 show the chemical analysis and physical properties, respectively, of fly ash according to ASTM 618 type C [14].

TABLE 1. Chemical Composition of Fly Ash Type C by XRF (Wt%)

Oxides	Content %
SiO ₂	38.63
Al ₂ O ₃	22.16
Fe ₂ O ₃	5.9
CaO	22.3
MgO	6.86
K ₂ O	0.29
SO ₃	0.82
TiO ₂	0.58
L.O.I	1.68
Na ₂ O	0.22
P ₂ O ₅	0.56
	Σ= 100

TABLE 2. Fly ash physical characteristics

Characteristics	Outcomes
Nature of form	Fine powder
Specific weight	2.35
Color	Near light white
Moisture content (%)	1.15
Surface area, cm ² /g	6560

2. 2. Sodium Hydroxide Caustic soda (sodium hydroxide) is a small flake available in the local market. To prepare the solution from these flakes, it is necessary to dissolve (404) g of NaOH flakes in (596) g of distilled water to obtain the required concentration of (14 M) in this work [15].

2. 3. Sodium Silicate Sodium Silicate Liquid is manufactured in the United Arab Emirates. The properties of Na₂SiO₃ are shown in Table 3.

2. 4. Water Tap water was used in this work as additional water to the design mixture for improve workability and obtaining the desired homogeneity.

2. 5. Fine Aggregate Natural sand taken from Karbala region (Al-Ukhaidir region) was used and conformity with ASTM C33 [16].

2. 6. Coarse Aggregate In this work, used crushed natural gravel (with grade 4.75-19.5) for all mixtures as coarse aggregates taken from the Salah al-din region (Al-Nabei area). After conducting the gradient test with sieves for gravel according to ASTM C33 [16].

2. 7. Plasticizer The super-plasticizer, condensed formaldehyde modified with sulfonated naphthalene is necessary for the development of geopolymer concrete and complies with ASTM C494 [17].

2. 8. Pigments Two types of pigment powder were used in this work (FeOH yellow and green Cr₂O₃). In different proportions (0, 1, 2, 3) by weight % of fly ash in the mixture bearing in mind that the pigments are imported from China.

2. 9. Final Preparation of Liquid Alkali After the NaOH flakes are dissolved in water, they are mixed with a Na₂SiO₃ solution where the solutions were stirred for a few minutes and the mixture must be completed at least 24 hours before it is used in the mixtures [18].

TABLE 3. Properties of Sodium Silicate

Description	Value
SiO ₂ / Na ₂ O (%)	2.35 ± 0.05
H ₂ O (% wt.)	53.4
Na ₂ O (% wt.)	13.60
SiO ₂ (% wt.)	33
Density(g/cm ³) @20° C	2.5
Specific Gravity	1.525
Viscosity (CPS)@ 20°C	800
Appearance	Vaporous

3. LABORATORY WORK

3. 1. Design of Mixtures

Seven colored geopolymer concrete mixtures were designed to study the effect of adding different percentages of colored oxides (yellow and green) [18]. Details of fly ash-based geopolymer concrete mixtures are summarized in Table 4.

3. 2. Colored Geopolymer Concrete Mixing Procedure

It has been reported that the geopolymer concrete can be manufactured by applying the old traditional methods that were used in the manufacture of ordinary concrete [18, 19]. First, the dry ingredients (fly ash, pigment, fine aggregate, and coarse aggregate) are mixed for 2-3 minutes using an electric mixer (capacity 250 liters), then water, plasticizer, and prepared alkaline liquid are added and all mixed for (4-5 minutes). This mixing procedure of geopolymer concrete was according to a previous study [18].

3. 3. Curing In this work, the samples were placed inside the oven in the laboratory at a temperature of 30 °C [20].

3. 4. Tests

3. 4. 1. Compressive Strength Testing

Testing was performed in accordance with ASTM C39 [21] on a specified set of three cylinders, dimensions: (150 mm diameter x 300 mm height) for each colored geopolymer mixture. A hydraulic press (3500 kN) was used as shown in Figure 1. This test was performed after samples were cured when they reached the age of 28 days. The compressive strength can be calculated by applying a simple mathematical relationship:

$$\sigma = \frac{P \text{ (in N)}}{A \text{ (in mm}^2\text{)}} \quad (1)$$

where:

σ : Compression strength (MPa)

P: Max load applied (N)

A: Area under load (mm²)

3. 4. 2. Rebound Hammer Test

This test requires the surface to be hammered with a Schmidt hammer based on ASTM C 805 [22] as shown in Figure 2 and is performed on a set of cubes of dimensions (150 x 150 x 150) mm³ each with a geopolymer color mixture ratio. The sample is installed in a pressure tester and subjected to a load of approximately 15% of the expected failure load, and several readings are taken from several locations on the sample surface.

TABLE 4. Design of reference and color geopolymer mixtures

Mix.	FA (kg)	Alkaline Liquids (kg)	Gravel (kg)	Sand (kg)	Added water (kg)	HRSPA (kg)	Pigments (kg)	Na ₂ SiO ₃ /NaOH (%)	Molarity of NaOH
Mr	10	3.544	30.05	14.79	0.95	0.39	0	2.5	14
MY1	9.9	3.544	30.05	14.79	0.95	0.39	0.1	2.5	14
MY2	9.8	3.544	30.05	14.79	0.95	0.39	0.2	2.5	14
MY3	9.7	3.544	30.05	14.79	0.95	0.39	0.3	2.5	14
MG1	9.9	3.544	30.05	14.79	0.95	0.39	0.1	2.5	14
MG2	9.8	3.544	30.05	14.79	0.95	0.39	0.2	2.5	14
MG3	9.7	3.544	30.05	14.79	0.95	0.39	0.3	2.5	14



Figure 1. Test of compressive strength



Figure 2. Schmidt hammer test

3. 4. 3. Ultrasound Pulse Velocity Test (UPV) Test

Ultrasound is one of the most important NDTs. This test was carried out on three cubes of dimensions (150 x 150 x 150) mm using probes at a frequency of (54) kHz, according to ASTM C 597 [23] as shown in Figure 3.

3. 4. 4. Shear Modulus (G_d), Dynamic Modulus (E_d)

Mechanical properties such as the dynamic modulus of elasticity (E_d) and the shear modulus of elasticity (G_d) can be determined by the equations below, which can be applied to measure and estimate the values of the elastic properties of the samples by calculating (VS), which represents the shear velocity as well as (VL) which means the velocity of Longitudinal wave [24].

$$E_d = \frac{\rho V_s^2 (3V_l^2 - 4V_s^2)}{V_l^2 - V_s^2} \quad (2)$$

$$G_d = V_s^2 * \rho \quad (3)$$

when:

E_d : Dynamic modulus (GPa).

G_d : Shear modulus (GPa).

V_l : Longitudinal velocity (m/s).

V_s : Shear velocity (m/s).

ρ : Density of the samples (kg/m³).

It is possible to calculate the value of the speed of the transverse waves using (S-wave transducer probes), as shown in Figure 4.



Figure 3. U P V direct test



Figure 4. UPV test by using (S-wave) transducer

4. RESULTS AND DISCUSSION

4. 1. Compressive Strength

The results of the compressive strength samples from a group of geopolymer concrete mixtures of two colors in various proportions are summarized in Table 5.

Pigments in the percentages of (0, 1, 2, 3)% were added for yellow and green colored samples. Addition of color (2%) gave the highest value in the compressive strength of green-colored geopolymer concrete, but when adding more than (2%) of green color, the compressive strength results decreased. However, the use of 1% of yellow color within geopolymer concrete was the best ratio because it achieved the highest compressive strength, but when increasing the color percentages, the opposite behavior will appear in the compressive strength results as the result showed a gradual decrease in compressive strength. These effects are due to the following reasons

- The pigments used (yellow and green) tend to absorb water molecules before they interact with FA because their molecules are finer than FA molecules. Therefore, the process of reducing water that interacts with the basic binder FA tends to improve the compressive strength and on the contrary, increasing the amount of water leads to reducing the bonding between the molecules of the basic bonding material [25].
- Adding pigments as a filler will reduce the pores inside the total volume of the colored geopolymer to some extent and lead to an increase in the compressive strength of geopolymer concrete. However, when adding an excessive amount of it increases above the point and the saturation limit (excessive addition of pigment will reduce the pressure due to the agglomeration of these particles pigment. Which leads to the formation of a region of separation and weakness) inside the colored geopolymer concrete because the pigments are non-pozzolanic materials. Thus, the pigments are not enter into the chemical reactions that occurs (polymerization) inside the colored geopolymer concrete [25].

TABLE 5. Compressive strength readings for samples of geopolymer concrete mixtures

Mixes	Compressive Strength(N/mm ²)
Mr0	37.36
MY1	38.47
MY2	36.80
MY3	34.86
MG1	38.07
MG2	40.42
MG3	37.28

4. 2. Rebound Hammer In Table 6, the results of the rebound hammer test were listed.

In general, addition of pigments leads to higher values of geopolymer concrete rebound number when added with a small percent, and this increase in values is due to the role of pigments that act as fillers for the internal and surface pores of the samples and thus reduce the surface roughness of the samples. The highest values of rebound number were obtained when using green pigment (2%) by weight of fly ash and (1%) by weight when using yellow pigment.

But when increased the percentage of additional pigments, can lead to the agglomeration of the pigments and cause areas of isolation and areas of less interconnection due to the decrease in the binder, and this, in turn, reduces the value of the rebound number.

4. 3. UPV Test The results of the UPV test are shown in Table 7.

From the above table, it can be noticed that there is an increase in the speed of pulse penetration when adding pigments, but with an increase in the percentage of additional pigments, the values of the wave penetration speed begin to decrease, and the reason for this is attributed to two factors:

TABLE 6. Results of Rebound Number for colored geopolymer concrete mix

Mix.	Results of Rebound Number
Mr0	39.12
MY1	44.88
MY2	43.01
MY3	40.45
MG1	42.21
MG2	43.90
MG3	40.07

TABLE 7. The results of the UPV test were listed

Mixes	UPV(m/s)
Mr0	3630
MY1	3691
MY2	3631
MY3	3528
MG1	3708
MG2	3736
MG3	3672

- Positive effect: It is due to the role of pigments in filling the voids and pores due to having a higher surface area than fly ash.
- Negative effect: When the percentage of pigments increases, this can lead to the agglomeration of pigment molecules, which replaces the binder (where the binder plays a role in the bonding and convergence of the molecules of the other components of the mixture and increases its density).

4. 4. Dynamic Modulus, Shear Modulus The results of the NDT calculations are shown in Table 8.

It is clear from Table 8 that the dynamic modulus of elasticity and the dynamic shear modulus behave in similar behavior to the UPV because the dynamic modulus of elasticity and the dynamic shear modulus are directly proportional to the UPV (based on the mathematical equations).

4. 5. Mathematical Relationship Between Compressive Strength Test And NDT (RN and UPV)

An equation was derived from the experimental data in this study using Curve Expert Pro 2.7.3 program for colored geopolymer concrete (based on fly ash) is:

$$\text{Compressive strength} = a + RN^b \times UPV^c \quad (4)$$

TABLE 8. Density, longitudinal velocity, shear velocity, dynamic young modulus, and shear modulus results of colored geopolymer concrete mix

Mix.	Density (kg/m ³)	Longitudinal pulse velocity(m/s)	Shear pulse velocity (m/s)	Dynamic elastic modulus (GPa)	Dynamic modulus of shear (GPa)
Mr0	2410	3630	2268	29.25	12.39
MY1	2437	3691	2278	30.15	12.64
MY2	2411	3631	2253	29.05	12.23
MY3	2372	3528	2240	27.66	11.90
MG1	2451	3708	2284	30.54	12.78
MG2	2464	3736	2290	30.98	12.92
MG3	2430	3672	2267	29.77	12.48

where:

$$a = -97.13$$

$$b = 0.026$$

$$c = 0.586$$

Correlation Coefficient: 0.96

Equation (4) is limited only for geopolymer concrete with compressive strength ranging between 30-40 MPa. This is due to the fact that the geopolymer concrete may consist of various ingredients with different characteristics that could change its mechanical and physical properties (see Figure 5).

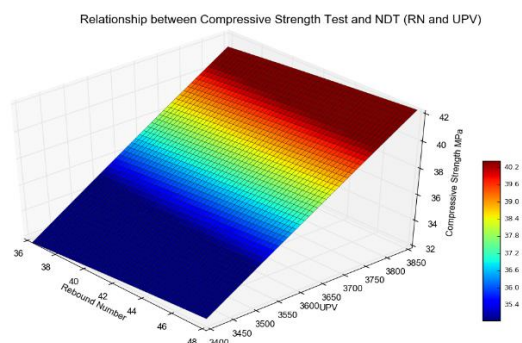


Figure 5. Mathematical relationships between (RN and UPV) test and the compressive strength test of colored geopolymer concrete

5. CONCLUSION

According to the experimental results shown above, the optimum percentage of adding chromium oxide is 2% of the weight of the fly ash, and the optimum percentage of adding iron oxide hydroxide is 1% of the weight of the fly ash, because the pigments addition of more than the above-mentioned percentages causes a deterioration of the colored geopolymer concrete properties. While in the case of adherence to the percentages as mentioned above, an increase in compressive strength characteristic was obtained by 8% and 3% for both green and yellow colors, respectively. Also, a mathematical relationship was found between the NDTs and the compressive strength, through which we can estimate the compressive strength through the NDTs.

6. REFERENCES

- Wallah, S. and Rangan, B.V., "Low-calcium fly ash-based geopolymer concrete: Long-term property", Curtin University of Technology, Curtin University of Technology, (2006), doi: 10.1201/9781420007657-31.
- Davidovits, J., "Geopolymers: Ceramic-like inorganic polymers", *Journal of Ceramic Science and Technology*, Vol. 8, No. 3, (2017), 335-350. doi: 10.4416/JCST2017-00038.
- Rangan, B.V., "Low-calcium, fly-ash-based geopolymer concrete, concrete construction engineering handbook, Taylor and Frances, (2010), doi: 10.1201/9781420007657-31.
- Al-Sultani, S.A.J., Al-Hydary, I.A.D. and Al-dujaili, M.A.A., "Taguchi- grey relational analysis for optimizing the compressive strength and porosity of metakaolin-based geopolymer", *International Journal of Engineering, Transactions B: Applications*, Vol. 34, No. 11, (2021), 2525-2533 doi: 10.5829/ije.2021.34.11b.15.
- Raj, S.R., Arulraj, P.G., Anand, N., Balamurali, K. and Gokul, G., "Influence of various design parameters on compressive strength of geopolymer concrete: A parametric study by taguchi method", *International Journal of Engineering, Transactions A: Basics*, Vol. 34, No. 10, (2021), 2351-2359 doi: 10.5829/ije.2021.34.10a.16.
- Kumar Das, S., "Parametric study of flyash based geopolymer concrete", *International Journal of Engineering and Technology*, Vol. 7, No. 2, (2018), 196-198. doi: 10.14419/ijet.v7i2.31.13439.
- Lavanya, G. and Jegan, J., "Durability study on high calcium fly ash based geopolymer concrete", *Advances in Materials Science and Engineering*, Vol. 2015, (2015), doi: 10.1155/2015/731056.
- Yahya, Z., Abdullah, M., Ramli, N.M., Burduhos-Nergis, D. and Abd Razak, R., "Influence of kaolin in fly ash based geopolymer concrete: Destructive and non-destructive testing", in IOP Conference Series: Materials Science and Engineering, Vol. 374, No. 1, (2018), 012068, IOP Publishing, doi: 10.1088/1757-899x/374/1/012068.
- Noori, A.S., Oweed, K.M., Raouf, R.M. and Abdulrehman, M.A., "The relation between destructive and non-destructive tests of geopolymer concrete", *Materials Today: Proceedings*, Vol. 42, (2021), 2125-2133, doi: 10.1016/j.matpr.2020.12.296.
- Craeye, B., Kondo, E. and Stoop, J., "Reduced scaling of colored concrete pavements by means of super absorbing polymers", in IABSE Spring Conference, Rotterdam, The Netherlands, (2013), 354-355, doi: 10.2749/222137813806501623.
- Huang, J.-M., Yang, W.-D., Wang, H.-Y. and Kao, T.-C., "Engineering properties of colorful mortar with inorganic color paste", *Applied Sciences*, Vol. 11, No. 14, (2021), 6297, doi: 10.3390/app11146297.
- EL-Awadly, N.Z., Sharobim, K. and Hussein, N., "Advantage and disadvantage of colored concrete in structural engineering", *Port-Said Engineering Research Journal*, Vol. 19, No. 1, (2015), 1-10, doi: 10.21608/psrj.2015.36715.
- Nguyen, D.T. and Phan, V.T.A., "Engineering properties of soil stabilized with cement and fly ash for sustainable road construction", *International Journal of Engineering, Transactions C: Aspects*, Vol. 34, No. 12, (2021), 2665-2671, doi: 10.5829/ije.2021.34.12c.12.
- "ASTM c618-12a, standard specification for coal fly ash and raw or calcined natural pozzolan for use in concrete", American Society for Testing and Materials, (2012), doi: 10.1520/c0618-12a.
- Hardjito, D. and Rangan, B.V., "Development and properties of low-calcium fly ash-based geopolymer concrete", Research Report GC 1, Faculty of Engineering Curtin University of Technology Perth, Australia (2005), doi: 10.1201/9781420007657-31.
- "ASTM c33/c33m-11a: "Standard specification for concrete aggregates", American Society for Testing and Materials, (2011), doi: 10.1520/c0033_c0033m-13.
- "ASTM c494 "standard specification for chemical admixtures for concrete", American Society for Testing and Material Standards, (2004), doi: 10.1520/c0494_c0494m-12.

18. Lloyd, N. and Rangan, V., "Geopolymer concrete with fly ash", in Proceedings of the Second International Conference on sustainable construction Materials and Technologies, UWM Center for By-Products Utilization. (2010), 1493-1504 doi: 10.1201/9781420007657-31.
19. Sanni, S.H. and Khadiranaikar, R., "Performance of alkaline solutions on grades of geopolymer concrete", *International Journal of Research in Engineering and Technology*, Vol. 2, No. 11, (2013), 366-371, doi: 10.15623/ijret.2013.0213069.
20. Patil, A.A., Chore, H. and Dode, P., "Effect of curing condition on strength of geopolymer concrete", *Advances in Concrete Construction*, Vol. 2, No. 1, (2014), doi: 10.12989/acc.2014.2.1.029.
21. "ASTM C39, standard test method for"compressive strength of cylindrical concrete specimens", American Society for Testing and Material Standards, (2014), doi: 10.1520/c0039_c0039m-09a.
22. "ASTM C805"test for rebound number of hardened concrete"", American Society for Testing and Material Standards, (1993), doi: 10.1520/c0805_c0805m-18.
23. "ASTM C597 "standard test method for pulse velocity through concrete"", American Society for Testing and Materials, (2003), doi: 10.1520/c0597-97.
24. Lee, B.J., Kee, S.-H., Oh, T. and Kim, Y.-Y., "Evaluating the dynamic elastic modulus of concrete using shear-wave velocity measurements", *Advances in Materials Science and Engineering*, Vol. 2017, (2017), 1651753 doi: 10.1155/2017/1651753.
25. Mohammed Hameed, M. and Mohammed Ali, A., "Using of metakaolin to produce colored geopolymer concrete", *Journal of Physics: Conference Series*, Vol. 2114, No. 1, (2021), 012018 doi: 10.1088/1742-6596/2114/1/012018.

Persian Abstract

چکیده

در این کار برخی از خواص فیزیکی و مکانیکی بتن ژئوپلیمری رنگی بر پایه خاکستر بادی مورد بررسی قرار گرفت. بتن ژئوپلیمری با استفاده از دو نوع رنگ (اکسید کروم که رنگ سبز می دهد و اکسید آهن هیدروکسید که رنگ زرد می دهد) رنگ آمیزی گردید. نمونه های بتن ژئوپلیمری تحت شرایط بعمل آوری کنترل شده در دمای ۳۰ درجه سانتیگراد قرار گرفتند. در سن ۲۸ روزگی، تمامی نمونه ها تحت بارگذاری فشاری مورد آزمایش قرار گرفتند و آزمایش های غیرمخرب (NDTs) مانند سرعت پالس اولتراسونیک، چکش اشیمیت، مدول الاستیک دینامیکی و مدول برشی دینامیکی نیز انجام شد. از نتایج آزمایش برای به دست آوردن یک رابطه ریاضی بین مقاومت فشاری از یک طرف و آزمون های NDTs از طرف دیگر استفاده شد. این رابطه را می توان برای تخمین مقاومت فشاری بتن ژئوپلیمر رنگی با استفاده از NDT ها استفاده کرد. علاوه بر این، نتایج نشان داد که درصد افزودن ۲ درصد رنگ (برای رنگ سبز) و ۱ درصد رنگ (برای رنگ زرد) درصد بهینه افزودن است.



A New Technique for Online Open Switch Fault Detection and Location in Single-phase Pulse Width Modulation Rectifier

M. Arehpanahi*, A. M. Entekhabi

Electrical Engineering Department, Tafresh University, Tafresh, Iran

PAPER INFO

Paper history:

Received 28 October 2021

Received in revised form 25 June 2022

Accepted 01 July 2022

Keywords:

Open Switch Fault

Fault Diagnosis

PWM Rectifier

Online Detection

Input Voltage of Rectifier and Fault Location

ABSTRACT

Open switch fault detection in the single-phase pulse width modulation (PWM) rectifier using line current analysis technique is very applicable, but no-fault detection at high switching frequency is the main drawback of this technique. In this paper, a new online diagnosis technique for detection and location of open switch fault in the single-phase PWM rectifier is proposed. The proposed diagnosis method is based on instantaneous input voltage of the rectifier analysis. The proposed method can detect the fault in half of the power frequency under high switching frequency and load conditions. Simulation results showed the proposed technique can detect and locate all open switch faults at any switching frequency under different load conditions. In addition, the second-order output filter that is necessary for line current technique can be removed in the proposed technique.

doi: 10.5829/ije.2022.35.09c.12

NOMENCLATURE

d_1, d_2	Fault indicators	C_d	DC-link capacitor (f)
C_f	Filter capacitance (f)	F_s	Switching frequency (Hz)
L_f	Filter inductance (H)	V_{ab}	Input voltage of rectifier (v)
V_N	Source voltage (v)	L_N	source inductance (H)
R_N	source resistance (Ω)	R_L	Load (Ω)

1. INTRODUCTION

Single and three-phase PWM rectifiers are well known and widely used in industries such as electric vehicle chargers, electric drives and micro grid applications. Switch fault is one of the main faults in PWM rectifier topology, which leads to decreasing reliability, and unsafe operation of the rectifiers. The most common failures in the power electronic switches are short-circuited, gate faults and open switch faults [1, 2]. Open switch fault is one of the most common faults, which occurred in PWM rectifiers. There are many techniques for diagnosis of the open switch fault in the power electronic converters [1, 4]. A technique based on a mixed logical dynamic model and state estimator presented by Xie and Ge [3]. This technique employed for open switch fault diagnosis in the single-phase cascade H-bridge rectifiers. A new open-switch fault

detection for a neutral-point clamped rectifier discussed by Chen et al. [4]. A new calculation method based on phase-to-phase pole voltage deviations proposed for diagnosis process improvement. A combination of two techniques i.e., normalized DC current calculation and false alarm strategy, employed for open switch fault diagnosis. A new fast method presented by Ben et al. [5] using a residual generation between measured and observed current form factors (CFFs).

Gou et al. [6] carry out a mixed logical dynamic model and residual generation fault diagnosis. The hardware implementation of this method is simple, but the software implementation process is complicated.

Diagnosis of open switch fault using line current analysis in the frequency domain presented by Tian and Xinglai [7]. An online open switch fault diagnosis based on instantaneous line current analysis, proposed in Lai et al. [8]. This technique is powerful at low switching

*Corresponding Author: arehpanahi@tafreshu.ac.ir (M. Arehpanahi)

frequency (railway application), but misdiagnosis at high switching frequencies and load variations, are the main drawbacks of this technique. An improved fault detection based on deep belief networks (DBN) and least square support vector machine (LSSVM), investigated by Tiancheng et al. [9]. A method based on the residual changing rate for a single insulated gate bipolar transistor in the single-phase PWM converter presented by Dong et al. [10]. The fault detection technique was directly implemented by Huangan [11] via analyzing the mismatch signal between the applied switching states and the estimated one. An improved diagnosis system for open-circuit faults of a three-phase PWM rectifier based on line current analysis presented by Shi et al. [12]. The diagnosis module employs a hysteresis comparator to analyze the changing trend of the currents and thereby diagnoses the single open-circuit (OC) faults. Open-switch fault diagnosis and tolerant control methods for a Vienna-rectifier using bidirectional switches presented by Seok and Lee [13]. These articles have a common problem in open switch fault detection i.e., misdiagnosis at high switching frequency.

The basis of Lai et al. [8] for open switch fault diagnosis is line current analysis. The most important drawback of Lai et al. [8] work was its dependence on the output filter and the switching frequency value in the open switch fault detection. Misdiagnosis at high switching frequency was the main disadvantage of Lai et al. [8] work. Therefore, in the proposed method, these problems are resolved. The proposed diagnosis technique is based on voltage analysis. In other words, the proposed method indicates the open-switch fault by using analysis of the PWM rectifier input voltage without any additional devices. Detection and location of open switch fault in all switching frequencies ranges and load conditions, is the main advantage of the proposed technique.

2. DIAGNOSIS PRINCIPLE OF OPEN SWITCH FAULT

The schematic of the single-phase PWM boost rectifier illustrated in Figure 1. During normal operation of the rectifier, if one of the switches is open-circuited, the line current i_L and input voltage of the rectifier V_{ab} , will be distorted. If this distortion is not removed, the rectifier will be severely damaged. Therefore, identification of this fault is necessary. One of the usual technique to detect this fault is line current monitoring. Using an analyzing of the line current, open switch fault could be detected. A method based on line current monitoring for diagnosis of open switch fault was proposed by Lai et al. [8]. The main disadvantages of that are:

1. No-fault diagnosis at high switching frequency
2. No-fault diagnosis under different load conditions

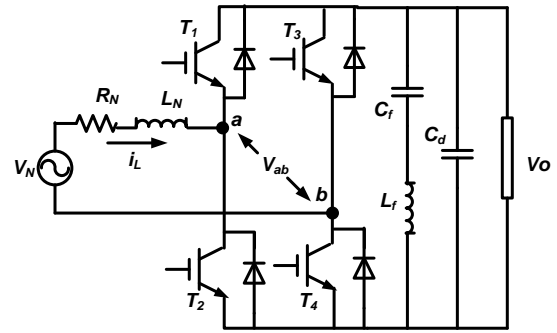


Figure 1. Topology of single phase PWM boost rectifier

To overcome these problems, in this paper, a new online technique for detection and location of open switch fault in all ranges of the switching frequency presented.

In the proposed technique, instantaneous input voltage of the rectifier " V_{ab} " has been selected as a fault indicator. The waveforms of the switches states (S_1 , S_2 , S_3 , S_4) and V_{ab} pre and post-fault in T_1 illustrated in Figure 2. According to Figure 2, it is clear that the negative half cycle of V_{ab} during post-fault is distorted. This distortion will create in the positive half cycle, if an open switch fault takes place for T_2 or T_3 . During post-fault, the minimum/maximum values of V_{ab} waveform based on the defective switch number, are changed in any switching cycle. Therefore, detection of the open switch fault could be carried out by a minimum/ maximum points tracking process of V_{ab} waveform at any switching cycles.

3. PROPOSED DIAGNOSIS TECHNIQUE

Detection and location of open switch fault in proposed technique is done by a particular sampling process of V_{ab} waveform. The specific sampling process is accomplished by two sequence signals (Ps_1 , Ps_2). These signals produced by a comparison of the PWM carrier signal with two references sine wave signals (with 180-

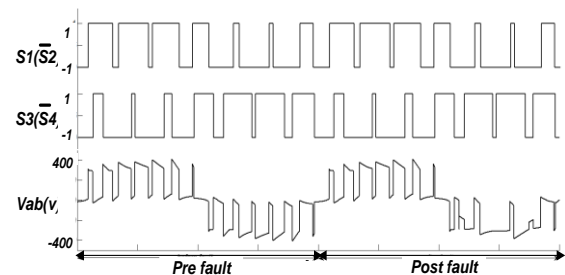


Figure 2. V_{ab} waveform and switching states (S_1 , S_2 , S_3 , S_4) pre and post-fault

degree phase shift with respect to each other) which was used by Lai et al. [8]. The block diagram of the proposed fault diagnosis process shown in Figure 3.

According to Figure 3, V_{ab} are sampled by two sequences pulses P_{s1} and P_{s2} which are called f_{s1} , f_{s2} . The sampled signals f_{s1} , f_{s2} are passed through the two filters (Low Pass Filter (LPS) and Band Pass Filter (BPF)) for extracting the fundamental component of V_{ab} . In the next step, the filter outputs are divided by the average value of the V_{ab} for insensitive to the grid voltage variation which are called d_1 , d_2 as the fault indicators. For example, the proposed fault indicators (d_1 , d_2) and input voltage of the rectifier waveform V_{ab} for 350 Hz switching frequency illustrated in Figure 4.

The open switch fault happened in T_1 at time 0.35 s. According to Figure 4, it is clear the diagnosis signals d_1 , d_2 in pre-fault, are very close together, but during faulty conditions ($t > 0.35$ s) they separate from each other in less than half of the fundamental cycle. Consequently, the online detection of the fault is done by analysis of the d_1 , d_2 waveforms, based on Figure 4 and several simulation results at different switching frequencies and load variations, the proposed conditions for open switch fault detection and location are listed in Table 1.

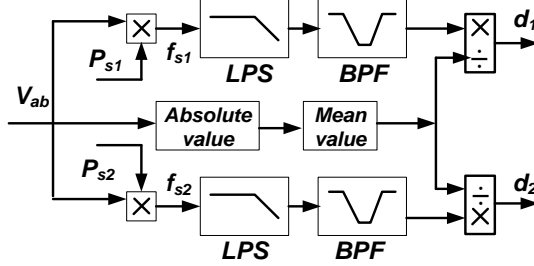


Figure 3. Block diagram of the proposed technique

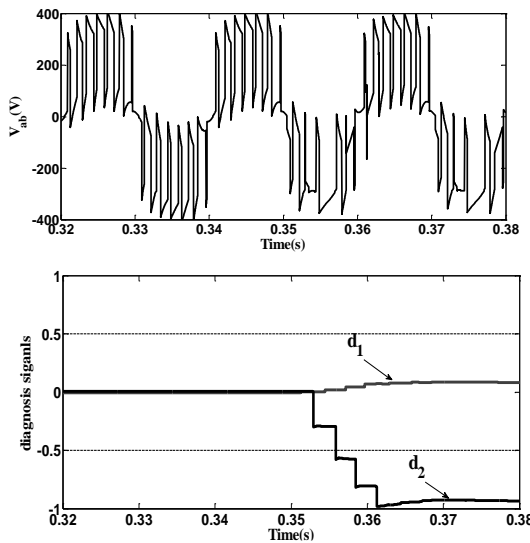


Figure 4. V_{ab} and diagnosis signals for T_1 switch fault

TABLE 1. The proposed conditions for open switch fault diagnosis

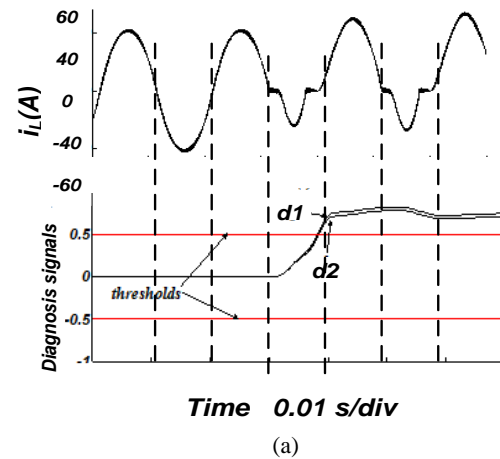
d_1	d_2	Faulty switch
$ d_1 < 0.5$	$d_2 < -0.5$	T_1
$d_1 > 0.5$	$ d_2 < 0.5$	T_2
$ d_1 < 0.5$	$d_2 > 0.5$	T_3
$d_1 < -0.5$	$ d_2 < 0.5$	T_4

For example, if $d_1 > 0.5$ and $|d_2| < 0.5$ the switch T_2 is open-circuited. In addition, in the proposed technique, the second order output filter (C_f , L_f) could be removed, but in the line current technique it is necessary.

4. SIMULATION RESULTS

In order to performance analysis of the proposed technique in online diagnosis of the open switch fault, a typical case study considered (Figure 1). The circuit parameters are: input voltage, $V_N = 220$ V; source resistance, $R_N = 0.05 \Omega$; source inductance $L_N = 1.2$ mH; DC output reference voltage $V_{ref} = 300$ V; DC-link capacitance, $C_d = 3$ mF; filter capacitance $C_f = 4.56$ mF, filter inductance $L_f = 0.603$ mH and load $R_L = 15 \Omega$. The line current analysis and proposed technique are applied to the case study. The PWM rectifier operates under nominal load with 10 kHz switching frequency. The line current waveform and its fault indicators based on literature [8] for open switch fault are shown in Figure 5. The input voltage of the rectifier and its fault indicators (proposed technique) are illustrated in Figure 6.

According to Figure 5, the line current analysis could not detect any open switch faults in T_1 , T_2 , T_3 and T_4 because separating of the fault indicators (based on



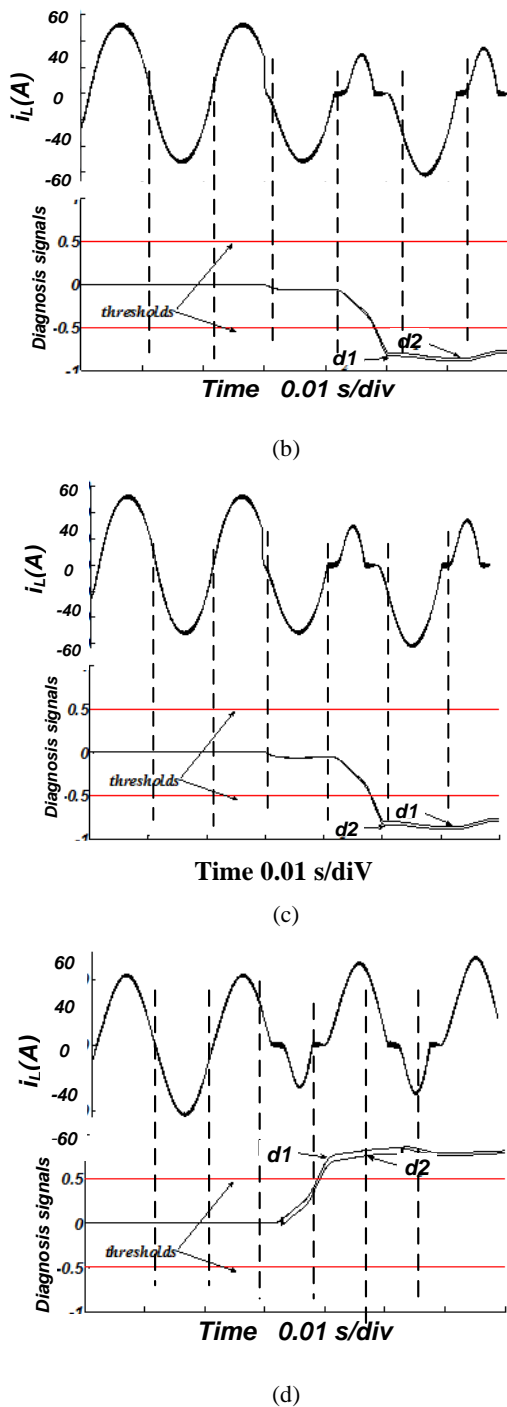
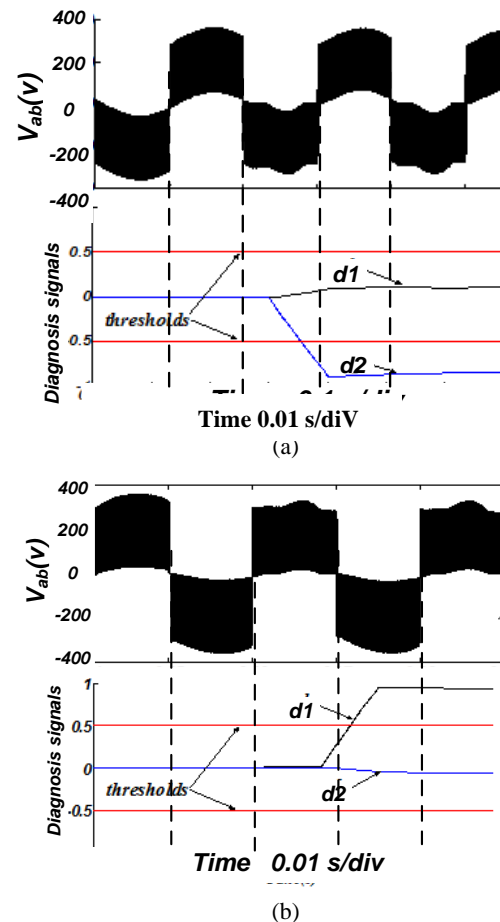


Figure 5. Simulation results based on [8] (a) i_L , $d1, d2$ pre and post open switch fault in T1 (b) i_L , $d1, d2$ pre and post open switch fault in T2 (c) i_L , $d1, d2$ pre and post open switch fault in T3 (d) i_L , $d1, d2$ pre and post open switch fault in T4

literature [8]) is complicated and almost impossible. In the proposed technique, (Figure 6), the difference between the fault indicators in the post-fault time (for all faulty switches) is significant enough for detecting the

fault simply. Therefore, all of the switch faults can be easily detected and located by the proposed technique. In Figures 5 and 6 each x-axis segmentation is 0.01 second. In other words, the distance between the vertical dashed lines is 0.01 second. The detection time in the proposed technique in all of the faulty switches, is less than half of the grid voltage cycle that is the best time for online fault identification and fault location. Existence of LC filter for Lai et al. [8] is necessary, but in the proposed technique, because of the suitable difference between the fault indicators in all ranges of the switching frequencies, it could be removed. The diagnosis signals values $d1$, $d2$ in Figure 5 are very close together therefore, detection of fault is not possible practically. Consequently, the line current technique could not detect any open switch fault at high switching frequencies.

Figure 6 indicates the difference between diagnosis signals $d1$, $d2$ is significant to easily detect the fault at high switching frequencies. In other words, the proposed fault detection and location technique is independent of the switching frequency value. Therefore, the proposed method can be detected and located open switch fault at any switching frequencies easily which is significant of this paper. The summary of three recent techniques (line



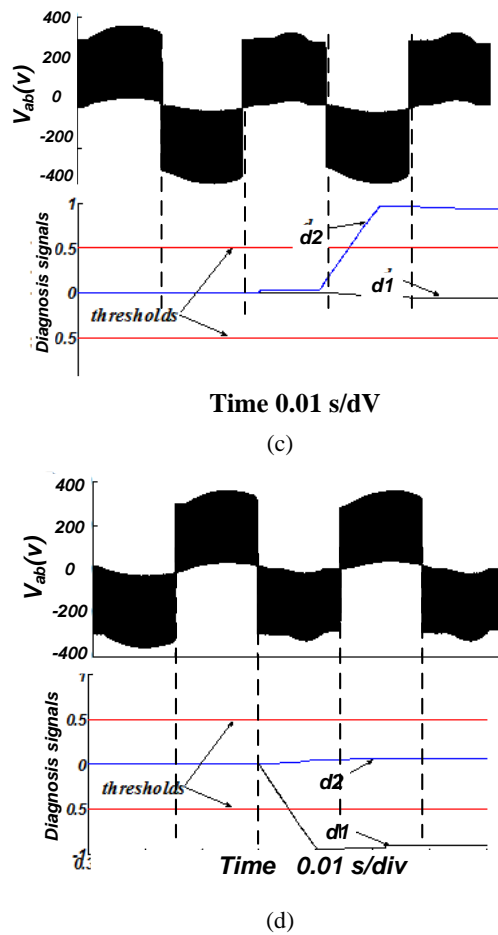


Figure 6. Simulation results of proposed technique (a) V_{ab} , $d1$, $d2$ pre and post open switch fault in T1 (b) V_{ab} , $d1$, $d2$ pre and post open switch fault in T2 (c) V_{ab} , $d1$, $d2$ pre and post open switch fault in T3 (d) V_{ab} , $d1$, $d2$ pre and post open switch fault in T4

current [8], AC current residual [10] and proposed technique) results at different switching frequencies and load conditions, listed in Table 2. The load range varied from 50% to 120% of the full load. Switching frequency is changed from 0.35kHz to 10 kHz. Based on Table 2 results, it is clear that the proposed technique could detect and locate all of the open switch faults at any switching frequencies and different load conditions, but the line current technique could not detect any fault at high switching frequency ($>1\text{kHz}$) and load conditions.

Another problem of the line current technique based on Table 2 results, is no-fault detection at light loads ($\leq 50\%$ of full load). Because, the line current fluctuations at light loads in the PWM rectifier, is very high therefore, sometimes fault indicators values are out of Table 1 range and sometimes they are in range. Consequently, it cannot detect the faults, but in the proposed technique, this problem has been fixed

TABLE 2. Comparison of line current and proposed technique

Switching frequency (kHz)	Load (% nominal)	line current method [8]	AC current residual [10]	Proposed technique
0.35	50	No detect	Detect and locate	
	100	Detect and locate	Detect and locate	detect and locate
	120	detect and locate	detect and locate	
1	50	No detect		
	100	detect and locate	Detect and locate	detect and locate
	120	detect and locate		
2	50			
	100	No detect	No detect	detect and locate
	120			
5	50			
	100	No detect	No detect	detect and locate
	120			
10	50			
	100	No detect	No detect	detect and locate
	120			

completely. The technique of Dong et al. [10] could detect and locate open switch fault at switching frequency lower than 2 kHz but at higher switching frequency i.e. $>2\text{kHz}$, it could not detect any faults.

5. CONCLUSION

In this paper, a new online technique for open switch fault diagnosis in the single-phase PWM rectifier is proposed. A technique that is based on the instantaneous input voltage of the rectifier analysis can detect and locate any open switch fault in all switching frequencies and different load conditions. Other techniques such as line current analysis and AC current residual technique, cannot detect open switch fault at high switching frequencies. The line current technique cannot diagnosis the open switch fault at light load but the proposed technique, detect and locate open switch fault at light loads. A particular sampling process of the PWM rectifier input voltage detect the open switch fault in the proposed technique. Simulation results demonstrate the powerful of the proposed technique for faulty switch identification at any switching frequencies and load conditions related to other techniques effectively.

6. REFERENCES

1. Masomi Kazraji S., M. R. Feyzi, M. B. B. Sharifin, and S. Tohid "Sensorless Model Predictive Force Control with a Novel Weight Coefficients for 3-Phase 4-Switch Inverter Fed Linear Induction Motor Drives," *International Journal of Engineering, Transactions C: Aspects*, Vol. 31, No. 9, (2018), 1536-1545. doi: 10.5829/ije.2018.31.09c.09
2. Park J.H., Lee, J.S., Kim, M.Y. and Lee, K.B., "Diagnosis and Tolerant Control Methods for an Open-Switch Fault in a Vienna Rectifier" *IEEE Journal of Emerging and Selected Topics in Power Electronics*, Vol. 9, No. 6, (2021), 7112-7125. doi: 10.1109/JESTPE.2021.3084803
3. Xie D. and Ge X. , "Open-circuit fault diagnosis for single-phase cascaded H-bridge rectifiers in electrical traction systems" IEEE Transportation Electrification Conference and Expo, Asia-Pacific (ITEC Asia-Pacific)', (2017), 1-6. doi: 10.1109/ITEC-AP.2017.8080930
4. Chen M., He Y. and Sui C., "Open-switch fault diagnosis in three-level rectifiers based on selective calculation method for instant voltage deviation" *IET Power Electronics*, Vol. 14, No. 5, (2021), 923-935. https://doi.org/10.1049/pel2.12075
5. Ben, A.B., El Khil, S.K. and Belkhdja, I.S. "Open-circuit fault diagnosis and voltage sensor fault tolerant control of a single phase pulsed width modulated rectifier" *Mathematics and Computers in Simulation*, Vol. 131, (2017), 234-252. https://doi.org/10.1016/j.matcom.2015.10.005
6. Gou, B., Ge, X., Wang, S., Feng, X., Kuo, J.B. and Habetler, T.G., "An Open-Switch Fault Diagnosis Method for Single-Phase PWM Rectifier Using a Model-Based Approach in High-Speed Railway Electrical Traction Drive System", *IEEE Transactions on Power Electronics*, Vol. 31, No. 5, (2016), 3816-3826. doi: 10.1109/TPEL.2015.2465299
7. Tian, Z., Xinglai G. "An on-line fault diagnostic method based on frequency-domain analysis for IGBTs in traction PWM rectifiers", 8th International Power Electronics and Motion Control Conference (IPEMC-ECCE Asia), (2016), 22-26, doi: 10.1109/IPEMC.2016.7512841
8. Lai X., Jun-Kai G. and Liu, Y.C., "Online open-switch fault diagnosis method in single-phase PWM rectifiers", *Electronics Letters*, Vol. 51, No. 23, (2015), 1920-1922. https://doi.org/10.1049/el.2015.1194
9. Tiancheng S. He, Y., Wang, T. and Li, B., "Open Switch Fault Diagnosis Method for PWM Voltage Source Rectifier Based on Deep Learning Approach" *IEEE Access*, Vol. 7, (2019), 66595-66608. doi: 10.1109/ACCESS.2019.2917311 .
10. Dong X., Pu, J. and Ge, X., "AC Current residual-based method for open circuit fault diagnosis in single-phase PWM converter" *IET Power Electronics*, Vol. 11, No. 14, (2018), 2279-2285. https://doi.org/10.1049/iet-pel.2018.5444
11. Huang W., Luo L., Du, J., Xiang, B., Mei, S., Zhou, L. and Fan, Q., "Open-Circuit Fault Detection in PMSM Drives Using Model Predictive Control and Cost Function Error", *IEEE Transactions on Transportation Electrification*, Vol. 8, No. 2, (2022), 2667-2675. doi: 10.1109/TTE.2021.3135039
12. Shi T., He, Y., Wang, T., Tong, J., Li, B. and Deng, F. "An Improved Open-Switch Fault Diagnosis Technique of a PWM Voltage Source Rectifier Based on Current Distortion", *IEEE Transactions on Power Electronics*, Vol. 34, No. 12, (2019), 12212-12225. doi: 10.1109/TPEL.2019.2905296
13. Seok J.S., Lee KB. "Open-Switch Fault Diagnosis and Tolerant Control Methods for a Vienna Rectifier Using Bi-Directional Switches" *IEEE Energy Conversion Congress and Exposition (ECCE)*, (2018), 23-27. doi: 10.1109/ECCE.2018.8558280

Persian Abstract

چکیده

تشخیص خطای کلید باز در یکسو کننده مدولاسیون عرض پالس (PWM) تک فاز با استفاده از تکنیک پایش جریان خط بسیار کاربردی است. اما عدم تشخیص عیب در فرکانس سوئیچینگ بالا نقطه ضعف اصلی این تکنیک است. در این مقاله یک تکنیک تشخیص برخط جدید برای تشخیص و مکان یابی عیب کلید باز در یکسو کننده تک فاز پیشنهاد شده است. روش تشخیص پیشنهادی مبتنی بر پایش لحظه ای ولتاژ ورودی یکسو کننده به عنوان نشانگر خطا است. تجزیه و تحلیل این سیگنال با فرآیند نمونه برداری ویژه انجام می شود. اگر فرکانس سوئیچینگ یا تغییر بار تغییر کند، تکنیک پیشنهادی می تواند خطا را در نیمی از فرکانس منبع تشخیص دهد. نتایج شبیه سازی نشان می دهد که روش پیشنهادی در تشخیص و مکان یابی خطای کلید باز در هر فرکانس سوئیچینگ با تغییرات بار در مقایسه با تحلیل جریان خط برتری دارد. علاوه بر این در تکنیک پیشنهادی فیلتر خروجی مرتبه دوم می تواند حذف شود.



The Reliability Assessment of a Ship Structure under Corrosion and Fatigue, using Structural Health Monitoring

M. Sadeghian*

Department of Mechanic Engineering, Malek –e Ashtar University of Technology, Isfahan, Iran

PAPER INFO

Paper history:

Received 29 April 2022

Received in revised form 12 June 2022

Accepted 17 June 2022

Keywords:

Corrosion

Fatigue

Reliability

Structural Health Monitoring

ABSTRACT

Reliability of a ship structure has been investigated in this study under two factors of fatigue and corrosion failure using structural health monitoring data. In order to use structural health monitoring data in assessing the reliability, Bayesian inference method has been used to update the distribution of loads applied on the structure. This study used structural health monitoring data to assess the reliability of a ship construction under two conditions: fatigue and corrosion failure. A Bayesian inference method was utilized to update the distribution of loads applied to the structure to employ structural health monitoring data in determining reliability. The load distribution obtained from the equations was used to assess the reliability of a ship structure during corrosion. The proposed mathematical model was examined using the data output of the force sensors installed on the commercial ship in the laboratory, whose model has been scale tested. According to the reliability analysis, the reliability index of the structure decreases with time as a result of corrosion and fatigue failures. The utilization of structural health monitoring data has boosted confidence in the reliability index for estimating the structure's real-life as determined by the study. The findings suggest that using the reliability criterion and health monitoring data during the design stage can provide a better knowledge of the structure's performance throughout time, according to the environmental conditions.

doi: 10.5829/ije.2022.35.09c.13

1. INTRODUCTION

It is critical to ensure the safe operation of marine ships as well as the prevention of contamination caused by the destruction of these structures. To accomplish this, a thorough understanding of the ship's structure and the loads applied to it is essential. Because the loads applied to the structure of ships are uncertain, and correct identification of damages generated in the structure is difficult and expensive, it is required to develop a realistic analytical process for the structure. To account for existing uncertainties and give a realistic analysis, the use of probabilistic approaches in the study of engineering structures has increased in recent years. The use of structural reliability analysis methods has increased due to the strength of the structure and the loads applied to it to determine the remaining life, determine the periods of inspection and maintenance at the time of

service of the structures, and is becoming a major trend in the study of these structures. Existing uncertainties in structural and loading characteristics are determined using mathematical theories of probabilities, stochastic variables, random and statistical processes. Analysis, design, and optimization of high-risk structures such as nuclear power plants, dams, maritime structures, and other high-risk industries are among the areas of application. The range of structural behavior includes stress analysis, dynamic, deformation control, creep and release, failure, fatigue, and structural stability. Preliminary studies in this field have been conducted by Freudenthal [1] undertook preliminary research in this area, taking into consideration statistical and probabilistic methodologies in characterizing the nature of the reliability index. Engineers and academics have significantly applied reliability estimation and analysis methodologies for structures with defects in pressurized

*Corresponding Author Institutional Email: sadeghian2@aut.ac.ir
(M. Sadeghian)

components with the development of reliability engineering and probabilistic failure mechanics.

By categorizing tasks into random variables, stochastic process reliability analysis models, and stochastic field reliability models, Bjerager [2] presents a case of structural reliability methods.

Cizelj et al. [3] employed first and second-order reliability methodologies, as well as various modeling methods, to assess the safety of steam generator pipes with axial stress corrosion cracking. They calculated data scatter relating to pipe geometry, material parameters, and crack progression using the probabilistic failure mechanics model. They focused on the impact of the maintenance technique and compared the outcomes of real-world numerical examples from each method. Using the supplied formulae for loads applied to the structure, on the other hand, may result in unrealistic analytical results.

As a result, using the findings of structural health monitoring can provide meaningful data to analysts when evaluating the ship structure's performance accuracy. Vibrational methods have a specific place in damage identification among structural health monitoring techniques. Applying these techniques for monitoring structural health, in addition to the possibility of using them during ship operations, can assist in detecting damages early in their development and preventing major structural damage. These techniques rely on sensors and equipment deployed on the structure to extract information from measured signals. The vibrational properties of each structure are unique. As a result, variations in these vibrational qualities imply structural damage. These techniques rely on sensors and equipment deployed on the structure to extract information from measured signals. The vibrational properties of each structure are unique. As a result, variations in these vibrational properties imply structural damage. According to previous study, more than 40% of fatigue-induced failures in ship structures, such as cracks, occur in the side shell of the hulls and at the junction of longitudinal and transverse stiffeners [4].

As a result, studies have been carried out to identify damages caused by fatigue due to cracks in an aluminum stiffener plate in a ship's hull [5] as well as damages caused by corrosion of the ship's hull plate [6, 7]. These damages will increase due to the compressive forces created by the impact of sea waves on the ship's side shell, potentially causing serious damage. Removing a ship from operation for health monitoring or structural repairs is time-consuming and expensive. Therefore, the health of the ship's side shell joints should be monitored continually and throughout operation using methods such as vibration methods and their vibration characteristics, which can vary as a result of damage.

Fatigue failure is also one of the most serious damage events that can occur on a ship [8, 9]. Sea waves and the

surrounding environment cause fatigue failure on ships. Estimating a ship's expected life is a difficult and generally ambiguous process. The development of high-strength steel, however, has resulted in the design of ships that can withstand higher stresses. As a result, experts have performed substantial research in this area. With this in mind, Chen et al. [10] have established a relationship between microstructures and fatigue life in steel marine structures. Bea et al. [11] devised and established a method for determining the fatigue life of critical marine ship components. They also examined a set of cracks that had formed on a ship. They discovered that around 40% of the cracks were formed at the intersection of the ship's vertical bulkheads, 10% in the ship's floor bulkheads, and 10% in the ship's transverse stiffeners, out of a total of 3,600 cracks. Many cracks in marine ships originate at the intersection of the ship's vertical walls and transverse bulkheads in general. These locations are subjected to the most dynamic loads [12].

Currently, extensive activities have been performed related to the reliability-based design in the field of the ship structure reliability assessment [13]. Based on the moments given to both calm water and waves, Akpan et al. [14] computed the ultimate strength of the ship's middle section. They evaluated their model for corrosion and fatigue-induced cracking, as well as estimating structural reliability under random loads. Liu et al. [15] used data from structural health monitoring systems in conjunction with a failure mechanics technique based on S-N diagrams to estimate and analyze reliability using probabilistic distribution functions to estimate the ship's lifespan under fatigue-induced damage. Based on structural uncertainties, statistical data and S-N diagrams were utilized to assess longevity and reliability.

Okasha et al. [16, 17] assessed the reliability and damage detection of a fast mono-hull ship based on structural health monitoring. By integrating the information obtained from structural health monitoring through Bayesian method, they determined the reliability of the structure under the uncertainties exist in a ship considering corrosion-induced damage. Deco et al. [18] evaluated the reliability of the ship structure based on the initial and ultimate failure in different sea forces. Kwon and Frangopol [19, 20] evaluated the reliability of a ship structure under simultaneous corrosion and fatigue failures. In this study, they presented their results on stormy sea forces as well as various damage scenarios. Also, assessed and estimated the life cycle of the fast ship structures under fatigue-induced damages. In this study, fatigue and its due failure are presented based on the S-N failure criterion using the model test results in the pond. Zayed et al. [21] evaluated the stability of a ship structure under static moments caused by calm water and wave-induced moments. The employment of rapid techniques has been addressed in this study to calculate moments and

section modulus of a commercial ship under the uncertainties imposed by the ship's geometry.

Zhu et al. [22] used information and data generated by health monitoring systems to evaluate the structural reliability of three different sections of big and commercial ships and analyzed the structural reliability under different sea forces.

Campanile et al. [23] investigated the reliability of a cargo ship in both intact and damaged states under a pure moment. In this study, the second-order reliability method was used to estimate the reliability under corrosion-induced damage. Doshi et al. [24] have investigated the reliability of a large cargo ship with a failure mechanics approach under the uncertainties of the ship structure. They used a Bayesian method to update the forces applied to the ship.

In this study, the reliability assessment of the ship structure is reported, using structural health monitoring data under the two damage factors of fatigue and corrosion. A Bayesian inference method was utilized to update the distribution of loads applied to the structure to implement the structural health monitoring data. The proposed mathematical model is studied and analyzed using the data output of the force sensors installed on the commercial ship in the laboratory, whose model has been scale tested. The planned ship's reliability under corrosion and fatigue damage, as well as the existing uncertainties, demonstrates that the structure's reliability will decrease with time.

2. THEORY

2. 1. The limit State of Ultimate Resistance (Range of Strength)

The ship hull risk assessment requires the determination of the limit resistance function with respect to the ship hull structure. The ship hull consists of a continuous and integrated girder under transverse load caused by still water without considering the waves. The model governing the ultimate resistance state can be calculated from the following Equation (1) [14]:

$$g(t) = U(t) - M_L(t) \quad (1)$$

where $U(t)$ is the ship's ultimate resistance capacity model and $M_L(t)$ is the external load effect model on the ship. The overall resistance capability of a ship's hull is reduced due to the wear of the ship's hull over time. The vertical bending moment parameters, which include the hull curvature, are specified in Equation (3). Random functions 2 and 3 define the final failure function of the primary carrying girder.

$$U(t) = M_u(t) \quad (2)$$

$$M_L(t) = M_{sw}(t) + k_w[M_w(t) + k_D + M_{dyn}(t)] \quad (3)$$

where M_u is the ultimate capacity of the bending moment of the main beam, M_{sw} shows the bending moment resulted from the still water surface, M_w is the bending moment caused by the wave, k_D is the correction coefficient between the bending moment of the wave and the dynamic bending moment, M_{dyn} indicates dynamic bending moment. k_w is the correlation coefficient that depends on the bending due to stress in the sagging state or stress in the hogging state [25, 26].

2. 2. Fatigue Assessment and Analysis Methods

There are two fundamental approaches for determining a structure's fatigue life:

1. Using lab data (such as the stress-life method or strain-life method),
 2. Using the failure mechanics method (Paris law),
- Stress-life or strain-life methods are prepared by performing several tests on the connection with specific details under intermittent loads with a high number of repetitions (the required number of repetitions for fatigue failure) at a specified stress level, whereas in the failure mechanics method, the crack growth rate in an existing defect and its development are taken into account.

2. 2. 1. S-N Diagram Method in Reliability Assessment

The S-N diagram method is considered the baseline strength and estimates the crack starting from a critical component of the structure as a function of some stress cycles. To perform this, the Palmgren-Miner rule (usually a linear sum) is applied [27]. The S-N curve is determined experimentally based on the type of material and the type of structure (geometry, direction, and welding quality), environmental conditions (air, corrosion, or cathodic protection), and by using linear regression analysis of the test results for a given confidence interval [28, 29].

$$\Delta S = \left(\frac{K}{N}\right)^{\frac{1}{m_f}} \quad (4)$$

where ΔS is the stress changes, N shows the number of cycles required for fatigue failure with a constant double value of the stress amplitude, m_f is the negative slope of the S-N curve, plotted on the log-log diagram, and K is the S-N curve parameter for a given confidence interval. Damage can be written as Equation (5):

$$D = \frac{N_s}{K} E[\Delta S^{m_f}] \quad (5)$$

where N_s is the total number of cycles during the operation time and $E[\Delta S^{m_f}]$ is the expected or mean value of ΔS . the long-term density probability function of the stress amplitude can be evaluated with respect to the local load using the Weibull distribution [30, 31]:

$$f(\Delta S) = \frac{\zeta}{w} \left(\frac{\Delta S}{w}\right)^{\zeta-1} \exp\left(-\frac{\Delta S}{w}\right)^{\zeta} \quad (6)$$

where ζ is the shape factor, W is the scale factor, and ΔS shows the stress changes. Thus, considering Weibull distribution, the amount of stress amplitude is:

$$S_{re} = E[\Delta S^{m_f}] = W^{m_f} \Gamma\left(1 + \frac{m_f}{\zeta}\right) \quad (7)$$

Also, the mean value of the stress amplitude can be obtained according to the relation provided by Miner [19]:

$$S_{re} = \left[\sum_{i=1}^{n_i} \frac{n_i}{n_{total}} S_{ri}^{m_f} \right]^{\frac{1}{m_f}} \quad (8)$$

where n_i is the number of cycles in stress amplitude. According to the changes of the occurrence probability according to the sea forces and the speed of the ship, it can be written [19]:

$$S_{re}^* = \left[\sum_{i=1}^{SS} \sum_{j=1}^{SP} \sum_{k=1}^{WH} P_{SS,i} P_{SP,j} P_{WH,k} S_{re,ijk}^{m_f} \right]^{\frac{1}{m_f}} \quad (9)$$

where $P_{SS,i}$ is the occurrence probability at i th sea forces, $P_{SP,j}$ shows the occurrence probability in j th velocity, and $P_{WH,k}$ is the occurrence probability in k th wave of the forecastle. Also, for the number of cycles, we have:

$$N_{avg}^* = \left[\sum_{i=1}^{SS} \sum_{j=1}^{SP} \sum_{k=1}^{WH} P_{SS,i} P_{SP,j} P_{WH,k} N_{avg,ijk} \right]^{\frac{1}{m}} \quad (10)$$

Finally, the number of annual cycles is equal to:

$$N(y) = N_{avg}^* \alpha 365y \quad (11)$$

where α coefficient expresses the service percentage by the ship at sea ($\alpha = 50\% .75\% .90\%$). ultimately, the limit state function is extracted to evaluate the reliability based on the S-N curve, as Equation (12) [32]:

$$g(y) = \Delta - D(t) \rightarrow g(t) = \Delta - \frac{N(y)}{K} E[\Delta S^{m_f}] \quad (12)$$

2. 3. Corrosion Assessment and Analysis Methods

Ship structure oldness overtime result to decrease of final strength capacity. The Equation (1) is specified the vertical bending moment parameters such as hull

bending. Final bending moment capacity of hull girder is calculated by Equation (13) [14]:

$$M_u(t) = \phi \sigma_u Z(t) \quad (13)$$

That ϕ non-dimensional factor known as buckling knock down factor, σ_u ultimate strength of the ship hull cross section and $Z(t)$ is the midship hull elastic section modulus. In cases where a relationship between damage, such as fatigue crack and corrosion, and σ_u can be established, σ_u should be replaced with that relationship. It is well known that structural degradations will affect the hull girder capacity by reducing the section modulus $Z(t)$ depends on time. The impact of the degradation mechanisms and the modeling strategies that are adopted herein are presented in the following sections. The buckling knock down factor is of high variability and depends on the ship type or class and the location of a section.

Corrosion decreases the section modulus of the ship hull structure by thinning the thickness of primary structural members and also it reduces the ability of the structure to resist the externally induced bending moment. Some several models of general corrosion growth have been suggested [33]. The current model in this paper is the Equation (14) [14].

$$r(t) = C_1(t - t_0)^{C_2} \quad (14)$$

where $r(t)$ is thickness decreasing rate, t_0 is the life of coating by year, t is the age of the vessel by year, C_1 and C_2 are coefficients of random variables. C_1 represents rate of annual corrosion and although C_2 can take values ranging from 1/3 to 1. The life of coating varies for different vessels and depends on the coating type [14]. Thus the moment capacity is given by:

$$M_u(t) = \phi \sigma_u \begin{cases} Z(r(t_0)) & t \leq t_0 \\ Z(r(t)) & t > t_0 \end{cases} \quad (15)$$

According to Equation (15) $Z(t)$ is presented as collected data from Figure 1, prediction equation for reducing of hull girder section module compare to initial amounts bring at Table 1.

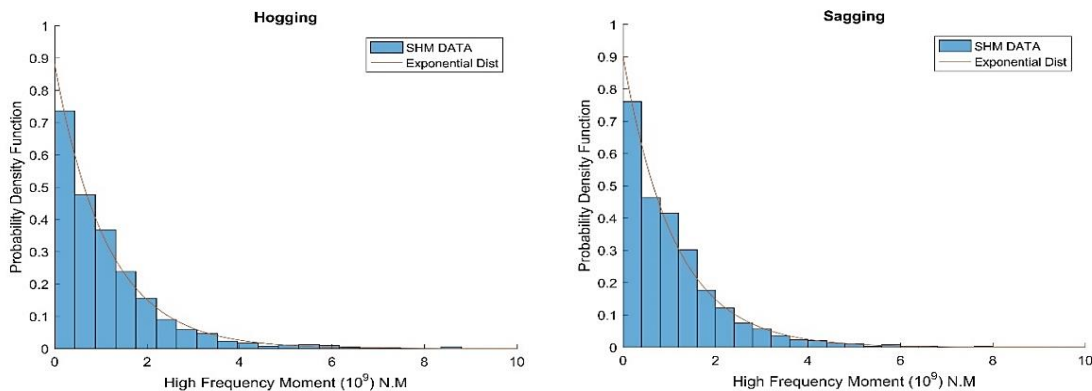


Figure 1. Histogram and probability density function for high frequency moments in sagging and hogging modes

TABLE 1. The equation of prediction mean amount and reducing of hull girder section module standard deviation [34]

Amount	Reducing of hull girder section module	Year
mean	$R_m(t) = \frac{0.62(t - 6.5)^{0.67}}{100}$	$t > 6.5$
mean + standard deviation	$R_{m+\sigma}(t) = \frac{0.8(t - 5)^{0.75}}{100}$	$t > 5$
Standard deviation	$R_{m+\sigma} = R_{m+\sigma}(t) - R_m(t)$	$t > 6.5$

The replacement of mean amount equation plus standard deviation at Equation (15) concluded to main hull girder bending moment capacity.

$$M_u(t) = x_u \phi \sigma_u S_m \left[1 - \left(0.8 \frac{(t-5)^{0.75}}{100} \right) \right] \quad (16)$$

where x_u is the random variable representing modeling uncertainty in ultimate strength and S_m is main or initial hull girder bending moment capacity [34].

2. 4. Bayesian Theory and Inference Method

Bayesian theory can also be generalized from discrete to continuous problems. Assuming that a set of parameters (θ) must be inferred, all current knowledge of these parameters is represented by $f'(\theta)$, which is called the prior distribution. The choice of the prior distribution type reflects the perceptual knowledge associated with the uncertainty of the parameter before observing the new event. In fact, it is assumed that this distribution has the ability to explain the data with some degrees of uncertainty. Measuring observed data (D) has been done on a value corresponding to (θ). This information can be used to update the distribution (θ) to achieve the posterior distribution $f''(\theta)$ as follows [35]:

$$f''(\theta) = \frac{L(\theta)f'(\theta)}{\int L(\theta)f'(\theta)d\theta} \quad (17)$$

In the above relation, $L(\theta)$ is the likelihood function θ , which is proportional to the probability $P(D|B)$, and is equal to the probability of observing the data D under the condition θ . The denominator to the right of the above relation is equal to a normalizing constant value which is called normalizer. According to this constant, the above relation is represented as Equation (18) [22]:

$$f''(\theta) \propto L(\theta)f'(\theta) \quad (18)$$

Using the law of total probability of the posterior predictive distribution for the variable x are calculated on the basis of the updated variables in Equation (19).

$$f'_x(x) = \int_{-\infty}^{\infty} f_x(x|\theta)f''(\theta)d\theta \quad (19)$$

In the current study, the posterior distribution has a log-normal distribution. The univariate log-normal distribution is equal to [36]:

$$f(\mu_n) = \frac{1}{\zeta \mu_n \sqrt{2\pi}} \exp \left[-0.5 \left(\frac{\ln \mu_n - \lambda}{\zeta} \right)^2 \right] \quad (20)$$

where λ and ζ are the parameters of the log-normal distribution and are calculated as Equation (21):

$$\zeta = \sqrt{\ln \left(1 + \frac{\sigma^2}{\mu^2} \right)} \quad (21)$$

$$\lambda = \ln \mu - 0.5\zeta^2$$

Also, for two-variable log-normal distribution, it can be written [22, 36]:

$$f(\mu_n, \alpha_n) = \frac{1}{2\pi\zeta_1\zeta_2\sqrt{1-\rho^2}} * \frac{1}{\mu_n\alpha_n} * \exp \left(-\frac{1}{2(1-\rho^2)} (A^2 - 2\rho AB + B^2) \right) \quad (22)$$

For A and B , we have:

$$A = \frac{\log(\mu_n) - \lambda_1}{\zeta_1} \quad (23)$$

$$B = \frac{\log(\alpha_n) - \lambda_2}{\zeta_2}$$

Also, λ_1 , λ_2 , ζ_1 and ζ_2 are distribution parameters. The likelihood distribution in current study has a final value distribution (extreme value theory) of the first kind. For this distribution you can write [35]:

$$f_{Y_n} = \frac{1}{\alpha_n} \exp \left(-\frac{(y-\mu_n)}{\alpha_n} \right) \exp \left(-\exp \left(-\frac{(y-\mu_n)}{\alpha_n} \right) \right) \quad (24)$$

where μ_n and α_n are Farin distribution parameters. Also, the relation between these parameters and standard deviation is equal to:

$$\mu = \mu_n + 0.57721\alpha_n \quad (25)$$

$$\sigma = \frac{\alpha_n \pi}{\sqrt{6}}$$

2. 5. Reliability Assessment

Based on the reliability theory, the limit state function can be defined based on the difference between stress (load) and resistance [29, 37].

$$g(t) = R - S \quad (26)$$

where $g(t)$ is the limit state function, R is resistance and S shows stress or applies load. If $g(t) \geq 0$, the operation of the structure can be in the safe margin, but if $g(t) \leq 0$, it indicates the failure range. The probability of failure is expressed as follows:

$$P_F = P(L(t) < 0) \quad (27)$$

Given the complexity of Equation (27), it will be very difficult to evaluate and analyze the equation. Therefore, in order to evaluate and analyze in this case, the reliability index assessment method can be used.

3. APPLICATIONS

3. 1. The Model under Study In this study, health monitoring data, which was scale-tested by body-mounted sensors in the laboratory, was used to assess reliability [38]. The specifications of the middle section of the ship in study for the implementation of reliability evaluation calculations is shown in Table 2. Auther used data from the ship's middle section, which included 21 tests at a speed of 35 knots, a temperature of 0° , and seven sea forces. Each test consisted of approximately 3200 to 4000 samples. There were 73,800 data points in total. The sample rate was set to 200 HZ. The duration of the test was around 6.15 minutes. All data was converted, taking into account the landing scale factor in the ship's actual dimensions. Bending moment, time and modulus of section were converted with the scales of $1.025\lambda^4$, $\sqrt{\lambda}$ and $0.346\lambda^4$, respectively. The measured time of the full-scale experiment was 42.28 minutes. The signals obtained from the structural health monitoring in the middle section of the ship are filtered and the high and low-frequency waves are separated. A developed extraction algorithm has been used to extract the maximum moments obtained from the wave cycle [38].

3. 1. 1. Middle Section Resistance Modeling

The bending strength for the initial failure and the ultimate flexural bending strength are calculated. For this purpose, the calculations are conducted according to the random variables, t plate thickness, E elasticity modulus, σ_{yp} yield stress, and σ_{ys} stiffener yield stress which have a log-normal distribution with COV of 0.05, 0.03, 0.1 and 0.1, respectively. The amount of residual stress is also considered equal to 5% of the plate yield stress. For each sample, the initial and ultimate bending moments of the failure are calculated and the results of the total moments

in each case are used for fitting the probability distribution. This has been repeated for 30 years over a period of 2 years, each time the web thickness and the flange stiffener has increased due to the decrease in thickness caused by corrosion over time. Table 3 shows the standard deviation and the mean annual normal log corrosion rate assumed for parameter C1 relative to the location of the stiffener plate.

3. 1. 2. High-frequency Waves Modeling

The choice of exponential distribution can be criticized since its value in the most probable case is zero. In fact, for evaluation and design, the obtained results require extrapolation to distribute the final values. The values obtained for the two modes of sagging and hogging are presented in Table 4.

3. 1. 3. Calculating the Previous Loads

The bending moment due to still and wavy water has been calculated using the equations provided by the International Association of Classification Societies (IACS (95)) [39, 40]. The change of these moments is calculated by considering the moment caused by still water and the bending moment caused by the wave with normal distribution and the first kind of final value with COV equal to 0.15 for both moments. A summary of these results is shown in Table 5.

3. 2. Updating Parameters

3. 2. 1. Structural Reliability Assessment Considering Previous Loads

The reliability of the middle section of the ship is assessed for two modes of sagging and hogging over a period of 30 years. For this purpose, the reliability of the structure has been evaluated using Equation (3). The specifications of the parameters are presented in Table 6.

TABLE 2. Geometrical profiles of the components [38]

Stiffener number	Stiffener plate height $d(mm)$	Stiffener plate thickness $t_w(mm)$	Stiffener plate width $b(mm)$	Flange plate thickness $t_f(mm)$
1	125.5	4.4	100.6	5.3
2	200.4	4.3	100.1	5.2
3	250.7	4.8	100.6	5.3
4	206	6.2	102.1	8
5	304.5	5.6	101.3	6.7
6	308.9	6	101.9	8.9
7	258.3	6.1	146.1	9.1
8	349	5.8	127	8.5
9	204.7	7.2	166.1	11.8
10	173.5	7.7	203.2	13.5
11	616.7	13.2	230.1	22.1
12	616.2	14	325.1	21.6
13	628.4	16.5	327.7	27.7
14	911.4	19.6	418.3	32

TABLE 3. Parameter C1 for corrosion model in different parts of the ship [17]

Location	Mean (mm/year)	Standard deviation (mm/year)
Deck plates	0.008125	0.000406
Deck stiffeners	0.008125	0.000406
Wall plates	0.003750	0.000188
Wall stiffeners	0.003750	0.000188
Ship floor plates	0.021250	0.001063
Ship floor stiffeners	0.008125	0.000406

TABLE 4. The final value distribution parameters for high-frequency loads

Loading parameter	Mean (N · M)	Coefficient of variation	Distribution
Sagging	1.183*e+9	0.134	First kind final value
Hogging	1.185*e+9	0.134	First kind final value

TABLE 5. Statistical description and distribution of previous applied loads

Loading parameter	Mean (N · M)	Coefficient of variation	Distribution
Sagging for still water	1.823*e+9	0.15	Normal
Sagging for wave	3.867*e+6	0.15	First kind final value
Hogging for still water	3.283*e+9	0.15	Normal
Hogging for wave	2.729*e+9	0.15	First kind normal value

TABLE 6. Random parameters specifications

Variable	Mean	COV	Distribution
x_u	1	0.1	Normal
x_{sw}	1	0.05	Normal
x_w	0.9	0.15	Normal
k_d	1	-	-
M_{sw}	μ	0.15	Normal
M_w	μ	0.15	First kind final value

The reliability index has been calculated based on previous data. Also, the strength of the structure is considered for the both initial and ultimate failure modes. The reliability index obtained from the analysis with respect to the previous data is shown in Figure 2.

As can be seen, reliability reduces over time because of the increase in the corrosion rate as well as considering the fact that the loads applied to the structure are constant due to the effect of corrosion. The amount of reliability index in the initial failure mode is less than the ultimate failure, because in the initial failure mode, our criterion is the failure of the first component. In Hogging mode, the slope of decreasing the reliability index is higher, which can be attributed to the magnitude of wave loads in hogging mode and its incremental effect in this mode.

3. 2. 2. Time-dependent Reliability

The final strength of the ship hull $M(u)$ decreases with time in the presence of fatigue mechanisms; thus, the probability of failure is also a function of time. By changing the period t from 0 to 1, the expected service life, the amount of final strength reduction can be estimated. Therefore, the probability of instantaneous failure at a time t , can be deduced regardless of the ship's conditions in the past, using Equation (28). However, the successive annual loads and annual values, the reduction of the final strength of the ship, are interdependent and must be taken into account to estimate the reliability. This is done using advanced or time-dependent reliability estimates based on conditional probability theory. For continuous systems, the hazard rate is defined by Equation (28) [41].

$$h(t) = \frac{P_f(t_i)}{1 - \sum_{j=1}^{i-1} P_f(t_j - 1)} \quad (28)$$

where $P_f(t_i)$ is the failure probability at i th time. The value of the probability of instantaneous and time-dependent failure is shown in Figure 3.

3. 2. 3. Updating Parameter μ_n Loading data is updated considering previous loads and results obtained from structural health monitoring. For this purpose, the data is updated using the Bayesian inference method. In this research, first, the parameter μ_n of the final value distribution is considered as the desired parameter for updating the load distribution. The MCMC method has also been used to approximate this parameter with respect to Bayesian inference. The parameter μ_n is presented as a variable with a log-normal distribution whose mean is equal to the value of the prior distribution and its standard

deviation with respect to COV is equal to 10%. The results obtained from updating the parameter μ_n are shown in Figure 4.

According to Figure 4, it can be seen that after updating μ_n , the mean of μ_n has decreased in both sagging and hogging modes. The loading distribution is evaluated according to the parameter μ_n update (Figure 5). The reliability index was calculated according to the main load distribution without considering the data obtained from structural health monitoring in the previous section, which is again presented in the following Figure. By updating the load and considering the structural health monitoring data in evaluating the reliability index, which includes low- and high-frequency loads, the reliability index was evaluated in this case and compared with the previous case (Figure 6).

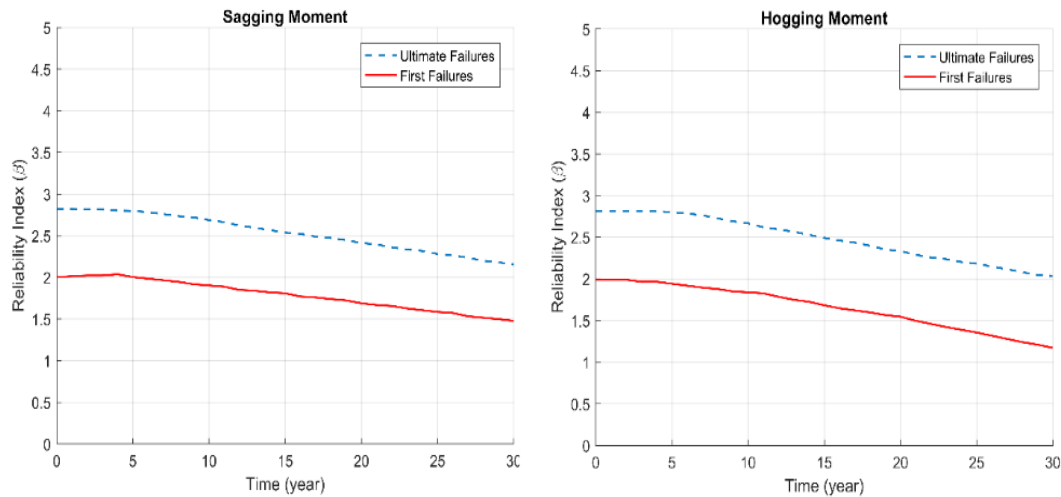


Figure 2. Reliability index considering previous loads in sagging and hogging modes

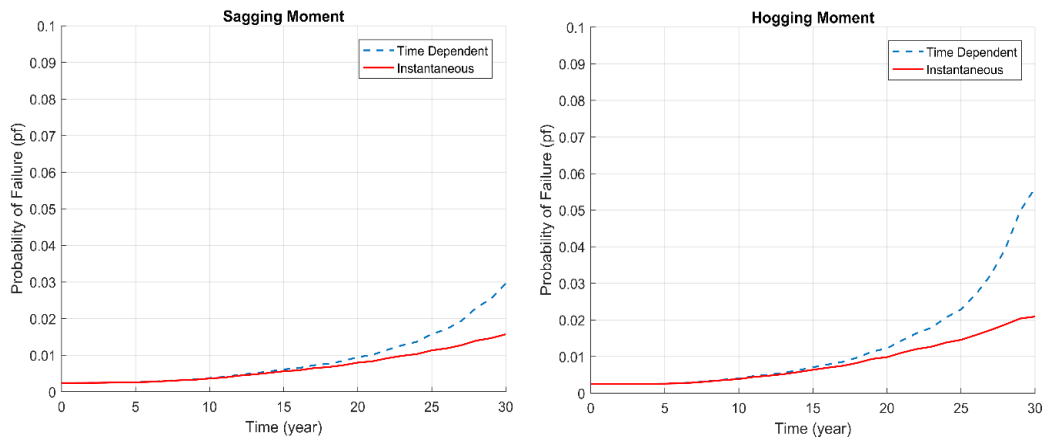


Figure 3. The probability of instantaneous and time-dependent failure

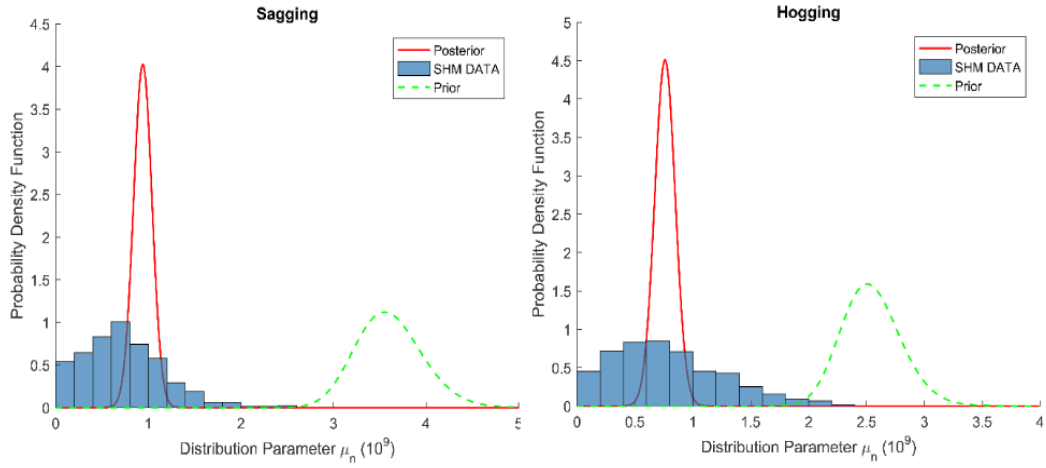


Figure 4. Updated Bayesian results for the parameter μ_n in both sagging and hogging modes

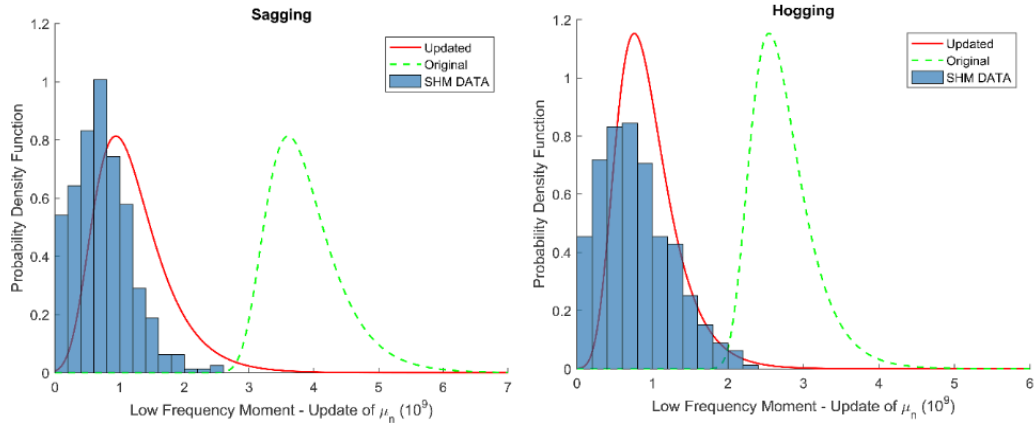


Figure 5. Main and updated loading distributions in both sagging and hogging modes according to μ_n update

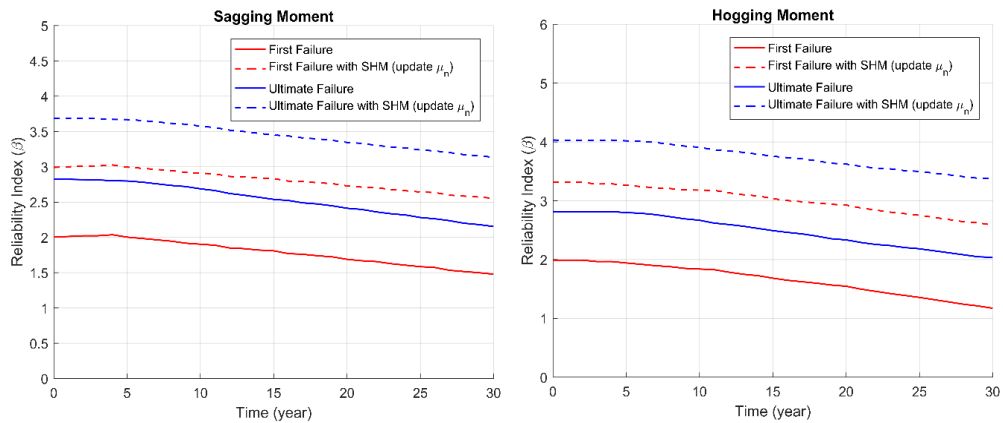


Figure 6. Reliability index evaluated according to previous data and parameter μ_n update

3. 2. 4 Updating Parameter α_n The parameter α_n of the final value distribution with the log-normal distribution has been updated, whose mean is equal to the value of the prior distribution and its standard deviation

is 10% with respect to COV. The updated distribution of the parameter α_n is shown in Figure 7.

According to Figure 7, it can be seen that the value of the parameter α_n has increased after the update. Also, the

main load distribution and the updated distribution according to the α_n update are presented in Figure 8.

According to Figure 8, it can be seen that after updating α_n , the updated loading distribution has a mean equal to the main distribution, but its standard deviation has increased. It shows that loading uncertainty has increased by considering the parameter α_n as the update criterion. The reliability index is shown in Figure 9 with respect to the main and updated loading distribution.

According to Figure 9, it can be seen that after updating α_n , the reliability index has decreased sharply, which is due to the increase in standard deviation (increase in distribution range) and the stability of the mean of distribution.

3. 3. Reliability Assessment of Fatigue

The reliability index of the ship is assessed considering data obtained from the structural health monitoring using Equation (4) to (12) and (3) values of α (0.5, 0.75, and 0.9). According to the Figures 10 and 11 are illustrated above, it can be seen that the probability of fatigue failure increases over time as well as with an increase in the value of α .

3. 4. Reliability of the Ship under Simultaneous Fatigue and Corrosion Damages

The simultaneous impact of these two phenomena on the reliability of the ship has been evaluated. The results are presented in Figure 12.

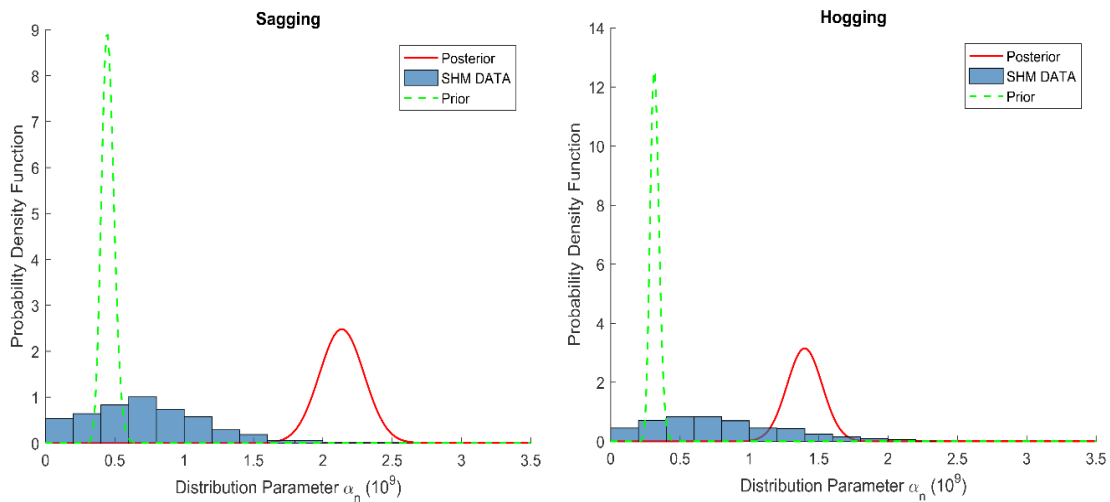


Figure 7. Updated Bayesian results for parameter α_n in both sagging and hogging modes

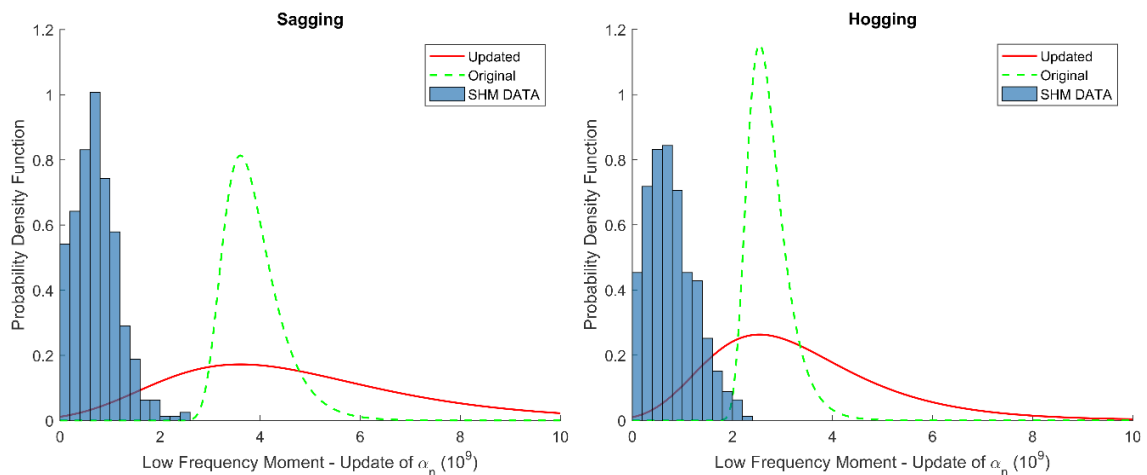


Figure 8. Main and updated distributions of loading in both sagging and hogging modes according to α_n update

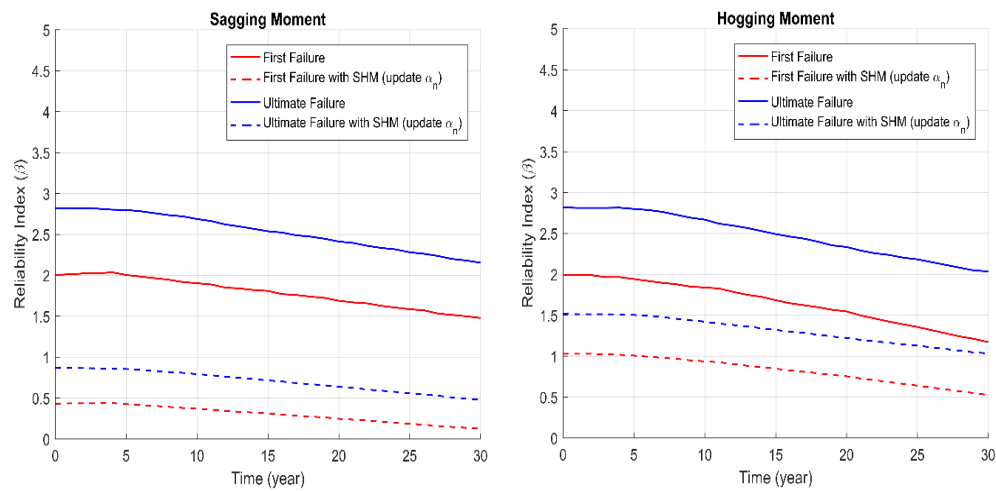


Figure 9. Reliability index assessed with respect to the previous data and parameter α_n update

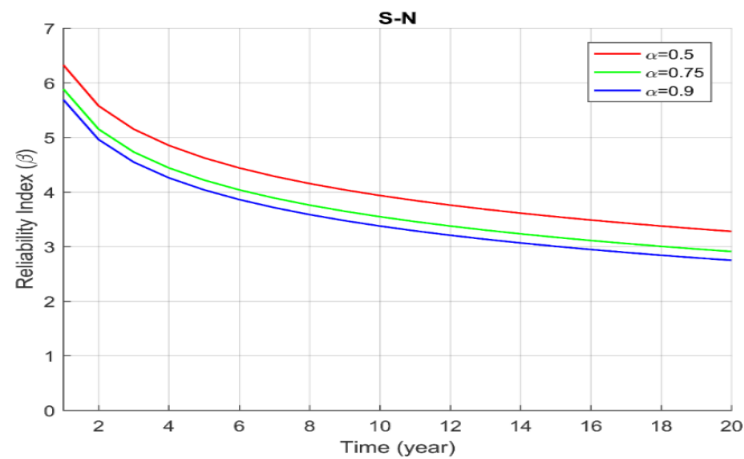


Figure 10. Reliability index of the ship versus fatigue failure considering data obtained from the structural health monitoring

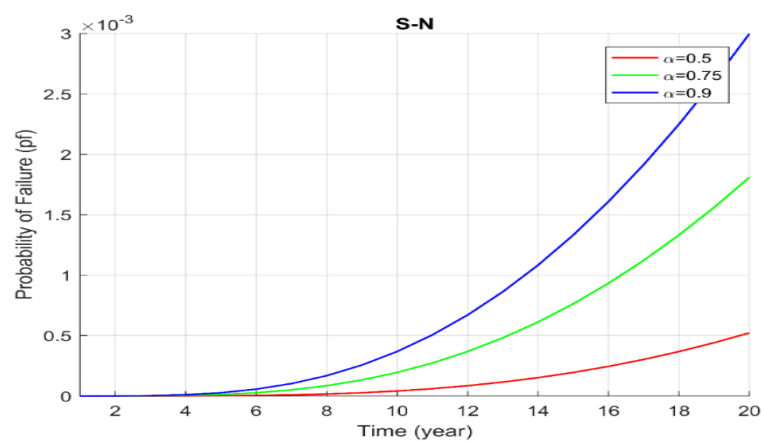


Figure 11. Failure probability of the ship versus fatigue failure considering data obtained from the structural health monitoring

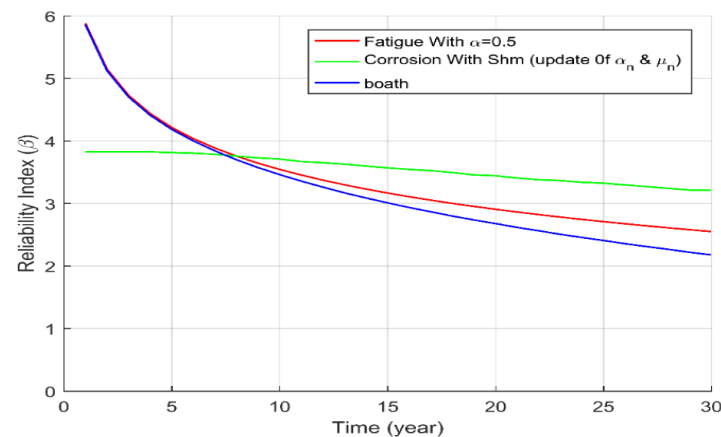


Figure 12. Reliability of the ship under the impact of fatigue, corrosion (in hogging mode) and the simultaneous impact of fatigue and corrosion

4. CONCLUSION

The reliability assessment of the ship structure is expressed under two factors: fatigue and corrosion failures-using structural health monitoring data on a commercial ship. In order to use structural health monitoring data in assessing reliability, a Bayesian inference method has been used to update the distribution of the loads applied to the structure. Given the distribution of the loads obtained from the equations in initial and ultimate failure modes, the reliability of the structure shows that considering the initial failure as an analysis criterion can lead to conservative results. The mean value of the distribution of the loads applied to the structure of the ship is decreased after updating μ_n and α_n parameters, and the value of the standard deviation of the distribution is updated and slightly increased. It leads to an increase in reliability in relation to the first case. The reliability index obtained from the structural fatigue analysis shows that in the early years of service, the ship has a very high-reliability index, but over time it has decreased sharply. Comparing the reliability index obtained from fatigue analysis with corrosion analysis shows that structural fatigue can be very dangerous, because the reliability index obtained from fatigue analysis is reduced over time with a very steep slope compared to the reliability index obtained from corrosion analysis. Also, the evaluation of the reliability index of the structure indicates that the simultaneous corrosion and fatigue damages increase the downward slope of the reliability index over time.

5. REFERENCES

- Freudenthal, A.M., "The safety of structures", *Transactions of the American Society of Civil Engineers*, Vol. 112, No. 1, (1947), 125-159, doi: 10.1061/TACEAT.0006015.
- Bjerager, P., "On computation methods for structural reliability analysis", *Structural Safety*, Vol. 9, No. 2, (1990), 79-96, doi: 10.1016/0167-4730(90)90001-6.
- Cizelj, L., Mavko, B. and Riesch-Oppermann, H., "Application of first and second order reliability methods in the safety assessment of cracked steam generator tubing", *Nuclear Engineering and Design*, Vol. 147, No. 3, (1994), 359-368, doi: 10.1016/0029-5493(94)90218-6.
- Zubaydi, A., Haddara, M. and Swamidass, A., "Damage identification in a ship's structure using neural networks", *Ocean Engineering*, Vol. 29, No. 10, (2002), 1187-1200, doi: 10.1016/S0029-8018(01)00077-4.
- Kurata, M., Lynch, J.P., Law, K.H. and Salvino, L.W., Bayesian model updating approach for systematic damage detection of plate-type structures, in Topics in model validation and uncertainty quantification, Vol. 4, (2012), Springer.85-94.
- Stull, C.J., Earls, C.J. and Koutsourelakis, P.-S., "Model-based structural health monitoring of naval ship hulls", *Computer Methods in Applied Mechanics and Engineering*, Vol. 200, No. 9-12, (2011), 1137-1149, doi: 10.1016/J.CMA.2010.11.018.
- Dong, Y., Garbatov, Y. and Soares, C.G., "Strain-based fatigue reliability assessment of welded joints in ship structures", *Marine Structures*, Vol. 75, (2021), 102878, <https://doi.org/10.1016/j.marstruc.2020.102878>.
- Zhao, W., Leira, B.J., Feng, G., Gao, C. and Cui, T., "A reliability approach to fatigue crack propagation analysis of ship structures in polar regions", *Marine Structures*, Vol. 80, (2021), 103075, <https://doi.org/10.1016/j.marstruc.2021.103075>.
- Silva-Campillo, A., Suárez-Bermejo, J. and Herreros-Sierra, M., "Design recommendations for container ship side-shell structure under fatigue strength assessment", *Ocean Engineering*, Vol. 246, (2022), 110655, <https://doi.org/10.1016/j.oceaneng.2022.110655>.
- Chen, N.-Z., Sun, H.-H. and Soares, C.G., "Reliability analysis of a ship hull in composite material", *Composite structures*, Vol. 62, No. 1, (2003), 59-66, doi: 10.1007/s00773-007-0258-5.
- Bea, R., Pollard, R., Schulte-Strathaus, R. and Baker, R., "Structural maintenance for new and existing ships: Overview, fatigue cracking and repairs", in Proceedings of the Marine Structural Inspection, Maintenance and Monitoring Symposium, II-A., (1991), 1-25.
- Bea, R., Cramer, E., Schulte-Strathaus, R., Mayoss, R., Gallion, K., Ma, K., Holzman, R. and Demsetz, L., "Ship's maintenance project", Conducted at University of California, Berkeley for US Coast Guard/Ship Structure Committee (SSC), SSC-386, (1995).

13. Mansour, A., Wirsching, P., Luckett, M. and Plumpton, A., *Assessment of reliability of existing ship structures*. 1997, DTIC Document.
14. Akpan, U.O., Koko, T.S., Ayyub, B. and Dunbar, T.E., "Risk assessment of aging ship hull structures in the presence of corrosion and fatigue", *Marine Structures*, Vol. 15, No. 3, (2002), 211-231, doi: 10.1016/S0951-8339(01)00030-2.
15. Liu, M., Frangopol, D.M. and Kwon, K., "Fatigue reliability assessment of retrofitted steel bridges integrating monitored data", *Structural Safety*, Vol. 32, No. 1, (2010), 77-89, doi: 10.1016/j.strusafe.2009.08.003.
16. Okasha, N.M., Frangopol, D.M., Saydam, D. and Salvino, L.W., "Reliability analysis and damage detection in high-speed naval craft based on structural health monitoring data", *Structural Health Monitoring*, Vol. 10, No. 4, (2011), 361-379, doi: 10.1177/1475921710379516.
17. Okasha, N.M., Frangopol, D.M. and Decò, A., "Integration of structural health monitoring in life-cycle performance assessment of ship structures under uncertainty", *Marine Structures*, Vol. 23, No. 3, (2010), 303-321, doi: 10.1016/j.marstruc.2010.07.004.
18. Decò, A., Frangopol, D.M. and Okasha, N.M., "Time-variant redundancy of ship structures", *Journal of Ship Research*, Vol. 55, No. 3, (2011), 208-219, doi: 10.5957/jsr.2011.55.3.208.
19. Kwon, K. and Frangopol, D.M., "System reliability of ship hull structures under corrosion and fatigue", *Journal of Ship Research*, Vol. 56, No. 4, (2012), 234-251, doi: 10.5957/JOSR.56.4.100038.
20. Kwon, K., Frangopol, D.M. and Kim, S., "Fatigue performance assessment and service life prediction of high-speed ship structures based on probabilistic lifetime sea loads", *Structure and Infrastructure Engineering*, Vol. 9, No. 2, (2013), 102-115, doi: 10.1080/15732479.2010.524984.
21. Zayed, A., Garbatov, Y. and Soares, C.G., "Time variant reliability assessment of ship structures with fast integration techniques", *Probabilistic Engineering Mechanics*, Vol. 32, No., (2013), 93-102, doi: 10.1016/j.probenmech.2013.01.002.
22. Zhu, B. and Frangopol, D.M., "Reliability assessment of ship structures using bayesian updating", *Engineering Structures*, Vol. 56, (2013), 1836-1847, <https://doi.org/10.1016/j.engstruct.2013.07.024>.
23. Campanile, A., Piscopo, V. and Scamardella, A., "Time-variant bulk carrier reliability analysis in pure bending intact and damage conditions", *Marine Structures*, Vol. 46, (2016), 193-228, <https://doi.org/10.1016/j.marstruc.2016.02.003>.
24. Doshi, K., Roy, T. and Parihar, Y.S., "Reliability based inspection planning using fracture mechanics based fatigue evaluations for ship structural details", *Marine Structures*, Vol. 54, (2017), 1-22, <https://doi.org/10.1016/j.marstruc.2017.03.003>.
25. Mansour, A. and Hovem, L., "Probability-based ship structural safety analysis", *Journal of Ship Research*, Vol. 38, No. 4, (1994), 329-339, <https://doi.org/10.5957/jsr.1994.38.4.329>.
26. Ayyub, B.M., Assakkaf, I. and Atua, K., "Reliability-based load and resistance factor design (LRFD) of hull girders for surface ships", *Naval Engineers Journal*, Vol. 112, No. 4, (2000), 279-296, <https://doi.org/10.1111/j.1559-3584.2000.tb03337.x>.
27. Veritas, D.N., *Fatigue design of offshore steel structures*. 2010, DNV-RP-C203.
28. Mansour, A. and Thayamballi, A., *Probability based ship design; loads and load combinations*. 1993, DTIC Document.
29. Kerdabadi, M.S., Sakaki, A. and Izadi, A., "Evaluation of ship structure reliability during design, maintenance, and repair phases", *Zeszyty Naukowe Akademii Morskiej w Szczecinie*, (2018).
30. Bowman, M. and Munse, W., "Fatigue behavior of welded steel butt joints containing artificial discontinuities", *WELDING J.*, Vol. 62, No. 2, (1983), 36.
31. DESIGN, P.B.S., "Ssc-392 probability based ship design: Implementation of design guidelines".
32. Beghin, D., "Fatigue of ship structural details, Society of Naval Architects and Marine Engineers, (2007).
33. Paik, J.K., Kim, S.K. and Lee, S.K., "Probabilistic corrosion rate estimation model for longitudinal strength members of bulk carriers", *Ocean Engineering*, Vol. 25, No. 10, (1998), 837-860, [https://doi.org/10.1016/S0029-8018\(97\)10009-9](https://doi.org/10.1016/S0029-8018(97)10009-9).
34. Câmara, M.C. and Cyrino, J.C.R., "Structural reliability applications in design and maintenance planning of ships subjected to fatigue and corrosion", in ASME 2012 31st International Conference on Ocean, Offshore and Arctic Engineering, American Society of Mechanical Engineers., (2012), 503-514.
35. Box, G.E. and Tiao, G.C., "Bayesian inference in statistical analysis, John Wiley & Sons, Vol. 40, (2011).
36. De Haan, L. and Ferreira, A., "Extreme value theory: An introduction, Springer Science & Business Media, (2007).
37. Choi, S.-K., Grandhi, R.V. and Canfield, R.A., "Reliability-based structural design, Springer Science & Business Media, (2006).
38. Devine, E.A., "An overview of the recently-completed jhss monohull and trimaran structural seaways loads test program", Naval Surface Warfare Center, Carderock Division (NSWCCD), PowerPoint Briefing, Vol. 30, (2009).
39. Nikolaidis, E., Ghiocel, D.M. and Singhal, S., "Engineering design reliability applications: For the aerospace, automotive and ship industries, CRC Press, (2007).
40. Mansour, A.E., Wirsching, P., Luckett, M., Plumpton, A., Lin, Y., Jensen, J., Jeom, K.P., Richardson, W., Hess, P. And Hutchison, B., "Structural safety of ships. Discussion. Authors' closure", *Transactions-Society of Naval Architects and Marine Engineers*, Vol. 105, (1997), 61-98.
41. De Finetti, B. and de Finetti, B., "Theory of probability, volume i", *Bull. Amer. Math. Soc.*, Vol. 83, (1977), 94-97.

Persian Abstract

چکیده

در پژوهش حاضر روند ارزیابی قابلیت اطمینان سازه کشتی تحت دو عامل خرابی خستگی و خوردگی و با استفاده از داده‌های پایش سلامت سازه بیان شده است. به منظور استفاده از داده‌های پایش سلامت سازه در ارزیابی قابلیت اطمینان، از روش استنباط بیزین برای بروز رسانی توزیع بارهای وارد بر سازه استفاده شده است. قابلیت اطمینان سازه یک کشتی تحت عامل خوردگی و با توجه به توزیع بارهای به دست آمده از معادلات، ارزیابی شده است. به منظور استفاده از داده‌های پایش سلامت سازه، از روش استنباط بیزین برای بروز رسانی توزیع بارهای وارد بر سازه استفاده شده است. از خروجی داده‌های سنسورهای نیرویی نصب شده بر روی شناور تجاری در آزمایشگاه که مدل آن بصورت مقیاس تست شده است، جهت بررسی و تحلیل مدل ریاضی پیشنهادی استفاده گردیده است. تحلیل قابلیت اطمینان عیوب خوردگی و خستگی نشان دهنده کاهش شاخص قابلیت اطمینان سازه در طول عمر آن می-باشد. استفاده از داده‌های پایش سلامت سازه، موجب افزایش اعتماد به شاخص قابلیت اطمینان تخمین عمر واقعی سازه به دست آمده از تحلیل شده است. نتایج نشان می‌دهد با استفاده از معیار قابلیت اطمینان و استفاده از داده‌های پایش سلامت در مرحله طراحی، می‌توان درک بهتری از کارکرد سازه در طول عمر سازه با توجه به شرایط محیطی بدست آورد.



Influence of Tensile Load on Bonding Strength of Asphalt Concrete Containing Modified Buton Asphalt and Polyethylene Terephthalate Waste: A Case Study of Indonesian Roads

M. Pasra^a, M. W. Tjaronge^a, M. A. Caronge^a, A. R. Djamaluddin^a, F. E. P. Lopian^b, M. Tumpu^c

^a Civil Engineering Department, Hasanuddin University, Makassar, Indonesia

^b Merauke National Road Implementation Centre, Papua Province, Indonesia

^c Disaster Management Department, Hasanuddin University, Makassar, Indonesia

PAPER INFO

Paper history:

Received 05 April 2022

Received in revised form 27 June 2022

Accepted 29 June 2022

Keywords:

Tensile Load

Bonding Strength

Modified Buton Asphalt

Polyethylene Terephthalate Waste

ABSTRACT

The natural bitumen coalesced with the sediment in Buton Island, Indonesia, is known as Buton rock asphalt (BRA). Modified Buton Asphalt (MBA) is one of the latest bitumen processing that extracted bitumen from BRA and furtherly mixed with petroleum bitumen. In Indonesia drinking bottle is made by used extensively the polyethylene terephthalate (PET) for domestic consumption. This research used PET waste of 0.5% to 2.5% of the total weight of aggregates and filler, while MBA was the main binder to produce AC-WC mixture. One mixture without PET waste and five mixtures containing PET waste of 0.5%, 1.0%, 1.5%, 2.0% and 2.5% were produced to determine the compatibility of PET with MBA related to the bonding strength of the AC-WC mixture. Indirect tensile strength test equipped with deformation measurement devices was carried out with the aim to understand the bonding strength related to the vertical stress-strain relationship, peak tensile stress, Modulus of elasticity in tension and toughness index of each mixture. The test results showed that MBA was compatible with blending with PET waste in producing compacted specimens. The results of quantitative observations showed that the presence of PET waste made the mixtures better than the mixture without PET in terms of stiffness and elastic region. The peak tensile stress of mixture increased by 45.2% to 96.8% with PET waste compared to the mixture without PET. The mixture containing PET waste was 56.09% to 157.18% higher than the mixture without PET in terms of Et. Toughness index (TI) increased with the use of PET waste up to 2.0%, but was smaller at 2.5% PET waste compared to the mixture without PET waste.

doi: 10.5829/ije.2022.35.09c.14

NOMENCLATURE

SNI	Standard National Indonesia	ASTM	American Standard Testing and Material
BRA	Buton Rock Asphalt	kPa	kilo Pascal
MBA	Modified Buton Asphalt	N	Newton
PET	Polyethylene Terephthalate	AC-WC	Asphalt Concrete Wearing Course
TI	Toughness Index	Et	Modulus of elasticity in tension
ITS	Indirect Tensile Strength	LVDT	Linear Variable Displacement Transducer

1. INTRODUCTION

In recent decades, the population growth has made the urban areas with transportation infrastructures increase in size. The sprawl in the size of transportation networks is a crucial factor in economic development of urban areas.

Development of transportation networks supported by rigid pavement, flexural pavement, and others paved road provides efficient movement of people between different areas and improves supply chain and goods distribution. In addition, an increase in vehicle volume is accompanied by the increase in vehicle axle loads.

*Corresponding Author Institutional Email: mubapasra@unhas.ac.id
(M. Pasra)

Related to the conditions mentioned above, it is necessary to develop reliable road networks with paved roads to improve safety and comfort when driving.

A reliable transportation network needs to be supported by a road layer that can bear heavy vehicle axle loads. In this regards, highway engineers continuously develop innovations to use materials at affordable prices to improve the performance of asphalt mixtures. Intensive efforts to improve the performance of asphalt mixtures for flexible roads using polymers have been reported in technical and scientific papers [1-4]. However, there is an additional cost when using virgin polymer in asphalt modification.

Today, as in many big cities in the world, people in many cities of Indonesia use plastics, including PET plastic, increasing from year to year. Plastic is a material that is difficult to decompose hence it will be stored for long time in the landfills. The lack of infrastructure to recycle plastic waste has resulted in a lot of plastic waste dumping, including PET waste being disposed in the landfills, frequently dumped into drainage or rivers that further pollute the surrounding environment.

One of the effective efforts to reduce the environmental impact caused by plastic waste, inclusive of PET waste is the utilization of PET waste as a building material, including as an additive for asphalt mixtures. PET can be categorized as one of the polymer types [4]. The potential use of PET waste as an additive material has been studied, where the test results showed the use of PET waste could improve the performance of asphalt mixtures such as stone mastic asphalt mixture [5, 6].

In Indonesia, the sustainability of national transportation infrastructure has become a prominent issue in recent decades. The effort for sustainability has driven the reuse of waste material such as PET waste, thereby decreasing the PET waste dumping and the consumption of virgin polymer.

At the same time, there are several areas in the southern part of Buton Regency, Bau-Bau Island, Indonesia, containing natural asphalt in the form of rock. A large amount of bitumen has been fused with minerals to form Buton rock asphalt (BRA), where it is estimated that the mineral and bitumen amounts are 70 and 30 percents, respectively. The bitumen contained in BRA has physical properties similar to petroleum bitumen [7, 8]. Continuous efforts are being made to optimize the use of BRA. The use of BRA in a granular form known as Buton garnural asphalt (BGA) has been widely reported to have favorable compatibility in improving the asphalt mixtures properties [9-11]. Currently, a number of BRA processing plants have succeeded in extracting bitumen from BRA. Modified Buton asphalt (MBA) is the latest product of BRA processing and development. MBA is made from bitumen extraction from BRA, which is then mixed with petroleum bitumen. The use of MBA to produce reliable hot asphalt mixtures has been widely

reported [12, 13]. However, the compatibility of MBA with waste materials such as plastic waste needs to be studied more deeply in relation to the development of eco-asphalt mixtures that support sustainable technology.

In order to obtain a reliable asphalt mixture at an affordable price, a design process is needed, which includes carrying out tests in the laboratory. Many studies promote indirect tensile strength (IDT) test as an appropriate laboratory cracking test for part of the mixture design and production control mechanism. The failure pattern of asphalt concrete specimens, the behavior of asphalt concrete under load as degeneration of the material and the limit of elasticity, can be reflected by the tensile stress-strain relationship of asphalt concrete in tensile [14-16].

One of Indonesia's most widely used road surface layers is Asphalt Concrete Wearing Course (AC-WC). This study used one of the local resources that have been developed in the form of MBA with PET waste as materials for making AC-WC. In order to understand the compatibility of PET waste with MBA concerning the bonding strength of the AC-WC mixture, one mixture without PET waste and mixtures containing PET waste from 0.5% to 2.5% by total weight of aggregates and filler (with 0.5% increments) were considered. Furthermore, this present study carried out ITS test, which was equipped with a set of LVDTs to quantify the bonding strength of AC-WC mixtures. The report presented in the present study focused on bonding strength in terms of the relationship of tensile stress-strain, tensile strength, modulus of elasticity in tension (Et) and toughness index. The present experimental investigation based on the ITS test was conducted to comprehend the influence of MBA and PET waste concurrently in the hot mixture asphalt production (AC-WC).

2. MATERIALS AND METHODS

2. 1. Modified Buton Asphalt

MBA that was obtained from a national refinery was used to fabricate asphalt concrete specimens. MBA is fairly recent production in which bitumen extracted from BRA was mixed with petroleum bitumen, and it was introduced in several national road pavement constructions in recent years.

The physical properties of the reference MBA are presented in Table 1 and fulfill by Indonesia requirement for road construction.

2. 2. PET Waste

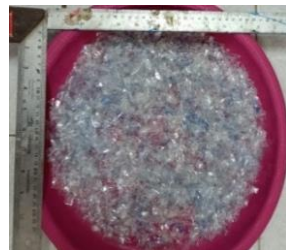
Figure 1 (a) displays the used PET bottle as a source of PET in this study. PET bottles were cut into small pieces to facilitate mixing with other materials when producing hot mixture asphalt. Figure 1 (b) shows the small sheets of PET waste obtained from

TABLE 1. Physical properties of the MBA

Property	Test Value
Penetration before loss (mm)	53.00
Softening point (°C)	53.60
Ductility at 25°C, 5cm/minute (cm)	128.50
Flash point (°C)	286.00
Specific gravity	1.11
Penetration after loss (mm)	95.80
Weight loss (TFOT)	0.20



(a) Used PET bottle



(b) Small sheets of PET waste

Figure 1. PET waste

the used bottle. The natural state, glass transition temperature and softening point of PET were a semi-crystalline resin [17-19] about 70°C and 260°C, respectively [20-22]. The average size of small pieces which are cutted by 5-10 mm.

2. 3. Aggregates and Filler

Two fractions of crushed river stone were used as coarse aggregate, viz coarse aggregate with diameter 5-10 mm and with diameter 10-20 mm, respectively. (coarse aggregate pass sieve No. ½" and retained on sieve No. 4). Coarse aggregate with diameter of 10 – 20 mm had water absorption of 2.04%, saturated surface dry density of 2.67 and abrasion of 24.26%, respectively. Coarse aggregate with a 5 – 10 mm diameter had a water absorption of 2.03%, saturated surface dry density of 2.66 and abrasion of 25.32%, respectively. The stone dust obtained from the river rock crushing process was used as fine aggregate and filler, respectively. Stone dust (fine aggregate pass sieve No. 8 and retained on sieve No. 200 (0.075 mm) that used as fine aggregate in this study had a water absorption of 2.18%, saturated surface dry density of 2.63 and sand equivalent of 89.63%, respectively. Stone dust used as filler (pass sieve no. 200) in this study had water absorption of 2.28% and saturated surface dry density of 2.65, respectively.

2. 4. Material Preparation

Preliminary research based on Marshall properties resulted the optimum level of MBA in the mixture without PET was 6.25% by weight of the mixture. MBA content of 6.25% by weight of the mixture was maintained for all mixtures in this experimental study. Table 2 shows the combination of aggregates, filler and PET waste. The use of PET waste was from 0.5 to 2.5% of the total weight of the aggregates and filler. The use of PET waste was taken into account to adjust the combined composition of aggregates, filler,

TABLE 2. The combination of aggregate, filler and PET waste

Aggregate, filler and MBA	PET Waste content (g)					
	Without PET	0.5% (5.63 g)	1.0% (11.25 g)	1.5% (16.88 g)	2.0% (22.50 g)	2.5% (28.13 g)
3/4"	-	-	-	-	-	-
1/2"	45.03	44.47	43.91	43.34	42.78	42.22
3/8"	102.03	101.47	100.91	100.35	99.78	99.22
No. 4	259.04	258.48	257.91	257.35	256.79	256.23
No. 8	228.79	228.23	227.67	227.11	226.54	225.98
No. 16	168.10	167.53	166.97	166.41	165.85	165.28
No. 30	88.50	87.94	87.38	86.82	86.25	85.69
No. 50	58.05	57.48	56.92	56.36	55.80	55.23
No. 100	54.02	53.45	52.89	52.33	51.77	51.20
No. 200	26.65	26.09	25.52	24.96	24.40	23.84
Filler	94.79	94.23	93.67	93.10	92.54	91.98
MBA				75.00 g		
Total (Aggregate, filler, MBA and PET waste)				1,200 g		

and PET waste. The combined composition of aggregates and filler changes according to the amount of PET waste content in the mixtures, but overall it does not change the composition of AC-WC mixture.

MBA, PET waste, aggregates and filler were mixed with the dry method. The mixing method in this study follows previous research and can be found elsewhere [5]. The asphalt mixtures without and with PET waste were prepared and compacted in the laboratory for indirect tensile testing. Marshall hammer was used with seventy-five blows on each side of top and bottom to produce a compacted specimen with a diameter of 101.5 mm and height of approximately 65 mm [22]. In general, three IDT specimens were tested to characterize the bond strength of each mixture design. Prior to testing, all specimens were immersed in water at room temperature for 24 hours, weighed, and subsequently immersed in water at 60°C for 30 minutes.

2. 5. Indirect Tensile Strength Test

The ITS test was carried out by applying an increasing monotonic load at a rate of 50 mm/min, which acts along the diameter of the specimen. A load cell was used to measure the load applied to the specimen. Displacements was measured using two LVDTs mounted vertically on the specimen. Load and displacements were monitored and recorded continuously using a computer-connected data logger. ITS (σ) was determined using Equation (1). Strain was obtained using Equation (2). The stress-strain relationship was obtained by using widely available software in the market. Figure 2 shows ITS test equipment. Vertical strain were derived via two linear variable differential transducers (LVDTs) measuring platen to platen displacement. The recording equipment consists of digital interface unit (data logger) connected to a computer that utilized to monitor and record data from the load actuator and LVDTs.

$$C = \frac{2P}{\pi d t} \quad (1)$$

where :

σ = Maximum stress component in the x direction on the vertical line (kPa)

P = Applied vertical load (N)

d = Diameter of the specimen (mm)

t = Thickness of the specimen (mm)

$$\varepsilon_v = \frac{\left(\frac{\Delta 1 + \Delta 2}{2}\right)}{d} \quad (2)$$

where :

ε_v = Vertical strain (mm/mm)

$\Delta 1$ = Displacement of the right part of the specimen (mm)

$\Delta 2$ = Displacement of the left part of the specimen (mm)

d = Diameter of the specimen (mm)

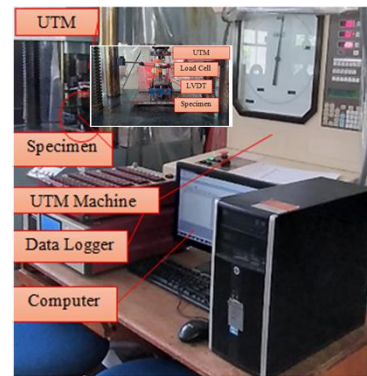


Figure 2. Indirect tensile strength test equipment

2. 6. Toughness Index (TI)

Research conducted by others [13-16] used the results of the ITS test to determine the toughness index (TI) to characterize the fatigue resistance of asphalt mixtures. TI is determined using the Equation (3).

The TI values can be used to describe the behavior of the material post-peak stress until it reaches complete failure. The amount of stress-strain energy required to accomplish the failure of the material is denoted by TI.

There is no post-peak load if the TI value is zero, and represents a brittle material. The TI was calculated using the following Equation (3) from a typical stress-strain diagram as shown in Figure 3 where, TI = toughness index, A_e = area under the stress-strain curve up to strain ε_p , A_p = area under the stress-strain curve up to strain ε_p , ε_p = horizontal strain corresponding to the peak stress, and ε = horizontal strain at the point of interest. For this study, most of the specimens pointed a maximum of 3% strain rate therefore, a strain level was selected at point of interest for calculating the TI.

$$TI = \frac{A_e - A_p}{\varepsilon - \varepsilon_p} \quad (3)$$

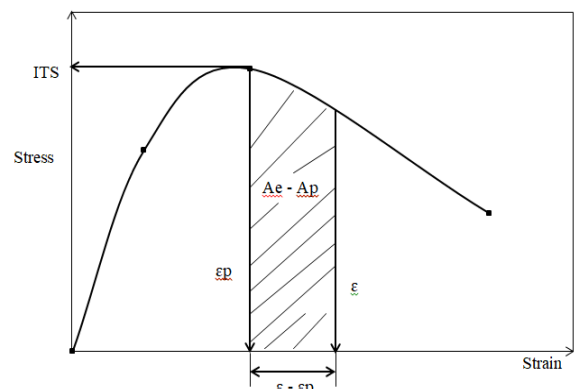


Figure 3. Toughness index

3. RESULTS AND DISCUSSION

3. 1. External Appearances of Compacted Specimen

As mentioned earlier, that the melting temperatures of MAB and PET are very different, it is very important to evaluate the compatibility between the two materials early. In this study, the initial stage of evaluating the compatibility between PET waste and MBA was visual observation during mixing. It can be observed that even mixing occurred hence the aggregates can be covered with MAB in the mixture without PET waste, as well as even mixing can be achieved in all mixtures containing PET waste, where there were no visible lumps of PET waste moreover without bleeding and segregation.

After compaction process and removed from the mold, the external appearances of specimens were observed to evaluate the compaction result. It can be observed that all specimens containing PET waste and without PET waste were successfully compacted without bleeding, as well as no visible segregation in the form of lumps of fine aggregate at specific points. Coarse aggregate skeletal with mastic containing MBA, PET waste, fine aggregate and filler was well bonded through the compaction process which was indicated by the absence of peeling of coarse aggregate or fine aggregate and no cracks due to compaction. After being removed from the immersion bath, the specimens were visually checked for external appearances to evaluate the compaction results and the effects of immersion for 24 hours at room temperature of 25 °C, followed by immersion at water with at temperature of 60 °C for 30 minutes.

3. 2. Stress-Strain Relationship under Tensile

Figure 4 shows the stress-strain relationship of mixtures used MBA as the main binder and containing PET waste and without PET waste due to tensile loads. All mixture containing PET waste from 0.5% to 2.5% have steeper slope than the mixture without PET waste. This finding shows that the stiffness of the mixture becomes better with the presence of PET waste in the mixture compared with that without PET waste.

At the relationship between tensile stress and vertical strain of mixture without PET, it can be seen that the upward path formed concave part which indicates the settling of the specimen when responding the load, where no appearance of the concave upward path of the mixtures containing PET waste. This explains that mastic asphalt made of MBA and PET waste provided better stiffness compared to mixture made only of MBA.

The relationship between stress and strain due to tensile load in mixture containing PET waste of 0.5%, 1.0%, 1.5%, 2.0% and 2.5% formed straight line up to

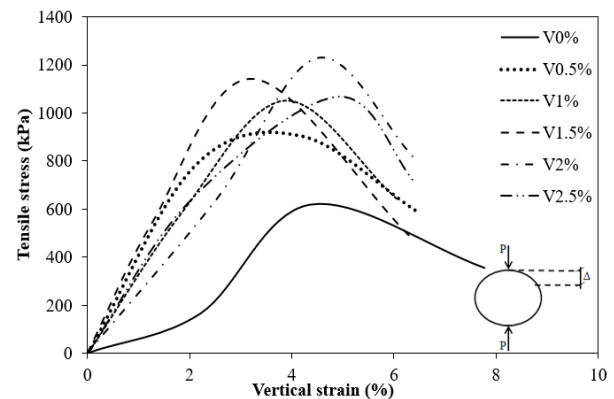


Figure 4. Tensile stress and vertical strain relationship

55%, 58%, 60%, 62% and 55% of the peak tensile stress, respectively. The elastic area is reflected by the linear portion of the tensile stress-strain curve. The presence of PET waste from 0.5 to 2.0% resulted tend to increase the linear area and then decline at 2.5% of PET.

3. 3. Peak Indirect Tensile Stress (Indirect Tensile Strength)

Figure 5 compares the average indirect tensile values of the mixtures without PET waste and containing PET waste considered in the present experimental program. The error bars presented represent one standard deviation for each mixture. The value of the indirect tensile strength of mixture without PET waste was 620 kPa while for mixture containing PET waste of 0.5%, 1.0%, 1.5%, 2.0% and 2.5% was higher about 45.8%, 69.52%, 84.03%, 98.06% and 71.93%, respectively. In addition, after the inclusion of PET from 0.5% to 2.0%, the indirect tensile strength value rises until it attains the peak point, after which it begins to decline at 2.5% of PET waste.

As the above figure depicts, after the inclusion of PET from 0.5% to 2.0%, the indirect tensile strength value

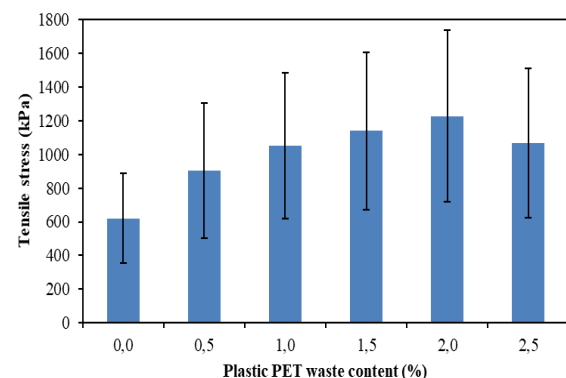


Figure 5. Peak indirect tensile stress

risks until it attains the peak point, after which it begins to decline at 2.5% of PET waste. The decrease in tensile strength at the 2.5% PET content may be attributed to the excessive PET waste enlarge the surface area that needs to be covered with MBA-based mastic, which further reduces the thickness of MBA-based mastic that bonds the aggregates.

As clearly measured in Figure 5, an increase in the value of the indirect tensile strength of the mixture containing PET waste of 0.5%, 1.0%, 1.5%, 2.0% and 2.5% toward the mixture without PET waste was 45.2%, 69.4%, 83.9%, 96.8% and 71%, respectively. The finding contributes insight that the incorporation of PET waste positively influenced the bonding strength of asphalt mixture related to indirect tensile strength.

3. 4. Tensile Modulus Elasticity (Et)

Figure 6 shows the relationship between waste PET content and the average value of the modulus of elasticity in tension. It can be observed that the average value of the modulus of elasticity in the tension of mixture containing PET waste of 0.5%, 1.0%, 1.5%, 2.0% and 2.5% was 56.09%, 92.22%, 149.06%, 157.18% and 53.66% higher than that of without PET waste. This can result from the higher bonding strength of the mixtures containing PET compared to that without PET waste.

3. 4. Toughness Index (TI)

Figure 7 displays the TI index of each mixture that represents the residual bonding strength to carry tensile loads until fracture occurs at post-peak tensile stress. The TI value of the mixture containing 2.5% PET waste was less than that without PET, while the TI value of the mixtures containing 0.5% to 2.0% PET waste was increased between 0.77% - 9.3% than the mixture without PET waste. The result confirms that the bonding strength of mixtures containing waste PET provided higher cracking resistance than that without PET waste regarding the post peak tensile stress features.

It can be observed that the average of the peak indirect tensile stress, tensile modulus elasticity and toughness

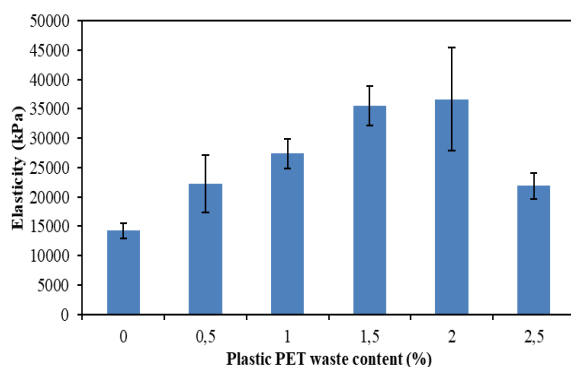


Figure 6. Tensile modulus elasticity

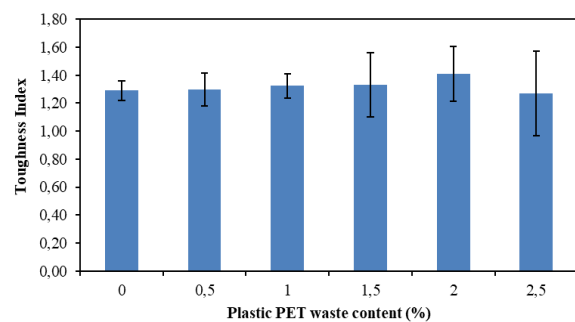


Figure 7. Toughness index

index of asphalt mixture increased until it raised the maximum value, which corresponds to 2% of the PET content, and then it decreased slightly at 2.5% of the PET.

It can be stated that the optimum value of adding waste PET is up to 2.0% to increase the bonding strength of the asphalt mixture made with MBA. The decrease in bonding strength with the addition of PET to 2.5% is based on the fact that PET changes at a temperature of around 70°C and has a high melting point of about 250°C while the maximum temperature for producing hot mix asphalt is around 180°C hence the PET in the mixture is still maintained in the semi-crystalline resin nature with little deformation. So in this study, an increase in the surface area due to addition of PET up to 2.5% caused a decrease in the thickness of the layer covered by MBA which reduces the bonding strength between MBA based mastic and coarse and fine aggregates. The results obtained by the study indicate that the physical characteristics of MBA are similar to petroleum bitumen which has the strength to cover and bind waste PET with in turn to increase the adhesive or bonding strength between mastic and aggregates and this result in line with the research conducted by Ahmadinia et al. [5-6] that used PET to improve mechanical properties of petroleum bitumen based stone mastic asphalt (SMA) mixture.

4. CONCLUSIONS

This paper experimentally evaluated the influence of tensile load on bonding strength of asphalt concrete containing MBA and PET waste. From the test results some important finding is concluded as follows:

1. The relationship between tensile stress and strain in the vertical direction shows that PET waste produced the mixture better than the mixture without PET in terms of stiffness and elastic region. Peak tensile stress (tensile strength) is higher 45.2% to 96.8% with waste PET compared to the mixture without PET. The mixture containing PET was higher 52.9% to 151.9% than the mixture without PET in terms of tensile modulus of elasticity. TI increases with PET

waste up to 2.0%, but is smaller at 2.5% PET waste compared to a mixture without PET waste.

2. This condition that observed in the experimental results showed that PET waste contributed positively to an increase in indirect tensile strength value. Besides, increased indirect tensile strength also can occur due to the modified Buton asphalt integrated adequately with PET waste to improve bonding strength between aggregate and mastic.

5. ACKNOWLEDGMENT

The research was prepared and conditioned at the Eco Material and Concrete Laboratory at the Civil Engineering Department of Hasanuddin University, Indonesia. The authors would like to express their sincere thanks to Hajrianti Yatmar, M. Eng and Muhammad Hamdar Yusri, ST, for this research through their assistance with providing helps during this study.

6. REFERENCES

1. Abdul-Mawjoud, A. and Thanoon, L., "Evaluation of sbr and ps-modified asphalt binders and hma mixtures containing such binders", *Applied Research Journal*, Vol. 1, No. 9, (2015), 460-469.
2. Ameri, M., Mansourian, A., Ashani, S.S. and Yadollahi, G., "Technical study on the iranian gilsonite as an additive for modification of asphalt binders used in pavement construction", *Construction and Building Materials*, Vol. 25, No. 3, (2011), 1379-1387, <https://doi.org/10.1016/j.conbuildmat.2010.09.005>
3. Hao, G., Huang, W., Yuan, J., Tang, N. and Xiao, F., "Effect of aging on chemical and rheological properties of sbs modified asphalt with different compositions", *Construction and Building Materials*, Vol. 156, (2017), 902-910, <https://doi.org/10.1016/j.conbuildmat.2017.06.146>
4. Leng, Z., Sreeram, A., Padhan, R.K. and Tan, Z., "Value-added application of waste pet based additives in bituminous mixtures containing high percentage of reclaimed asphalt pavement (RAP)", *Journal of cleaner Production*, Vol. 196, (2018), 615-625, <https://doi.org/10.1016/j.jclepro.2018.06.119>
5. Ahmadinia, E., Zargar, M., Karim, M.R., Abdelaziz, M. and Shafigh, P., "Using waste plastic bottles as additive for stone mastic asphalt", *Materials & Design*, Vol. 32, No. 1, (2011), 484-494, <https://doi.org/10.1016/j.matdes.2011.06.016>
6. Ahmadinia, E., Zargar, M., Karim, M.R., Abdelaziz, M. and Ahmadinia, E., "Performance evaluation of utilization of waste polyethylene terephthalate (PET) in stone mastic asphalt", *Construction and Building Materials*, Vol. 36, (2012), 984-989, <https://doi.org/10.1016/j.conbuildmat.2012.06.015>
7. Tjaronge, M.W. and Irmawaty, R., "Influence of water immersion on physical properties of porous asphalt containing liquid asbuton as bituminous asphalt binder", in Proceedings of 3rd International conference and Sustainable Construction Material and Technologies-SCTM., Kyoto, Japan. Vol. 153, (2013).
8. Arisona, A., Nawawi, M., Nuraddeen, U. and Hamzah, M., "A preliminary mineralogical evaluation study of natural asphalt rock characterization, southeast sulawesi, indonesia", *Arabian Journal of Geosciences*, Vol. 9, No. 4, (2016), 1-9, <https://doi.org/10.1007/s12517-015-2288-3>
9. Li, R., Karki, P., Hao, P. and Bhasin, A., "Rheological and low temperature properties of asphalt composites containing rock asphalts", *Construction and Building Materials*, Vol. 96, (2015), 47-54, <https://doi.org/10.1016/j.conbuildmat.2015.07.150>
10. Tumpu, M., Tjaronge, M., Djameluddin, A., Amiruddin, A. and One, L., "Effect of limestone and buton granular asphalt (BGA) on density of asphalt concrete wearing course (ac-wc) mixture", in IOP Conference Series: Earth and Environmental Science, IOP Publishing. Vol. 419, (2020), 012029
11. Mabui, D., Tjaronge, M., Adisasmita, S. and Pasra, M., "Performance of porous asphalt containing modified buton asphalt and plastic waste", *GEOMATE Journal*, Vol. 18, No. 65, (2020), 118-123, <https://doi.org/10.21660/2020.65.67196>
12. Lv, S., Fan, X., Yao, H., You, L., You, Z. and Fan, G., "Analysis of performance and mechanism of buton rock asphalt modified asphalt", *Journal of Applied Polymer Science*, Vol. 136, No. 1, (2019), 46903, <https://doi.org/10.1002/app.46903>
13. Lapien, F.E., Ramli, M.I., Pasra, M. and Arsyad, A., "The performance modeling of modified asbuton and polyethylene terephthalate (PET) mixture using response surface methodology (RSM)", *Applied Sciences*, Vol. 11, No. 13, (2021), 6144, <https://doi.org/10.3390/app11136144>
14. Kim, M., Mohammad, L.N. and Elseifi, M.A., "Characterization of fracture properties of asphalt mixtures as measured by semicircular bend test and indirect tension test", *Transportation Research Record*, Vol. 2296, No. 1, (2012), 115-124, <https://doi.org/10.3141/2296-12>
15. Modarres, A., "Investigating the toughness and fatigue behavior of conventional and sbs modified asphalt mixes", *Construction and Building Materials*, Vol. 47, (2013), 218-222, <https://doi.org/10.1016/j.conbuildmat.2013.05.044>
16. Barman, M., Ghabchi, R., Singh, D., Zaman, M. and Commuri, S., "An alternative analysis of indirect tensile test results for evaluating fatigue characteristics of asphalt mixes", *Construction and Building Materials*, Vol. 166, (2018), 204-213, <https://doi.org/10.1016/j.conbuildmat.2018.01.049>
17. Raabe, D. and Chen, N., "Recrystallization in deformed and heat treated pet polymer sheets", in Materials Science Forum, Trans Tech Publ. Vol. 467, (2005), 556-551, 4.
18. Seyler, R., "Semi-crystalline polymers: Two phases or three? An overview and perspective", *Journal of Thermal Analysis and Calorimetry*, Vol. 49, No. 1, (1997), 491-498, <https://doi.org/10.1007/bf01987476>
19. Gueguen, O., Ahzi, S., Makradi, A. and Belouettar, S., "A new three-phase model to estimate the effective elastic properties of semi-crystalline polymers: Application to pet", *Mechanics of Materials*, Vol. 42, No. 1, (2010), 1-10, <https://doi.org/10.1016/j.mechmat.2009.04.012>
20. Shu, X., Huang, B. and Vukosavljevic, D., "Laboratory evaluation of fatigue characteristics of recycled asphalt mixture", *Construction and Building Materials*, Vol. 22, No. 7, (2008), 1323-1330, <https://doi.org/10.1016/j.conbuildmat.2007.04.019>
21. Lapien, F.E., Ramli, M.I., Pasra, M., Arsyad, A. and Yatmar, H., "Application of surface response methodology (RSM) for improving the marshall quotient of ac-wc mixtures containing pet plastic waste", in Proceedings of the International Conference on Civil, Offshore and Environmental Engineering, Springer. (2021), 966-975.
22. Lapien, F., Ramli, M., Pasra, M. and Arsyad, A., "Opportunity applying response surface methodology (rsm) for optimization of performing butonic asphalt mixture using plastic waste modifier: A preliminary study", in IOP Conference Series: Earth and Environmental Science, IOP Publishing. Vol. 419, (2020), 012032.

Persian Abstract

چکیده

قیر طبیعی ترکیب شده با رسوبات جزیره بوتون اندونزی به آسفالت سنگ بوتون (BRA) معروف است. آسفالت بوتون اصلاح شده (MBA) یکی از آخرین فرآوری های قیر است که قیر را از BRA استخراج کرده و سپس با قیر نفتی مخلوط می کند. در اندونزی بطری نوشیدنی با استفاده گسترده از پلی اتیلن ترفتالات (PET) برای مصرف داخلی ساخته می شود. در این تحقیق از ضایعات PET ۰/۵ تا ۲/۵ درصد از وزن کل سنگدانه ها و پرکننده استفاده شد، در حالی که MBA چسب اصلی برای تولید مخلوط AC-WC بود. یک مخلوط بدون ضایعات PET و پنج مخلوط حاوی ضایعات PET، ۰/۵٪، ۱/۰٪، ۱/۵٪، ۲/۰٪، ۲/۵٪ برای تعیین سازگاری PET با MBA مربوط به استحکام پیوند مخلوط AC-WC تولید شد. آزمایش مقاومت کششی غیرمستقیم مجهز به دستگاه های اندازه گیری تغییر شکل با هدف درک استحکام پیوند مربوط به رابطه تنش-کرنش عمودی، تنش کششی اوج، مدول الاستیسیته در کشش و شاخص چقرمگی هر مخلوط انجام شد. نتایج آزمایش نشان داد که MBA با اختلاط با ضایعات PET در تولید نمونه های فشرده سازگار است. نتایج مشاهدات کمی نشان داد که وجود ضایعات PET باعث می شود که مخلوط ها از نظر سفتی و ناحیه الاستیک بهتر از مخلوط بدون PET باشند. حداکثر تنش کششی مخلوط با ضایعات PET در مقایسه با مخلوط بدون PET ۴۵/۲٪ به ۹۶/۸٪ افزایش یافت. مخلوط حاوی ضایعات PET ۰۹/۵۶٪ تا ۱۵۷/۱۸٪ بیشتر از مخلوط بدون PET از نظر Et بود. شاخص چقرمگی (TI) با استفاده از ضایعات PET تا ۲/۰٪ افزایش یافت، اما در ۲/۵٪ زباله PET در مقایسه با مخلوط بدون زباله PET کوچکتر بود.



Effect of Elevated Temperature on Engineered Cementitious Composites using Natural River Sand

S. Naveen*, G. Bhat

Department of Civil Engineering, National Institute of Technology, Raipur, India

PAPER INFO

Paper history:

Received 29 May 2022

Received in revised form 29 June 2022

Accepted 30 June 2022

Keywords:

Elevated Temperature

Engineered Cementitious Composites

Microstructure

Residual Compressive Strength

River Sand

ABSTRACT

Engineered cementitious composites (ECC) is a recent construction material with better properties than conventional concrete. Currently, post-earthquake, fire in a building is one of the most serious disasters. The amount and size of sand used in ECC are important parameters for the performance under thermal conditions. Micro silica sand is utilized in the majority of ECC experiments related to thermal response. The study aim is to explore the impact of river sand (RS) on the ECC performance exposed to elevate temperatures up to 800°C, through a series of experimental tests on compressive strength, mass losses, ultrasonic pulse velocity (UPV) and microstructure. For this purpose, mixes were prepared with the incorporation of RS with varying particle sizes (2.36mm, 1.18mm, 0.60mm) instead of micro silica sand. There's no spalling in ECC containing RS of varying particle sizes. The compressive strength, mass loss and UPV all reduced with increasing temperature, according to the findings. However, RS-ECC performs better with 0.60mm than 1.18mm and 2.36mm RS.

doi: 10.5829/ije.2022.35.09c.15

1. INTRODUCTION

ECC is also known as Strain Hardening Cementitious Composites (SHCC) due to its high ductility in tension [1]. Micro silica sand is used in the majority of PVA-ECC and is of 200 microns size [2]. It is expensive and difficult to obtain, using local river sand of normal size would allow ECC to be used in more practical engineering applications while saving both material cost and manufacturing cost [3, 4]. In terms of environment, it is advantageous to use waste materials like waste polymers and recycled aggregate [5].

In recent years, numerous researchers have conducted studies on the performance of ECC under high temperature. The components used (fly ash, PVA fiber and aggregate) have an effect on how well ECC performs after a fire. Additionally, variations in fly ash amount, fiber percentage, and fiber type, ECC's performance at high temperatures may vary. According to Lachemi and Li [6], the use of PVA fiber improves eliminates explosive spalling. Also, the fire resistance of ECC is improved with the addition of fly ash. The authors also

noted that when the temperature approached 400°C, the majority of the fibers melted [7]. Liu et al. [8] investigated residual properties and spalling resistance of ECC using class C fly ash rather than class F fly ash with PVA and steel fibers. Pourfalah [9] found that utilizing steel fibers increased the integrity of ECC exposed to high temperatures. According to Liu and Tan [10] adding two types of fibers (PVA and steel) is also helpful at preventing explosive spalling of ECC at high temperatures. The improvement is also observed in concrete as well like self-compacting concrete containing steel and hybrid fibers has higher mechanical properties and spalling resistance with temperature increase [11]. Wang et al. [12] briefly highlighted improved residual compressive strength under high temperatures with basalt and PVA fibers. Concrete with polypropylene fiber has a higher relative compressive strength than concrete without fibers [13]. Existing research also investigated the effect of the curing period, duration of temperature exposure and specimen type of ECC. Compared to air cooled, water quenched specimens developed better mechanical properties [14]. ECC has a high spalling

*Corresponding Author Institutional Email:
snaveen.phd2019.ce@nitrr.ac.in (S. Naveen)

resistance even after six hours of exposure to 600°C [15]. The residual characteristics of ECC are not influenced by the size of the specimen [16].

The earlier research on the impact of high temperatures on ECC using micro-sized sand has yielded important insights (110-300 microns). However, characterization of the mechanical behaviour of fiber reinforced cementitious composites under high temperature is developed, in that quartz sand is used instead of micro silica sand [17]. Another study performed on high strength ECC under impact of elevated temperatures, RS of 2 mm particle size is used [18]. One more study conducted on effect of elevated temperatures on nano-silica-modified self-consolidating ECC, as a fine aggregate RS of an average size of 450 microns is used [19], but the effect of various particle sizes at high temperatures has not been well understood. Based on the aggregate type and particle size, as well as the curing procedure, the size and connectivity of pores in a gel network may change [20]. Several studies have already pointed out the relation between the aggregate type and particle size [21]. Changes in aggregate also contribute to the overall loss of structural safety. The strength reduction depends on the specimen's moisture content, cement paste and aggregate [22]. Therefore, it is crucial to consider the impact of local RS particle size under fire. However, research on the RS-ECC with different particle sizes of RS under high temperatures is not conducted so far.

The objective of the current study is to assess the performance of RS-ECC under high-temperature for that, experimental research is done to determine how the ECC performs both before and after temperature exposure. In particular, UPV, mass loss and compressive strength are assessed. A Scanning Electron Microscope (SEM) is also used to analyze the microstructure of the composite.

2. EXPERIMENTAL PROGRAM

Figure 1 describes the flow chart of the current study and characterization methodology. For compressive strength test, 70.7 mm x 70.7 mm x 70.7 mm size cube, a 500 mm x 100 mm x 100 mm prism for flexural test are used. The flowability test is conducted to investigate the fresh characteristics of ECC.

2. 1. Materials and Specimen Preparation

ECC mixes are produced from Ordinary Portland Cement (OPC) 43 grade, Class F FA and RS confirms to zone II is used. Table 1 displays the chemical composition of binder materials and RS. In this study, Polyvinyl Alcohol (PVA) fibers with a diameter 40 microns, length 12 mm and volume fraction of 1%, were utilized. Also, PVA fibers have elastic modulus (40.0 GPa), elongation (6%).

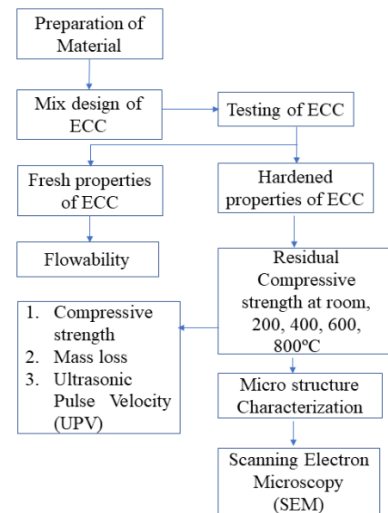


Figure 1. Flow chart of current study

To achieve the appropriate flow of mixes, a superplasticizer (Polycarboxylic type) is added.

2. 2. Specimen Preparation

In the ECC mix design, the mix proportion of a standard ECC mixture M45 (Table 2) is adopted according to literature [23]. In all the mixes, the particle sizes of RS were varied (2.36mm, 1.18mm and 0.60mm). The volume percentage of fibers is used only 1% for all mixes, higher content may leads to fiber clumping due to the larger aggregate size used in the current study. water content and superplasticizer is adjusted according to local ingredient condition and to achieve good fiber dispersion. A standard ECC mixing process is used in the production of ECC mixes [24]. The specimens were demoulded after 48 hours and cured in water before being tested.

2. 3. Elevated Temperature Exposure

The RS-ECC specimens are heated in a muffle furnace once water curing is completed. The exposure temperatures are 200°C, 400°C, 600°C and 800°C [6] and the time of exposure is determined according to ISO 834 guidelines

TABLE 1. Chemical composition of binder materials and RS from Energy-Dispersive X-ray Spectroscopy (EDS)

Chemical Composition (wt%)	CaO	Al ₂ O ₃	SiO ₂	MgO	Fe ₂ O ₃	K ₂ O	Na ₂ O
Cement	68.62	4.71	15.11	1.32	3.84	2.55	0.83
Fly ash	1.36	25.23	62.84	0.61	4.68	2.43	0.13
River sand	2.21	11.47	67.65	0.31	7.10	9.68	-

TABLE 2. Mix proportion

Mix	Mix proportion (% by weight of cement)					Volume ratio (%)
	Cement	Fly ash	Water	River sand	Superplasticizer	PVA
M0ECC [23]	1	1.2	0.66	0.8	0.013	2
M1	1	1.2	0.64	0.8	0.015	1
M2	1	1.2	0.64	0.8	0.015	1
M3	1	1.2	0.64	0.8	0.015	1

[25]. M0ECC (reference mix) and in the Mix the M letter indicates particles size T letter indicates the exposure temperature. For example, M1, M2 and M3 are Mix with 2.36mm, 1.18mm and 0.60mm passing RS and T0, T1, T2, T3 and T4 represent 28°C, 200°C, 400°C, 600°C and 800°C respectively.

3. RESULTS AND DISCUSSION

3.1. Flowability The spreading flow of RS-ECC reduced when the gradation varied from 2.36mm to 0.60mm in flowability tests for the three-particle size distribution of RS. Table 3 summarized the percentage drop in flowability concerning M1. Due to the increased specific surface area of finer RS, the flowability of RS-ECC decreases when the particle size of RS is lowered (M3). It's worth mentioning that the superplasticizer dosage is kept constant to assess the influence of RS on flowability. The spread flow achieved by M1, M2 and M3 is similar to that described by Huang et al. [26]. The flowability of ECC normal [27] is lower than the RS-ECC in current study the difference may be due change in aggregate size and fiber content.

3.2. Compressive Strength Figure 2 depicts the change in strength as a function of RS particle size. The strength of M3 is greater than that of M1 and M2. The enhancement of compressive strength is improved by finer RS particles. The possibility for fiber

agglomeration reduces as the aggregate particle size decreases. Given that 0.60mm, RS particles are significantly smaller than 2.36mm and 1.18mm RS particles, 0.60mm presented a lower probability of fiber agglomeration, which results in a weak area within the composite. Furthermore, because of its small particle size, 0.60mm may act as a filler material, thus enhancing particle packing and the matrix's microstructure. As a result, improvements in the strength of RS-ECC at all ages may be possible [28]. After 90 days the strength of M3 is 63.898 MPa. ECC employing micro silica sand achieved a similar result, according to Liu et al. [29] and Sherir et al. [30]. The strength of RS-ECC is higher than ECC normal [31], the reason may be due to change in fiber content and aggregate size.

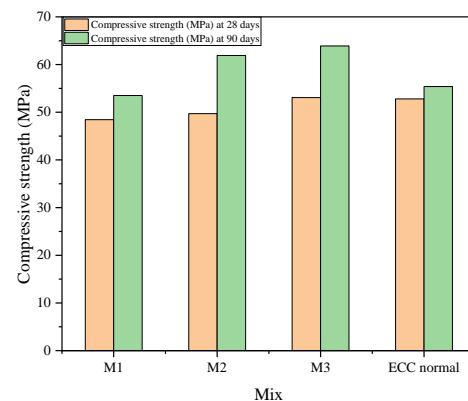
3.3. Ultrasonic Pulse Velocity

For all, the quality grading of all RS-ECC mixes meets IS 13311: 1992 criteria. Table 4 shows that the UPV of M3 is slightly higher as compared to M1 and M2. The RS-ECC increases from a particle size of 2.36mm to 0.60mm as the particle size of the sand gradation gets finer. M3 increased UPV may be related to its better compactness.

3.4. Experimental Results After Temperature Exposure

3.4.1. Mass Loss and Appearance

Figures 3 and 4 show the mass loss of the RS-ECC specimens, it is

**Figure 2.** RS-ECC Compressive strength and ECC normal at room temperature**TABLE 3.** Flowability of RS-ECC

Mix	Flowability (mm)	Percentage variation concerning M1 (%)
ECC normal [27]	180	-
M1	210	0
M2	195	7.142
M3	185	11.90

TABLE 4. UPV and the percentage variation of RS-ECC at room temperature

Mix	UPV (m/s) in days		Percentage (%) variation concerning M1 in days	
	28	90	28	90
M1	3854	3862	0	0
M2	3867	3883	0.337	0.543
M3	3911	3918	1.478	1.450

noticed that when the temperature rises, the weight of all RS-ECC specimens decreased. Dehydration happened as the temperature increases, and moisture escapes from the matrix. As a result, the specimen undergoes internal damage and weight loss. Up to 800°C, considerable weight loss occurred is seen for all the mixes. Due to the denser formation in the cementitious system, which leads to decreases hydrates decomposition rate, mass loss is lower than higher particle sizes at all exposure temperatures for 28 and 90 days [18]. Due to reduced water in the microstructure of RS-ECC, mass loss is somewhat lower at 90 days than 28 days [32].

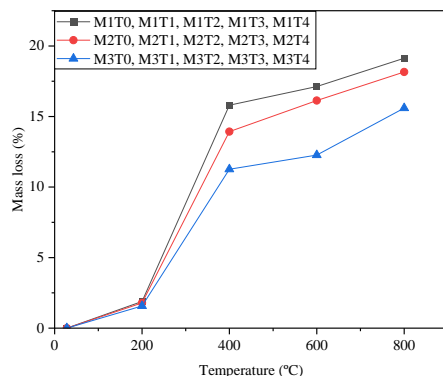


Figure 3. Mass loss of RS-ECC of 28 days after temperature exposure

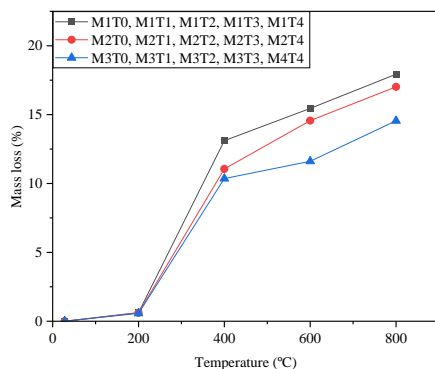


Figure 4. Mass loss of RS-ECC at 90 days after temperature exposure



Figure 5. The appearance of RS-ECC after temperature exposure: **A** 28 days; **B** 90 days

3. 4. 2. Compressive Strength at Various Temperatures

Figures 6 and 7 demonstrate the variations of normalized residual compressive strength (N_{CS}) of RS-ECC at 28 and 90 days. N_{CS} is expressed by $C_{S, T} / C_S$, where $C_{S, T}$ is the residual strength of the specimens after exposure to different temperatures, and C_S is the compressive strength at 28°C. The strength of RS-ECC increased (7% and 4%) at 200°C and 400°C after 28 days. In other study the phenomenon is obtained [33]. It is due to accelerated pozzolanic reaction, but for 90 days it shows 6.8% and 10% reduction in strength. When the specimens were exposed to 600°C the RS-ECC mix retained 76% and 63% of Compressive strength, while the residual strengths are 43% and 36% at 800°C at 28 and 90 days. The decrease in strength is due to melting of fibers, partial dehydration of C-S-H occurs between 200°C to 400°C. The dehydration of hydration products, enhanced micro-cracking and coarsening of the pore structure are the major causes of the rapid decrease in N_{CS} between 400°C and 600°C [32]. The bonding between the aggregates and the hydration products is deteriorated significantly [34]. The major reason for the loss in compressive strength after exposure to 600°C is both the

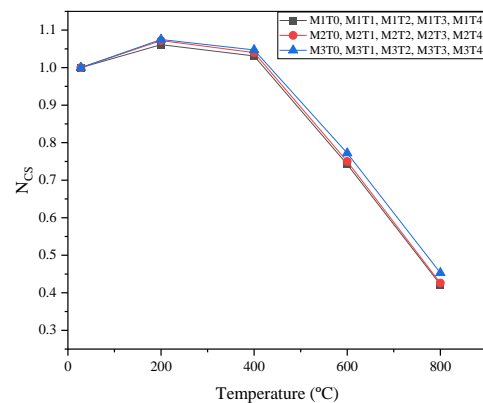


Figure 6. Normalized residual compressive strength at 28 days

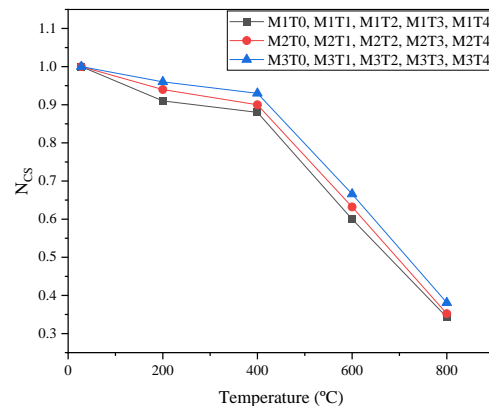


Figure 7. Normalized residual compressive strength at 90 days

physical transformation of the matrix and the chemical transformation of the hydration products [14]. Another cause might be that, due to the higher particle sizes, thermal incompatibility is expected more severe in the mix with 2.36mm and 1.18mm RS, resulting in more micro-cracks and a lower strength after exposure [35]. At varied temperature exposure for 28 and 90 days, the lower particle size of RS has greater normalized strength than the higher particle size of RS.

Figure 8 compares the normalized compressive strength of standard M45 ECC collected from literature [6, 16, 36]. The difference in strength is due to the fiber content up to 400°C, after 400°C the difference in strength is comparable with the reference literature with micro silica sand.

3. 4. 3. Stress-strain Curves The ultimate stress decreased as the temperature increases, especially when the temperature is above 400°C (Figure 9). As expected, the post-peak stress drops rapidly as the exposure temperature rises, as predicted, resulting in a smaller post-peak area under the curve. When the exposure temperature reaches 800°C, this behaviour becomes clearer. RS-ECC specimens failed immediately after reaching their maximum stress. This means that when the exposed temperature rises, the ductile characteristic of RS-ECC tends to become brittle nature.

3. 5. Ultrasonic Pulse Velocity at Various Temperatures

Figures 10 and 11, show the normalized residual Ultrasonic Pulse Velocity (N_{UV}) of RS-ECC after being exposed to various temperatures. The value of N_{UV} is expressed by $U_{V,T} / U_{V}$, where $U_{V,T}$ is the residual Ultrasonic Pulse Velocity of the specimens after exposure, and U_V is the Ultrasonic Pulse Velocity at room temperature. The N_{UV} decreased from 200°C to 800°C for all mixes, indicating that more defects and pores are formed by the decomposition of hydrates and melting of PVA fibers [17]; but, lower loss in UPV is observed for smaller particle size.

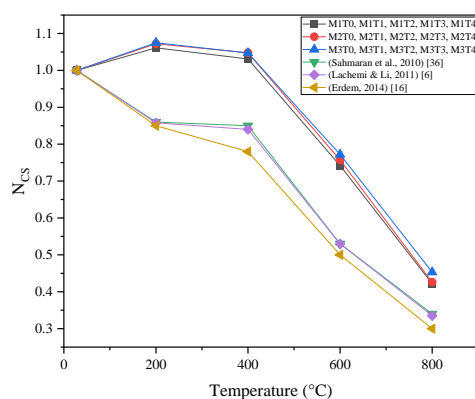


Figure 8. Comparison of Normalized compressive strength from different literature

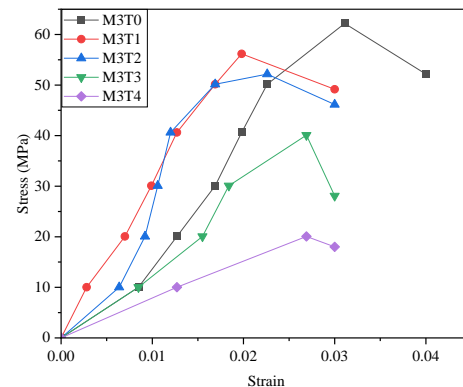


Figure 9. Stress-strain curves of RS-ECC at 90 days

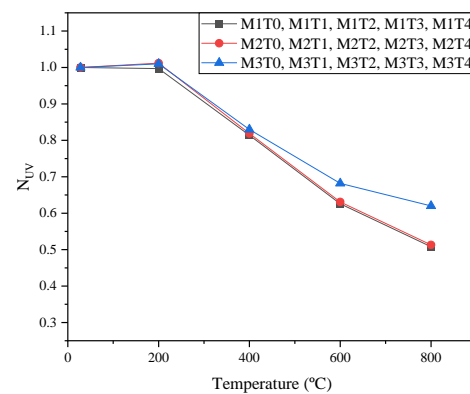


Figure 10. Normalized residual Ultrasonic Pulse Velocity at 28 days

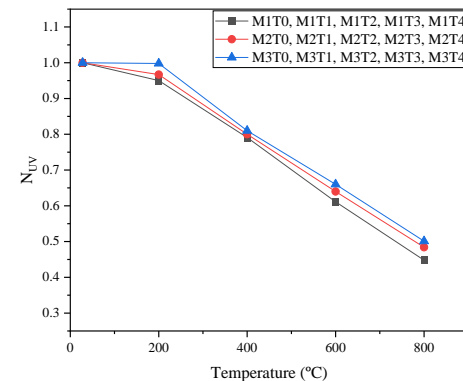


Figure 11. Normalized residual Ultrasonic Pulse Velocity at 90 days

3. 6. Microstructure of Composite Under SEM, Figure 12 shows the microstructure of post-exposure samples. It is evident that, as a result, the shrink PVA fibers separated from the matrix after exposure to 200°C, showing the burning behaviour of PVA fibers, weakening the interfacial transition zone, which might be the cause of performance loss at the macroscale. Fibers are no longer visible as the heating temperature increases to 400°C; Instead, needle-like channels developed in the

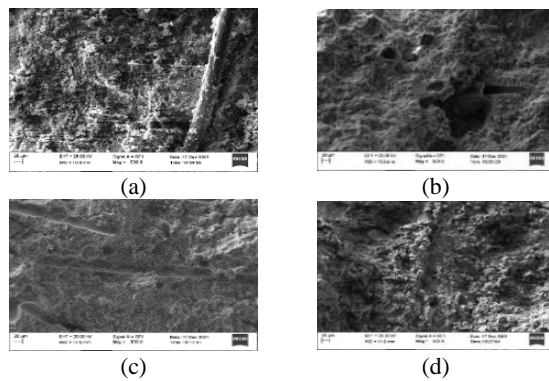


Figure 12. Transformation of PVA fibers in RS-ECC after exposure to various temperatures: A 200°C; B 400°C; C 600°C; D 800°C

PVA fiber sites. These channels offered additional pathways for water evaporation and energy dissipation, which contributed to the avoidance of spalling, longitudinal empty channels may function as an initial flaw in RS-ECC, facilitating the development of microcracks [18].

In Figure 13, it is observed that due to thermo-physicochemical reactions beyond 600°C, irregular bush-like structures are visible. Interestingly, the channels eventually fill with newly produced compounds, potentially affecting the Pore coarsening effect of cementitious composites at high temperatures. The connections and frictional forces are considerably decreased, resulting in severe damage to the strength of RS-ECC [18]. The FA had completely melted when the temperature reached 800°C. In the microstructure, more micro-pores from the inner FA are exposed, and dehydrated C-S-H gels, which are completely covered in melted FA, are not visible. The microstructure is seriously deteriorated as a result of the melting of the FA and decomposition of the C-S-H gels, resulting in strength and UPV reduction, increased mass-loss rates of RS-ECC [17, 33].

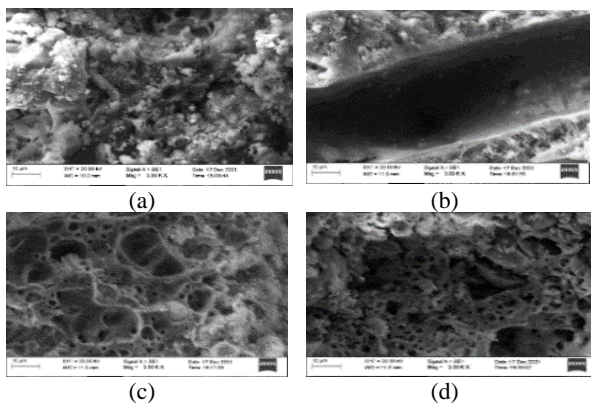


Figure 13. Microstructure of RS-ECC at various temperature exposures: A 200°C; B 400°C; C 600°C; D 800°C

4. CONCLUSIONS

The effects of varying particle sizes of river sand on the flow behavior of RS-ECC in a fresh state, as well as mechanical performance at room and elevated temperatures, are investigated. The conclusions are drawn based on study:

1. The flowability of RS-ECC is reduced for smaller particle size as compared with larger particle sizes at a constant rate of superplasticizer.
2. The compressive strength of RS-ECC mixes increased with both curing ages. But the strength is observed in with smaller particle size as compared with larger particle sizes at room temperature. With tan increase in temperature, the strength is reduced for all particle sizes, but strength loss is lower for smaller particle sizes. No spalling is observed in all RS-ECC mixes.
3. The UPV at room temperature showed slight increase for the mix with smaller particle size in comparison with larger particle sizes. Whereas at higher temperatures for smaller particle size lower loss in UPV is observed.
4. The colour of RS-ECC changed from darker at 200°C to yellowish grey at 800°C, the appearance of specimens is comparable at both 28 and 90 days.
5. At different exposure temperatures, the mass-loss increased for all RS-ECC mixes. Among all the lower mass loss is observed in the mix with smaller particle size.

5. CONTRIBUTIONS

In summary, the RS-ECC developed in this study, In the area of concrete structural engineering, certain reliable and useful experimental data is also useful to researchers and structural engineers. This would provide some theoretical background for repairing concrete structures at high temperatures. The research results are also favorable to researchers and practical engineers in the subject of ECC fire proofing.

6. LIMITATIONS

The study is considered to evaluate the residual strength under compression with lower PVA fiber content. The study results are suited for air cooled contained instead of water quenching after temperature exposure.

7. FUTURE WORK RECOMMENDATIONS

The following issues should be investigated on how elevated temperatures affect RS-ECC:

The influence of increased fiber content on RS-ECC with different particle sizes on mechanical characteristics both before and after exposure.

The impact of high-temperature on properties of hybrid fibers on RS-ECC with different particle sizes.

8. ACKNOWLEDGEMENTS

The authors expressed gratitude to Ultra Tech Cement and Sika India Pvt. Ltd. for their support.

9. FUNDING

This work was supported by IEI R&D Grant-in-Aid Scheme, India (Grant No. DR2020013), as well as the Ministry of Education, New Delhi.

10. REFERENCES

- Wu, H., Zhang, D., Ellis, B.R. and Li, V.C., "Mechanical behavior of carbonated mgo-based engineered cementitious composite (ecc) after high temperatures exposure", *Cement and Concrete Composites*, Vol. 124, (2021), 104255. doi: 10.1016/j.cemconcomp.2021.104255.
- Sahmaran, M., Li, M. and Li, V.C., "Transport properties of engineered cementitious composites under chloride exposure", *ACI Materials Journal*, Vol. 104, No. 6, (2007), 604-611. doi: 10.14359/18964.
- Yu, K., Guo, Y., Zhang, Y. and Soe, K., "Magnesium oxychloride cement-based strain-hardening cementitious composite: Mechanical property and water resistance", *Construction and Building Materials*, Vol. 261, (2020), 119970. doi: 10.1016/j.conbuildmat.2020.119970.
- Nateghi-A, F. and Ahmadi, M.H., "Prediction of engineered cementitious composite material properties using artificial neural network", *International Journal of Engineering*, Vol. 32, No. 11, (2019), 1534-1542. doi: 10.5829/ije.2019.32.11b.04.
- Al-Hasan, S.J.A., Balamuralikrishnan, R. and Altarawneh, M., "Eco-friendly asphalt approach for the development of sustainable roads", *Journal of Human, Earth, and Future*, Vol. 1, No. 3, (2020), 97-111. doi: 10.28991/hef-2020-01-03-01.
- Şahmaran, M., Özbay, E., Yücel, H.E., Lachemi, M. and Li, V.C., "Effect of fly ash and pva fiber on microstructural damage and residual properties of engineered cementitious composites exposed to high temperatures", *Journal of Materials in Civil Engineering*, Vol. 23, No. 12, (2011), 1735-1745. doi: 10.1061/(ASCE)MT.1943-5533.0000335.
- Du, Q., Wei, J. and Lv, J., "Effects of high temperature on mechanical properties of polyvinyl alcohol engineered cementitious composites (PVA-ECC)", *International Journal of Civil Engineering*, Vol. 16, No. 8, (2018), 965-972. doi: 10.1007/s40999-017-0245-0.
- Liu, J.-C., Tan, K.H. and Fan, S., "Residual mechanical properties and spalling resistance of strain-hardening cementitious composite with class c fly ash", *Construction and Building Materials*, Vol. 181, (2018), 253-265. doi: 10.1016/j.conbuildmat.2018.06.009.
- Pourfalah, S., "Behaviour of engineered cementitious composites and hybrid engineered cementitious composites at high temperatures", *Construction and Building Materials*, Vol. 158, (2018), 921-937. doi: 10.1016/j.conbuildmat.2017.10.077.
- Liu, J.-C. and Tan, K.H., "Fire resistance of strain hardening cementitious composite with hybrid pva and steel fibers", *Construction and Building Materials*, Vol. 135, (2017), 600-611. doi: 10.1016/j.conbuildmat.2016.12.204.
- AL-Radi, H.H.Y., Dejian, S. and Sultan, H.K., "Performance of fiber self compacting concrete at high temperatures", *Civil Engineering Journal*, Vol. 7, No. 12, (2021), 2083-2098. doi: 10.28991/cej-2021-03091779.
- Wang, Z.-b., Han, S., Sun, P., Liu, W.-k. and Wang, Q., "Mechanical properties of polyvinyl alcohol-basalt hybrid fiber engineered cementitious composites with impact of elevated temperatures", *Journal of Central South University*, Vol. 28, No. 5, (2021), 1459-1475. doi: 10.1007/s11771-021-4710-1.
- Benali, R., Mellas, M., Baheddi, M., Mansouri, T. and Boufarh, R., "Physico-mechanical behaviors and durability of heated fiber concrete", *Civil Engineering Journal*, Vol. 7, No. 9, (2021), 1582-1593. doi: 10.28991/cej-2021-03091745.
- Yu, K.-q., Lu, Z.-d. and Yu, J., "Residual compressive properties of strain-hardening cementitious composite with different curing ages exposed to high temperature", *Construction and Building Materials*, Vol. 98, (2015), 146-155. doi: 10.1016/j.conbuildmat.2015.08.041.
- Bhat, P.S., Chang, V. and Li, M., "Effect of elevated temperature on strain-hardening engineered cementitious composites", *Construction and Building Materials*, Vol. 69, (2014), 370-380. doi: 10.1016/j.conbuildmat.2014.07.052.
- Erdem, T.K., "Specimen size effect on the residual properties of engineered cementitious composites subjected to high temperatures", *Cement and Concrete Composites*, Vol. 45, (2014), 1-8. doi: 10.1016/j.cemconcomp.2013.09.019.
- Zeng, D., Cao, M. and Ming, X., "Characterization of mechanical behavior and mechanism of hybrid fiber reinforced cementitious composites after exposure to high temperatures", *Materials and Structures*, Vol. 54, No. 1, (2021), 1-11. doi: 10.1617/s11527-021-01622-z.
- He, J., Wang, Q., Yao, B. and Ho, J., "Impact of elevated temperatures on the performance of high-strength engineered cementitious composite", *Journal of Materials in Civil Engineering*, Vol. 33, No. 9, (2021), 04021222. doi: 10.1061/(asce)mt.1943-5533.0003812.
- Mohammed, B.S., Achara, B.E., Liew, M.S., Alaloul, W. and Khed, V.C., "Effects of elevated temperature on the tensile properties of ns-modified self-consolidating engineered cementitious composites and property optimization using response surface methodology (RSM)", *Construction and Building Materials*, Vol. 206, (2019), 449-469. doi: 10.1016/j.conbuildmat.2019.02.033.
- Sasui, S., Kim, G., Nam, J., van Riessen, A., Hadzima-Nyarko, M., Choe, G., Suh, D. and Jinwuth, W., "Effects of waste glass sand on the thermal behavior and strength of fly ash and ggbs based alkali activated mortar exposed to elevated temperature", *Construction and Building Materials*, Vol. 316, (2022), 125864. doi: 10.1016/j.conbuildmat.2021.125864.
- Sahmaran, M., Lachemi, M., Hossain, K.M., Ranade, R. and Li, V.C., "Influence of aggregate type and size on ductility and mechanical properties of engineered cementitious composites", *ACI Materials Journal*, Vol. 106, No. 3, (2009), 308. doi: 10.14359/56556.
- Pathak, N. and Siddique, R., "Effects of elevated temperatures on properties of self-compacting-concrete containing fly ash and spent foundry sand", *Construction and Building Materials*, Vol. 34, (2012), 512-521. doi: 10.1016/j.conbuildmat.2012.02.026.
- Li, M. and Li, V.C., "Rheology, fiber dispersion, and robust properties of engineered cementitious composites", *Materials*

- and Structures*, Vol. 46, No. 3, (2013), 405-420. doi: 10.1617/s11527-012-9909-z.
24. Choi, J.-I., Lee, B.Y., Ranade, R., Li, V.C. and Lee, Y., "Ultra-high-ductile behavior of a polyethylene fiber-reinforced alkali-activated slag-based composite", *Cement and Concrete Composites*, Vol. 70, (2016), 153-158. doi: 10.1016/j.cemconcomp.2016.04.002.
 25. Nuaklong, P., Worawatnalunart, P., Jongvivatsakul, P., Tangaramvong, S., Pothisiri, T. and Likitlersuang, S., "Pre-and post-fire mechanical performances of high calcium fly ash geopolymer concrete containing granite waste", *Journal of Building Engineering*, Vol. 44, (2021), 103265. doi: 10.1016/j.jobe.2021.103265.
 26. Huang, B.-T., Wu, J.-Q., Yu, J., Dai, J.-G. and Leung, C.K., "High-strength seawater sea-sand engineered cementitious composites (ss-ecc): Mechanical performance and probabilistic modeling", *Cement and Concrete Composites*, Vol. 114, No., (2020), 103740. doi: 10.1016/j.cemconcomp.2020.103740.
 27. Zhu, H., Zhang, D. and Li, V.C., "Centrifugally sprayed engineered cementitious composites: Rheology, mechanics, and structural retrofit for concrete pipes", *Cement and Concrete Composites*, Vol. 129, (2022), 104473. doi: 10.1016/j.cemconcomp.2022.104473.
 28. AbuFarsakh, R., Arce, G., Hassan, M., Huang, O., Radovic, M., Rupnow, T., Mohammad, L.N. and Sukhishvili, S., "Effect of sand type and pva fiber content on the properties of metakaolin based engineered geopolymer composites", *Transportation Research Record*, Vol. 2675, No. 12, (2021), 475-491. doi: 10.1177/03611981211029935.
 29. Liu, H., Zhang, Q., Li, V., Su, H. and Gu, C., "Durability study on engineered cementitious composites (ecc) under sulfate and chloride environment", *Construction and Building Materials*, Vol. 133, (2017), 171-181. doi: 10.1016/j.conbuildmat.2016.12.074.
 30. Sherir, M.A., Hossain, K.M. and Lachemi, M., "Fresh state, mechanical & durability properties of strain hardening cementitious composite produced with locally available aggregates and high volume of fly ash", *Construction and Building Materials*, Vol. 189, (2018), 253-264. doi: 10.1016/j.conbuildmat.2018.08.204.
 31. Yang, E.-H., Yang, Y. and Li, V.C., "Use of high volumes of fly ash to improve ecc mechanical properties and material greenness", *ACI Materials Journal*, Vol. 104, No. 6, (2007), 620. doi: 10.14359/18966.
 32. Kumar, D., Soliman, A.A. and Ranade, R., "Effects of fly ash content and curing age on high temperature residual compressive strength of strain-hardening cementitious composites", in RILEM-fib International Symposium on Fibre Reinforced Concrete, Springer., (2021), 3-12.
 33. Li, Q., Gao, X., Xu, S., Peng, Y. and Fu, Y., "Microstructure and mechanical properties of high-toughness fiber-reinforced cementitious composites after exposure to elevated temperatures", *Journal of materials in civil engineering*, Vol. 28, No. 11, (2016), 04016132. doi: 10.1061/(ASCE)MT.1943-5533.0001647.
 34. Guo, M.-Z., Chen, Z., Ling, T.-C. and Poon, C.S., "Effects of recycled glass on properties of architectural mortar before and after exposure to elevated temperatures", *Journal of cleaner production*, Vol. 101, (2015), 158-164. doi: 10.1016/j.jclepro.2015.04.004.
 35. Miah, M.J., Ali, M.K., Monte, F.L., Paul, S.C., Babafemi, A.J. and Šavija, B., "The effect of furnace steel slag powder on the performance of cementitious mortar at ambient temperature and after exposure to elevated temperatures", in Structures, Elsevier. Vol. 33, (2021), 2811-2823.
 36. Sahmaran, M., Lachemi, M. and Li, V.C., "Assessing mechanical properties and microstructure of fire-damaged engineered cementitious composites", *ACI Materials Journal*, Vol. 107, No. 3, (2010). doi: 10.14359/51663759.

Persian Abstract

کامپوزیت های سیمانی مهندسی شده (ECC) یک مصالح ساختمانی مناسب با خواص بهتر نسبت به بتن معمولی است. در حال حاضر، پس از زلزله، آتش سوزی در یک ساختمان یکی از جدی ترین بلايا است. مقدار و اندازه ماسه مورد استفاده در ECC پارامترهای مهمی برای عملکرد در شرایط حرارتی هستند. ماسه میکرو سیلیس در اکثر آزمایشات ECC مربوط به پاسخ حرارتی استفاده می شود. هدف این مطالعه، بررسی تأثیر شن و ماسه رودخانه (RS) بر عملکرد ECC در معرض افزایش دما تا ۸۰۰ درجه سانتیگراد، از طریق یک سری آزمایش های تجربی بر روی مقاومت فشاری، تلفات جرم، سرعت پالس اولتراسونیک (UPV) و ریزساختار است. برای این منظور، مخلوط هایی با ترکیب RS با اندازه ذرات مختلف (۲.۳۶ میلی متر، ۱.۱۸ میلی متر، ۰.۶۰ میلی متر) به جای ماسه میکرو سیلیس تهیه گردید. در ECC حاوی RS با اندازه های مختلف ذرات، پوسته پوسته شدن وجود ندارد. بر اساس یافته ها، مقاومت فشاری، کاهش جرم و UPV همگی با افزایش دما کاهش می یابند. با این حال، RS-ECC با ۰.۶۰ میلی متر بهتر از ۱.۱۸ میلی متر و ۲.۳۶ میلی متر RS عمل می کند.



Sustainable Utilization of Dumped Concrete Wastes as Fine Aggregates in Concrete – An Experimental Study

J. Sivamani*

Department of Civil Engineering, Sona College of Technology, Salem, Tamilnadu, India

PAPER INFO

Paper history:

Received 23 May 2022

Received in revised form 14 June 2022

Accepted 29 June 2022

Keywords:

Fine Recycled Aggregate

Adhered Mortar

Pre-Saturation

Mortar Mixing Approach

Interfacial Transition Zone

Natural Fine Aggregate

ABSTRACT

Dumped construction waste (municipal solid waste) is a major threat to the environment in recent times due to its abundance in generation resulting from increased construction activities. Perhaps, the scarcity of construction materials is also alarming due to urbanization necessitating an alternative suitable material. Concerning the above complications, this research encompasses the sustainable use of concrete fractions of the construction waste as a suitable replacement for natural fine aggregate (NFA) termed fine recycled aggregate (FRA). However, the use of FRA disrupts the concrete properties due to a weak interfacial transition zone (ITZ) ensuing from the adherence of cement particles and finer dust particles. This study investigates the effective utilization of FRA through the mortar mixing approach (MMA) technique with varying percentages of FRA. The optimum proportion of FRA as a substitute to NFA was observed to be 30%, with an increase in the concrete strength by 7.85%, while it decreased by 23.5% with 100% of FRA at 28 days. Through MMA, the strength of concrete was increased by 9.93%, while it is decreased by 19.45% with 100% of FRA at 28 days. The stiff concrete matrix developed as a result of MMA tends to strengthen the ITZ and improve the strength of concrete.

doi: 10.5829/ije.2022.35.09c.16

1. INTRODUCTION

The generation of construction wastes is rapidly increasing, which necessitated the option of recycling and reuse. European Aggregate Association (EAA) reported that nearly 843 metric tons of construction wastes were generated in 2016, and China reported 2.14 metric tons of construction wastes in 2018 [1, 2]. Also, 30 to 40% of construction and demolition (C&D) wastes among other municipal states, the European union (EU) reports 36%, and the USA reports nearly 67% [3]. Such generated C&D wastes are dumped in the landfills causing environmental degradation. In recent times, the use of FRA as a suitable alternative to NFA is increasing to overcome the effect of its scarcity and in the production of sustainable concrete. However, several research have described the adverse impacts of utilizing construction wastes as aggregates (both coarse

& fine) in concrete owing to its increased porosity ensuing from the smeared cement particles [4-6]. The behaviour of recycled aggregate (both coarse & fine) depends on percentage replacement, size fraction, super plasticizers, source etc.

Concerning to optimal replacement of FRA, Ozbakkaloglu et al. [7] replaced NFA with 97% of FRA and 3% of brick aggregates and observed that substitution of FRA exceeding 25% affects the concrete properties due to its increased porosity. Similarly, Martinez et al. [8] utilized 50, 75 and 100% of recycled concrete, mixed and ceramic fractions as a substitute to NFA and inferred that all three aggregates possess inferior density and higher water absorption (5 to 10%) compared to NFA resulting in sub-stranded concrete properties. However, the study suggests that conforming to the limitations framed by the manufacturers can increase its possibility of utilization even up to 100%. It could be observed that percentage replacement of FRA tend to vary depending on the type of recycled aggregate and its absorption capacity. To counteract the

*Corresponding Author Institutional Email:
jagan.civil@sonatech.ac.in (J. Sivamani)

effect of higher absorption of FRA on concrete properties. Cartuxo et al. [9] used high range superplasticizers with 0, 10, 30, 50 and 100% of FRA and infer that with 100% of FRA, slump was increased to 16%, bulk density was reduced to 3.7%, strength was reduced to 29% and shrinkage was reduced to 57%. However, with the use of high range water reducers, the study observed an improvement in the behaviour of above-mentioned properties due to the compensation of water requirement by FRA with the addition of superplasticizers. However, Zhao et al. [10] prepared recycled aggregate concrete with 0/0.63, 0.63/1.25, 1.25/2.5, 2.5/5 mm fractions of FRA at 0.5 and 0.6 w/c and concluded that higher fineness in FRA resulted in higher water absorption by FRA and thus inferior properties to concrete. Anastasiou et al. [11] observed that optimized utilization of FRA from construction wastes improves the properties of the concrete which in way promotes sustainability in the field of construction. Also, the study observed that higher water absorption by FRA (8%) reduces its replacement level in the concrete.

Vinay Kumar et al. [12] found that the use of FRA beyond 20% reduces the workability and strength of the recycled aggregate concrete (RAC), and in such cases, higher dosage of superplasticizers is required to achieve equivalent slump and better strength. Lizancos et al. [13] analyzed the kinetics of elastic modulus of RAC and its relationship with the strength and reported a negative influence of FRA on the elastic modulus at first 12 hours followed by an equivalent rise in the substitution of FRA with the loss of elastic modulus of the RAC. With respect to the source of collection, Pedro et al. [14] investigated the behaviour of RAC with FRA collected from laboratory and pre-casting plant and observed that increase in substitution of FRA decreases the strength of the RAC irrespective to the source. Fan et al. [15] collected FRA from diverse sources and found that in all cases, with an increase in the FRA, the slump of the RAC decreases, wherein the slump of the RAC reduces from 210 mm to 185 mm. Pereira et al. [16] observed that the reduction in the strength of RAC was counteracted with the addition of superplasticizers, even with higher substitution of FRA. The effect of a decrease in the workability of RAC due to an increase in the porosity of FRA was offset by inclusion of superplasticizers.

Al Hasan et al. [17] investigated the practical implications of recycled materials observed that use of 75% of RCA with 15% of polymer promote sustainable eco-friendly roads with enhanced properties. From the literature review, it is found that all the dependent parameters of recycled aggregates tend to affect the properties of concrete due to the weak ITZ resulting from the higher porosity of FRA.

So, various advanced mixing techniques were developed to overcome the effect of higher porosity of

recycled aggregates. Tam et al. [18] proposed a two-stage mixing approach (TSMA) and observed that the strength of RAC was improved by 12.2% and 6.09% at 28 and 56 days. The study infers that thin slurry developed impregnates into the microcracks on the surface of RCA, filling the pores, improving the ITZ of the RAC, and thus resulting in better strength than normal mixing approach (NMA). Similarly, Tam et al. [19, 20] performed studies with TSMA and observed better properties in RAC even with 100% of recycled aggregates. Kong et al. [21] developed triple mixing approach (TMA) and double mixing approach (DMA) and found that the workability of RAC was equivalent to normal aggregate concrete (NAC), and the strength of RAC was reduced only by 19.4% with DMA and 12.02% with TMA. Liang et al. [22] proposed advanced mixing techniques and observed that RAC manufactured at 0.43 w/c by sand enveloped mixing approach (SEMA) and 0.49 w/c by mortar mixing approach (MMA) exhibit improved strength to RAC even with 100% of RCA.

Thus, it could be observed that advanced mixing techniques tend to improve RAC properties deprived of any treatments to recycle aggregates. However, the above mixing techniques were performed only with RCA, and no studies infer the influence of advanced mixing techniques with FRA. Thus, the present study investigates the properties of RAC with 0%, 10%, 30%, 50%, 70%, and 100% of FRA manufactured by MMA. The behaviour of concrete with different proportions of FRA manufactured by NMA and MMA was investigated by mechanical properties such as compression, tension, flexural and elastic modulus at 7, 14 and 28 days.

2. METHODOLOGY

43 grade ordinary Portland cement (OPC) as per IS 269 (2015) was used as binding material in the study. The properties of OPC determined as per IS 4031 (1988) are summarized in Table 1. The NFA was collected and sieved to 1.18~2.36 mm and NCA was quarried and sieved to 10 mm~20 mm sizes. The specific gravity and water absorption of NCA were found to be in the range of 2.59~2.71 and 0.15%~0.19%. The concrete fractions of the construction wastes were collected from the demolished building at the institution, crushed using a jaw crusher, sieved to 1.18 mm~2.36 mm, and used as FRA. Figure 1 depicts the appearance of FRA and NFA used in the study. It could be observed that the surface of FRA was highly rough and angular compared to NFA. The gradation curves of NFA and FRA are shown in Figure 2. The physical properties of NFA and FRA determined as per IS 383 are given in Table 2. It is found that except for water absorption, all the

characteristics of FRA were found to be within the BIS limitations. The presence of excess silt content ($>5\%$) and smeared cement mortar increases the porosity of FRA [23-25], hence the FRA was surface saturated prior to its utilization in the concrete.

TABLE 1. Properties of OPC

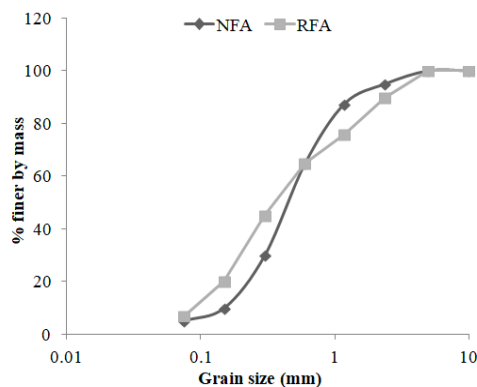
TESTS	RESULTS
Initial set (s)	1500
Final set (s)	34500
Compressive strength (kg/cm ²)	439.90
Consistency (%)	28.6



(a)



(b)

Figure 1. Visual appearance (a) NFA (b) FRA**Figure 2.** Gradation of fine aggregates**TABLE 2.** Properties of fine aggregates

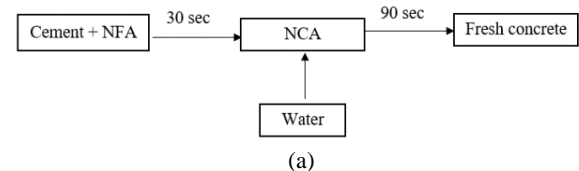
TESTS	NFA	FRA
Relative density	2.65	2.5
Water absorption (%)	0.87	6.93
Bulk density (kg/m ³)	1560	1456
Fineness modulus	3.15	3.79
Silt (%)	2.38	5.67

2. 1. Concrete Mixtures and Testing of Specimens

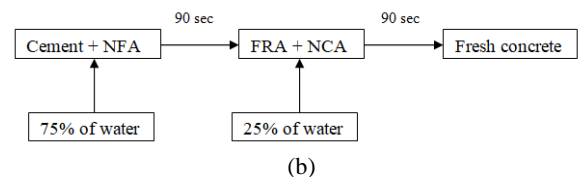
In this study, NMA and MMA technique was adopted to manufacture M20 grade concrete. Figure 3 shows the illustration of the NMA and MMA adopted in the study. The NFA was replaced by 0%, 10%, 30%, 50%, 70%, and 100% of FRA by its weight in the concrete. The quantities of raw materials required for the preparation of concrete mixtures are given in Table 3. The workability of the concrete mixtures with NFA and FRA was determined as per IS 1199 (1999). The compression, tension, flexure and elastic modulus of hardened concrete were evaluated with 100 mm cubes, 100 mm x 200 mm cylinders, and 500 mm x 100 mm x 100 mm prisms at 7, 14, and 28 days as per IS 516 (1959) in triplicate. After the respective ages, the specimens were tested in 1000 kN supporting universal testing machine (UTM) loaded at a 0.5 mm/min rate.

TABLE 3. Mix proportions (1-NMA; 2- MMA)

Materials	(kg/m ³)					
	F-0	F-	F-	F-	F-	F-100
Cement	372	372	372	372	372	372
NFA	829	746.1	580.3	414.5	248.7	0
FRA	0	82.9	248.7	414.5	580.3	829
NCA	1015	1015	1015	1015	1015	1015
w/c ratio	0.5	0.5	0.5	0.5	0.5	0.5
Mixing	1,2	1,2	1,2	1,2	1,2	1,2
Density	2295	2221	2208	2197	2173	2164



(a)



(b)

Figure 3. Schematic illustration of mixing approach (a) NMA (b) MMA

3. RESULTS AND DISCUSSIONS

3. 1. Characterization of Aggregates

Figure 4 shows the XRD images of FRA used in the study. As we know, in NFA, the optimal compound would be quartz (SiO_2) that reacts with the calcium compounds from the cement to form C-S-H and that enhances the concrete's strength. In case of FRA, apart from the presence of quartz, traces of Portlandite (CH) and CaCO_3 owing to the smearance of cement mortar on the FRA were identified. Figure 5 shows the microstructure images of NFA and FRA magnified at $2\mu\text{m}$. The observations on the microstructure image of NFA indicate irregular, angular and spherical-shaped particles. The observations on the SEM image of FRA indicate high angular shaped particles with pores and microcracks on the surface due to the different stages involved in crushing the large size concrete boulders into finer fractions.

3. 2. Workability

The workability of the concrete mixtures is shown in Figure 6. The workability of the concrete reduces with increment in the percentage of FRA. This is due to the incidence of excess fine particles and adherence of mortar, thus increasing the

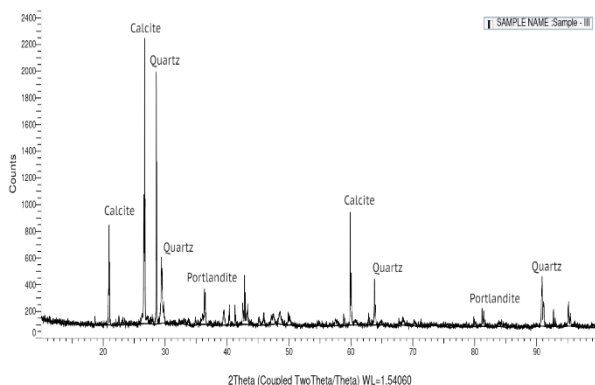
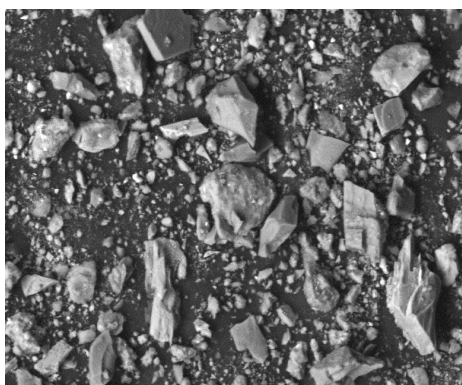
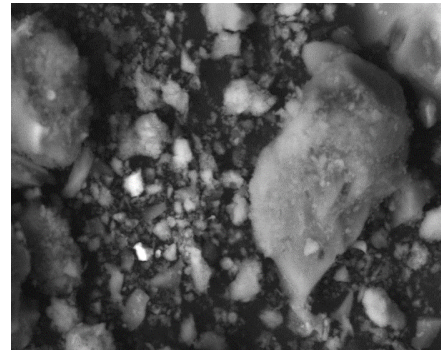


Figure 4. XRD pattern of FRA



(a)



(b)

Figure 5. SEM images (a) NFA (b) FRA

FRA's porosity and decreasing the workability of the concrete mixes [26, 27]. So, the FRA was pre-saturated for 24 hours and dried up for 5 hours to attain surface saturated dry density condition. Upon pre-saturation, improvement in the workability of the concrete was observed. The pre-saturation of FRA prevents the additional water absorption by the FRA particles during concrete mixing. With MMA, the workability of the concrete tends to improve further. This is because the stiff less-porous mortar developed due to MMA coats the FRA particles, impregnates and seals the microcracks on the adhered surface of FRA particles. This, in turn, reduces the additional water requirement by FRA particles during mixing and thus improving the workability.

3. 3. Mechanical Properties

The mechanical properties such as compressive strength, split tensile strength, flexural strength and elastic modulus determined at 7, 14 and 28 days for NMA and MMA; data are stated in Tables 4 and 5.

3. 3. 1. Improvement in Mechanical Properties

Figure 7 shows the percentage improvement in the mechanical properties of MMA mixes compared NMA

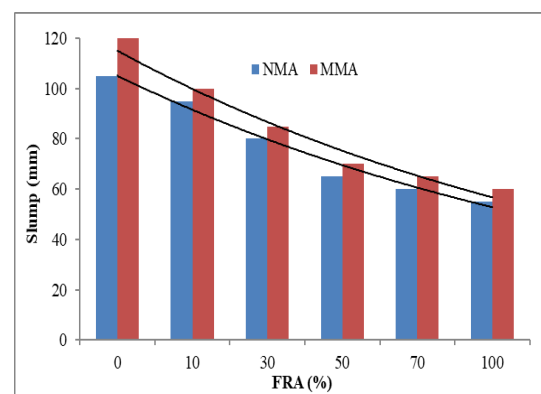


Figure 6. Workability of concrete mixes

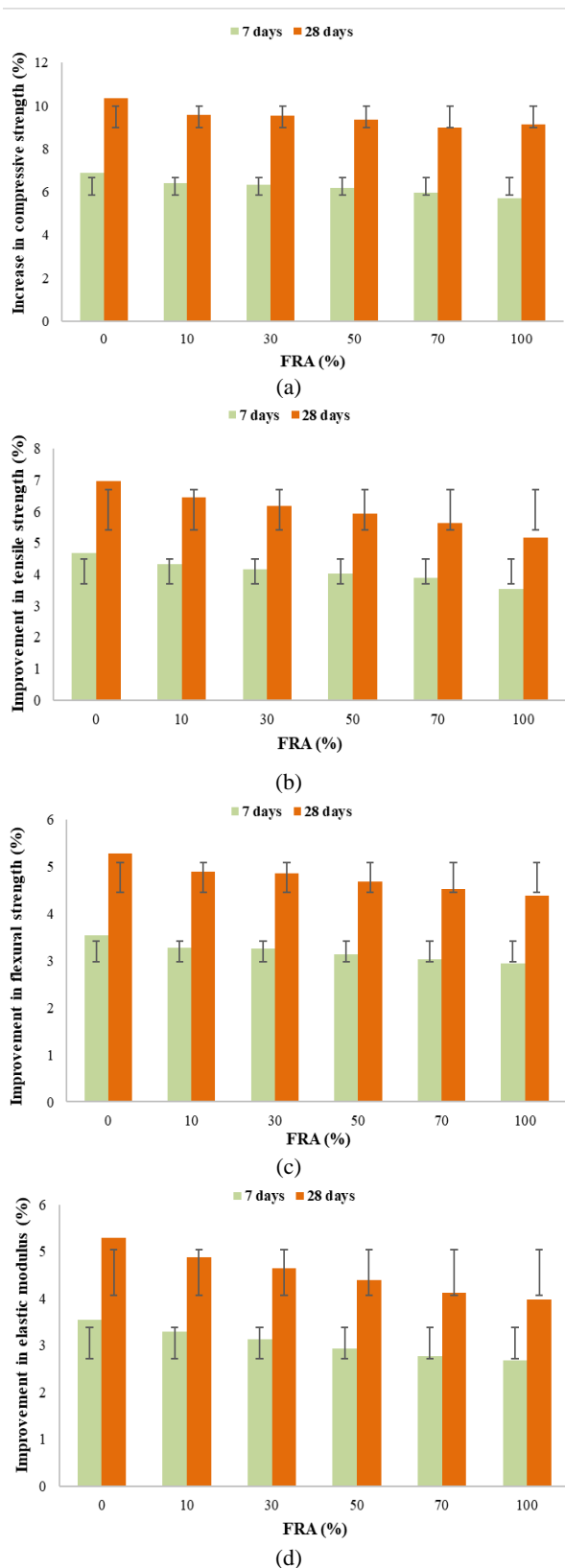


Figure 7. Improvement in the mechanical properties at 7 and 28 days (a) Compressive strength (b) Tensile strength (c) Flexural strength (d) Elastic modulus

mixes. The mechanical properties of the concrete reduce with increase in the replacement of FRA. The optimal proportion of FRA in the concrete was found to be 30%. The compressive strength of F – 10 and F – 30 was 7.05% and 8.57% higher than F – 0 at 7 days and 9.48% and 9.93% higher than F – 0 at 28 days. This is due to the higher angularity of FRA and effective particle packing of FRA with NFA [24]. However, the replacement of FRA beyond 30% decreases the strength of FRA mixes. The compressive strength of F – 50, F – 70, and F – 100 were 15.81%, 22%, and 23.50% less than F – 0 at 28 days. Such reduction is owing to the increased perviousness of FRA ensuing from the presence of smeared cement particles and high dust content [13, 22, 28]. However, with MMA, the compressive strength of the FRA mixes is found to be more than NMA mixes. The compressive strength of F – 10 and F – 30 mixes prepared by MMA was found to be 16.41% and 17.04% higher compared to F – 0 mix prepared by NMA at 7 days and 17.25% and 17.89% higher compared to F – 0 mix prepared by NMA at 28 days. Similarly, the compressive strength of F – 50, F – 70, F – 100 mixes prepared by MMA was only 6.15%, 12.96%, 15.09% less than the F – 0 mixes prepared by NMA at 28 days.

The tensile strength of F – 10 and F – 30 was 4.48% and 5.64% higher than F – 0 at 7 days and 6.52% and 6.93% higher than F – 0 at 28 days. However, similar to compressive strength, substitution of FRA beyond 30% reduces the tensile strength of FRA mixes also. The tensile strength of F – 50, F – 70, and F – 100 were 10.89%, 14.85%, and 16.17% less than F – 0 at 28 days. The smearance of cement particles on the FRA increases its porosity and thus reducing the split tensile strength of the concrete [12, 15]. Nevertheless, with MMA, the tensile strength of the FRA mixes is found to be more than NMA mixes. The strength of F – 10 and F – 30 mixes prepared by MMA was found to be 11.02% and 11.69% higher compared to F – 0 mix prepared by NMA at 7 days and 11.91% and 12.42% higher compared to F – 0 mix prepared by NMA at 28 days. Similarly, the strength of F – 50, F – 70, F – 100 mixes prepared by MMA was only 4.29%, 8.91%, 10.23% less than the F – 0 mixes prepared by NMA at 28 days.

The flexural strength of F – 10 and F – 30 was 3.63% and 4.50% higher than F – 0 at 7 days and 4.91% and 5.14% more than F – 0 at 28 days. However, similar to compressive strength, replacement of FRA beyond 30% decrease the flexural strength of FRA mixes. The flexural strength of F – 50, F – 70, and F – 100 were 8.26%, 11.36%, and 12.40% less than F – 0 at 28 days. The microcracks on the adhered surface of FRA absorb more water and thus leaving only less water for concrete mixing. This reduces the workability of the concrete and thus affects the flexural strength of the FRA mixes [26, 29]. Though with MMA, the flexural strength of the

TABLE 4. Mechanical properties for NMA

FRA (%)	COMPRESSIVE STRENGTH (MPa)			TENSILE STRENGTH (MPa)			FLEXURAL STRENGTH (MPa)			ELASTIC MODULUS (GPa)		
	7days	14days	28days	7days	14days	28days	7days	14days	28days	7days	14days	28days
0	20.68	27.48	30.55	2.34	2.82	3.03	3.18	3.67	3.87	22.74	26.21	27.64
10	22.25	30.37	33.75	2.45	3.02	3.24	3.30	3.86	4.07	23.58	27.55	29.05
30	22.62	30.52	33.92	2.48	3.03	3.25	3.33	3.87	4.08	23.78	27.62	29.12
50	17.41	23.14	25.72	2.08	2.52	2.70	2.92	3.37	3.55	20.86	24.05	25.36
70	16.13	21.63	24.07	1.98	2.41	2.58	2.81	3.26	3.43	20.08	23.25	24.53
90	15.82	21.11	23.46	1.95	2.37	2.54	2.78	3.22	3.39	19.89	22.97	24.22
100	20.68	27.48	30.55	2.34	2.82	3.03	3.18	3.67	3.87	22.74	26.21	27.64

TABLE 5. Mechanical properties for MMA

FRA (%)	COMPRESSIVE STRENGTH (MPa)			TENSILE STRENGTH (MPa)			FLEXURAL STRENGTH (MPa)			ELASTIC MODULUS (GPa)		
	7days	14days	28days	7days	14days	7days	14days	28days	7days	7days	7days	14days
0	20.68	27.48	30.55	2.34	2.82	3.03	3.18	3.67	3.87	22.74	26.21	27.64
10	22.25	30.37	33.75	2.45	3.02	3.24	3.30	3.86	4.07	23.58	27.55	29.05
30	22.62	30.52	33.92	2.48	3.03	3.25	3.33	3.87	4.08	23.78	27.62	29.12
50	17.41	23.14	25.72	2.08	2.52	2.70	2.92	3.37	3.55	20.86	24.05	25.36
70	16.13	21.63	24.07	1.98	2.41	2.58	2.81	3.26	3.43	20.08	23.25	24.53
90	15.82	21.11	23.46	1.95	2.37	2.54	2.78	3.22	3.39	19.89	22.97	24.22
100	20.68	27.48	30.55	2.34	2.82	3.03	3.18	3.67	3.87	22.74	26.21	27.64

FRA mixes is found to be more than NMA mixes. The strength of F – 10 and F – 30 mixes prepared by MMA was found to be 8.62% and 9.14% higher compared to F – 0 mix prepared by NMA at 7 days and 8.94% and 9.36% more compared to F – 0 mix prepared by NMA at 28 days. Similarly, the flexural strength of F – 50, F – 70, F – 100 mixes prepared by MMA was only 3.10%, 6.45%, 7.75% less than F – 0 mix prepared by NMA at 28 days.

The elastic modulus of F – 10 and F – 30 was 3.59% and 4.38% higher than F – 0 at 7 days and 4.87% and 5.11% more than F – 0 at 28 days. However, replacement of FRA beyond 30% decreases the elastic modulus of FRA mixes. The elastic modulus of F – 50, F – 70, and F – 100 were 9.17%, 12.34%, and 13.87% less than F – 0 at 28 days. The smearance of old mortar on the FRA disrupts its adherence with the new matrix, reducing the stiffness and thus reducing the elastic modulus of the concrete. When the concrete mixes are prepared by MMA, the elastic modulus of the FRA mixes is found to be more than NMA mixes. The elastic

modulus of F – 10 and F – 30 mixes prepared by MMA was found to be 8.53% and 8.71% higher compared to F – 0 mix prepared by NMA at 7 days and 9.01% and 9.73% more compared to F – 0 mix prepared by NMA at 28 days. Similarly, the elastic modulus of F – 50, F – 70 and F – 100 mixes prepared by MMA was only 3.14%, 6.72%, 7.94% less than F – 0 mix prepared by NMA at 28 days.

Various studies infer that inferior quality of FRA was due to its higher perviousness ensuing from the smearance of cement particles on the surface of FRA. So, the FRA was pre-saturated and even after pre-saturation, higher perviousness of FRA weakens the ITZ of the concrete and thus affecting the properties of concrete. However, even after pre-saturation, no improvement in the properties were observed as in previous studies [8, 15] and so the concrete mixtures were prepared by MMA. Liang et al. [22] developed the MMA approach for RCA wherein a stiff non-porous matrix was developed under two stages of mixing, filling the microcracks on the surface of RCA. The same

technique was implemented in this study with FRA particles. Upon mixing, it is observed that the stiff non-porous matrix formed during the first stage covers the FRA particles added during the second stage and finally develops a dense concrete structure with fewer voids. The hardened concrete prepared by MMA was evaluated for its compressive strength, split tensile strength, and flexural strength at 7, 14, and 28 days. The results indicate the optimum replacement of FRA as 30% for both NMA and MMA mixes. However, at all replacement percentages and various curing period, MMA mixes show improved properties than NMA. This is attributed to the densification of ITZ in RAC mixes owing to MMA. The FRA concrete mixes comprise dual ITZ, the former among the new matrix and FRA and the latter among the old matrix and the new matrix. Since the latter is the weakest zone with micro-cracks that affect the concrete's strength, the MMA technique was developed. The MMA approach develops a solid matrix that enhances the weak ITZ and thus improves the hardened properties of the concrete.

4. CONCLUSIONS

The effect of NMA and MMA on the properties of FRA concrete was studied, and the results were compared with NFA concrete. Nevertheless, higher porosity of FRA resulting from increased replacement affects the properties of the concrete. Based on the investigation, the following conclusions are drawn as follows:

1. All the properties of FRA were equivalent to NFA, whereas the water absorption of FRA (6.93%) was 87.44% higher than the NFA (0.87%) owing to the adhered mortar and thus affecting the concrete properties.
2. The optimal proportion of FRA for NFA in the concrete was observed to be 30% as far as it affects the properties of the concrete.
3. An increase in the substitution of FRA affects the workability of the concrete, owing to its inferior properties ensuing from the smearance of cement particles on its surface. Even though the workability of MMA mixes reduces with an increase in the FRA, but the values are higher than NMA mixes.
4. The compressive strength, tensile strength, flexural strength and elastic modulus of concrete mixtures with optimal percentage of FRA prepared to MMA was 17.04%, 12.42%, 9.36% and 9.73% more compared to the NMA at 28 days. However, with 100%, the properties of MMA mixed was reduced by only 15.09%, 10.23%, 7.75% and 7.94% at 28 days.
5. The concrete manufactured by MMA technique perform better in terms of fresh and hardened

properties than NMA mixes at various replacement levels and curing ages.

This study could provide a clear evident on enhancement in the RAC properties by variation in the mixing approaches even at high replacement of FRA. Further research on its durability aspects would promote the utilization practice of FRA in industries and thus counteracting the consequence of shortage of river sand and ensuing the sustainability in the construction.

5. REFERENCES

1. Arenas, C., Luna-Galiano, Y., Leiva, C., Vilches, L., Arroyo, F., Villegas, R. and Fernández-Pereira, C., "Development of a fly ash-based geopolymeric concrete with construction and demolition wastes as aggregates in acoustic barriers", *Construction and Building Materials*, Vol. 134, (2017), 433-442. <https://doi.org/10.1016/j.conbuildmat.2016.12.119>
2. Xiao, J., Li, W., Fan, Y. and Huang, X., "An overview of study on recycled aggregate concrete in china (1996–2011)", *Construction and Building Materials*, Vol. 31, (2012), 364-383. <https://doi.org/10.1016/j.conbuildmat.2011.12.074>
3. Ginga, C.P., Ongpeng, J.M.C., Daly, M. and Klarissa, M., "Circular economy on construction and demolition waste: A literature review on material recovery and production", *Materials*, Vol. 13, No. 13, (2020), 2970. doi: 10.3390/ma13132970.
4. Sim, J. and Park, C., "Compressive strength and resistance to chloride ion penetration and carbonation of recycled aggregate concrete with varying amount of fly ash and fine recycled aggregate", *Waste Management*, Vol. 31, No. 11, (2011), 2352-2360. <https://doi.org/10.1016/j.wasman.2011.06.014>
5. Zega, C.J. and Di Maio, Á.A., "Use of recycled fine aggregate in concretes with durable requirements", *Waste Management*, Vol. 31, No. 11, (2011), 2336-2340. <https://doi.org/10.1016/j.wasman.2011.06.011>
6. Pedro, D.d., De Brito, J. and Evangelista, L., "Structural concrete with simultaneous incorporation of fine and coarse recycled concrete aggregates: Mechanical, durability and long-term properties", *Construction and Building Materials*, Vol. 154, (2017), 294-309. <https://doi.org/10.1016/j.conbuildmat.2017.07.215>
7. Ozbakkaloglu, T., Gholampour, A. and Xie, T., "Mechanical and durability properties of recycled aggregate concrete: Effect of recycled aggregate properties and content", *Journal of Materials in Civil Engineering*, Vol. 30, No. 2, (2018), 04017275. doi: 10.1061/(ASCE)MT.1943-5533.0002142.
8. Martínez, P.S., Cortina, M.G., Martínez, F.F. and Sánchez, A.R., "Comparative study of three types of fine recycled aggregates from construction and demolition waste (CDW), and their use in masonry mortar fabrication", *Journal of Cleaner Production*, Vol. 118, (2016), 162-169. <https://doi.org/10.1016/j.jclepro.2016.01.059>
9. Cartuxo, F., De Brito, J., Evangelista, L., Jimenez, J.R. and Ledesma, E., "Rheological behaviour of concrete made with fine recycled concrete aggregates—influence of the superplasticizer", *Construction and Building Materials*, Vol. 89, (2015), 36-47. <https://doi.org/10.1016/j.conbuildmat.2015.03.119>
10. Zhao, Z., Remond, S., Damidot, D. and Xu, W., "Influence of fine recycled concrete aggregates on the properties of mortars", *Construction and Building Materials*, Vol. 81, (2015), 179-186. <https://doi.org/10.1016/j.conbuildmat.2015.02.037>

11. Anastasiou, E., Filikas, K.G. and Stefanidou, M., "Utilization of fine recycled aggregates in concrete with fly ash and steel slag", *Construction and Building Materials*, Vol. 50, (2014), 154-161. <https://doi.org/10.1016/j.conbuildmat.2013.09.037>
12. Kumar, B.V., Ananthan, H. and Balaji, K., "Experimental studies on utilization of recycled coarse and fine aggregates in high performance concrete mixes", *Alexandria Engineering Journal*, Vol. 57, No. 3, (2018), 1749-1759. <https://doi.org/10.1016/j.aej.2017.05.003>
13. Velay-Lizancos, M., Martinez-Lage, I., Azenha, M., Granja, J. and Vazquez-Burgo, P., "Concrete with fine and coarse recycled aggregates: E-modulus evolution, compressive strength and non-destructive testing at early ages", *Construction and Building Materials*, Vol. 193, (2018), 323-331. <https://doi.org/10.1016/j.conbuildmat.2018.10.209>
14. Pedro, D., De Brito, J. and Evangelista, L., "Performance of concrete made with aggregates recycled from precasting industry waste: Influence of the crushing process", *Materials and Structures*, Vol. 48, No. 12, (2015), 3965-3978. <https://doi.org/10.1617/s11527-014-0456-7>
15. Fan, C.-C., Huang, R., Hwang, H. and Chao, S.-J., "Properties of concrete incorporating fine recycled aggregates from crushed concrete wastes", *Construction and Building Materials*, Vol. 112, (2016), 708-715. <https://doi.org/10.1016/j.conbuildmat.2016.02.154>
16. Pereira, P., Evangelista, L. and De Brito, J., "The effect of superplasticizers on the mechanical performance of concrete made with fine recycled concrete aggregates", *Cement and Concrete Composites*, Vol. 34, No. 9, (2012), 1044-1052. <https://doi.org/10.1016/j.cemconcomp.2012.06.009>
17. Al-Hasan, S.J.A., Balamuralikrishnan, R. and Altarawneh, M., "Eco-friendly asphalt approach for the development of sustainable roads", *Journal of Human, Earth, and Future*, Vol. 1, No. 3, (2020), 97-111. doi: 10.28991/HEF-2020-01-03-01.
18. Tam, V.W., Gao, X. and Tam, C.M., "Microstructural analysis of recycled aggregate concrete produced from two-stage mixing approach", *Cement and Concrete Research*, Vol. 35, No. 6, (2005), 1195-1203. <https://doi.org/10.1016/j.cemconres.2004.10.025>
19. Tam, V.W. and Tam, C.M., "Assessment of durability of recycled aggregate concrete produced by two-stage mixing approach", *Journal of Materials Science*, Vol. 42, No. 10, (2007), 3592-3602. <https://doi.org/10.1007/s10853-006-0379-y>
20. Tam, V.W., Wang, K. and Tam, C.M., "Assessing relationships among properties of demolished concrete, recycled aggregate and recycled aggregate concrete using regression analysis", *Journal of Hazardous Materials*, Vol. 152, No. 2, (2008), 703-714. doi: <https://doi.org/10.1016/j.jhazmat.2007.07.061>
21. Kong, D., Lei, T., Zheng, J., Ma, C., Jiang, J. and Jiang, J., "Effect and mechanism of surface-coating pozzalanic materials around aggregate on properties and itz microstructure of recycled aggregate concrete", *Construction and Building Materials*, Vol. 24, No. 5, (2010), 701-708. <https://doi.org/10.1016/j.conbuildmat.2009.10.038>
22. Liang, Y.-c., Ye, Z.-m., Vernerey, F. and Xi, Y., "Development of processing methods to improve strength of concrete with 100% recycled coarse aggregate", *Journal of Materials in Civil Engineering*, Vol. 27, No. 5, (2015), 04014163.
23. Berredjem, L., Arabi, N. and Molez, L., "Mechanical and durability properties of concrete based on recycled coarse and fine aggregates produced from demolished concrete", *Construction and Building Materials*, Vol. 246, (2020), 118421. doi: <https://doi.org/10.1016/j.conbuildmat.2020.118421>
24. Kirthika, S. and Singh, S., "Durability studies on recycled fine aggregate concrete", *Construction and Building Materials*, Vol. 250, (2020), 118850. <https://doi.org/10.1016/j.conbuildmat.2020.118850>
25. Cho, S.-W., "Effect of silt fines on the durability properties of concrete", *Journal of Applied Science and Engineering*, Vol. 16, No. 4, (2013), 425-430. <https://doi.org/10.6180/jase.2013.16.4.10>
26. Li, L., Zhan, B.J., Lu, J. and Poon, C.S., "Systematic evaluation of the effect of replacing river sand by different particle size ranges of fine recycled concrete aggregates (FRCA) in cement mortars", *Construction and Building Materials*, Vol. 209, (2019), 147-155. <https://doi.org/10.1016/j.conbuildmat.2019.03.044>
27. Leite, M. and Santana, V., "Evaluation of an experimental mix proportion study and production of concrete using fine recycled aggregate", *Journal of Building Engineering*, Vol. 21, (2019), 243-253. <https://doi.org/10.1016/j.jobe.2018.10.016>
28. Khatib, J.M., "Properties of concrete incorporating fine recycled aggregate", *Cement and Concrete Research*, Vol. 35, No. 4, (2005), 763-769. <https://doi.org/10.1016/j.cemconres.2004.06.017>
29. Evangelista, L. and De Brito, J., "Durability performance of concrete made with fine recycled concrete aggregates", *Cement and Concrete Composites*, Vol. 32, No. 1, (2010), 9-14. <https://doi.org/10.1016/j.cemconcomp.2009.09.005>

Persian Abstract

چکیده

پسماند جامد شهری به دلیل تولید فراوان ناشی از افزایش فعالیت های عمرانی، تهدیدی بزرگ برای محیط زیست در دوران اخیر محسوب می شود. شاید کمبود مصالح ساختمانی نیز به دلیل شهرنشینی که نیاز به مصالح مناسب جایگزین دارد، نگران کننده باشد. با توجه به عوارض فوق، این تحقیق استفاده پایدار از قطعات بتنی زباله های ساختمانی را به عنوان جایگزین مناسب برای سنگدانه های ریز طبیعی (NFA) که به عنوان سنگدانه بازیافتی ریز (FRA) نامیده می شود، در بر می گیرد. با این حال، استفاده از FRA به دلیل افزایش تخلخل ناشی از چسبیدن ذرات سیمان و ذرات ریز گرد و غبار، خواص بتن را مختل می کند. همچنین، مطالعات متعددی به عملکرد ضعیف بتن به دلیل ضعف ناحیه انتقال سطحی (ITZ) در نتیجه ملات چسبیده اشاره کرده اند. بنابراین، این مطالعه با هدف بررسی استفاده موثر از FRA برای تهیه مخلوط بتن با خواص افزایش یافته است. بخش های بتنی زباله های ساختمانی از دانشگاه جمع آوری و خرد شد تا FRA آماده شود. هر دو FRA و NFA از قبل اشباع شده بودند و مخلوط های بتن با روش اختلاط ملات (MMA) با درصدهای متفاوت FRA تهیه می شوند. تأثیر FRA در بتن از طریق کارایی، مقاومت فشاری، مقاومت کششی، مقاومت خمشی و مدول الاستیک بررسی شد. نسبت بهینه FRA به عنوان جایگزین 30 NFA % با افزایش مقاومت بتن 9.93 % مشاهده شد، در حالی که با 100 % FRA در 28 روز 23.5 % کاهش یافت.

AIMS AND SCOPE

The objective of the International Journal of Engineering is to provide a forum for communication of information among the world's scientific and technological community and Iranian scientists and engineers. This journal intends to be of interest and utility to researchers and practitioners in the academic, industrial and governmental sectors. All original research contributions of significant value focused on basics, applications and aspects areas of engineering discipline are welcome.

This journal is published in three quarterly transactions: Transactions A (Basics) deal with the engineering fundamentals, Transactions B (Applications) are concerned with the application of the engineering knowledge in the daily life of the human being and Transactions C (Aspects) - starting from January 2012 - emphasize on the main engineering aspects whose elaboration can yield knowledge and expertise that can equally serve all branches of engineering discipline.

This journal will publish authoritative papers on theoretical and experimental researches and advanced applications embodying the results of extensive field, plant, laboratory or theoretical investigation or new interpretations of existing problems. It may also feature - when appropriate - research notes, technical notes, state-of-the-art survey type papers, short communications, letters to the editor, meeting schedules and conference announcements. The language of publication is English. Each paper should contain an abstract both in English and in Persian. However, for the authors who are not familiar with Persian, the publisher will prepare the latter. The abstracts should not exceed 250 words.

All manuscripts will be peer-reviewed by qualified reviewers. The material should be presented clearly and concisely:

- *Full papers* must be based on completed original works of significant novelty. The papers are not strictly limited in length. However, lengthy contributions may be delayed due to limited space. It is advised to keep papers limited to 7500 words.
- *Research notes* are considered as short items that include theoretical or experimental results of immediate current interest.
- *Technical notes* are also considered as short items of enough technical acceptability with more rapid publication appeal. The length of a research or technical note is recommended not to exceed 2500 words or 4 journal pages (including figures and tables).

Review papers are only considered from highly qualified well-known authors generally assigned by the editorial board or editor in chief. Short communications and letters to the editor should contain a text of about 1000 words and whatever figures and tables that may be required to support the text. They include discussion of full papers and short items and should contribute to the original article by providing confirmation or additional interpretation. Discussion of papers will be referred to author(s) for reply and will concurrently be published with reply of author(s).

INSTRUCTIONS FOR AUTHORS

Submission of a manuscript represents that it has neither been published nor submitted for publication elsewhere and is result of research carried out by author(s). Presentation in a conference and appearance in a symposium proceeding is not considered prior publication.

Authors are required to include a list describing all the symbols and abbreviations in the paper. Use of the international system of measurement units is mandatory.

- On-line submission of manuscripts results in faster publication process and is recommended. Instructions are given in the IJE web sites: www.ije.ir-www.ijeir.info
- Hardcopy submissions must include MS Word and jpg files.
- Manuscripts should be typewritten on one side of A4 paper, double-spaced, with adequate margins.
- References should be numbered in brackets and appear in sequence through the text. List of references should be given at the end of the paper.
- Figure captions are to be indicated under the illustrations. They should sufficiently explain the figures.
- Illustrations should appear in their appropriate places in the text.
- Tables and diagrams should be submitted in a form suitable for reproduction.
- Photographs should be of high quality saved as jpg files.
- Tables, Illustrations, Figures and Diagrams will be normally printed in single column width (8cm). Exceptionally large ones may be printed across two columns (17cm).

PAGE CHARGES AND REPRINTS

The papers are strictly limited in length, maximum 8 journal pages (including figures and tables). For the additional to 8 journal pages, there will be page charges. It is advised to keep papers limited to 3500 words.

Page Charges for Papers More Than 8 Pages (Including Abstract)

For International Author ***	\$55 / per page
For Local Author	100,000 Toman / per page

AUTHOR CHECKLIST

- Author(s), bio-data including affiliation(s) and mail and e-mail addresses).
- Manuscript including abstracts, key words, illustrations, tables, figures with figure captions and list of references.
- MS Word files of the paper.



Scopus®

